Strojniški vestnik

Journal of Mechanical Engineering

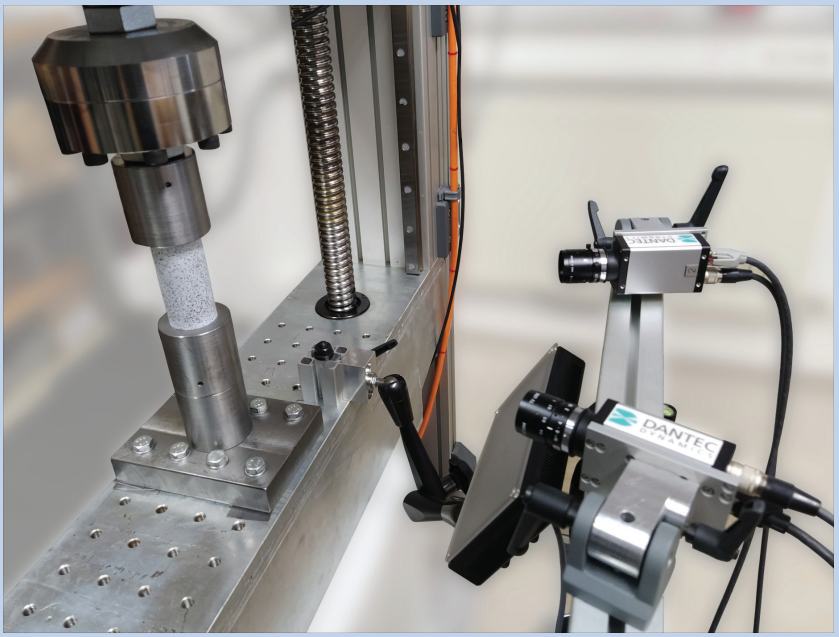

no. 5-6
year 2024
volume 70

Strojniški vestnik – Journal of Mechanical Engineering (SV-JME)

Aim and Scope
The international journal publishes original and (mini)review articles covering the concepts of materials science, mechanics, kinematics, thermodynamics, energy and environment, mechatronics and robotics, fluid mechanics, tribology, cybernetics, industrial engineering and structural analysis.
The journal follows new trends and progress proven practice in the mechanical engineering and also in the closely related sciences as are electrical, civil and process engineering, medicine, microbiology, ecology, agriculture, transport systems, aviation, and others, thus creating a unique forum for interdisciplinary or multidisciplinary dialogue.
The international conferences selected papers are welcome for publishing as a special issue of SV-JME with invited co-editor(s).

Editorial Office
University of Ljubljana, Faculty of Mechanical Engineering
SV-JME, Aškerčeva 6, SI-1000 Ljubljana, Slovenia
Phone: 386 (0)1 4771 137
Fax: 386 (0)1 2518 567
info@sv-jme.eu, http://www.sv-jme.eu

Print: Demat d.o.o., printed in 240 copies

Founders and Publishers
University of Ljubljana, Faculty of Mechanical Engineering, Slovenia
University of Maribor, Faculty of Mechanical Engineering, Slovenia
Association of Mechanical Engineers of Slovenia
Chamber of Commerce and Industry of Slovenia, Metal Processing Industry Association

Cover:
Uniaxial compression test of cylindrical sandstone specimen with stereo DIC measurement setup (top). Cylindrical sandstone specimen (bottom left). Cylindrical sandstone specimen with random speckle pattern applied for strain measurement with DIC (bottom centre). Numerical model of sandstone specimen with inhomogenous structure containing random inclusions (bottom right).

Image Courtesy:
University of Ljubljana, Faculty of Mechanical Engineering, Laboratory for numerical modelling and simulation, Slovenia

General information
Strojniški vestnik – Journal of Mechanical Engineering is published in 6 double issues per year.

Institutional prices include print & online access: institutional subscription price and foreign subscription €100,00 (the price of a single issue is €10,00); general public subscription and student subscription €50,00 (the price of a single issue is €5,00). Prices are exclusive of tax. Delivery is included in the price. The recipient is responsible for paying any import duties or taxes. Legal title passes to the customer on dispatch by our distributor. Single issues from current and recent volumes are available at the current single-issue price. To order the journal, please complete the form on our website. For submissions, subscriptions and all other information please visit: *http://www.sv-jme.eu.*

You can advertise on the inner and outer side of the back cover of the journal. The authors of the published papers are invited to send photos or pictures with short explanation for cover content.

We would like to thank the reviewers who have taken part in the peer-review process.

ISSN 0039-2480, ISSN 2536-2948 (online)

The journal is subsidized by Slovenian Research and Inovation Agency.

SV-JME is indexed / abstracted in: SCI-Expanded, Compendex, Inspec, ProQuest-CSA, SCOPUS, TEMA. The list of the remaining bases, in which SV-JME is indexed, is available on the website.

Strojniški vestnik - Journal of Mechanical Engineering is available on *https://www.sv-jme.eu*.

Contents

Strojniški vestnik - Journal of Mechanical Engineering
volume 70, (2024), number 5-6
Ljubljana, May-June 2024
ISSN 0039-2480

Published every two months

Papers

Strojniški vestnik - Journal of Mechanical Engineering 70(2024)5-6, 211-222
DOI:10.5545/sv-jme.2024.966
Original Scientific Paper
Received for review: 2024-02-29
Received revised form: 2024-03-08
Accepted for publication: 2024-03-26

On Experimental Determination of Poisson's Ratio for Rock-like Materials using Digital Image Correlation

Pino Koc*
University of Ljubljana, Faculty of Mathematics and Physics, Slovenia

This article compares the two most used strain determination experimental techniques, the strain gauges and the digital image correlation (DIC), which are used here to determine the static Poisson's ratio of rock-like materials under a compressive loading. While the strain gauge technique measures the strains on the small patch of the underlying material on the spot, where the strain gauge is applied, DIC is a novel optical full-field technique that can measure the strains over the entire region of interest of the specimen. The key research question presented in this paper and research significance is to what extent the measurement of Poisson's ratio is improved by leveraging the richness of the full-field measurements compared to the conventional strain gauge technique. To this purpose, the hypothesis was tested through virtual experiments in which a numerical simulation of a uniaxial compression test with a cylindrical, rock-like sample was created to mimic the strain gauge and DIC measurement techniques, as well as by conducting an actual compression test on a sandstone material. In contrast to conventional strain gauges, novel optical techniques such as stereo DIC proved to be able to capture the macroscopic Poisson coefficient with higher precision, thus reducing the margin of error.

Keywords: Poisson's ratio, digital image correlation, strain gauge, rock-like materials, uniaxial compression test

Highlights

- *The concept of virtual experimentation is used to compare strain gauge and DIC techniques to evaluate the standard deviation of the reconstructed population of Poisson's ratio.*
- *To measure the Poisson's ratio and compare both techniques, a uniaxial compression test was performed on a cylindrical sandstone sample.*
- *In contrast to conventional strain gauges, novel optical techniques such as stereo DIC proved to be able to measure the macroscopic Poisson's ratio with a higher precision.*
- *Since the determination is influenced by signal-to-noise ratio, a simple engineering criterion for calculation is proposed.*

0 INTRODUCTION

The rock mass is a diverse geological material typically characterized by numerous intrinsic defects such as cracks, joints, bedding planes, and faults embedded in aggregates of crystals and amorphous particles bound by varying amounts of cementing materials [1] and [2]. These intrinsic inhomogeneities contribute to a heterogeneous microstructural response at the microscale, often resulting in complex material behaviour [3]. To accurately model the macroscopic response of such rock structures, a homogenization principle using a representative volume element (RVE) [4] and [5] is commonly applied [6] and [7] to predict the effective material behaviour at the macroscale [8] and [9]. Such models are based on bonded particle modelling techniques that have been proposed to account for different mechanical responses and behaviours of geomaterials [10]. For example, Zhou et al. [11] and [12] comprehensively investigated the importance of modelling the internal microstructure and interaction effects through bonded particle model–μ-discrete fracture network (BPM–μDFN) modelling to analyse the size effect and associated strength variability for rock considering the microstructure and strain rate.

Typically, in such models a set of material parameters must be determined from an experimental response of corresponding mechanical test [13]. For this purpose, contact and noncontact techniques can be used to measure the mechanical response, and specifically, with an advent development of optical technologies, new possibilities for material characterization have been opened. The use of 3D scanners and cameras enabled a precise measurement of displacements and strains of the tested sample, enabling engineers to assess material behaviour [14] and [15] and to make informed design decisions [16].

The digital image correlation (DIC) [17] is one of the most commonly used optical techniques for strain measurement. In DIC, the sequentially captured images are processed to extract valuable information for observation of both local and global behaviour of structures. In addition, DIC can operate in real time and provides the ability to monitor structural responses under dynamic loading conditions. This feature makes DIC a powerful tool for various applications ranging from material testing [18] and [19] and characterisation [20] and [21], to structural analysis [22] and product

*Corr. Author's Address: University of Ljubljana, Faculty of Mathematics and Physics, Jadranska 19, 1000 Ljubljana, Slovenia, pino.koc@fmf.uni-lj.si

development [23]. A concise literature survey listing studies of DIC applications to geotechnical materials, using different materials, test types, specimen shapes and loading conditions is given in the work of Tang et al. [24].

Using of DIC has unlocked the potential for the development of novel material characterization strategies like virtual fields method (VFM) [25] and finite element model updating (FEMU) [26] to [29], where the richness of measured displacements and strains over the entire region of interest (ROI) can be analysed to accurately capture material behaviour. As an example, Zhang et al. [30] developed a novel DIC-based methodology for crack identification in a jointed rock mass. Their DIC results obtained on synthetic sandstone specimens demonstrate that the cracking process is successfully identified by the displacement vectors and strain localization. Similarly, Chai et al. [31] used DIC for damage characterisation of rock-like specimens under uniaxial compression, where they showed that the failure mechanism of the sample is shear failure followed by tensile failure. In a recent study, Chen et al. [32] investigated the influence of the arrangement of flaw geometry on the interaction of flaw configurations and failure characteristics of sandstone specimens. Utilising the potential of full-field DIC measurements, the crack configuration was found to have a significant influence on the failure characteristics of the rock, and three typical crack coalescence modes were found. The results and experiments provide a better understanding of the interaction between flaws and the failure characteristics of the rock under compressive and shear loading.

The full potential of full-field strain measurement using DIC was clearly demonstrated by Luo et al. [33]. They investigated the deformation mechanisms of stratified rock-like material when different interlayer thickness ratios and length-to-width ratios of the specimens were selected. Similarly, Wang et al. [34] utilised the potential of DIC and acoustic emission techniques to monitor the evolution of the heterogeneous strain field and development of microcracks in specimens in a real time. They concluded that the strain localisation zones developed mainly near the holes and joints, that both the shape of the holes and the inclination of the joints had a significant influence on the collapse mode of specimens, and that the inclination of the joints played a dominant role of mechanical responses of the double-hole specimens.

While the above studies were conducted for static test configurations, Xing et al. [35] utilised DIC for dynamic testing of cylindrical rock specimens using the Hopkinson pressure bar system. In their study, they observed the propagation of compression waves within the sandstone specimen at different strain rates from quasi-static to 120 s^{-1} and measured the corresponding stress-strain curves using conventional strain gauges and the DIC technique.

A particularly interesting result of their analysis is that strain gauges show an increase in Young's modulus with increasing strain rate and ductile properties after the peak stress, which is different from a static measurement. Interestingly, the curves obtained with DIC give different results. The modulus is unchanged at all strain rates, and the higher the strain rate, the higher the strain at peak stress. Obviously, improper strain measurement can lead to erroneous results and incorrect characterisation. A similar conclusion was reached by Zhang and Zhao [36], who found that the measurement of specimen strains using the signals from strain gauges on the bars is not very accurate because the strain to failure is very small for brittle and quasi-brittle materials.

While strain gauges are widely used for metallic materials, their use for rock-like materials is somewhat limited. Hsieh et al. [37] measured both axial and circumferential strains of cylindrical specimens using diametrically positioned strain gauges. However, Liu et al. [38] point out that the measurement error of this method is large because the adhesion of the strain gauges increases the local stiffness of the specimens. The application of this method is cumbersome, and the strain gauges are disposable. In their work, they developed a new test method for measuring circumferential strains, but the test has its limitations as it does not provide information about the strain field in the entire area. In addition, Isah et al. [39] presented that the strain gauges do not capture the strains after the post-peak regime, which is mainly due to the damage of the strain gauges by cracks in the rock. As presented in their study, strain gauges are also inclined to measure the local response of the underlying material structure and represent the response at the mesoscale. Sun et al. [40] have recently discussed this aspect and analysed the influence of position and number of strain gauges on the characterisation of attenuation and moduli of rocks with mesoscopic heterogeneities.

The main focus and research significance of this study is to analyse to what extent the measurement of Poisson's ratio is improved by DIC full-field measurements compared to the strain gauge technique. To this end, the margin of error in the measurement of the static Poisson's ratio is evaluated for both

measurement methods when applied to a virtual and a real experiment with rock-like material. For the virtual experiment, the linear-elastic two-phase material with hard rock inclusions is modelled for the compression test of a cylindrical sample. It is shown that with DIC the richness of the measured strain field can be exploited, resulting in a lower margin of error [41], whereas conventional strain gauges tend to measure the local response of the material beneath the gauge. Therefore, a large number of measurements need to be repeated to obtain accurate values. This is particularly problematic with specimens for which only a few test opportunities are available. Comparison of both methods gives us insight into advantages of full-field DIC measurements and potential drawbacks when using strain gauges.

In this article the experimental work is divided into two parts. The first part, given in article's Section 1, introduces the concept of virtual experimentation. Within this concept, (i) the FEM is used to model the response of the cylindrical compression specimen; then, calculated surface strains are exported from FEM model for further manipulation (ii) to mimic the virtual strain gauge measurement, and (iii) to mimic a complete DIC measurement chain from image deformation to the calculation of surface strains. Once the strains are reconstructed by both virtual strain gauges and DIC, the measurements are repeated for hundreds of different positions of the strain gauges on the same deformed sample. Similarly, the DIC measurement was repeated for hundreds of different ROI positions. Using the measured strains, a population of Poisson's ratios is calculated, and the margin of error is evaluated for both the strain gauge and the DIC technique.

This method is used to analyse the extent to which the strain gauge measurement is influenced by the heterogeneity of the material structure, as the measurement is taken over a limited area over which the strain gauge is bonded. On the other hand, DIC allows the data are captured not only for a single small area, but for the entire surface of the sample. These data are used to determine the mean value of the Poisson's ratio with a higher precision than with the conventional strain gauge technique.

In the second experimental part, Section 2 of this article, the same procedure is repeated for a real experiment using a cylindrical sandstone sample. However, it should be emphasised that performing a real strain gauge measurement for hundreds or dozens of repetitions is cumbersome. Therefore, the concept of virtual strain gauge was used in the DIC to mimic the strain gauge data. Since the quality of the DIC measurement is dependent on the signal-to-noise ratio, an optimal DIC settings [42] are desirable to accurately measure the strains at low loads. While the optimal DIC settings are usually determined by performance analysis [43], the representative value of the Poisson's ratio for the selected DIC settings is determined here by a simple engineering method.

The results of both experimental parts are presented in Section 3.

1 VIRTUAL EXPERIMENTATION

In this section a methodology of virtual experimentation using DIC is presented. The concept has been first introduced by Lava et al. [44]. The idea is to perform a FEM simulation of experiment with known outcome, followed by synthetic deformation of synthetically generated random speckle pattern to obtain deformed images for DIC processing. Finally, the deformed images are processed by DIC to obtain displacement and strain fields, which can be easily compared with original FEM result. The methodology is employed for a comparison of Poisson's ratio obtained with virtual strain gauge technique and virtual full field DIC measurements.

1.1 FEM Model

The most common test for determination of Poisson's ratio of rock is uniaxial compression test of cylindrical sample [45], which is in case of virtual experimentation replicated by FEM simulation in ABAQUS computational software [46]. Based on similar studies, literature and FEM modelling approaches [47] to [50], a numerical model of cylindrical rock-like specimen was created with diameter of 50 mm and height of 100 mm. To capture heterogeneous structure on the mesoscale, two-phase material model is used: a softer matrix with harder rock grain spherical inclusion. Both phases are considered as a linear elastic with material properties given in Table 1.

Table 1. *Material properties*

Phase	Elastic modulus [GPa]	Poisson's ratio [/]
Matrix	70	0.1
Inclusions (rock grains)	140	0.2

For the hard inclusion phase, a model with randomly distributed spherical inclusions with a variable diameter of 0.5 mm to 2 mm is used. It is important to note that despite the assumption

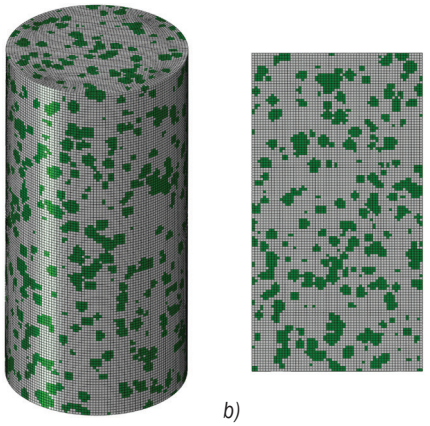

a) b)

Fig. 1. *a) Domain discretization with inclusions in green, and b) its diametral plane cross-section*

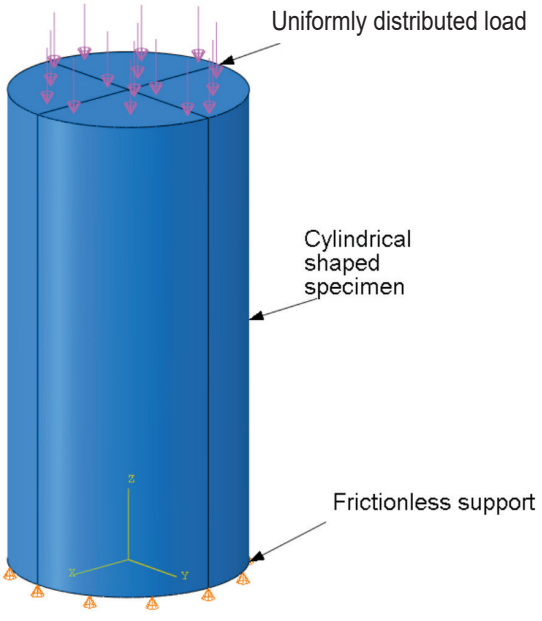

Fig. 2. *Numerical model of cylindrical specimen*

of spherical inclusions in the model, the resulting inclusion phase is not necessarily spherical due to the coalescence of inclusions. The volume ratio of the inclusion phase to the total volume of the specimen is 23 %. To integrate the inclusion phase into the numerical model, a dense mesh of small cubes was initially created. For each cube the material properties of the matrix or inclusion is assigned, depending on its position. For this purpose, mathematical model is developed using the Python scripting language to simulate a space populated by randomly distributed spheres, each varying in size. If the element centroidal coordinate is located inside a sphere, the inclusion modulus of elasticity and Poisson's ratio is assigned to the element. Otherwise, the material properties of the element are belonging to the matrix phase. The global seed size of the mesh was set to 0.8 mm and linear hexahedral elements (ABAQUS designation C3D8R) with reduced integration were used. Fig. 1 shows the mesh of the numerical model, with the matrix elements in grey and the hard rock inclusion elements in green.

The model is supported on the bottom surface in axial direction, whereas the radial and circumferential displacements are not restrained. On the top surface, uniformly distributed force of magnitude 30 kN is compressing the cylinder. Loading conditions are shown on Fig. 2.

1.2 Determination of Poisson's Ratio

Only surface strains from the simulation results that could also be measured in the actual experiment are used to calculate the Poisson's ratio. The strains used for the calculation are extracted in two ways: firstly, to mimic the conventional strain gauge measurements and secondly, to mimic the DIC full-field measurements. With both methods, the Poisson's ratio is calculated for a population of randomly positioned strain gauges and ROIs from DIC results. Finally, the Poisson's ratios obtained for both methods are compared.

1.2.1 Strain Gauge Imitation

Two rectangles, representing strain gauges, are placed next to each other and randomly on the surface of the specimen. The rectangles are 20 mm long and 10 mm wide. One rectangle is oriented vertically to determine the axial strain and the other horizontally to determine the circumferential strain.

The axial or circumferential strains are extracted from the model as the averaged strains of the finite elements within the rectangle. This value is then assigned to the individual strain gauge measurement. This is repeated for both vertically and horizontally oriented rectangles, resulting in an average axial strain $\varepsilon_{\parallel,i}$ and circumferential strain $\varepsilon_{\perp,i}$. The index i represents an individual position of a pair of rectangles, as shown in Fig. 3.

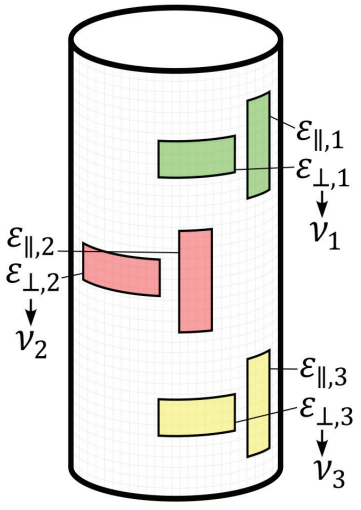

Fig. 3. *Poisson's ratio determination from multiple randomly positioned quasi strain gauges*

Poisson's ratio for i^{th} location is then calculated as

$$\nu_i = -\frac{\varepsilon_{\perp,i}}{\varepsilon_{\parallel,i}}, \tag{1}$$

and the calculation procedure repeated n-times, which finally represents the population of Poisson's ratios ν_i, $i \in \{1, 2, ..., n\}$. From these results we can observe scattering of locally determined Poisson's ratios on inhomogeneous strain field.

1.2.2 DIC Virtual Experimentation

The aim of the virtual DIC experiments is to analyse how the measured strain fields are influenced by systematic and random errors that propagate throughout the entire DIC measurement chain. For this purpose, the measurement itself must be compared with the "ground truth" result, which can be obtained from a finitelement simulation, for example. Essentially, such a methodology can be used to analyse not only the influence of the material structure itself, but also the influence of the DIC system settings on the final result. For this purpose, a concept of virtual DIC experimentation is presented in Fig. 4.

In the first step (Fig. 4a), a FEM simulation with 60 monotonically increasing load increments up to the axial force 30 kN is carried out in accordance with Section 1.1. From the simulation, the displacements of the specimen's surface and the corresponding reference strain fields are calculated. The displacement field is then used in the MatchID software to generate a synthetically deformed images (Fig. 4b) of a reference speckle pattern (Bossuyt et al. [51]). These images serve as a surrogate for the actual images normally captured by charge-coupled device (CCD) or complementary metal–oxide–semiconductor (CMOS) cameras. In this case, however, the deformation of the images is known, as it was imposed by the reference simulation. In the final step, the deformed images are processed with the DIC algorithm to reconstruct the reference displacement and the strain field under the applied DIC settings (Fig. 4c). Assuming that the image deformation algorithm does not introduce significant errors into the FEM displacements, the difference between the reconstructed DIC and FEM displacement and strain field results solely from the digitalisation process and the DIC algorithm.

Poisson's ratios are finally calculated for randomly positioned regions of interest over a complete circumference of the specimen, typically covering approximately 80 % of the total height of the cylinder and 80° of its circumferences to mimic the ROI normally captured with a stereo DIC.

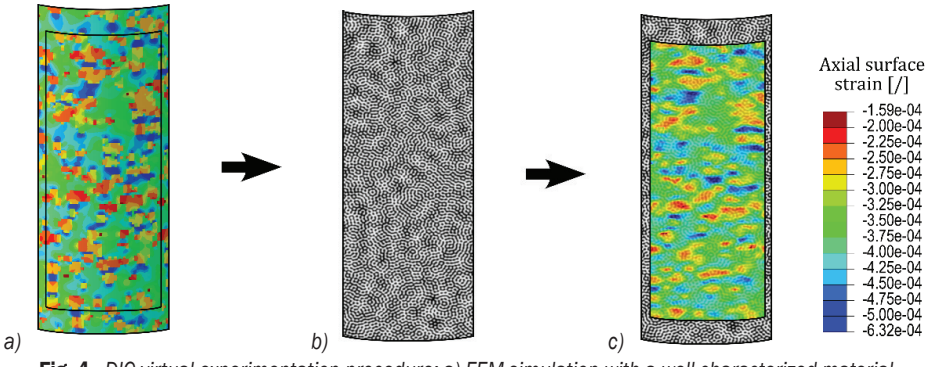

Fig. 4. *DIC virtual experimentation procedure: a) FEM simulation with a well-characterized material, b) deformed images based on the calculated displacement field and a random speckle pattern, and c) reconstruction of strain fields from the deformed images using the DIC algorithm*

2 EXPERIMENTAL TEST

For validation, the uniaxial compression test is performed experimentally, whereby the Poisson's coefficient is measured by (i) the quasi-strain gauge technique, and (ii) with DIC. The reason for using quasi strain gauges instead of true strain gauges is that gluing dozens of strain gauges is impractical and unfeasible because the adhesive would eventually impair the surface of the sample. For this reason, a similar method to that described in Section 1.2.1 was used, but instead of the strains from the FEM simulation, the strains from the DIC were used. Of course, such an approach only mimics an averaging effect of the strain gauge measurement and completely neglects the uncertainties caused by the physical measurement chain.

However, based on the retrieved data on strains either with quasi strain gauge or DIC, the Poisson's ratio from the quasi strain gauge and the DIC strain field measurements is finally calculated and compared.

2.1 Experimental Setup

A cylindrical specimen with a diameter of 42 mm and a height of 82 mm is used for the uniaxial compression test. The samples consist of sandstone material with visible inclusions on the surface of the sample (Fig. 5) and is manufactured according to the ASTM-D4543 [52] requirements. The samples are machined to produce smooth surfaces and parallel contact surfaces in order to create homogeneous loading conditions on the macro level.

Fig. 5. *Sandstone cylindrical specimen with visible inclusions on the surface*

The specimen is placed on flat steel platens in a custom-made universal testing machine (load capacity 50 kN with 50 kN Class 1 force transducer for the measurement of static or dynamic loads in tension or compression) and tested according to the ASTM D7012 [53]. The strain fields are measured using stereo DIC equipment, with the cameras mounted at an angle of approximately 30°, as shown in Fig. 6.

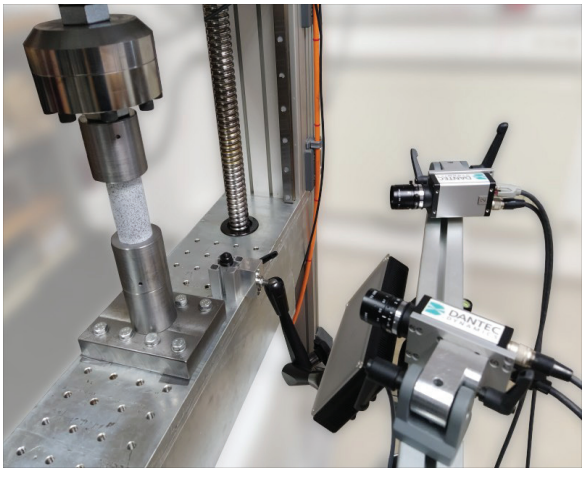

Fig. 6. *Uniaxial compression test setup with stereo DIC measurement system*

The black coloured random speckle pattern is applied on the white painted cylindrical surface as shown on Fig. 7. The strain resolution has been measured by taking a pair of still images which were postprocessed by DIC algorithm [54]. Here, a strain resolution of $\varepsilon = 2.6 \times 10^{-4}$ was found for both circumferential and axial direction. The adopted DIC equipment and settings are specified in Table 1 [55] while at the same time avoiding strain concentrations near sample edges where Digital Image Correlation (DIC.

Fig. 7. *Random black speckle pattern on the white background colour applied to the surface of the actual specimen*

Table 1. *DIC and setup settings used to process the deformed images and determine the strain fields*

Technique and DIC software	2D DIC, Dantec Dynamics, Istra 4D
Cameras	Manta G-201B, Allied Vision, 2 pieces
Image resolution	2464 px × 1228 px
Objective focal distance	300 mm (approximate)
Field of view	64 mm × 26 mm
Stereo angle	26.5° (approximate)
Illumination colour temp.	4400 K
Pattering technique	white composite surface with black speckles
Pattern feature size	13 px
DIC technique	stereo
Subset size	61px
Step size	31px
Subset weight	uniform
Subset shape function	affine
Matching criterion	Approximated sum of squared differences
Interpolant	Local bicubic spline interpolation
Strain calculation method	Direct from the subset shape function
Reference image	Fixed
Data points	860
Temporal smoothing	none
Acquisition frequency	3.3 Hz
Specimen length	82 mm
Specimen width	42 mm
Loading speed	0.02 mm/s

The specimen was loaded 80 times at a displacement rate of 0.02 mm/s until the maximum force of 33 kN was reached. For each measurement, different portion of the specimen was recorded and postprocessed by the DIC algorithm to obtain the strain fields. The cameras were repositioned and recalibrated between the tests.

2.2 Postprocessing

To validate the results of the virtual experiments from Section 1, quasi strain gauge data is extracted from the measured strain fields, which is done in a similar way to Section 1.2.1. The mean value of the axial and circumferential strain is extracted from vertically and horizontally arranged rectangular areas. The rectangles represent strain gauges that are 20 mm long and 10 mm wide. A pair of rectangles is placed side by side approximately in the centre of the region of interest. The Poisson's ratio is calculated based on the extracted strains of the quasi-strain gauges. The procedure is repeated for each measurement to obtain a distribution of the calculated Poisson's ratios, extracted at the maximum load.

When using DIC, the ROI is constrained to the centre of the sample within the field of view as presented in Fig. 8. To avoid edge effects, the ROI occupies about 80 % of the height of the sample, similar to the virtual experiment. The Poisson's ratio is calculated individually for each strain measurement and the calculated values are then averaged to obtain a single value for the Poisson's ratio for one measurement. Typical strain measurement is presented in Fig. 8. Finally, the procedure is repeated for each measurement.

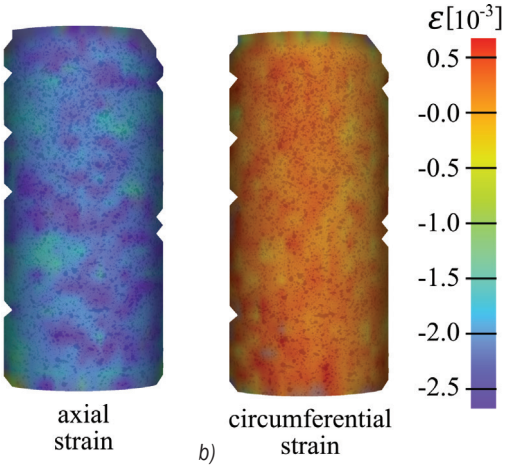

Fig. 8. *a) Axial, and b) circumferential strain field measured by DIC*

3 RESULTS

In this section the distributions of calculated Poisson's ratio are presented for virtual and experiments for quasi strain gauge and DIC processed data.

3.1 The Results of Virtual Testing

As described in Section 1, the data from the randomly placed quasi strain gauges are extracted from the FEM simulation results and used to calculate the Poisson's ratios. Similarly, the DIC data is reconstructed from the FEM simulation results using the concept of virtual experiments. For both quasi-strain gauges and DIC, 1000 repetitions of the measurement were independently analysed for the probability distribution of the Poisson's coefficient. The mean value of the coefficient when using strain gauges and DIC is 0.131 for both cases, while the standard deviation when using strain gauges is about 3.4 times larger (0.00588 for the strain gauge measurement compared to 0.00173 for DIC). The probability distributions for both measurement methods are shown in the histogram in Fig. 9, where the green bars correspond

to the population determined with quasi-strain gauges and the red bars to the measurement with DIC. The statistical data of the populations are shown in tabular form as insets.

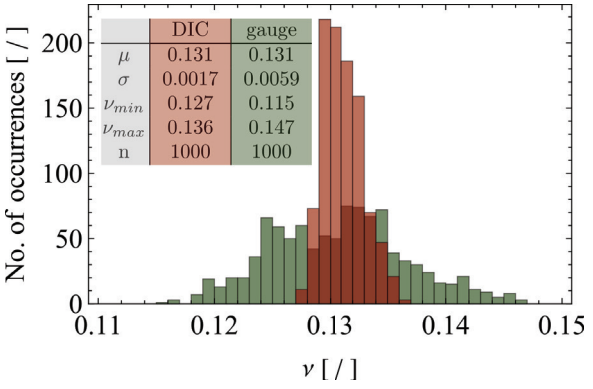

Fig. 9. *Distribution of Poisson's ratios determined by virtual strain gauge (green) and full-field DIC data (red)*

3.2 Experimental Test Results

The same analysis was performed for the actual experimental data. In this particular case, a total of 80 repetitions of the actual experiment were performed for both quasi strain gauges and DIC. The probability distributions for both measurement methods are shown in Fig. 10, with the green bars corresponding to the strain gauge measurements and the red bars to the DIC measurements.

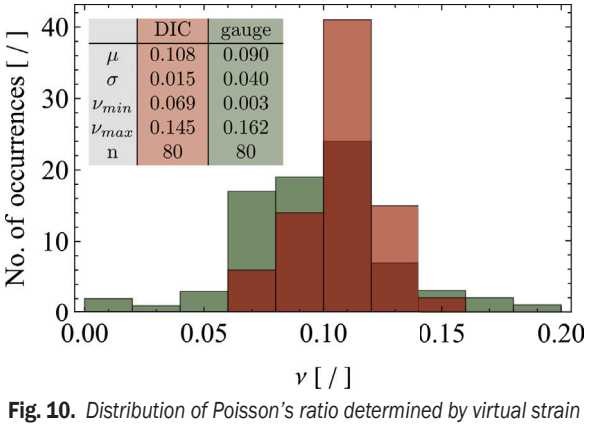

Fig. 10. *Distribution of Poisson's ratio determined by virtual strain gauge data (green) and full-field DIC measurements (red)*

The measured mean value of the Poisson's coefficients for the quasi strain gauge technique is 0.0896, while the value for DIC is slightly higher (0.108). When analysing the standard deviation of the two measured populations, a consistent result with the virtual experiment is obtained. In the particular case, the standard deviation for quasi strain gauge data is 0.0404, while this value for DIC is 0.0152, which is approximately 2.7 times smaller.

3.3 RVE Value for Poisson's Ratio

Despite the superiority of DIC measurements over conventional strain gauge measurement technology, the reliability of DIC measurements in terms of spatial resolution, accuracy, precision, and sensitivity as well as data accuracy is still debated today. For example, it is known that there is a trade-off between spatial resolution and precision, which is determined and influenced by the DIC settings [56]. Furthermore, determining the spatial resolution of a measurement is not as straightforward and often requires à priori tests with the same test conditions as the actual tests or the specification of a synthetic displacement field with known variations in the displacement field [57].

In this particular case, the measurement of small strain fields with strain gauges or DIC is a challenge due to the signal-to-noise ratio in the strain fields [58]. For this purpose, an alternative criterion is proposed to determine the accurate value of Poisson's ratio with DIC under the assumption that the material behaviour is isotropic at the macro level.

When analysing the complete strain fields in the sample, DIC has a considerable advantage over strain gauges. In particular, not only can a complete strain field be measured, as shown in Fig. 8, but these strains can also be analysed in different coordinate systems, as shown in Fig. 11.

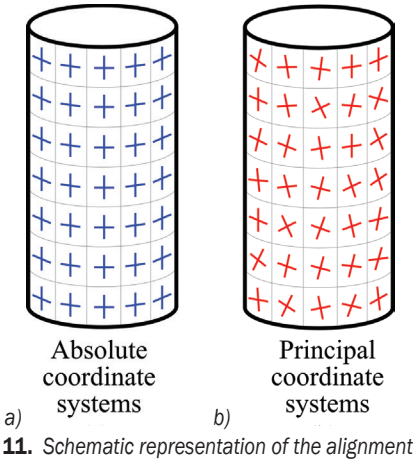

Fig. 11. *Schematic representation of the alignment of absolute, and principal coordinate systems*

As demonstrated in the figure, the strain field can be observed in the absolute (Cartesian) coordinate system, with axes aligned in axial and circumferential directions or in the principal strains coordinate system.

In the latter case, if the observed strains are dominated by noise, the principal directions in different material points on specimen's surface are not aligned, they are randomly oriented, instead. In the undesired case of non-alignment of platens and specimen's contact surfaces the principal strain axes also differ from absolute coordinate system axes. However, in that case the principal coordinate system follows some regular pattern on the specimen's surface (strain trajectories).

Typical axial and circumferential strain evolution of individual subset in absolute coordinate system is presented in Figs. 12 and 13, respectively.

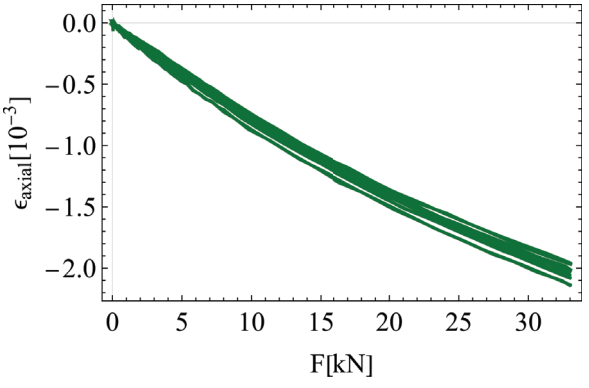

Fig. 12. *Evolution of axial strain in relation to the magnitude of applied load in absolute coordinate system*

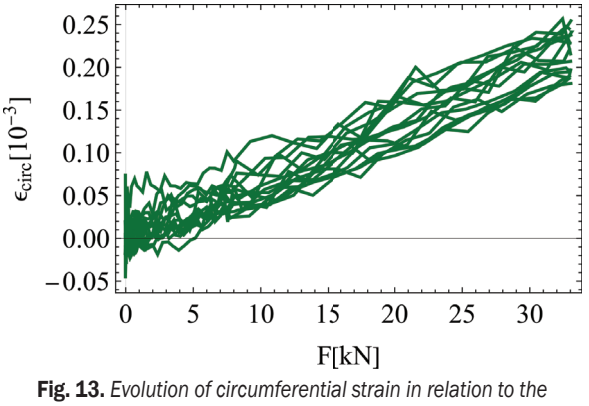

Fig. 13. *Evolution of circumferential strain in relation to the magnitude of applied load in absolute coordinate system*

In Fig. 14, the mean value of the Poisson's ratio calculated from these measured strain fields is displayed with blue curves. As shown, high variations of the Poisson's ratio gradually diminish as the loading force increases. The higher the load, the higher the signal, while the noise floor level remains roughly constant for DIC. Red curves represent the mean Poisson's ratio, defined as a ratio of minor versus major strain, i.e., the ratio is calculated in principal strains coordinate system. Similar to the absolute coordinate system, due to the low signal-to-noise ratio a high variation of Poisson's ratio at the beginning of loading can be seen. The degree of alignment between absolute and principal coordinate systems can be measured by calculating the relative difference in the mean values of the Poisson's ratio. In order to ensure a satisfactory level of alignment, a threshold of 5 % is employed.

For the particular case from Fig. 14, this occurs at force of 15 kN. This value represents the smallest force required to reliably measure the representative value of the Poisson's ratio for the given specimen size and material composition.

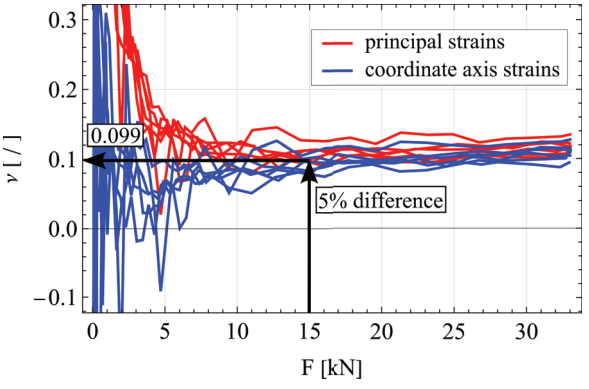

Fig. 14. *Poisson's ratio versus loading rate*

4 DISCUSSION AND CONCLUSIONS

While the strain gauge measuring technique has not evolve in the recent decades, DIC has flourished with the development of computational technology. The equipment has nowadays become publicly and commercially accessible and user-friendly.

The results presented in Section 3.1 and Section 3.2 show that the Poisson's ratio can be measured with DIC with a smaller margin of error than with the conventional strain gauge technique. Smaller margin of error can be generally achieved in DIC by improving strain resolution via increasing subset size or image resolution. In the synthetic experiment, the difference between the standard deviation of the population of measured values is 3.4 times larger in favour of DIC, while this value is 2.7 in the actual experiment. The main reason for this is that DIC provides a larger population of values since the measurement is performed for a complete region of interest each time and the richness of the measured field can be utilised for the particular case when the representative value is determined from the mean. On the other hand, when using conventional strain gauges, there is always the possibility that a local response of the substructure to

which the gauge is attached is measured. To avoid this problem and possibly eliminate this systematic error, it is advisable to repeat the experiment several times. To substantiate this claim, consider the simulated and measured strain field in Fig. 4. As shown, the inclusion phase locally influences the axial strain field, which can be accurately reproduced by the DIC (note that the legend for the FEM simulation and the DIC results is the same and the strain field distribution is obviously very similar). This example demonstrates (i) the importance of virtual DIC testing for experiment design and (ii) the ability of DIC to measure and exploit the richness of resulting strain fields. In addition, for most samples with only few test opportunities available, the full-field methods are advantageous over the conventional strain gauge method. If the experiment is carried out to failure, the captured images can be processed repeatedly using DIC with different settings, which can be optimised by performance analysis **[37]**.

Finally, it should be noted that the measurement of the Poisson ratio is constrained by the signal-to-noise ratio. When observing the mean and standard deviation of the ratio, a larger standard deviation can be observed at lower load magnitudes. However, this value decreases as the load increases. At this stage, DIC proves to be advantageous compared to strain gauges because the strain fields can be observed in multiple coordinates systems simultaneously, for example in the principal and absolute coordinate systems. If the Poisson's ratio is also defined in the principal coordinate system, the comparison of the coefficient immediately indicates whether the coordinate systems are not aligned or not. The relative discrepancy between the mean values measured in both coordinate systems can be used to determine an engineering criterion for the smallest load value required to reliably measure the representative value of the coefficient.

5 ACKNOWLEDGEMENT

The author would like to thank the staff of the Laboratory for Numerical Modelling and Simulation at the University of Ljubljana, Faculty of Mechanical Engineering, for the use of laboratory equipment and for generously providing access to the MatchID software, which was crucial for the realization of this research.

6 REFERENCES

[1] Jaeger, J.C., Cook, N.G.W., Zimmerman, R. (2009). *Fundamentals of Rock Mechanics*, John Wiley & Sons, Hoboken.

[2] Zhou, T., Chen, J., Xie, H., Zhou, C., Wang, F., Zhu, J. (2022). Failure and mechanical behaviors of sandstone containing a pre-existing flaw under compressive-shear loads: Insight from a digital image correlation (DIC) analysis. *Rock Mechanics and Rock Engineering*, vol. 55, no. 7, p. 4237-4256, **DOI:10.1007/s00603-022-02861-4**.

[3] Bernabé, Y., Fryer, D.T., Shively, R.M. (1994). Experimental observations of the elastic and inelastic behaviour of porous sandstones. *Geophysical Journal International*, vol. 117, no. 2, p. 403-418, **DOI:10.1111/j.1365-246X.1994.tb03940.x**.

[4] Schultz, R.A. (1996). Relative scale and the strength and deformability of rock masses. *Journal of Structural Geology*, vol. 18, no. 9, p. 1139-1149, **DOI:10.1016/0191-8141(96)00045-4**.

[5] Sari, M. (2021). Determination of representative elementary volume (REV) for jointed rock masses exhibiting scale-dependent behavior: a numerical investigation. *International Journal of Geo-Engineering*, vol. 12, no. 1, p. 34, **DOI:10.1186/s40703-021-00164-1**.

[6] Wang, X., Zhao, Y., Lin, X. (2011). Determination of mechanical parameters for jointed rock masses. *Journal of Rock Mechanics and Geotechnical Engineering*, vol. 3, p. 398-406, **DOI:10.3724/SP.J.1235.2011.00398**.

[7] Wu, Q., Kulatilake, P.H.S.W. (2012). REV and its properties on fracture system and mechanical properties, and an orthotropic constitutive model for a jointed rock mass in a dam site in China. *Computers and Geotechnics*, vol. 43, p. 124-142, **DOI:10.1016/j.compgeo.2012.02.010**.

[8] Cao, Y.J., Shen, W.Q., Shao, J.F., Wang, W. (2021). A multi-scale model of plasticity and damage for rock-like materials with pores and inclusions. *International Journal of Rock Mechanics and Mining Sciences*, vol. 138, 104579, **DOI:10.1016/j.ijrmms.2020.104579**.

[9] Yu, Z., Shao, J.-F., Vu, M.-N., Armand, G. (2021). Numerical study of thermo-hydro-mechanical responses of in situ heating test with phase-field model. *International Journal of Rock Mechanics and Mining Sciences*, vol. 138, 104542, **DOI:10.1016/j.ijrmms.2020.104542**.

[10] Potyondy, D.O., Cundall, P.A. (2004). A bonded-particle model for rock. *International Journal of Rock Mechanics and Mining Sciences*, vol. 41, no. 8, p. 1329-1364, **DOI:10.1016/j.ijrmms.2004.09.011**.

[11] Zhou, C., Xie, H., Zhu, J. (2024). Revealing Size effect and associated variability of rocks based on BPM-μDFN modelling: Significance of internal microstructure and strain rate. *Rock Mechanics and Rock Engineering*, **DOI:10.1007/s00603-023-03653-0**.

[12] Zhou, C., Xie, H., Wang, Z., Zhou, T., Zhu, J. (2023). A novel fractal-statistical scaling model of rocks considering strain rate. *Journal of Rock Mechanics and Geotechnical Engineering*, vol. 15, no. 11, p. 2831-2841, **DOI:10.1016/j.jrmge.2023.02.033**.

[13] Zhou, C., Xu, C., Karakus, M., Shen, J. (2018). A systematic approach to the calibration of micro-parameters for the flat-jointed bonded particle model. *Geomechanics and Engineering*, vol. 16, no. 5, p. 471-482.

[14] Vrh, M., Halilovič, M., Starman, B., Štok, B. (2011). A new anisotropic elasto-plastic model with degradation of elastic modulus for accurate springback simulations. *International Journal of Material Forming*, vol. 4, no. 2, p. 217-225, **DOI:10.1007/s12289-011-1029-8**.

[15] Starman, B., Vrh, M., Halilovič, M., Štok, B. (2014). Advanced modelling of sheet metal forming considering anisotropy and Young's modulus evolution. *Strojniški vestnik - Journal of Mechanical Engineering*, vol. 60, no. 2, p. 84-92, **DOI:10.5545/sv-jme.2013.1349**.

[16] Halilovič, M., Starman, B., Coppieters, S. (2024). Computationally efficient stress reconstruction from full-field strain measurements. *Computational Mechanics*, **DOI:10.1007/s00466-024-02458-4**.

[17] Schreier, H., Orteu, J.-J., Sutton, M.A. (2009). *Image Correlation for Shape, Motion and Deformation Measurements: Basic Concepts, Theory and Applications*, Springer, Boston, **DOI:10.1007/978-0-387-78747-3**.

[18] Pierron, F. (2023). Material testing 2.0: A brief review. *Strain*, vol. 59, no. 3, e12434, **DOI:10.1111/str.12434**.

[19] Maček, A., Urevc, J., Halilovič, M. (2021). Flat specimen shape recognition based on full-field optical measurements and registration using mapping error minimization method. *Strojniški vestnik - Journal of Mechanical Engineering*, vol. 67, no, 5, p. 203-213, **DOI:10.5545/sv-jme.2021.7111**.

[20] Maček, A., Starman, B., Mole, N., Halilovič, M. (2020). Calibration of advanced yield criteria using uniaxial and heterogeneous tensile test data. *Metals*, vol. 10, no. 4, 542, **DOI:10.3390/met10040542**.

[21] Obid, Š., Halilovič, M., Urevc, J., Starman, B. (2023). Non-linear elastic tension-compression asymmetric anisotropic model for fibre-reinforced composite materials. *International Journal of Engineering Science*, vol. 185, 103829, **DOI:10.1016/j.ijengsci.2023.103829**.

[22] Verbruggen, S., De Sutter, S., Iliopoulos, S., Aggelis, D.G., Tysmans, T. (2015). Experimental structural analysis of hybrid composite-concrete beams by digital image correlation (DIC) and acoustic emission (AE). *Journal of Nondestructive Evaluation*, vol. 35, no. 1, 2, **DOI:10.1007/s10921-015-0321-9**.

[23] Maček, A., Urevc, J., Žagar, T., Halilovič, M. (2021). Crimp joint with low sensitivity to process parameters: numerical and experimental study. *International Journal of Material Forming*, vol. 14, no. 5, p. 1233-1241, **DOI:10.1007/s12289-021-01637-5**.

[24] Tang, Y., Zhang, H., Guo, X., Ren, T. (2022). Literature survey and application of a full-field 3D-DIC technique to determine the damage characteristic of rock under triaxial compression. I*nternational Journal of Damage Mechanics*, vol. 31, no. 7, p. 1082-1095, **DOI:10.1177/10567895221089660**.

[25] Marek, A., Davis, F.M., Pierron, F. (2017). Sensitivity-based virtual fields for the non-linear virtual fields method, *Computational Mechanics*, vol. 60, no. 3, p. 409-431, **DOI:10.1007/s00466-017-1411-6**.

[26] Zhang, Y., Yamanaka, A., Cooreman, S., Kuwabara, T., Coppieters, S. (2023). Inverse identification of plastic anisotropy through multiple non-conventional mechanical experiments. *International Journal of Solids and Structures*, vol. 285, 112534, **DOI:10.1016/j.ijsolstr.2023.112534**.

[27] Yin, Y., Liu, G., Zhao, T., Ma, Q., Wang, L., Zhang, Y. (2022). Inversion method of the young's modulus field and Poisson's ratio field for rock and its test application. *Materials*, vol. 15, no. 15, 5463, **DOI:10.3390/ma15155463**.

[28] Satošek, R., Pepelnjak, T., Starman, B. (2023). Characterisation of out-of-plane shear behaviour of anisotropic sheet materials based on indentation plastometry. *International Journal of Mechanical Sciences*, vol. 253, 108403, **DOI:10.1016/j.ijmecsci.2023.108403**.

[29] Starman, B., Vrh, M., Koc, P., Halilovič, M. (2019). Shear test-based identification of hardening behaviour of stainless steel sheet after onset of necking. *Journal of Materials Processing Technology*, vol. 270, p. 335-344, **DOI:10.1016/j.jmatprotec.2019.03.010**.

[30] Zhang, K., Zhang, K., Liu, W., Xie, J. (2023). A novel DIC-based methodology for crack identification in a jointed rock mass. *Materials & Design*, vol. 230, 111944, **DOI:10.1016/j.matdes.2023.111944**.

[31] Chai, J., Liu, Y., OuYang, Y., Zhang, D., Du, W. (2020). Application of digital image correlation technique for the damage characteristic of rock-like specimens under uniaxial compression. *Advances in Civil Engineering*, vol. 2020, e8857495, **DOI:10.1155/2020/8857495**.

[32] Chen, J., Yin, X., Zhou, C., Pan, M., Han, Z., Zhou, T. (2023). Interaction between flaws and failure characteristics of red sandstone containing double flaws under compressive-shear loading. *Engineering Fracture Mechanics*, vol. 292, 109664, **DOI:10.1016/j.engfracmech.2023.109664**.

[33] Luo, P., Li, D., Ma, J., Zhou, A., Zhang, C. (2023). Experimental investigation on mechanical properties and deformation mechanism of soft-hard interbedded rock-like material based on digital image correlation. *Journal of Materials Research and Technology*, vol. 24, p. 1922-1938, **DOI:10.1016/j.jmrt.2023.03.145**.

[34] Wang, F., Xie, H., Zhou, C., Wang, Z., Li, C. (2023). Combined effects of fault geometry and roadway cross-section shape on the collapse behaviors of twin roadways: An experimental investigation. *Tunnelling and Underground Space Technology*, vol. 137, 105106, **DOI:10.1016/j.tust.2023.105106**.

[35] Xing, H.Z., Zhang, Q.B., Ruan, D., Dehkhoda, S., Lu, G.X., Zhao, J. (2018). Full-field measurement and fracture characterisations of rocks under dynamic loads using high-speed three-dimensional digital image correlation. *International Journal of Impact Engineering*, vol. 113, p. 61-72, **DOI:10.1016/j.ijimpeng.2017.11.011**.

[36] Zhang, Q.B., Zhao, J. (2013). Determination of mechanical properties and full-field strain measurements of rock material under dynamic loads. *International Journal of Rock Mechanics and Mining Sciences*, vol. 60, p. 423-439, **DOI:10.1016/j.ijrmms.2013.01.005**.

[37] Hsieh, A., Dyskin, A.V., Dight, P. (2014). The increase in Young's modulus of rocks under uniaxial compression. *International*

Journal of Rock Mechanics and Mining Sciences, vol. 70, p. 425-434, **DOI:10.1016/j.ijrmms.2014.05.009**.

[38] Liu, Z., Wang, H., Yuan, L., Zhang, B., Wang, W., Ma, Z., Xue, Y., Li, Y. (2020). A new test method and system for the circumferential deformation of cylindrical standard specimens in geotechnical mechanics and its application. *Measurement*, vol. 149, 107041, **DOI:10.1016/j.measurement.2019.107041**.

[39] Isah, B.W., Mohamad, H., Ahmad, N.R., Harahap, I.S.H., Al-Bared, M.A.M. (2020). Uniaxial compression test of rocks: Review of strain measuring instruments. *IOP Conference Series: Earth and Environmental Science*, vol. 476, no. 1, 012039, **DOI:10.1088/1755-1315/476/1/012039**.

[40] Sun, C., Tang, G., Chapman, S., Zhang, H., Fortin, J., Wang, S., Pan, D., Yue, J. (2023). A numerical assessment of local strain measurements on the attenuation and modulus dispersion in rocks with fluid heterogeneities. *Geophysical Journal International*, vol. 235, no. 1, p. 951-969, **DOI:10.1093/gji/ggad289**.

[41] Maček, A., Starman, B., Coppieters, S., Urevc, J., Halilovič, M. (2024). Confidence intervals of inversely identified material model parameters: A novel two-stage error propagation model based on stereo DIC system uncertainty. *Optics and Lasers in Engineering*, vol. 174, 107958, **DOI:10.1016/j.optlaseng.2023.107958**.

[42] Yang, D., Bornert, M., Gharbi, H., Valli, P., Wang, L.L. (2010). Optimized optical setup for DIC in rock mechanics. *EPJ Web of Conferences*, vol. 6, 22019, **DOI:10.1051/epjconf/20100622019**.

[43] Gothivarekar, S., Coppieters, S., Van de Velde, A., Debruyne, D. (2020). Advanced FE model validation of cold-forming process using DIC: Air bending of high strength steel. *International Journal of Material Forming*, vol. 13, no. 3, p. 409-421, **DOI:10.1007/s12289-020-01536-1**.

[44] Lava, P., Cooreman, S., Coppieters, S., De Strycker, M., Debruyne, D. (2009). Assessment of measuring errors in DIC using deformation fields generated by plastic FEA. *Optics and Lasers in Engineering*, vol. 47, no. 7, p. 747-753, **DOI:10.1016/j.optlaseng.2009.03.007**.

[45] Xue, L., Qin, S., Sun, Q., Wang, Y., Lee, L. M., Li, W. (2014). A study on crack damage stress thresholds of different rock types based on uniaxial compression tests. *Rock Mechanics and Rock Engineering*, vol. 47, no. 4, p. 1183-1195, **DOI:10.1007/s00603-013-0479-3**.

[46] ABAQUS User's Manual (2012). *Fortran, Python*, SIMULIA, Providence.

[47] Li, M., Guo, P., Stolle, D., Liang, L. (2017). Modeling method for a rock matrix with inclusions distributed and hydraulic fracturing characteristics. *Journal of Petroleum Science and Engineering*, vol. 157, p. 409-421, **DOI:10.1016/j.petrol.2017.07.017**.

[48] Wu, Z., Wong, L.N.Y. (2013). Modeling cracking behavior of rock mass containing inclusions using the enriched numerical manifold method. *Engineering Geology*, vol. 162, p. 1-13, **DOI:10.1016/j.enggeo.2013.05.001**.

[49] Ren, M., Zhao, G., Zhou, Y. (2022). Elastic stress transfer model and homogenized constitutive equation for the multi-phase geomaterials. *Engineering Geology*, vol. 306, 106631, **DOI:10.1016/j.enggeo.2022.106631**.

[50] Tang, C.A., Fu, Y.F., Kou, S.Q., Lindqvist, P.-A. (1998). Numerical simulation of loading inhomogeneous rocks. *International Journal of Rock Mechanics and Mining Sciences*, vol. 35, no. 7, p. 1001-1007, **DOI:10.1016/S0148-9062(98)00014-X**.

[51] Bossuyt, S. (2013). Optimized patterns for digital image correlation, Jin, H. Sciammarella, C. Furlong, C., Yoshida, S. (eds.). *Imaging Methods for Novel Materials and Challenging Applications*, Volume 3, Springer, New York, p. 239-248, **DOI:10.1007/978-1-4614-4235-6_34**.

[52] ASTM (2019). *Standard Practices for Preparing Rock Core as Cylindrical Test Specimens and Verifying Conformance to Dimensional and Shape Tolerances*, ASTM International, West Conshohocken, **DOI:10.1520/D4543-19**.

[53] ASTM (2014). *Standard Test Methods for Compressive Strength and Elastic Moduli of Intact Rock Core Specimens under Varying States of Stress and Temperatures*, ASTM International, West Conshohocken, **DOI:10.1520/D7012-14E01**.

[54] Zhang, Y., Gothivarekar, S., Conde, M., de Velde, A.V., Paermentier, B., Andrade-Campos, A., Coppieters, S. (2022). Enhancing the information-richness of sheet metal specimens for inverse identification of plastic anisotropy through strain fields. *International Journal of Mechanical Sciences*, vol. 214, 106891, **DOI:10.1016/j.ijmecsci.2021.106891**.

[55] Jones, E.M.C., Corona, E., Jones, A. R., Scherzinger, W.M., Kramer, S.L.B. (2021). Anisotropic plasticity model forms for extruded Al 7079: Part II, validation. *International Journal of Solids and Structures*, vol. 213, p. 148-166, **DOI:10.1016/j.ijsolstr.2020.11.031**.

[56] Fazzini, M., Mistou, S., Dalverny, O., Robert, L. (2010). Study of image characteristics on digital image correlation error assessment. *Optics and Lasers in Engineering*, vol. 48, no. 3, p. 335-339, **DOI:10.1016/j.optlaseng.2009.10.012**.

[57] Forsström, A., Bossuyt, S., Scotti, G., Hänninen, H. (2020). Quantifying the effectiveness of patterning, test conditions, and DIC parameters for characterization of plastic strain localization. *Experimental Mechanics*, vol. 60, no. 1, p. 3-12, **DOI:10.1007/s11340-019-00510-6**.

[58] Acciaioli, A., Lionello, G., Baleani, M. (2018). Experimentally achievable accuracy using a digital image correlation technique in measuring small-magnitude (<0.1%) homogeneous strain fields. *Materials*, vol. 11, no. 5, 751, **DOI:10.3390/ma11050751**.

Strojniški vestnik - Journal of Mechanical Engineering 70(2024)5-6, 223-230
DOI:10.5545/sv-jme.2023.550
Original Scientific Paper
Received for review: 2023-02-22
Received revised form: 2023-05-31
Accepted for publication: 2023-06-22

The Double-Sided Upsetting of the End Thickenings on Rod Blanks

Anh Tu Do[1,*] – Aleksey Vladimirovich Chernyaev[2]
[1] Faculty of Mechanical Engineering and Mechatronics, Phenikaa University, Vietnam
[2] Tula State University, Russia

The known methods for the plastic shaping of axisymmetric parts with bilateral end thickenings and the die equipment used for their application have several significant drawbacks, which may reduce the quality of manufactured products, increase their cost, and limit the technological capabilities of production. As a rule, they provide alternate plastic shaping of end thickenings. In this paper, we propose a method of simultaneous stamping of end thickenings on a bar stock in split dies and a stamping device for its implementation. To establish the power modes of stamping we carried out the simulation of the process under study using the finite element method in the QForm software package. The dependencies of the stamping force on the geometric dimensions of the workpiece and friction conditions on the contact surfaces are established. The damageability of the workpiece material made of AA5056 alloy was assessed, and a diagram was obtained to determine the number of required stamping operations.

Keywords: cold forging, upsetting, end thickenings, force, material damageability

Highlights

- *A method is proposed for the simultaneous stamping of two end thickenings on a bar stock in split dies and a stamping device for its implementation.*
- *As a result of modeling, the nature of the influence of the geometric dimensions of the workpiece and friction conditions on the power mode of stamping was established.*
- *An assessment was made of the stress-strain state of the workpiece and the damage of the material at the final stage of stamping products from the alloy AA5056.*
- *A diagram was obtained to determine the number of necessary operations for stamping axisymmetric parts with end thickenings from AA5056 alloy.*

0 INTRODUCTION

Axisymmetrical parts with end thickenings and axial cavities are widely used in various industries. In particular, they are used as pistons in pumping equipment, elements of axial power transmission in diesel, hydraulic hammers, and pneumatic devices, and for the movements of actuators in various automated systems.

One way to obtain axisymmetrical parts is by machining. However, the low metal utilization factor and significant production time do not allow this method to be considered rational for use in series production.

The most effective way to obtain this kind of part is by cold forming **[1]** to **[6]**, which allows for obtaining parts with sufficient accuracy and minimal material loss. At the same time, productivity increases, and the resulting products have higher strength characteristics and wear resistance due to the hardening of the material.

The stamping of end thickenings can be performed using extrusion or closed die operations **[7]** to **[10]**. The thickening is formed, as a rule, on one of the product ends **[11]** and **[12]**. If it is necessary to obtain the thickening at both ends of the product, alternate plastic formations of end thickenings are used. In this case, complex stamping devices are employed, which require manual installation of blanks with pincers and removal of the forgings. Some devices have limited technological capabilities related to the size of the products, low productivity, and are not suitable for complex automation.

One promising direction in the development of forging and stamping production is the method of stamping by extrusion in split dies, the implementation of which is carried out both on universal equipment and on special presses. Unlike traditional stamping methods, the die has one or more parting planes, along which the parts of the die fit snugly against each other during the deformation of the workpiece. This method can be used for cold, semi-hot, and hot metal processing. The use of forging in split dies makes it possible not only to obtain forgings of a more complex shape with high dimensional accuracy but also to exclude the formation of a burr and its subsequent trimming, to reduce machining allowances, and to increase the productivity of forging **[13]** and **[14]**.

Thus, it is relevant to develop a method for the simultaneous double-sided cold forming of end

*Corr. Author's Address: Faculty of Mechanical Eng. and Mechatronics, Phenikaa University, Yen Nghia, Ha Dong, Hanoi 12116, Vietnam, tu.doanh@phenikaa-uni.edu.vn

thickenings on rod blanks and study a stamping device for its implementation.

We propose below a design of a punching device with split dies. This model enables the simultaneous deformation of both end thickenings on a rod blank. The results of theoretical studies of the stressed and deformed state and damageability of the workpiece material made of AA5056 alloy are also presented hereafter in order to make it possible to determine the required number of forming operations.

1 TECHNOLOGY

The procedure of simultaneous moulding of the front and rear end thickenings (ET) should be focused more on the technological processes of plastic moulding of axisymmetric parts with bilateral end thickenings (APWBET) (Fig. 1).

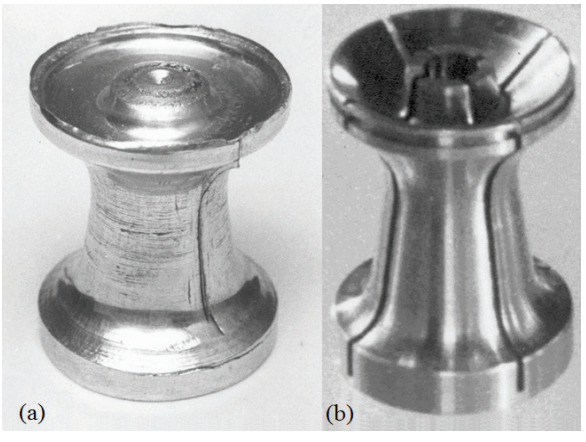

Fig. 1. *Axisymmetric part with end thickenings; a) before, and b) after machining*

The design of the stamping device should provide specified simultaneous moulding of ET in one stroke to make it possible to use conventional press equipment. This forming is carried out by upsetting the movable separable die 4 on the meridional plane (Fig. 2). In this case, geometrical dimensions, the shape of semi-finished product 2 before upsetting of ET, as well as its position relative to the tool (split die) at the moment of the beginning of plastic deformation, should be such as to ensure filling of both distant (from punch 1) ET in cavity 5 of a split die and distant (in the cavity 3) of the same die **[13]**.

The production technology of the APWBET can include operations of cutting off measured rod billets, preliminary upsetting, or direct extrusion of the middle part of the billet, and the final stamping of end thickenings of various profiles **[14]**. The final dimensions of the product are formed by machining operations. If the through hole in the product has a small diameter, it is advisable to stamp a solid billet with further registration of the central hole by drilling. The metal loss, in this case, is insignificant. Depending on the degree of deformation, stamping can be carried out in 1 or 2 passes. The regulating factor is the accumulated damageability of the workpiece material, which should not exceed the permissible values. Let us consider the process of obtaining the billet APWBET at one stamping position, which will significantly increase the productivity of its production as a result of reducing the number of shaping operations and the exclusion of intermediate annealing.

2 RESEARCH METHODS

Theoretical studies of force regimes and the stress-strain state of the workpiece during stamping APWBET are carried out using the basic provisions of the theory of plasticity of a rigid-plastic, incompressible, hardening material in the QForm

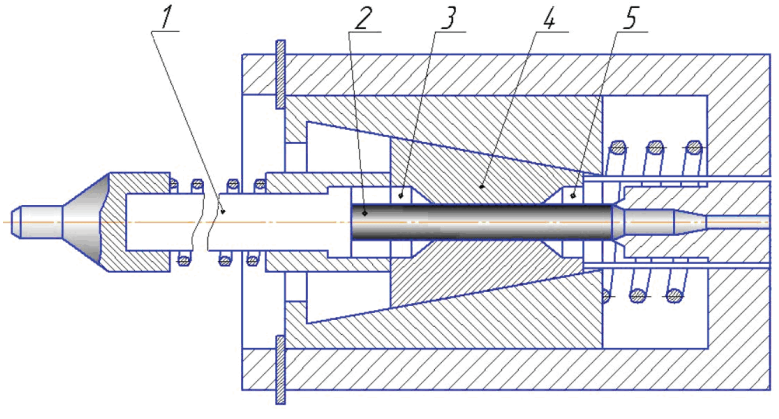

Fig. 2. *Simplified schematic of an upsetting device for simultaneous plastic forming of ET*

2D/3D software package based on the finite element method. Conditions accepted: stamping temperature 20 °C; strain rate ξ = 1 s^{-1}; Siebel friction model; lubricant - mineral oil; friction factor 0.15; test materials: 1010, C27400, AA5056; the number of finite elements of the workpiece mesh is 30,000. The number of forming operations was determined based on the value of damage capacity accumulated by the billet material based on the phenomenological fracture criterion considering the history of deformation.

3 FORGING POWER MODES

To assess the power modes of stamping of the APWBET, a simulation in the QForm 2D/3D software package was carried out. Stamping is performed in a die with split matrices. A cylindrical blank of length l = 28 mm and diameter d = 14.5 mm is deformed by two punches moving in the opposite direction (Fig. 3). Under the influence of the tool, metal fills the cavities with the die, forming end thickenings. At the same time, an inner cavity is formed at the end of the workpiece, which serves as a marker for drilling a through hole (Fig. 4).

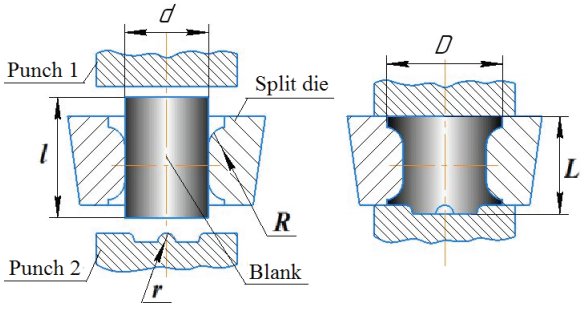

Fig. 3. *Schematic of the operation*

The workpiece material was assumed to be rigid, hardened plastic. The studies were performed for workpieces made of the following materials: 1010, C27400, and AA5056. The hardening curves of the studied materials are shown in Fig. 5 **[15]**.

Fig. 6 shows the graphical dependencies of the change in the force of the operation on the relative movement of the tool where and h is the current and final movements of the punches, respectively.

At the initial stage of stamping, an internal cavity of the radius is formed at the end of the blank, which is accompanied by a slight increase in the deformation force. This is followed by the stage of metal accumulation in the cavities of the split die with the formation of end thickenings, accompanied by a smooth increase in the force.

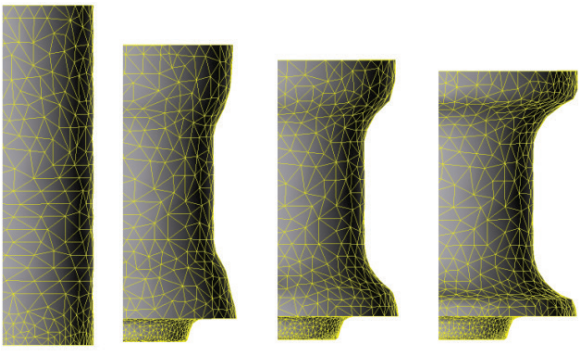

Fig. 4. *Sequence of shaping*

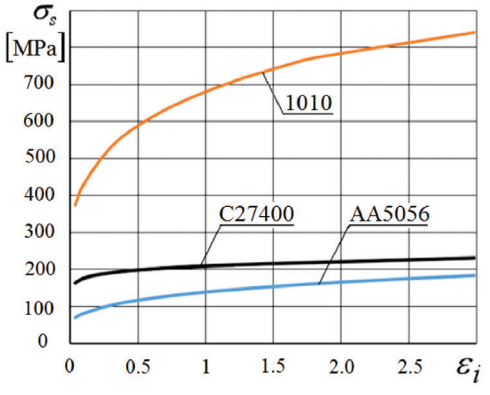

Fig. 5. Hardening curves of the studied materials (t = 20 °C , ξ = 1 s^{-1})

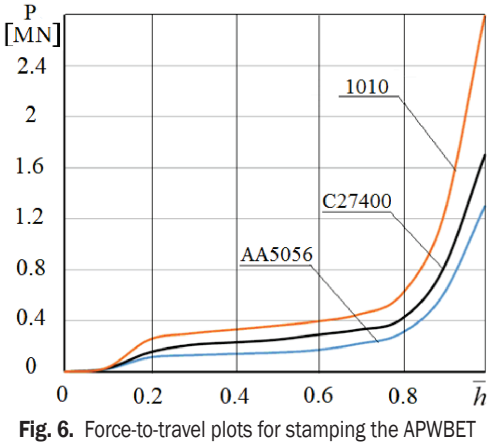

Fig. 6. Force-to-travel plots for stamping the APWBET (μ = 0.1, R = 5 mm, r = 2 mm, d = 14.5 mm, D = 21.8 mm)

At the final stage, the final design of the contour of the workpiece by filling the angular sections of the die occurs, which is manifested by a sharp increase in the force of the operation. The technological force reaches its maximum value at the final moment of stamping $\bar{h} = 1$. In further studies, its maximum value is taken as the operation force. The main factors affecting the force modes of stamping of the APWBET

are geometric parameters of the tool and workpiece: radius of curvature of the die cavity R, radius of curvature of the punch protrusion r, initial d and final D diameters of the workpiece, as well as friction conditions at the contact boundaries of the tool and workpiece, characterized by the friction coefficient μ. Theoretical studies of the forging force modes of the APWBET were performed in the following ranges of varying parameters: R = 3 mm, 5 mm, 7 mm, and 9 mm; r = 1 mm, 2 mm, 3 mm, and 4 mm; μ = 0.05, 0,10, 0.15, and 0.20. The diameter of the blank was taken as constant d = 14.5 mm, the diameter of the product mm, which corresponds to the values of the relative diameter. The length of the blank and the product were taken l = 28 mm, L = 22 mm. The results of the calculations are shown in Fig. 7.

It was found that the greatest influence on the force of stamping in the studied ranges of variation of varying parameters has a relative diameter. The decrease from 0.66 to 0.6, which corresponds to the increase in the diameter size of the product and, therefore, the degree of deformation with the unchanged dimensions of the blank, leads to an increase in the stamping force by 20 % to 30 %. The diametrical size of the product is determined by the requirements of the drawing and is not a subject of optimization of the force modes.

The radius of the inner cavities of the die R has a significant influence on the stamping force. Increasing R from 3 mm to 9 mm leads to a decrease in force by 15 % to 20 %, which is explained by more favourable conditions of metal flow with less energy required to change the trajectory. Increasing R, if allowed by the product drawing and operating conditions, leads to a decrease in force and increases the die resistance.

Increasing the radius r of the internal cavity at the end of the blank from 1 mm to 4 mm leads to an increase in force by 5 % to 10 %. The value of the specified radius is not significant in the design of the product because later, the central part of the blank will form a through hole, and the cavity formed during stamping, which is a marking, will be removed into the waste. Therefore, to reduce the stamping force, it is advisable to assign smaller values r. An increase in friction on the contact surfaces of the tool and workpiece can result in a 10 % increase in force. To reduce friction, it is advisable to use lubricants designed for this purpose and provide

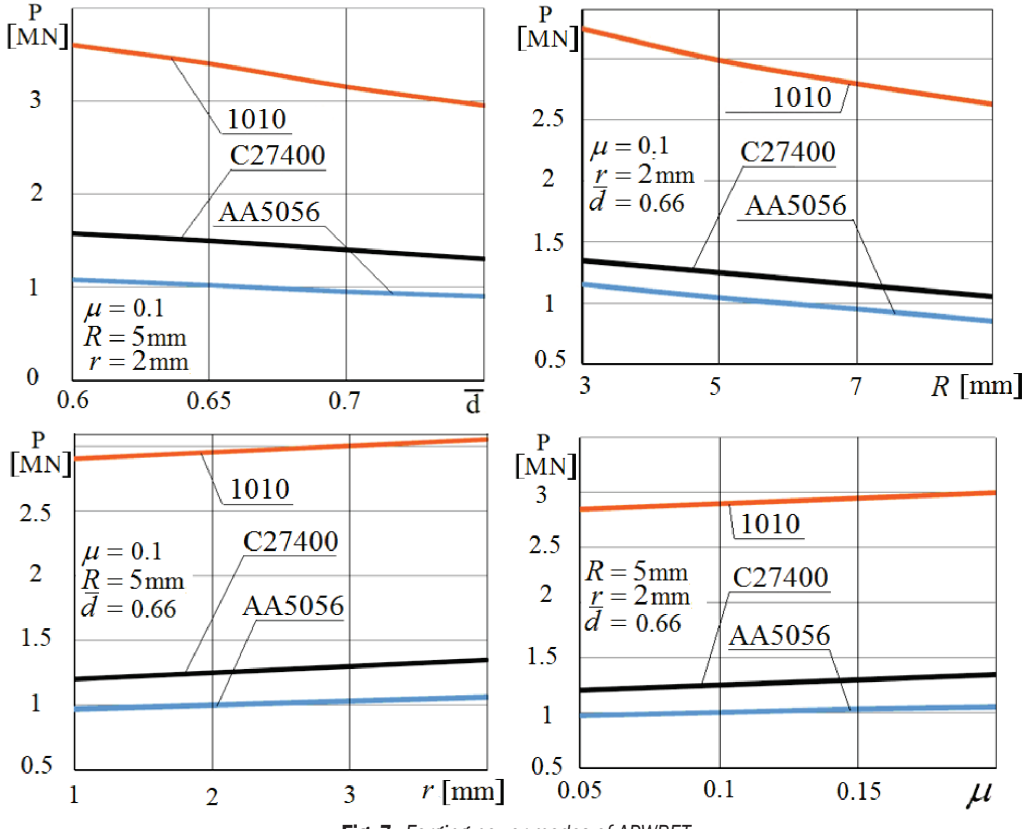

Fig. 7. *Forging power modes of APWBET*

careful treatment of the surfaces of the inner cavity of the die. During operation, it is necessary to monitor the condition of the working surfaces of the tool, to prevent wear and formation of scuffs, leading to an increase in force and deterioration of the appearance of products.

4 DAMAGEABILITY OF WORKPIECE MATERIAL

The processes of cold forging (CF) are characterized by high specific forces at significant degrees of deformation and are accompanied by significant strain hardening and accumulation of microdamage. The quality of products obtained by CF and the reliability of their operation depend on the level of accumulated damageability [16] and [17].

Material damageability ω during plastic deformation is often evaluated by the criterion proposed by Kolmogorov [17]. As a characteristic of material damageability, the degree of plasticity resource utilization is taken as a ratio of accumulated strain intensity to its limiting value on given characteristics of the stress and strain state of the elementary volume in the centre of plastic deformation:

$$\omega = \int_0^{\varepsilon_i} \frac{d\varepsilon_i}{[\varepsilon_i]} < 1, \tag{1}$$

where ε_i is the effective strain at a given stage of deformation; $[\varepsilon_i]$ is the effective strain at the moment of failure, depending on the stress state index.

$$\eta = \frac{3\sigma}{\sigma_i}, \tag{2}$$

where σ is mean stress, and σ_i effective stress. The value $[\varepsilon_i]$, as a rule, is found from experimentally obtained diagrams of ultimate plasticity.

To justify the number of necessary stamping operations, the stress and strain states of the blank in the process of forming were studied using the QForm 2D/3D software package. Fig. 8 shows the distribution patterns σ_i, ε_i, σ, and ω the final stage of the forging of APWBET of AA5056 alloy.

It was found that compressive stresses predominate in the deformation centre, which creates favourable conditions in terms of deformation without failure, contributing to the healing of micro-defects caused by plastic deformation and preventing the exhaustion of the plasticity resource of the material [16]. The greatest values ω are reached in the marginal areas of the end thickenings (points P_1 and P_2). Further studies were carried out on these points. Values σ, σ_i, and ε_i were calculated employing the QForm software package. The limiting values depending on η were set in the form of a data table for the corresponding

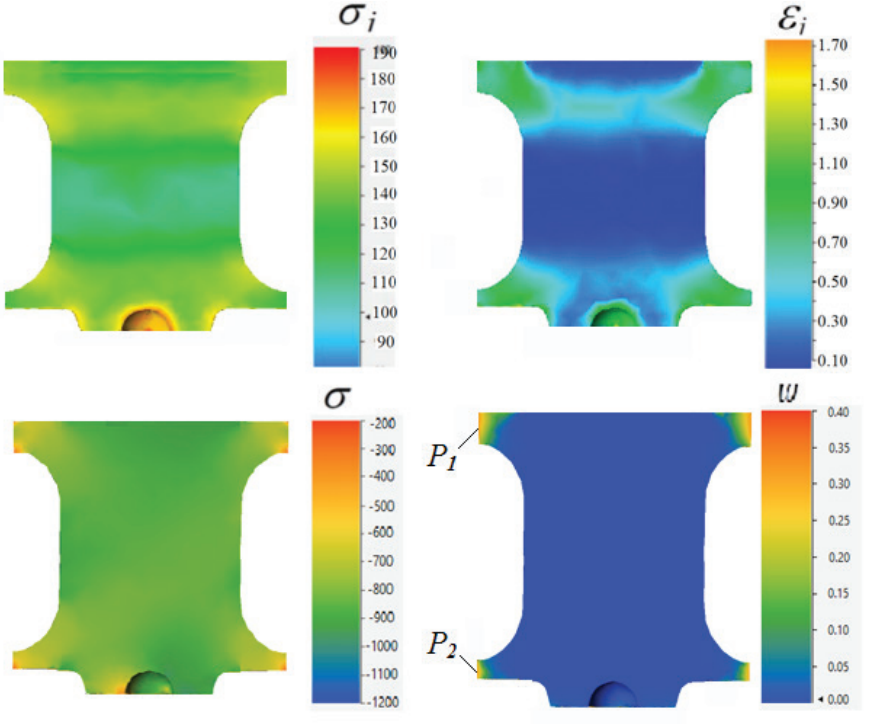

Fig. 8. Distribution σ_i, ε_i, σ, and ω at the final stage of stamping (material is AA5056 alloy; μ = 0.1, R = 5 mm, r = 2 mm, $\bar{d}$ =0.66)

subprogram of the complex QForm according to the results of the approximation of the limit plasticity diagram [17]. An example of the calculation of the damageability for points P_1 and P_2 when stamping the APWBET of AA5056 alloy is shown in Fig. 9. The plasticity limit diagram $[\varepsilon_i]$ and the deformation trajectories at points P_1 and P_2 are shown. For the example under consideration, at point

P_1: $\eta = -1.8$, $\varepsilon_i = 0.61$, $\varepsilon_{np} = 1.67$, $\omega = 0.36$;
P_2: $\eta = -1.6$, $\varepsilon_i = 0.47$, $\varepsilon_{np} = 1.61$, $\omega = 0.29$.

It was found that the values $\bar{d}$ and R have the greatest influence on the damageability of the workpiece material. Their decrease in the studied range ω decreases by 30 % to 40 % and 20 % to 30 %, respectively (Fig. 10).

It was found that at values $\bar{d} < 0.62$, the damageability of AA5056 alloy reaches a critical lev $\omega > 0.3$, which, according to the recommendations [16], is unacceptable for critical products. In this case, the stamping of the APWBET in one operation is impossible, and in the technological process, it is necessary to provide an additional transition of preliminary profiling - the upsetting of the end thickening of the cylindrical billet with subsequent annealing and the final dimensions are formed at the second operation (Fig. 11).

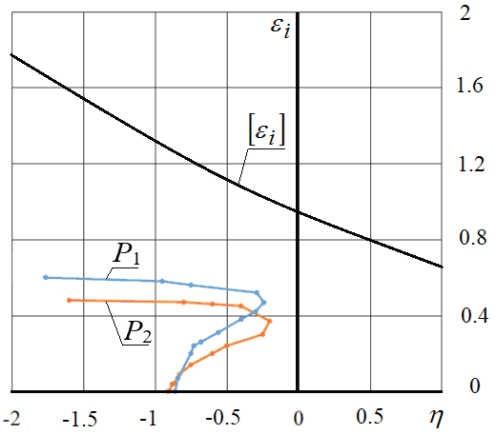

Fig. 9. *Assessment of the damageability of the material*

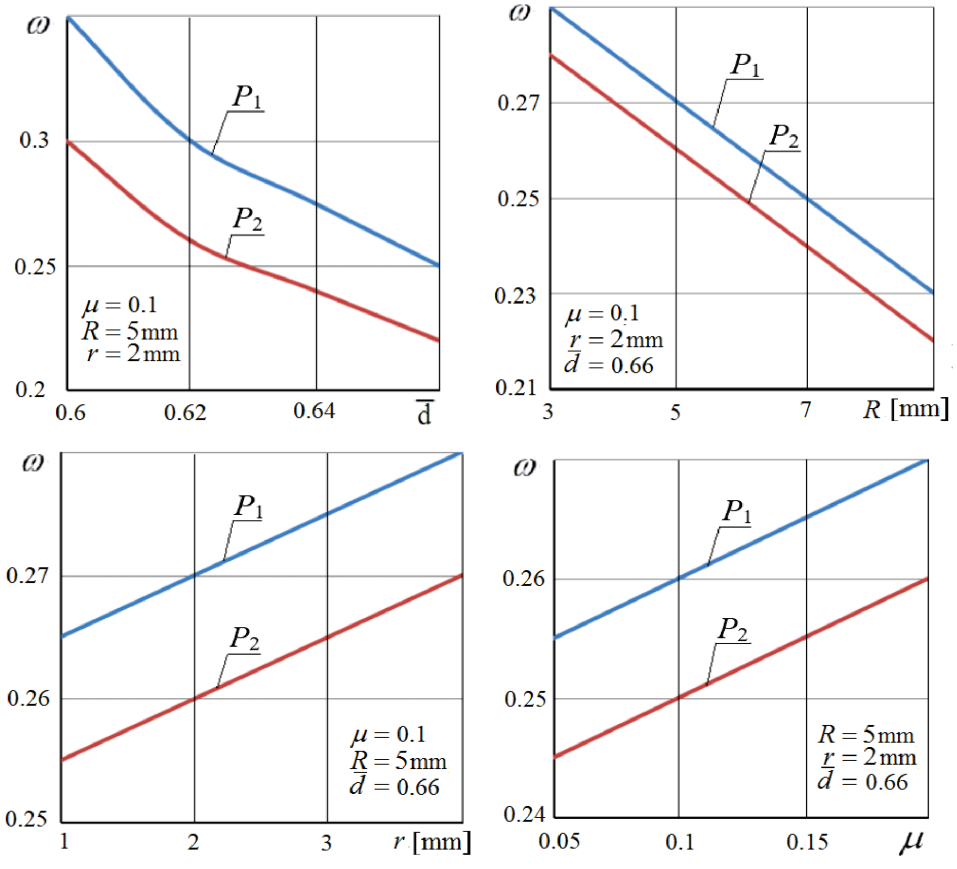

Fig. 10. *Damageability of the material when stamping the APWBET*

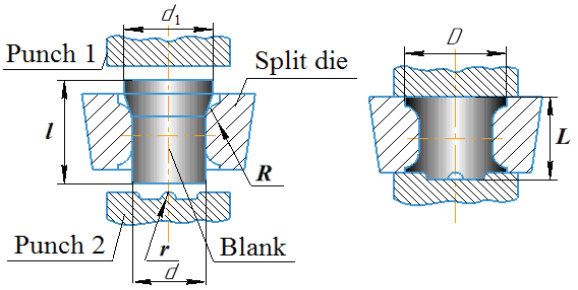

Fig. 11. *Schematic diagram of the forging of the APWBET from the profile billet*

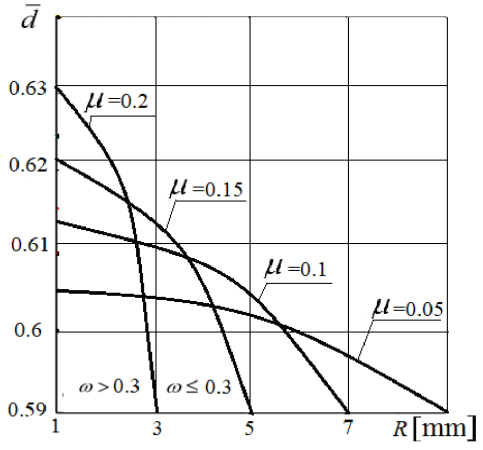

Fig. 12. *Determining the number of stamping operations (material - AA5056)*

When using a preformed billet with a diameter of the thickened part d_1 = 19 mm and length l = 25 mm, the damageability of the material at the final stamping operation is reduced, not exceeding the value ω = 0.25, which meets the requirements for products of the critical application.

Fig. 12 presents a diagram for determining the number of necessary forming operations when stamping the APWBET. The area of the diagram below each curve, corresponding to the coefficient of friction μ, at given $\bar{d}$ and R are characterized by the values of damageability $\omega > 0.3$, which means the necessity of the operation of preliminary profiling of the workpiece. In this case, the stamping is performed in two transitions. The area of the diagram over the above curves corresponds to the permissible values of damageability $\omega \leq 0.3$, which means that it is possible to obtain the product in one stamping operation.

Thus, with the given ratios of geometric parameters and the degree of deformation, the APWBET can be produced in one stamping operation with values of the degree of plasticity resource utilization acceptable for critical parts. When stamping the end thickenings of large diameter, it is necessary to use pre-profiling of the middle part of the APWBET to ensure rational kinematics of the flow of the deformed material and to reduce the damageability.

5 CONCLUSIONS

1. The stamping axisymmetric parts with end thickenings from a bar of continuous cross-section was proposed, expanding the technological capabilities of cold stamping of small, precise parts of complex shapes, providing increased productivity and reduced material losses.
2. As a result of modelling the stamping of solid APWBET from a cylindrical billet, we come to the conclusion that the factors influencing force modes of APWBET stamping are the geometric parameters of the tool and the billet: the radius of curvature of the die cavity R, the radius of curvature of the punch projection r, initial d and final D diameters of the blank, and also friction conditions at the contact boundaries of the tool and billet, characterized by friction coefficient μ. By doing so, a quantitative assessment of the influence of these parameters within the investigated range is given.
3. The assessment of the damageability of the blank material in dangerous points has been carried out. Thus, we establish the ranges of deformation degree and product geometry changes, at which the stamping of solid APWBET can be performed for one and two form-modifying operations.

6 REFERENCES

[1] Bulzak, T., Winiarski, G., Wójcik, L., Szala, M. (2022). Application of numerical simulation and physical modeling for verifying a cold forging process for rotary sleeves. *Journal of Materials Engineering and Performance*, vol. 31, p. 2267-2280, **DOI:10.1007/s11665-021-06314-x**.

[2] Winiarski, G., Bulzak, T., Wójcik, L., Szala, M. (2021). Cold forging of a hollow flanged part by an unconventional extrusion method. *Journal of Physics: Conference Series*, vol. 2130, art. ID 012019, **DOI:10.1088/1742-6596/2130/1/012019**.

[3] Wang, Z., Lu, J., Wang, Z.R. (2001). Numerical and experimental research of the cold upsetting-extruding of tube flanges. Journal of Materials Processing Technology,vol. 110, no. 1, p. 28-35, **DOI:10.1016/S0924-0136(00)00863-3**.

[4] Winiarski, G., Gontarz, A., Samołyk,G. (2019). Flange formation in aluminum alloy EN AW 6060 tubes by radial extrusion with the use of a limit ring. *Archives of Civil and Mechanical Engineering*, vol. 19, no. 4, p. 1020-1028, **DOI:10.1016/j.acme.2019.05.006**.

[5] Li, H.F., Luo, M., Xu, T.T., Li, Q.Z., Hou, Y.M. (2023). Optimization method of multi-parameter coupling for a hydraulic rolling

reshaper based on factorial design. *Strojniški vestnik - Journal of Mechanical Engineering*, vol. 69, no. 11-12, p. 483-496, **DOI:10.5545/sv-jme.2023.627**.

[6] Topgül, T. (2022). Design, manufacturing, and thermodynamic analysis of a gamma-type stirling engine powered by solar energy. *Strojniški vestnik - Journal of Mechanical Engineering*, vol. 68, no. 12, p. 757-770, **DOI:10.5545/sv-jme.2022.368**.

[7] Yuan, Y., Ren, Y., Wu, Q. (2022). Research on improvement of cold extrusion technology of connecting screws. *Journal of Physics: Conference Series*, vol. 2160, art. ID 012055, **DOI:10.1088/1742-6596/2160/1/012055**.

[8] Luh, Y.-P., Wang, H.-L., Ciou, J.-R., Jhang, J.-F. (2019). Study of the hardening in middle shaft during cold forging. *IOP Conference Series: Materials Science and Engineering*, vol. 538, art. ID 012013, **DOI:10.1088/1757-899X/538/1/012013**.

[9] Park, Y.B., Lee, K.H. (2001). Study on the deformation of die and product in closed die upsetting. *Journal of Materials Processing Technology*, vol. 118, no. 1-3, p. 417-421, **DOI:10.1016/S0924-0136(01)00915-3**.

[10] Na, R.S., Jia, K.F., Miao, S.J., Zhang, W.G., Zhang, Q. (2023). Analysis of the dynamic characteristics of a gear-rotor-bearing system with external excitation. *Strojniški vestnik - Journal of Mechanical Engineering*, vol. 69, no. 1-2, p. 17-31, **DOI:10.5545/sv-jme.2022.427**.

[11] Petrov, M., Kalpin, Y., Petrov, P. (2020). Numerical investigation of upsetting and transverse extrusion process for "rod with flange" parts and preforms production made from aluminium alloy 1013. *Procedia Manufacturing*, vol. 47, p. 1504-1511, **DOI:10.1016/j.promfg.2020.04.338**.

[12] Kim, S.J., Lee, T., Hwang, J.-K. (2020). High-strength bolt manufactured by an extrusion-based forming process using twinning-induced plasticity steel. *Journal of Manufacturing Processes*, vol. 59, p. 33-42, **DOI:10.1016/j.jmapro.2020.09.043**.

[13] Panfilov, G.V., Do, A.T., Le, M.D. (2021). Designing die tooling for manufacturing axisymmetric parts with end thickenings and their application. *Science-intensive Technologies in Mechanical Engineering*, no. 3, p. 7-15, **DOI:10.30987/2223-4608-2021-3-7-15**. (in Russian)

[14] Panfilov, G.V., Chernyaev, A.V., Do, A.T. (2021). Variants of multi-operated cold forging technologies for axially symmetrical parts with simultaneous end thickening. *Proceedings of Tula State University. Technical Sciences*, no. 6. p. 365-374.

[15] Polukhin, P.I., Gunn, G.Y., Galkin, A.M. (1983). *Plastic Deformation Resistance of Metals and Alloys. 2nd ed., Revised and Supplemented*. Metallurgy, Moscow. (in Russian)

[16] Bogatov, A.A., Mizhiritskiy, O.I., Smirnov, S.V. (1984). *Resource of Plasticity of Metals in Processing by Pressure.* Metallurgy, Moscow. (in Russian)

[17] Kolmogorov, V.L. (1970). *Stresses. Deformations. Destruction*. Metallurgy, Moscow. (in Russian)

Strojniški vestnik - Journal of Mechanical Engineering 70(2024)5-6, 231-246
DOI:10.5545/sv-jme.2023.776
Original Scientific Paper
Received for review: 2023-08-27
Received revised form: 2023-12-08
Accepted for publication: 2024-03-12

The Influence of Pump-Turbine Specific Speed on Hydraulic Transient Processes

Zdravko Giljen[1,*] – Miloš Nedeljković[1] – Yongguang Cheng[2]
[1] University of Belgrade, Faculty of Mechanical Engineering, Serbia
[2] Wuhan University, State Key Laboratory of Water Resources and Hydropower Engineering Science, Wuhan, China

The main porpose of this paper is to perform and present at transient process analysis on the influence of different specific speeds (nq) of the three-model pump-turbines that may implemented at the hydropower pump storage plant (HPSP) Bajina Basta, Serbia. The intention is to analyze the operation regimes along the S-shaped characteristic curve, which creates difficulties in calculations during the load-rejection process. These problems are manifested by an unusual increase in water pressure, followed by an increase in machine vibrations, thus threatening the stability of machine operation. The subject of this research is the four-quadrant (4Q) characteristic curves, presented in the form of Suter curves (the head and momentum parameters (Wh and Wm), in dependence of angle (θ)) for different wicket gate openings, of the three pump-turbine models with different specific speeds (nq = 27, nq = 38 and nq = 50). These 4Q characteristics are used as input data for numerical code developed to calculate the simultaneous load rejection of both pump-turbines. The numerical code is based on the method of characteristics and applied to the test case at HPSP. This is especially relevant when dealing with characteristic S-shaped curves that may lead to serious instability in operation during the transient process. The calculation results show changes in the pressure, speed of rotation and discharge of the machine operation regimes, but the important findings are reflected in further application of the results to determine the parametric flow and speed (Q_{11} and n_{11}) trajectories of the operating points, where the unstable behavior of a pump-turbine operating in turbine mode is presented and periodically the trajectories also pass through the reverse pump zone.

Keywords: hydraulic transients, pump-turbine, influence of the specific speed, load rejection, working point trajectory, method of characteristics

Highlights

- *The authors developed a numerical code for calculating transient processes based on the method of characteristics (MOC) and used this code to compute the transient processes for the test case at HPSP Bajina Basta, Serbia, as well as to calculate the operating point trajectory during shutdown.*
- *This paper presents the analysis of results obtained during the calculated transient processes of the two pump-turbines (the changes in pressure in the spiral casing, the pressure in the draft tube, the speed of rotation, discharge, and wicket gate opening), and for the analysis of the impact of nq - specific speed on the transient processes.*
- *The 4Q characteristics in $Q_{11}/{}_oQ_{11o}$ – $n_{11}/{}_on_{11o}$ diagrams for both pump-turbines show the trajectory of working points during load rejection from a turbine zone. ${}_oQ_{11o}$ is the rated unit discharge [-], and ${}_on_{11o}$ is the rated unit speed of rotation [-].*
- *The analysis of the trajectory of the working point for all three pump-turbine models (nq = 27, nq = 38 and nq = 50) during the transient process, is especially analyzed.*

0 INTRODUCTION

The detailed study of the available literature in the field of hydraulic machines showed that a small number of research papers dealt with the problem of the influence of specific speed (*nq*) on the shape of four-quadrant (4Q) performance curves, and consequently on their application in the calculation of transient processes. This was the main motivation for writing this paper where the analysis of transition processes of load rejection in the hydropower plant Bajina Basta, Serbia was performed.

The operating characteristics of pump-turbines, which in certain zones have the form of the letter *S* can lead to a relatively large hydraulic shock and pulsating pressures. These pressures and the high velocity of runaway during transients can directly damage the pipelines and shorten the life of the turbine.

Four-quadrant (4Q) hydraulic machinery performance curves are required to calculate transients in hydraulic systems, and as a rule in the literature, such curves are given only for three specific speeds: nq = 25 nq = 147, and nq = 261 (one radial, one semi axial and one axial turbomachine, respectively, in SI system units). When needed for some other *nq*, the performance curves nearest to such *nq* are used, even without any interpolation. To date, the influences of different specific speeds corresponding to the performance curves of turbomachinery (pumps, pump-turbines, and turbines) on transient processes have been scarcely studied and analyzed. Certain contributions in this area have been reported **[1] to [5]**. This paper discusses this influence on the concrete

*Corr. Author's Address: University of Belgrade, Faculty of Mechanical Engineering, Kraljice Marije 16, 11120 Belgrade, Serbia, zgiljen@gmail.com

example of the pumped-storage plant (PSP) Bajina Basta (also known as a reversible hydropower plant, RHPP), where two pump-turbines are installed (2 × 315 MW; this is the maximum power output in turbine mode). The transition process analyzed herein refers to the simultaneous load rejection of pump-turbines working in turbine modes, the first one with a power of 281 MW, and the second one with a power of 284 MW.

For the calculation of transient processes, as the input data, the 4Q characteristics are represented by Suter curves (*Wh* and *Wm* diagrams, where *Wh* is the non-dimensional characteristic head, and *Wm* is the non-dimensional characteristic moment) for three pump-turbine models with specific speeds of $nq = 27$, $nq = 38$ and $nq = 50$. All three sets of Suter curves are shown in Figs. 3 to 8, for various openings of the wicket gates. The diagrams are obtained by calculating the 4Q characteristics from the non-dimensional curves experimentally determined for defined pump-turbine models (where Q_{11} is unit discharge [-], n_{11} unit speed of rotation [-], M_{11} unit moment [-]). The key steps in the process of converting the 4Q characteristics into the form of Suter curves are presented in more detail in **[6]**.

The authors developed a numerical code for calculating transient processes based on the method of characteristics (MOC) **[7]** and used this code to compute the transient processes for the test case at HPSP Bajina Basta, Serbia, as well as for the calculation of the operating point trajectory during shutdown.

The literature survey reveals that although a lot of authors investigated the behavior of hydraulics phenomena in the pump-turbines during the transient processes, a relatively small number of them studied the influence of specific speed on transient processes.

In Donsky **[1]**, the complete operating characteristics of pumps were used to determine the effects of transient processes, including a water hammer in the inlet and drainage lines, on the normal or abnormal starting and stopping of the pumps. The three 4Q characteristics available in the literature (by Knapp and Stepanoff) were compared, and the influence of the specific speed on the calculation of transient processes was presented. Regarding the power failure of the pumps, the transient processes determined that the 4Q characteristics have the most unfavorable impact when a pump with the lowest specific speed is used.

In Brown and Rogers **[2]**, pumps in the southern Nevada system were employed to reveal that the specific speed can influence the transient process calculations. Pumps from three different manufacturers with different 4Q characteristic curves were installed in this system. The pressure at the discharge side was measured for these three pumps; under identical power failure conditions, and there were differences in the measured results due to the influence of the specific speed on the transient processes.

Giljen and Nedeljkovic **[4]** analyzed a transient process for a defined pump installation, and the influence of the specific speed (*nq*) on the results obtained during the calculation was determined. In the numerical code for calculating the transient processes, the values for the *Wh* and *Wm* characteristic curves obtained from model tests and from the originally derived universal equations for *Wh* and *Wm* were used for seven radial pump-turbine models and one radial pump model. A separate MATLAB program was utilized to obtain the Suter curves from the performance characteristics of these models and to establish universal equations (universal curves).

In Li et al. **[8]** 3D numerical simulations were carried out by the commercial software STAR-CCM+ to investigate the hydraulic transient and flow behaviors of a prototype pump-turbine during the normal shutdown process. The global characteristics and pressure fluctuations were analyzed as the pump-turbine run through the turbine mode, into the turbine braking mode, and finally into the reversed pump mode. Giljen **[9]** presented the transient process calculation results for the prototype Francis turbine installed at the hydropower plant (HPP) Piva. Giljen **[10]** also investigated and compared the pressure fluctuations in the draft tube of the prototype Francis turbine installed at HPP Piva during full load rejection. Capponi et al. **[11]** calculated transient processes by two different numerical models: first, the MOC was employed, and second, a frequency-domain model was developed as an impedance method (IM) model. Casartelli et al. **[12]** presented the computations of three different dynamic pump-turbine operating conditions. The results, using steady boundary conditions (BC) in the unstable region as well as transient BC like load-rejection and runaway, were computed with EARSM, showing its superiority compared to linear two equation models. Deniz et al. **[13]** focused on the flow instabilities of pump-turbines. The results of the experiments and computational fluid dynamics (CFD) simulations of the research carried out on a low-specific speed model pump-turbine are presented. In Fu et al. **[14]** the load rejection transient process of a pump-turbine was simulated with a three-dimensional (3D) large eddy simulation method and a dynamic mesh technology.

The simulation results were validated against the experimental data. In Xia et al. [15] the load rejection processes of two model pump-turbines with the same specific-speed but different in the runner blade inlet shape were investigated by a 3D numerical simulation method, were analyzed. Zheng et al. [16] presented the influences of rotational speed variations on the vibration performances of the whole unit with reversible pump-turbine (including the top cover, the upper and the lower brackets). The phenomenon is experimentally investigated with discussions of their sources and propagation characteristics, during the spin-no-load mode. Xia et al. [17] performed the analysis of the evolution of flow structures and pressure fluctuations in the S-shaped region of pump-turbines, and 3D numerical simulations were carried out for a model pump-turbine at four different guide-vane openings (GVOs). Hu et al. [18] performed an analysis of the hydraulic characteristics of pump-turbines in off-design conditions, especially the S-shaped characteristics, which are crucial for the safety and stability of the unit. To explore the *S*-characteristics of pump-turbines through a transient method, an experimental investigation was conducted based on a pumped-storage model system. Li et al. [19] performed an analysis of transient processes of a flow rate that increased and decreased in the pump mode of a model pump-turbine that were simulated through unsteady simulations using the shear stress transport (SST) k–ω turbulence model. Pump performance characteristics of pump-turbines in transient processes are significantly different from those in steady processes and are analyzed in this paper. Zhang et al. [20] performed the analysis of the pressure pulsations in the vaneless space of pump-turbines, which are extremely intense and always experience rapid time variations during transient scenarios, causing structural vibrations and even more serious accidents. The mechanism behind the rapid time variations of the vaneless space pressure pulsations in a model pump-turbine during runaway was analyzed through 3D numerical simulations. Zhu et al. [21] analyzed the two pump-turbine runners, one with a large positive blade lean and the other with a large negative lean, which are investigated numerically and experimentally. Frequent changes in the operating modes pose significant challenges in the development of a pump-turbine with high efficiency and stability. Fu et al. [22] analyzed the complex energy conversion and energy dissipation that occur in pump-turbines during the load rejection process. 3D transient turbulent flow in a pump-turbine was simulated using the method of coupling the rigid rotor motion with flow and dynamic mesh technology. Ran and Luo [23] performed the experiments in a medium specific-speed pump-turbine scaled model to investigate instability characteristics in pump mode, namely the head-drop phenomena. Two different head-drops are captured on a pump performance curve. The experimental investigations of the head-drop phenomenon, with the flowrate varying from 0.6 to 0.7 times of the design flowrate in the scaled model has also been presented. In Xiuli et al. [24] the transient flow characteristics are analyzed for a Francis-type reversible pump-turbine in generating mode by 3D numerical simulation with a moving mesh technique using the detached eddy simulation (DES) turbulent model. Yexiang et al. [25] analyze the S-shaped characteristic curves of pump-turbines that complicate synchronization with the electrical grid and affect system safety. Misaligned guide vanes (MGVs) are one of the most effective solutions to avoid S-shaped characteristics. Xia et al. [26] analyzed the understanding of the formation mechanism of the S-shaped characteristics (SSCs) and the relationship between flow structures and the runaway instability (RI), to optimize runner design for the promotion of operational reliability and flexibility. A new turbine equation is derived to reveal the prime cause of the SSCs, and the influence of geometric parameters on the SSCs was analyzed. Xia et al. [27] analyzed the pressure fluctuations and runner loads during the runaway process on a model pump-turbine runner at four guide vane openings (GVOs) using 3D (-CFD). In Li et al. [28] similarities of the flow in the rotor–stator interaction (RSI) affected region (stay vanes, guide vanes, and runner domain) in the prototype and the model Francis pump-turbines were analyzed, using numerical simulations with special attention to the influence of the Reynolds number. Zhang et al. [29] performed the analysis of the transient process, when hydro turbines may demonstrate some dynamic characteristics that differ from the corresponding static characteristics in steady operating conditions. Zeng et al. [30] analyzed the way that during the transitional processes of load rejection in a pumped-storage station, the S-shaped characteristics of the pump-turbines can result in relatively large water-hammer and pulsating pressures. These pressures and the high runaway speed during transient processes may directly damage the penstocks and shorten the life of the turbine. In that paper, different guide-vane closing schemes for reducing the maximum transient pressures, including the water-hammer and pulsating pressures, and runaway speed were investigated, and the principles for improving the closing schemes were

theoretically analyzed based on the transient characteristics in the *S*-shaped region. Cavazzini et al. [31] present a numerical aS-nalysis of the unstable behavior of a pump-turbine operating in turbine mode near the no-load condition. To study the unsteady phenomena which lead to the S-shape of the turbine characteristic, a load rejection scenario at constant and large guide vane opening was numerically analyzed by running through the flow-speed characteristic up to the turbine brake region. Zeng et al. [32] analyzed the way that pump-turbine characteristics greatly affect the operational stability of pumped-storage plants. In particular, the S-shaped region of the characteristic curves leads to severe instability during runaway conditions with servomotor failure. They investigated the runaway stability criterion by considering all the important effects in the hydro-mechanical system. Yu et al. [33] performed an analysis based on a numerical simulation of hydraulic transients in a PSP, and different closure laws were investigated for use when a high-head pump-turbine load rejection occurs. Sun et al. [34] analyzed the way that pump-turbine operation along the S-shaped curve can lead to difficulties in the load rejection process with unusual increases in water pressure. Pressure fluctuations are the primary reason for unstable operation of pump-turbines. Misaligned guide vanes (MGVs) are widely used to control the stability in the S-shaped region. Huang et al. [35] made a significant contribution when, they developed a method for predicting the complete four-quadrant characteristics of the Francis pump-turbine. A mathematical model was developed that describes the complete four-quadrant characteristics of the Francis pump-turbine, and Euler's equations and speed triangles on the impellers were used as the basis for developing this mathematical model. The most important contribution of that paper is reflected in the combination of the developed mathematical model with the regression analysis of characteristic operating points (COPs), and based on these the complete four quadrant characteristic curves for arbitrary specific speed are predicted. Pejovic et al. [36] analyzed the transient processes on reversible pump-turbine units, which were caused by a sudden load shedding of one or two reversible pump-turbine units. The authors of this paper also performed an analysis of the operation of the pump-turbine in the area where resonance can occur due to the instability of the pump and turbine in the runaway zone. They concluded that in hydropower plants with pump turbines of high capacity and high head, serious pressure fluctuations and dynamic stresses occur in certain parts of the plant. They also concluded that any asymmetry in aggregates, such as different loads, differences between the pump-turbine and the engine-generator, differences in the closing process of the intake valve and wicket gates of the conducting apparatus, asymmetry in the layout of the hydroelectric power plant constructions, etc., causes a phase shift. and, due to instability, significantly increased amplitude of pressure pulsations. Zeng et al. [37] designed a set of the four-quadrant characteristics of pump-turbines, which is of great importance, when the corresponding four-quadrant characteristics of pump-turbines cannot be used for replacement at the same specific speed. A major contribution of this paper is reflected in the newly developed method for the characterization of the pump turbines at any specific speed using a database of 25 available sets of the four-quadrant characteristics of pump turbines. The authors of this paper verified the developed method by comparing it with the measured four-quadrant characteristic curves of pump turbines with reasonable accuracy. Meniconi et al. [38] performed certain tests in water distribution networks and performed an analysis of the relevance of system configuration, energy dissipation phenomena, and pipe material characteristics in a real transmission network during the transient process. The aim was to create a numerical model that was progressively refined not only in terms of the governing equations but also by including more and representing the layout of the system and considering the actual functioning of the conditions. As a result, the unexpected role of smaller branches of the pipeline systems, i.e., pipes less than 1 % of the length of the main pipe – was indicated and a preliminary criterion for the system skeletonization was offered. Moreover, the importance of unsteady friction and viscoelasticity was assessed as a prominent remarkable effect of small defects. Simpson and Marchi [39] performed a detailed analysis of affinity laws relating to the four-quadrant characteristics of pumps operating at different speeds, and in the context of water distribution, affinity laws are commonly used to predict the pump curve for variable speed pumps. The research reported in this paper estimates the efficiency error for a wide range of pump sizes and tests the use of the previously proposed formula as an alternative to the affinity laws. The results show that a better estimate of the efficiency of small and medium pumps can be achieved with this formula. Moreover, the main contribution is that the formula can be easily implemented in hydraulic solvers. Zhou et al. [40] performed a detailed analysis of cavitation on the centrifugal pumps. They observed that cavitation produces a deterioration of the

hydraulic performance of centrifugal pumps. They also performed an analysis to prevent or reduce the damage it causes the cavitation on the centrifugal pump with an inducer and splitter blades. Soori and Asmael **[41]** performed an analysis showing that machining force and machining temperature can cause deflection errors in the machined turbine blades, and this effect needs to be minimized to increase the accuracy of machined blades. Their paper presented the application of a virtual machining system to predict and minimize the residual stress and deflection error in five-axis milling operations of turbine blades.

This paper presents the analysis of results obtained during the calculated transient processes of the two pump-turbines (the changes in pressure in the spiral casing, pressure in the draft tube, speed of rotation, discharge, and wicket gate opening). The 4Q characteristics in $Q_{11}/_oQ_{11o}$and $n_{11}/_on_{11o}$ diagrams for both pump-turbines show the trajectory of working points during load rejection from a turbine zone. $_oQ_{11o}$ is the rated unit discharge [-] and $_on_{11o}$ is the rated unit speed of rotation [-] The analysis of the trajectory of the working point for all three pump-turbine models (nq = 27, nq = 38 and nq = 50) during the transient process, is especially closely analyzed. The transient process was started in the turbine mode; thereafter the working point is moving from the turbine zone (III) to the reverse pump zone (IV). During this period the pump-turbines operated along the characteristic where the curve has an S-shape, which leads to difficulties during the load-rejected process manifested by an unusual increase in water pressure (for pump-turbine 1 a maximum head in the spiral casing of 940 m, 1175 m, and 1025 m were calculated for nq = 27, nq = 38, and nq = 50, respectively, while for pump-turbine 2 a maximum head in the spiral casing of 943 m, 1085 m, and 1010 m were calculated for nq = 27, nq = 38 and nq = 50, respectively). This leads to an increase in machine vibrations and threatens the stability of the machine. In-depth analysis on how much specific speed nq has a negative impact on this behavior is the main contribution of the paper.

1 DESCRIPTION OF PSP BAJINA BASTA

The first unit at HPSP Bajina Basta, was commissioned in June 1980, at that time, this PSP had the largest head in the world at 600 m. The HPSP is an accumulation-derivation plant with its upper reservoir located in Tara Mountain and its lower reservoir in the Drina River, which is the accumulation source for PSP. The connection between the upper and lower reservoirs is through a pipeline system, and the powerhouse is equipped with two pump-turbines.

The pipeline system consists of the following components: an upper entrance-exit building, located in the upper reservoir; an 8-km-long tunnel (6.3 m in diameter) that connects the upper reservoir to the upper penstock; a surge tank with a height of 141 m; a penstock valve; an underground upper penstock (consisting of a sloped part 738 m long and 4.8 m in diameter inclined at an angle of 45° and a horizontal part 635 m long and 4.2 m in diameter) that connects the pipeline to the pump-turbines and machine power house; a lower penstock (314 m long and 7 m in diameter) partly housed underground and partly passing through the existing dam that connects the machine power house to the lower exit-entrance

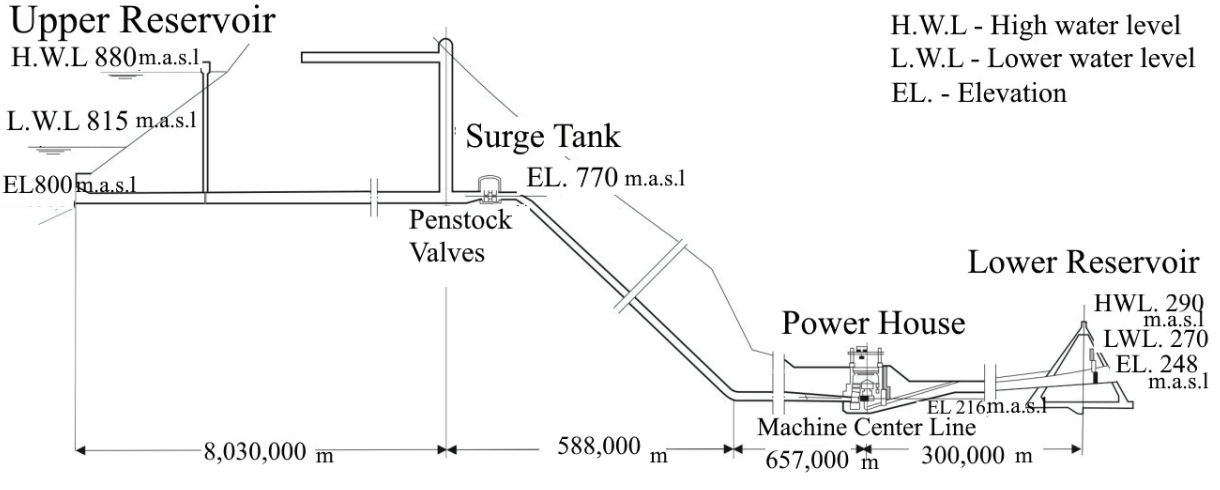

Fig. 1. *PSP Bajina Basta, Serbia – system disposition*

building; and a lower exit-entrance building located in the lower reservoir of the RHPP on the upstream slope of the existing concrete dam of HPP Bajina Basta, as shown in Fig. 1. According to the basic technical data of PSP, the plant has a total installed capacity of 630 MW (two units of 315 MW each), an average annual production of 1070 GWh, a useful accumulation volume of 150 × 10^6 m^3, a maximum net head of 600 m, and an installed discharge of 126 m^3/s.

2 4Q CHARACTERISTICS REPRESENTED BY *Wh* AND *Wm* SUTER CURVES FOR 3 PUMP-TURBINE MODELS

The performance curves corresponding to the 3 specific speeds nq = 27, nq = 38, and nq = 50 used in this paper were also incorporated into the performance curve analyses published in [6].

The specific speed is defined as:

$$nq = n\frac{\sqrt{Q}}{H^{3/4}}, \tag{1}$$

where nq is the specific speed [-], n is the speed of rotation (rpm,, Q is the discharge [m^3/s] and H is the rated head [m]. The Eq. (1) is used for calculation the nq specific speed [-] of the pump turbines (for turbine mod – rated head).

The Suter curves shown in Figs. 3 to 8 were obtained by converting the 4Q characteristics Q_{11}, n_{11}, and M_{11} (for different openings of the wicket gates), and 4Q characteristics $Q_{11} = Q/D_1 \times \sqrt{H}$, $n_{11} = n^x D_1/\sqrt{H}$, and $M_{11} = M/D_1{}^{3x}\sqrt{H}$ based on laboratory test data. Then, the points of highest efficiency for all four quadrant curves for various openings of guide vanes of pump-turbine models are determined and the one for the pump mode is chosen as the reference one. So, the data for H^*, Q^* and M^* from the optimum point of the pump-turbine model are further used in process of data conversion. Next, the values for H, M and Q for each point on the 4Q curve are calculated for each of the openings of the guide vanes of the model machine. After this procedure, the calculation of values for h, β, α and ν is conducted, where the relative head, is $h = H/H^*$, the relative moment $\beta = M/M^*$, the relative speed $\alpha = n/n^*$, and the relative discharge $\nu = Q/Q^*$. The complete conversion procedure is presented in [6], where the $Wh(\theta) = h/(\alpha^2 + \nu^2)$ are curves of the head characteristics and $Wm(\theta) = \beta/(\alpha^2 + \nu^2)$ curves of the torque characteristics, are expressed in the function of the angle θ defined as $\theta = arctg\ \alpha/\nu$. Suter curves are also presented for sixteen pump-turbine models and twenty-one pump models. Fig. 2 shows a sketch of the steps in the previous procedure of conversion from the 4Q curves with coordinates Q_{11}, n_{11}, M_{11} of the model into the Suter curves. Descriptions of the model laboratory tests and the method for obtaining the 4Q characteristics Q_{11}, n_{11}, and M_{11} may be seen in [42]. Additionally, the *Wh* and *Wm* Suter curves for nine models of radial pump-turbines are presented in [43].

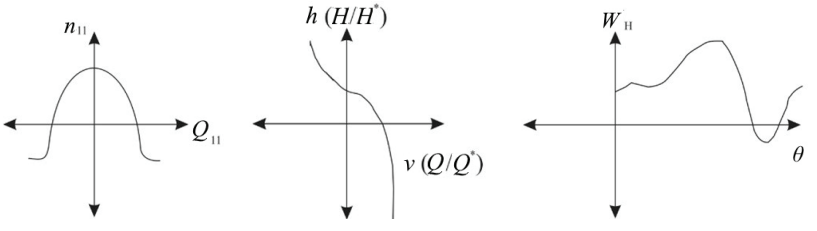

Fig. 2. *Graphic representation of the transition path from the values ($n_{11} - Q_{11}$)-model to the values (H/H*–Q/Q*)-model and then on the values ($Wh - \theta$)-model, (sketch of the calculation procedure)*

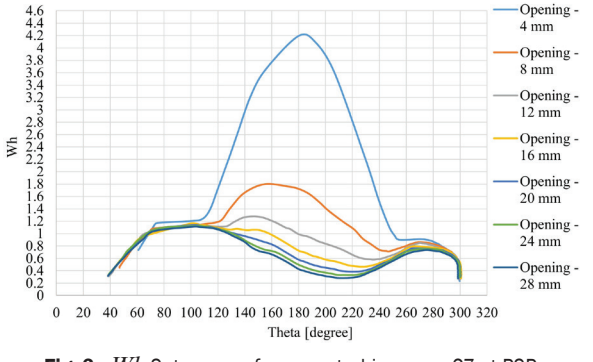

Fig. 3. *Wh* Suter curve for pump-turbine nq = 27 at PSP

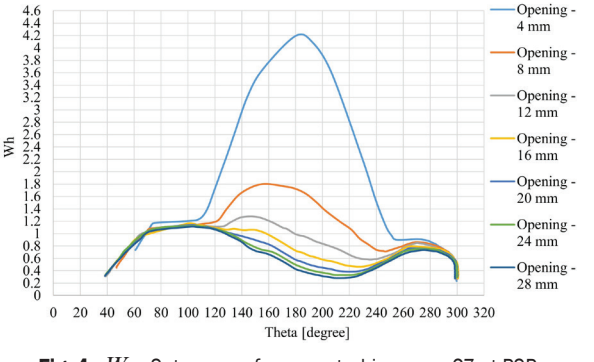

Fig. 4. *Wm* Suter curve for pump-turbine nq = 27 at PSP

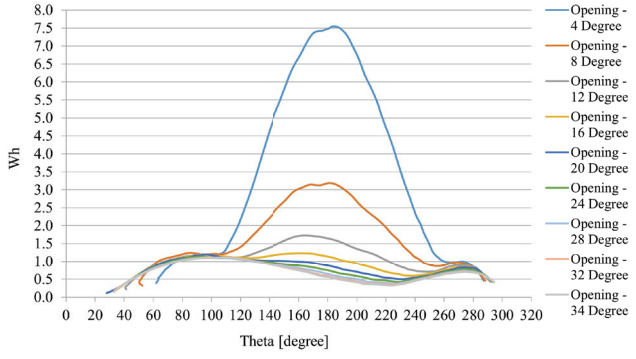

Fig. 5. *Wh* Suter curve for pump-turbine *nq* = 38 at PSP

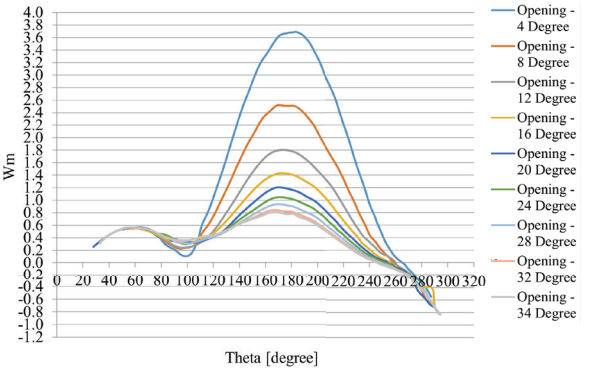

Fig. 6. *Wm* Suter curve for pump-turbine *nq* = 38 at PSP

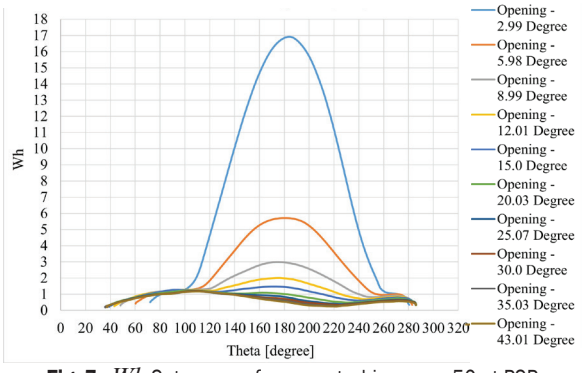

Fig. 7. *Wh* Suter curve for pump-turbine *nq* = 50 at PSP

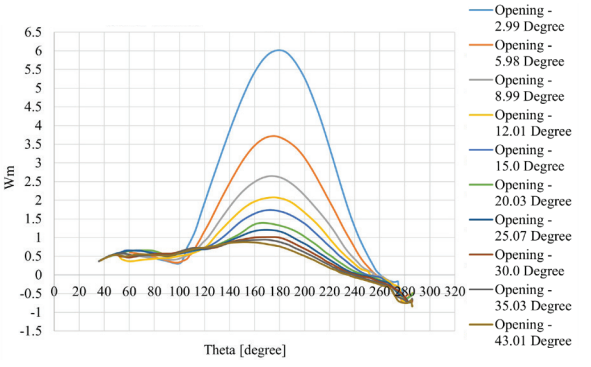

Fig. 8. *Wm* Suter curve for pump-turbine *nq* = 50 at PSP

The complete operating characteristics of pumps and pump-turbines with various specific speeds are not readily available. In general, the manufacturer supplies the head, brake horsepower, and the efficiency plotted against the discharge for the normal speed of operation. From these data, the characteristics of normal pump operation may be determined. However, it is necessary to have the complete characteristics of a pump and pump-turbines to determine the operation for all possible steady state conditions, or to determine transient conditions for normal or abnormal operations. The complete characteristics of a pump and pump-turbines consist of the zones of pump operation, turbine operation, and energy dissipation. These zones can be plotted as families of speed-ratio curves and torque-ratio curves on a (flow ratio-head ratio) coordinate system. In this form it is convenient to determine the transient water-hammer effects by graphical procedures. In addition, it is possible to determine by inspection the steady-state conditions existing at different heads or speeds under normal and abnormal conditions of operation.

3 GOVERNING EQUATIONS FOR MODELING TRANSIENT FLOWS AND THEIR NUMERICAL CALCULATION

In the one-dimensional (1D) mathematical model, the hydraulic system of PSP Bajina Basta is presented as a set of nodes (pump-turbines, surge tanks, storage basins, valves, and gates) connected by lines (tunnels, penstocks, pipes, and draft tubes).

A transient process occurs when the wicket gates are closing, and the resulting unsteady flow is described by the following equations in [7]:

- the equation of motion:

$$g\frac{\partial h}{\partial x}+v\frac{\partial v}{\partial x}+\frac{\partial v}{\partial t}+\frac{f}{2d}v|v|=0, \tag{2}$$

- the continuity equation:

$$\frac{\partial h}{t}+v\frac{\partial h}{\partial x}+\frac{a^2}{g}\frac{\partial v}{\partial x}-v\cdot\sin\alpha=0, \tag{3}$$

where v is the flow velocity [m/s], h is the piezometric head [m], a is the propagation velocity of circulation resulting wave [m/s], g is the acceleration due to gravity [m²/s], f is the Darcy-Weisbach friction factor, x is the spatial coordinate, d is the diameter of the

penstock [m], t is the time [s] and α is the inclination of the penstock in relation to the horizontal plane.

Eqs. (2) and (3) are partial differential equations of hyperbolic type. In the "x, t" plane there are two sets of lines, called "characteristic lines", defined by Eq. (4):

$$\frac{dx}{dt} = v \pm a. \tag{4}$$

Along these lines Eqs. (2) and (3) become ordinary differential equations, better suited for numerical integration. Details may be found in **[7]**.

Along a characteristic $dx/dt = v+a$:

$$\frac{g}{a}\frac{dh}{dt} + \frac{dv}{dt} - \frac{g}{a}v \cdot \sin\alpha + \frac{f}{2d}v|v| = 0. \tag{5}$$

Along a characteristic $dx/dt = v–a$:

$$-\frac{g}{a}\frac{dh}{dt} + \frac{dv}{dt} - \frac{g}{a}v \cdot \sin\alpha + \frac{f}{2d}v|v| = 0. \tag{6}$$

The boundary conditions at each node (pump-turbine) are analyzed. This mathematical model is based on the pump-turbine model test (the 4Q characteristics are presented in the form of *Wh* and *Wm* Suter curves) and the dynamic equation related to the unit, Eq. (7). Each component of the hydraulic system of PSP is included with the corresponding equations.

The authors developed a numerical code for calculating transient processes based on the MOC **[7]**, which was then upgraded with the following analysis of governor behavior.

Eq. (7) models the temporary speed droop governor with all its nonlinearities, where T_a is the time constant of the machine [s], ω^* is the normalized rotor angular speed [-], m_t is the unit hydraulic torque [-], m_e is the unit electrical torque [-], and D is the damping coefficient [-]:

$$T_a \frac{d\omega^*}{dt} = m_t - m_e - D\left(\omega^* - 1\right). \tag{7}$$

Eq. (8) represents the auxiliary servomotor and integrator, where y_1 is the auxiliary servomotor stroke [-], T_{y1} is the servomotor time constant [s], b_p is the permanent speed droop [-], K is the integrator gain [-], c is the command signal [-], e is the output of the temporary speed droop [-]:

$$\frac{dy_1}{dt} = -\frac{1}{T_{y1}}\left(1 + b_p K\right)y_1 - \frac{K}{T_{y1}}\left(\omega^* - c\right) - \frac{K}{T_{y1}}e,$$
$$0 < y_1 < 1. \tag{8}$$

Eq. (9) represents the temporary droop feedback, where T_d is the temporary speed droop time constant [s], b_t is the temporary speed droop [-]:

$$\frac{de}{dt} = -\left(\frac{1}{T_d} + \frac{b_t K}{Ty_1}\right)e - \frac{b_t}{T_{y_1}}\left(1 + b_p K\right)y_1 - \frac{b_t K}{T_{y_1}}\left(\omega^* - c\right). \tag{9}$$

Eq. (10) represents the guide vane servomotor, where a_o is guide vane opening [mm] is given as a function of y servomotor stroke [-], Ty is the servomotor time constant [s]. The details may be found in **[7]** and **[44]**.

$$\frac{dy}{dt} = \frac{1}{T_y}\left(y_1 - y\right), 0 \le y \le 1, \left|\frac{dy}{dt}\right| \le \left(\frac{dy}{dt}\right)_{\max}. \tag{10}$$

4 DISCUSSIONS ON INFLUENCE OF SPECIFIC SPEED ON TRANSIENT PROCESSES

4.1 Basic Parameters

The calculation results for the transient processes of the two pump-turbines installed at HPSP Bajina Basta are presented for simultaneous load rejection – namely, of pump-turbine 1 from a power of 281 MW (turbine mode) and of pump-turbine 2 from a power of 284 MW (turbine mode) (the powers measured when performing real load rejection). For nq = 27 (the original specific speed of the pump-turbines at the PSP), the calculated results can be compared with those obtained by on-site measurements, while for nq = 38 and nq = 50, only the calculation results can be presented. Table 1 shows the basic data for the analyzed pump-turbines, where D_r is the inlet diameter of the runner and has the values of 4.82 m, 4.86 m, and 5.259 m for these three different nq runners, Q_r is the rated discharge and has the values of 63.1 m³/s, 96.3 m³/s, and 176.1 m³/s, H_r is the rated head and has the values of 554.3 m, 447 m, and 195 m respectively, and all these values are used for calculating the nq specific speed [-], according to Eq. (1).

The moment of inertia of rotating masses of HPSP is 1625×10^3 kg×m². The initial values of net head 552.56 m, discharge 61 m³/s and rotational speed 428.57 rpm of pump-turbine units 1 and 2 are used in the numerical analysis.

Table 1. *Data for the three-prototype pump- turbines for the turbine mode of operation*

nq [-]	27	38	50
Dr [m]	4.82	4.86	5.259
Qr [m³/s]	63.1	96.3	176.1
Hr [m]	554.3	447	195
n [rpm]	428.6	375	250
Pr [MW]	294	382.7	306

The reason using these different specific speeds is that *nq* has a significant influence on the transient processes of pump-turbines based on the calculation results, is because of the next, very large difference in the ratio of inlet/outlet pump-turbine diameter, channel shape, and the other parameters of constructions of these three models of pump-turbines which is discussed in this paper. All the factors mentioned above have a bearing on the shape of the four-quadrant characteristics of these three models of pump-turbines which can be clearly seen in Figs. 14 to 19, especially in the area where the working point moves from the turbine zone (III) to the reverse pump zone (IV). In the area where the working point moves from the turbine zone (III) to the reverse pump zone (IV), the pump turbines operate along the characteristic S-shaped curve..

4.2 Calculated Performance Characteristics and Their Physical Behavior

Fig. 9 presents the curves of the head changes in spiral casings of pump-turbines 1 and 2 obtained by calculating the transient processes for all three specific speeds; the on-site measurements for each specific speed are also shown for comparison. In addition to the characteristics of the curves in certain zones, the influence of the specific speed is reflected by the different peak values. For instance, for pump-turbine 1 in the interval from 7 s to 11 s, a maximum pressure of 825 m was measured for nq = 27, while maximum pressures of 940 m, 1175 m, and 1025 m were calculated for nq = 27, nq = 38, and nq = 50, respectively. For pump-turbine 2 in the interval from 7 s to 11 s, a maximum pressure of 840 m was measured for nq = 27, while maximum pressures of 943 m, 1085 m, and 1010 m were calculated for nq = 27, nq = 38 and nq = 50, respectively.

Fig. 10 shows the curves of the change in discharge at pump-turbines 1 and 2 calculated under the same load rejection conditions. For pump-turbine 1 in the interval from 7 s to 11 s, for nq = 27, the discharge changes direction with the occurrence of reverse discharge (the operating point moves from the turbine zone to the reverse pump zone) and reaches a maximum of –31 m³/s in the reverse pump zone, which leads to pump-turbine instability. For; nq = 38, the discharge also changes direction (from the turbine zone to the reverse pump zone) and reaches a maximum of –32 m³/s in the reverse pump zone, which also leads to pump-turbine instability. For; nq = 50, the discharge also changes direction and reaches a maximum of –20 m³/s in the reverse pump zone, again leading to instability.

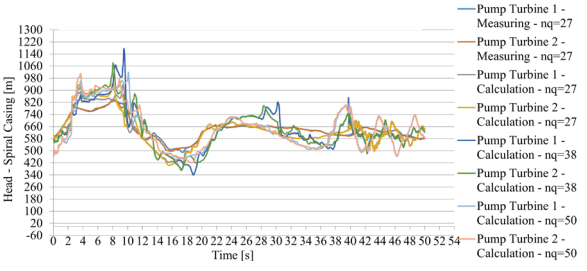

Fig. 9. Head in the spiral casing at PSP: transient process (simultaneous load rejection of pump-turbine 1 from a power of 281 MW and pump-turbine 2 from a power of 284 MW), measurements and calculations for nq = 27, only calculations for nq = 38 and nq = 50

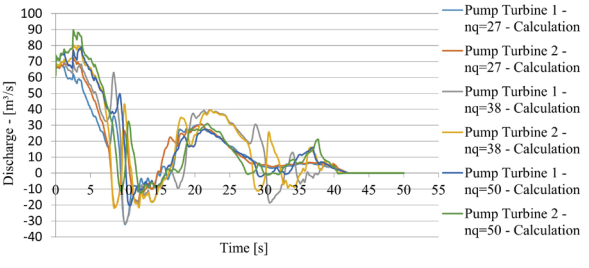

Fig. 10. Discharge at PSP: transient process (simultaneous load rejection of pump-turbine 1 from a power of 281 MW and pump-turbine 2 from a power of 284 MW); calculations for nq = 27, nq = 38, and nq = 50

For pump-turbine 2 in the interval from 7 s to 11 s, for nq = 27, the discharge changes direction (from the turbine zone to the reverse pump zone) and reaches a maximum of -23 m³/s in the reverse pump zone, which leads to the instability of pump turbine 2. For; nq = 38, the discharge similarly changes direction (from the turbine zone to the reverse pump zone) and reaches a maximum of –24 m³/s in the reverse pump zone, which also leads to instability of the pump-turbine. For; nq = 50, the discharge changes direction (from the turbine zone to the reverse pump zone) and reaches a maximum of –12 m³/s in the reverse pump zone, again leading to instability of the pump-turbine. In the interval from 7 s to 11 s, the pump-turbines 1

and 2 operated along the characteristic where the curve has an S-shape, which leads to difficulties during the load-rejected process, and are manifested by an unusual increase in water pressure, which leads to an increase in machine vibrations, and threatens the stability of the machine.

Fig. 11 presents the curves of the wicket gate openings for pump-turbines 1 and 2 obtained by calculating the transient processes; the on-site measurements are shown for comparison. For nq = 27, the curves of the wicket gate openings for both pump-turbines are obtained both by transient process calculations and by on-site measurements, while for nq = 38 and nq = 50, the wicket gate opening curves for both pump-turbines are obtained only by calculating the transient process. The curves of the wicket gate openings for both pump-turbines calculated for nq = 27, nq = 38, and nq = 50 are slightly different from the on-site measurement curves of the wicket gate openings for nq = 27. The presented trends of the wicket gate closing for pump-turbines 1 and 2 for nq = 27, nq = 38, and nq = 50 comprise three steps: the first step is a wicket gate opening of 90 % to 60 %, the second step is an opening of 60 % to 10 %, and the third step is an opening ranging from 10 % to 0 %. The total closing time for the completion of all three steps is 42 s.

Fig. 12 plots the curves reflecting the changes in the speed of rotation of pump-turbines 1 and 2 obtained both by calculations and by on-site measurements. For pump-turbine 1 in the interval from 7 s to 11 s, for nq = 27, the maximum measured speed of rotation was 575 rpm, while the maximum calculated speeds of rotation were 608 rpm, 697 rpm, and 702 rpm for nq = 27 for nq = 38, and nq = 50, respectively. For pump-turbine 2 in the interval from 7 s to 11 s, for nq = 27, the maximum measured speed of rotation was 577 rpm, while the maximum calculated speeds of rotation were 619 rpm, 678 rpm, and 699 rpm for nq = 27, nq = 38, and nq = 50, respectively.

Fig. 13 presents the curves of the calculated changes in the head within the draft tubes of pump-turbines 1 and 2. For pump-turbine 1 in the interval from 7 s to 11 s, the minimum calculated pressures were 20 m, -40 m, and -34 m for nq = 27, nq = 38, and nq = 50, respectively. For pump-turbine 2 in the interval from 7 s to 11 s, the minimum calculated pressures were 0.5 m, –50 m, and –15 m for nq = 27, nq = 38, and nq = 50, respectively. The physical results obtained during transient processes clearly

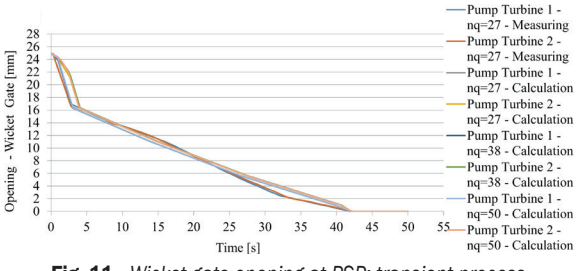

Fig. 11. *Wicket gate opening at PSP: transient process (simultaneous load rejection of pump-turbine 1 from a power of 281 MW and pump-turbine 2 from a power of 284 MW); measurements for nq = 27, calculations for nq =27, nq = 38, and nq = 50*

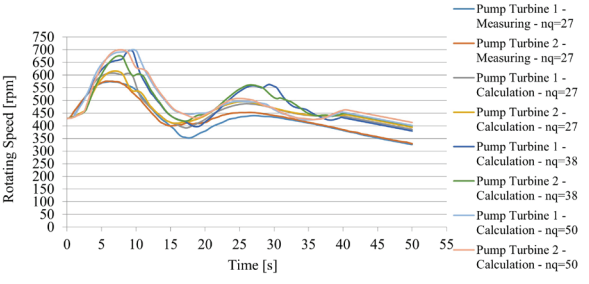

Fig. 12. *Speed of rotation at PSP: transient process (simultaneous load rejection of pump-turbine 1 from a power of 281 MW and pump-turbine 2 from a power of 284 MW); measurements for nq = 27, calculations for nq = 27, nq = 38, and nq = 50*

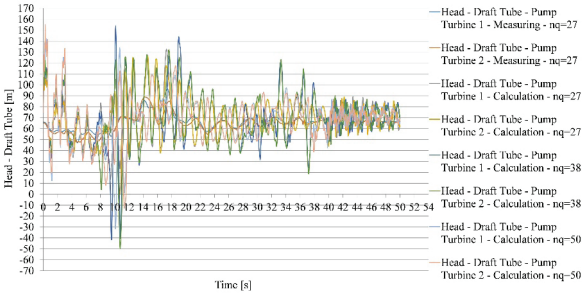

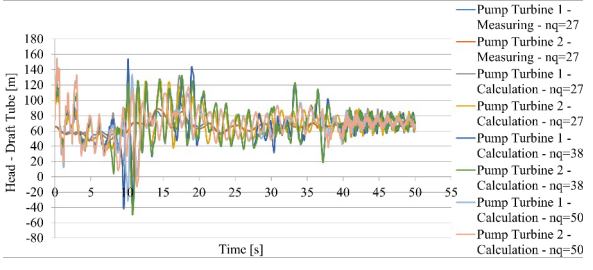

Fig. 13. *Head in the draft tube at PSP: transient process (simultaneous load rejection of pump-turbine 1 from a power of 281 MW and pump-turbine 2 from a power of 284 MW); measurements for nq = 27, calculations for nq = 27, nq = 38, and nq = 50*

show the influence of different specific speeds (*nq*) on the variations in the head within the spiral casing, head within the draft tube, speed of rotation, and discharge.

A detailed analysis of inlet conditions which was used during the simultaneous load rejection of pump-turbine 1 from a power of 281 MW and pump-turbine 2 from a power of 284 MW) was performed. Measurements for nq = 27, calculations for nq = 27, nq = 38, and nq = 50, confirmed that the same inlet conditions are used. In Figs. 9, 10, and 13 it is not easy to see the values of the initial conditions for the head in the spiral casing, discharge or the, head in the draft tube. This is because when starting the transient process the values for the head in the spiral casing, discharge,head in the draft tube for very short time 0.1 s the change the values and this is very difficult to see on diagrams presented on Figs. 9, 10, and 13

In Fig. 13 we can see that for pump-turbine 1 in the interval from 7 s to 11 s, the minimum calculated pressures were 20 m, –40 m, and –34 m for nq = 27, nq = 38, and nq = 50, respectively. For pump-turbine 2 in the interval from 7 s to 11 s, the minimum calculated pressures were 0.5 m, –50 m, and –15 m for nq = 27, nq = 38, and nq = 50, respectively. And the conclusion is the next: in the interval from 7 s to 11 s the pump-turbine 1 and 2 during the transient process coming in instability zone - coming in the instability zone of the S characteristic., the working point is moving from the turbine zone (III) to the reverse pump zone (IV). During this period the pump-turbines operated along the characteristic S-shaped curve). This is the reason why the head within the draft tubes of pump-turbines 1 and 2 for nq = 38 and nq = 50 arrives at the maximum negative values of –50 m. This clearly explains how much show the influence of different specific speeds (*nq*) on the variations in the head within the draft tube.

The level for pressure taps in the draft tube is 212 m above sea level, and the axis of the runner of the pump-turbine is 216 m above sea level. As discussed, it is clear that the pressure head in the draft tube is well below the liquid vapour pressure head which is physically not possible. The authors provide the following explanation related to this phenomenon: this effect does not influence the bulk pressure history significantly as our investigation has been focused on the effect of the machine characteristics.

4.3 Working Point Trajectories During Transient Processes and Discussion of Operating Regimes

The trajectories of the working points (operating regimes) of pump-turbines 1 and 2 for nq = 27 during the transient process (simultaneous load rejection of pump-turbine 1 from a power of 281 MW in turbine mode and pump-turbine 2 from a power of 284 MW in turbine mode) are shown in Figs. 14 and 15 as traced in their four quadrant characteristics diagram. The transient process starts in the turbine zone. Next, for both pump-turbines, the working point moves through the turbine zone and subsequently enters and moves within the reverse pump zone, which means that instabilities during operation will occur while working in this zone.

As is clearly present in Figs. 14 and 15 for pump-turbine 1, the working point reaches its most distant position (Q_{11}/Q_{11o} = 0.56, n_{11}/n_{11o} = –1.19) in 8.9 s, while that of pump-turbine 2 reaches its most distant position (Q_{11}/Q_{11o} = 0.38, n_{11}/n_{11o} = –1.11) in 10.3 s. Figs. 14 and 15 clearly show that pump-turbine 1 at 8.9 s and pump-turbine 2 at 10.3 s, operating along the characteristic where the curve has an S-shape, will have difficulties during the load-rejected process,

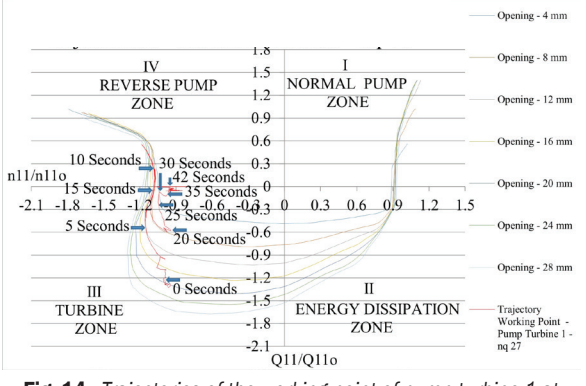

Fig. 14. *Trajectories of the working point of pump-turbine 1 at PSP during the transient process (simultaneous load rejection of pump-turbine 1 from a power of 281 MW and pump-turbine 2 from a power of 284 MW); calculation results for* nq *= 27*

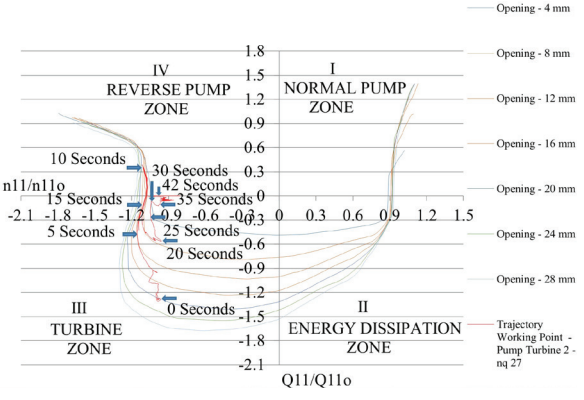

Fig. 15. *Trajectories of the working point of pump-turbine 2 at PSP during the transient process (simultaneous load rejection of pump-turbine 1 with a power of 281 MW and pump-turbine 2 with a power of 284 MW); calculation results for* nq *= 27*

which are manifested by an unusual increase in water pressure in the spiral case, which then leads to an increase in machine vibrations, and finally leads to a drop in the pressure in draft tube and threatens the stability of the machine.

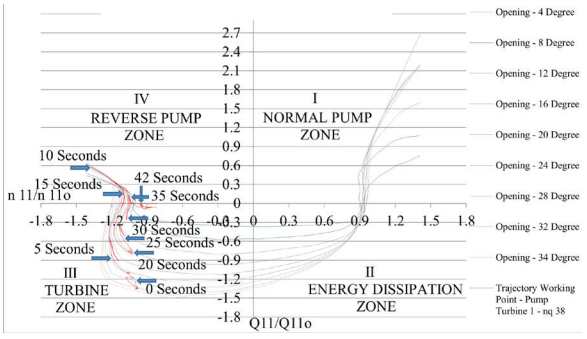

Fig. 16. *Trajectories of the working point of pump-turbine 1 at PSP during the transient process (simultaneous load rejection of pump-turbine 1 from a power of 281 MW and pump-turbine 2 from a power of 284 MW); calculation results for nq = 38*

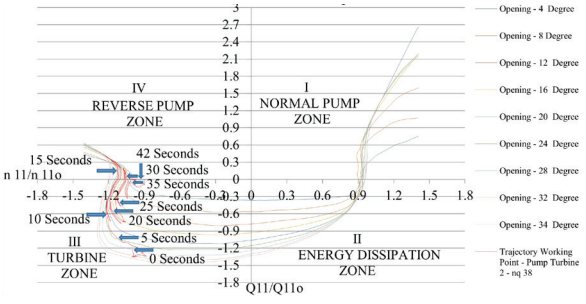

Fig. 17. *Trajectories of the working point of pump-turbine 2 at PSP during the transient process (simultaneous load rejection of pump-turbine 1 from a power of 281 MW and pump-turbine 2 from a power of 284 MW); calculation results for nq = 38*

Figs. 16 and 17 show the trajectories of the transient working points of pump-turbines 1 and 2, respectively, for $nq = 38$. The transient working points both start in the turbine zone. For pump-turbine 1, the working point moves through the turbine zone and then enters the reverse pump zone. In 10.1 s, the working point reaches its most distant position ($Q_{11}/Q_{11o} = 0.57$, $n_{11}/n_{11o} = -1.37$) in the reverse pump zone, which leads to the unstable operation of pump-turbine 1. Similarly, for pump-turbine 2, the working point moves through the turbine zone and then enters the reverse pump zone. In 11.5 s, the working point reaches its most distant position ($Q_{11}/Q_{11o} = 0.42$, $n_{11}/n_{11o} = -1.23$) in the same zone, leading to instability during the operation of pump-turbine 2. Figs. 16 and 17 clearly present that pump-turbine 1 at 10.1 s and pump-turbine 2 at 11.5 s, operating along the characteristic where the curve has an S-shape, have difficulties during the load-rejected process, which are manifested by an unusual increase in water pressure in the spiral case and, leads to an increase in machine vibrations. This then leads to a drop of pressure in the draft tube below the values of the vacuum and starts the process of cavitation on the runner, which threatens the stability of the machine. During the period of operating pump-turbine 2 (for $nq = 27$) along the characteristic where the curve has an S-shape, the maximum pressure of 840 m was measured. When, maximum pressures of 943 m were calculated, the discharge changes direction (from the turbine zone to the reverse pump zone) and reaches a maximum of –23 m³/s in the reverse pump zone, which leads to the instability of pump-turbine 2, when maximum calculated speeds of rotation were 619 rpm (max. measured values 577 rpm).

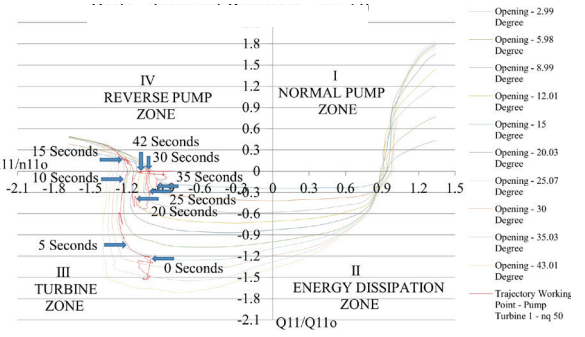

Fig. 18. *Trajectories of the working point of pump-turbine 1 at PSP during the transient process (simultaneous load rejection of pump-turbine 1 from a power of 281 MW and pump-turbine 2 from a power of 284 MW); calculation results for nq = 50*

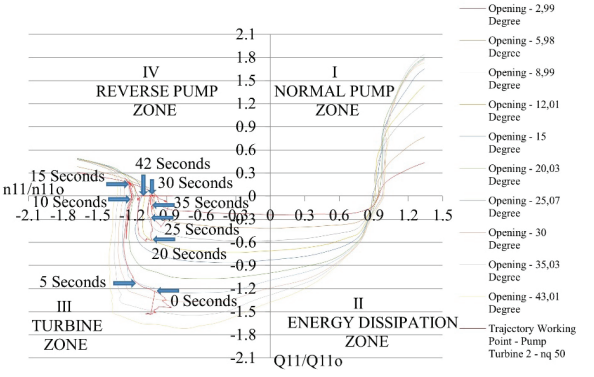

Fig. 19. *Trajectories of the working point of pump-turbine 2 at PSP during the transient process (simultaneous load rejection of pump-turbine 1 from a power of 281 MW and pump-turbine 2 from a power of 284 MW); calculation results for nq = 50*

Figs. 18 and 19 present the analog trajectories for $nq = 50$, for which the working points also start

in the turbine zone. The same movement trends may be noted for both working points, but they exhibit different peak points in the reverse pump zone: for pump-turbine 1, the peak is reached in 10.72 s at its most distant position (Q_{11}/Q_{11o} = 0.37, n_{11}/n_{11o} = –1.38), while for pump-turbine 2, the peak is reached in 11.8 s (Q_{11}/Q_{11o} = 0.23, n_{11}/n_{11o} = –1.26), which leads to the unstable operation of either turbine. Figs. 18 and 19 clearly present that pump-turbine 1 at 10.72 s and pump-turbine 2 at 11.8 s, operating along the characteristic where the curve has an S-shape, have difficulties during the load-rejected process, which are manifested by an unusual increase in water pressure in the spiral case, leading to an increase in machine vibrations, which then leads to a drop of pressure in the draft tube below the values of the vacuum starts the process of cavitation on the runner, and threatens the stability of the machine.

During the analyzed transient process span of 42 s, both working points move through the turbine zone, enter and remain for some period in the reverse pump zone, and then re-enter the turbine zone. Finally, when the discharge equals zero, the working points move along the n_{11}/n_{11o} axis until the pump-turbine stops, which occurs when the working point arrives at the zero point of the n_{11}/n_{11o} in Q_{11}/Q_{11o} coordinate system. The significant influences of the specific speed *nq* on the transient process can be seen from the presented diagrams and working points of all three models of pump-turbines coming in S-shaped zone.

5 REMARKS ON EXPERIMENTAL AND CALCULATION UNCERTAINTIES

Figs. 9 to 13 present comparisons between the measured and computed results for PSP in the case of the simultaneous load rejection of both pump-turbines. Generally, the computed results are confirmed by field tests. However, the comparison between the measured and computed results is hampered by uncertainties associated with these field tests. A common problem in water systems is that how much of air is trapped at certain locations in the system is unknown. During the transient process, in zones of low pressure, these dissolved gases can evolve. When small amounts of gas are released, the wave speed is greatly affected, and this phenomenon has considerable influences on the time and magnitude of pressure. In many cases, the actual characteristics of the pump-turbine, pump and turbine are not known in all working zones of the turbomachinery during failure. Since a computer simulation was performed in the absence of all the above parameters, it is difficult to expect that the calculated data will accurately match the field data, as there must be some error **[7].** During field measurements of the turbomachine main parameters (the heads in the spiral casing and draft tube, discharge, and speed of rotation), the expected error is between 1 % and 2 %. As shown in **[45],** the measurement errors during field measurements are ±1.2 % for the turbine efficiency, 0.866 % for the turbine power, 0.10 % for the turbine head or specific energy, and ±0.822 % for the turbine discharge).

6 CONCLUSIONS

The 4Q Suter curves for three pump-turbine models with specific speeds of *nq* = 27, *nq* = 38 and *nq* = 50 are presented and analyzed in this paper. These curves are used as input data for the numerical code to calculate the transient processes. The results of the calculations for PSP (spiral casing head, discharge, speed of rotation, and draft tube head) are mutually compared, revealing a significant difference among the results for the various specific speeds. The conclusion is that different specific speeds have significant influence on the transient processes of pump-turbines based on the calculation results.

Also, the important contribution of this paper is the detailed analysis of the trajectory of the working point for all three pump-turbine models during the transient process. The working point moves from the turbine zone (III) to the reverse pump zone (IV), while during this period the pump-turbines operated along the characteristic S-shaped curve. This led to difficulties during the load-rejection process manifested by an unusual increase in water pressure, and an increase in machine vibrations, threatening the machine stability. The analysis quantitatively revealed the negative impact of specific speed *nq* on this kind of machine behavior. The results carried out in this paper will be useful for the designers of pump-storage plants, allowing them to improve the selection of runners of the appropriate specific speed *nq*.

7 ACKNOWLEDGEMENTS

The special research, carried out on two pump-turbine models (*nq* = 38 and *nq* = 50) at the State Key Laboratory of Water Resources and Hydropower Engineering Science, Wuhan University, China, which provided the Q_{11}, n_{11}, and M_{11} 4Q characteristic data, is gratefully acknowledged.

8 NOMENCLATURES

a pressure wave velocity, [m/s]
a_0 guide vane opening, [mm], [-]
b_p permanent speed droop, [-]
b_t temporary speed droop, [-]
c command signal, [-]
d pipe diameter, [m]
D_r inlet diameter of runner, [m]
D damping coefficient, [-]
e output of the temporary speed droop, [-]
f coefficient of friction, [-]
g gravitational constant of acceleration, [m/s^2]
H_r rated head, [m]
h piezometric head, [m]
K integrator gain, [-]
M_{11} unit moment, [-]
m_t unit hydraulic torque, [-]
m_e unit electrical torque, [-]
nq specific speed, [-]
n speed of rotation, [rpm]
n_{11} unit speed of rotation, [-]
n_{110} rated unit speed of rotation, [-]
P_r rated power, [MW]
Q_r rated discharge, [m^3/s]
Q discharge, [m^3/s]
Q_{11} unit discharge, [-]
Q_{110} rated unit discharge, [-]
t time, [s]
T_a time constant of the machine, [s]
T_{y1}, T_y servomotor time constants, [s]
T_d temporary speed droop time constants, [s]
v velocity, [m/s]
W_h characteristic head, [-]
W_m characteristic moment, [-]
x coordinate measured along the pipe axis, [m]
y guide vane servomotor stroke, [-]
y_1 auxiliary servomotor stroke, [-]
ω^* normalized rotor angular speed, [-]
α inclination of the penstock in relation to the horizontal plane, [-]

9 REFERENCES

[1] Donsky, B. (1961). Complete pump characteristics and the effects of specific speeds on hydraulic transients. *Journal of Basic Engineering*, vol. 83, no. 4, p. 685-696, **DOI:10.1115/1.3662299**.

[2] Brown, R.J., Rogers, D.C. (1980). Development of pump characteristics from field tests. *Journal of Mechanical Design*, vol. 102, no. 4, p. 807-817, **DOI:10.1115/1.3254826**.

[3] Knapp, R.T. (1937). Complete characteristics of centrifugal pumps and their use in the prediction of transient behavior. *Transactions of ASME*, vol. 59, no. 8, p. 683-689, **DOI:10.1115/1.4020576**.

[4] Giljen, Z., Nedeljkovic, M. (2018). Radial hydraulic machinery four-quadrant performance curves dependent on specific speed and applied in transient calculations. *IOP 9IOP Conference Series: Earth and Environmental Science*, vol. 240, no, 4, art ID 042002, **DOI:10.1088/1755-1315/240/4/042002**.

[5] Thorley, A.R.D. (2004). *Fluid Transients in Pipeline Systems*. 2nd ed. Professional Engineering Publishing, London.

[6] Giljen, Z., Nedeljkovic, M., Cheng, Y.G. (2018). Analysis of four-quadrant performance curves for hydraulic machinery transient regimes. *17th International Conference on Fluid Flow Technologies Conference Proceedings*, paper no. 98.

[7] Wylie, E.B., Streeter, V.L. (1993). *Fluid Transients in Systems*. Prentice Hall, Upper Saddle River.

[8] Li, Z., Bi, H., Karney, B., Wang, Z., Yao, Z. (2017). Three-dimensional transient simulation of a prototype pump-turbine during normal turbine shutdown. *Journal of Hydraulic Research*, vol. 55, no. 4, p. 520-537, **DOI:10.1080/00221686.2016.1276105**.

[9] Giljen, Z. (2014). Numerical and field tests of hydraulic transients at Piva power plant. *IOP Conference Series: Earth and Environmental Science*, vol. 22, **DOI:10.1088/1755-1315/22/4/042010**.

[10] Giljen, Z. (2017). Pressure oscillations in Piva hydro power plant draft tube: case studies. *Proceedings of the ASME 2017 Fluids Engineering Division Summer Meeting*, art. ID V01AT03A014, **DOI:10.1115/FEDSM2017-69218**.

[11] Capponi, C., Zecchin, C.A., Ferrante, M., Gong, J.J. (2017). Numerical study on accuracy of frequency-domain modelling of transients. *Journal of Hydraulic Research*, vol. 55, no. 6, p. 813-828, **DOI:10.1080/00221686.2017.1335654**.

[12] Casartelli, E., Del Rio, A., Mangani, L., Schmid, A. (2022). Capturing the S-shape of pump-turbines by computational fluid dynamics simulations using an anisotropic turbulence model. *Journal of Fluids Engineering*, vol. 144, no. 2, art. ID 021203, **DOI:10.1115/1.4051809**.

[13] Deniz, S., Del Rio, A., Von Burg, M., Tiefenthaler, M. (2022). Investigation of the flow instabilities of a low specific speed pump-turbine part 1: Experimental and numerical analysis. *Journal of Fluids Engineering*, vol. 144, no. 7, art. ID 071209, **DOI:10.1115/1.4053900**.

[14] Fu, X., Zuo, Z., Chang, H., Li, D., Wang, H., Wei, X. (2021). Mechanism of low frequency high amplitude pressure fluctuation in a pump-turbine during the load rejection process. *Journal of Hydraulic Research*, vol. 59, no. 2, p. 280-297, **DOI:10.1080/00221686.2020.1780488**.

[15] Xia, L.S., Zhang, C.Z, Li, H. (2021). Influences of runner blade shape on the transient behaviours of pump-turbines in load rejection. *Journal of Hydraulic Research*, vol. 59, no. 3, p. 462-476, **DOI:10.1080/00221686.2020.1780503**.

[16] Zheng, X., Zhang, Y., Li, J., Zhang, Y. (2020). Influences of rotational speed variations on the flow-induced vibrational performance of a prototype reversible pump-turbine in spin-no-load mode. *Journal of Fluids Engineering*, vol. 142, no. 1, art. ID 011106, **DOI:10.1115/1.4045159**.

[17] Xia, L.S., Cheng, Y.G., Yang, J.D., Cai, F. (2019). Evolution of flow structures and pressure fluctuations in the S-shaped region of a pump-turbine. *Journal of Hydraulic Research*, vol. 57, no. 1, p. 107-121, **DOI:10.1080/00221686.2018.1459893**.

[18] Hu, J., Yang, J., Zeng, W., Yang, J. (2019). Constant-speed oscillation of a pump-turbine observed on a pumped-storage model system. *Journal of Fluids Engineering*, vol. 141, no. 5, art. ID 051109, **DOI:10.1115/1.4042763**.

[19] Li, D., Qin, Y., Zuo, Z., Wang, H., Liu, S., Wei, X. (2019). Numerical simulation on pump transient characteristic in a model pump-turbine. *Journal of Fluids Engineering*, vol. 141, no. 11, art. ID 111101, **DOI:10.1115/1.4043496**.

[20] Zhang, X., Zeng, W., Cheng, Y.G., Yang, Z., Chen, Q., Yang, J. (2019). Mechanism of fast transition of pressure pulsations in the vaneless space of a model pump-turbine during runaway. *Journal of Fluids Engineering*, vol. 141, no. 12, art. ID 121104, **DOI:10.1115/1.4044068**.

[21] Zhu, B., Tan, L., Wang, X., Ma, Z. (2018). Investigation on flow characteristics of pump-turbine runners with large blade lean. *Journal of Fluids Engineering*, vol. 140, no. 3, art. ID 031101, **DOI:10.1115/1.4037787**.

[22] Fu, X., Li, D., Wang, H., Zhang, G., Li, Z., Wei, X., Qin, D. (2018). Energy analysis in a pump-turbine during the load rejection process. *Journal of Fluids Engineering*, vol. 140, no. 10, art. ID 101107, **DOI:10.1115/1.4040038**.

[23] Ran, H., Luo, X. (2018). Experimental study of instability characteristics in pump-turbines. *Journal of Hydraulic Research*, vol. 56, no. 6, p. 871-876, **DOI:10.1080/00221686.2017.1422193**.

[24] Xiuli, M., Giorgio, P., Yuan, Z. (2018). Francis-type reversible turbine field investigation during fast closure of wicket gates. *Journal of Fluids Engineering*, vol. 140, no. 6, art. ID 061103, **DOI:10.1115/1.4039089**.

[25] Yexiang, X., Wei, Z., Zhengwei, W., Jin, Z., Soo-Hwang, A., Chongji, Z., Yongyao, L. (2018). Numerical analysis of the effect of misaligned guide vanes on improving S-shaped characteristics for a pump-turbine. *Journal of Fluids Engineering*, vol. 140, no. 3, art. ID 031102, **DOI:10.1115/1.4038077**.

[26] Xia, L.S., Cheng, Y.G., You, J., Zhang, X., Yang, J., Qian, Z. (2017). Mechanism of the S-shaped characteristics and the runaway instability of pump-turbines. *Journal of Fluids Engineering*, vol. 139, no. 3, art. ID 031101, **DOI:10.1115/1.4035026**.

[27] Xia, L.S., Cheng, Y.G., Yang, Z., You, J., Yang, J., Qian, Z. (2017). Evolutions of pressure fluctuations and runner loads during runaway processes of a pump-turbine. *Journal of Fluids Engineering*, vol. 139, no. 9, art. ID 091101, **DOI:10.1115/1.4036248**.

[28] Li, Z., Wang, Z., Wei, X., Qin, D. (2016). Flow similarity in the rotor-stator interaction affected region in prototype and model Francis pump-turbines in generating mode. *Journal of Fluids Engineering*, vol. 138, no. 6, art. ID 061201, **DOI:10.1115/1.4032298**.

[29] Zhang, X., Cheng, Y.G., Xia, L.S., Yang, J., Qian, Z. (2016). Looping dynamic characteristics of a pump-turbine in the S-shaped region during runaway. *Journal of Fluids Engineering*, vol. 138, no. 9, art. ID 091102, **DOI:10.1115/1.4033297**.

[30] Zeng, W., Yang, J., Hu, J., Yang, J. (2016). Guide-vane closing schemes for pump-turbines based on transient characteristics in S-shaped region. *Journal of Fluids Engineering*, vol. 138, no. 5, art. ID 051302, **DOI:10.1115/1.4032069**.

[31] Cavazzini, G., Covi, A., Pavesi, G., Ardizzon, G. (2016). Analysis of the unstable behavior of a pump-turbine in turbine mode: Fluid-dynamical and spectral characterization of the S-shape characteristic. Journal of Fluids Engineering, vol. 138, no. 2, art. ID 021105, **DOI:10.1115/1.4031368**.

[32] Zeng, W., Yang, J., Guo, W. (2015). Runaway instability of pump-turbines in S-shaped regions considering water compressibility. *Journal of Fluids Engineering*, vol. 137, no. 5, art. ID 051401, **DOI:10.1115/1.4029313**.

[33] Yu, X., Zhang, J., Miao, D. (2015). Innovative closure law for pump-turbines and field test verification. *Journal of Hydraulic Engineering*, vol. 141, no. 3, **DOI:10.1061/(ASCE)HY.1943-7900.000097**.

[34] Sun, H., Xiao, R., Liu, W., Wang, F. (2013). Analysis of S-characteristics and pressure pulsations in a pump-turbine with misaligned guide vanes. *Journal of Fluids Engineering*, vol. 135, no. 5, art. ID 051101, **DOI:10.1115/1.4023647**.

[35] Huang, W., Yang, K., Guo, X., Ma, J., Wang, J., Li, J. (2018). Prediction method for the complete characteristic curves of a Francis pump-turbine. *Water*, vol. 10, no. 2, art. ID 205, **DOI:10.3390/w10020205**.

[36] Pejovic, S., Krsmanovic, Lj., Jemcov, R., Crnkovic, P. (1976). Unstable operation of high-head reversible pump-turbines. *8th IAHR Symposium on Hydraulic Machinery Equipment and Cavitation*, Leningrad.

[37] Zeng, W., Yang, J., Cheng, Y.G. (2015). Construction of pump-turbine characteristics at any specific speed by domain-partitioned transformation. *ASME Journal of Fluids Engineering*, vol. 137, no. 3, art. ID 031103, **DOI:10.1115/1.4028607**.

[38] Meniconi, S., Brunone, B., Frisinghelli, M. (2018). On the role of minor branches, energy dissipation, and small defects in the transient response of transmission mains. *Water*, vol. 10, no. 2, art. ID 187, **DOI:10.3390/w10020187**.

[39] Simpson, A.R., Marchi, A. (2013). Evaluating the approximation of the affinity laws and improving the efficiency estimate for variable speed pumps. *Journal of Hydraulic Engineering*, vol. 139, no. 12, p. 1314-1317, **DOI:10.1061/(ASCE)HY.1943-7900.0000776**.

[40] Zhou, R., Chen, H., Dong, L., Liu, H., Chen, Z., Zhang, Y., Cheng, Z. (2022). Effect of vibration and noise measuring points distribution on the sensitivity of pump cavitation diagnosis. *Strojniški vestnik – Journal of Mechanical Engineering*, vol. 68, no. 5, p. 325-338, **DOI:10.5545/sv-jme.2022.59**.

[41] Soori, M., Asmael, M. (2021). Virtual minimization of residual stress and deflection error in the five-axis milling of turbine blades. *Strojniški vestnik – Journal of Mechanical Engineering*, vol. 67, no. 5, p. 235-244, **DOI:10.5545/sv-jme.2021.7113**.

[42] Giljen, Z., Nedeljkovic, M., Heninger, L. (2018). Complex testing on the installation of the radial pump-turbine model determination of four-quadrant characteristics. *International Conference Energy and Ecology Industry*, art. ID 1.3.

[43] Giljen, Z., Nedeljkovic, M., Cheng, Y.G. (2016). Pump-turbine characteristics for analysis of unsteady flows. *28th IAHR Symposium on Hydraulic Machinery and Systems*, art. ID 195.

[44] Obradovic, D., Arnautovic, D., Pejovic, S. (1988). Mathematical modeling of transient regimes in multi-unit hydro power plants. *XIV. IAHR Symposium on Hydraulic Machinery and Systems*, p. 163-176.

[45] Turboinštitut (2009). *PIVA HPP turbine site testing units 1, Report,* Ljubljana.

Strojniški vestnik - Journal of Mechanical Engineering 70(2024)5-6, 247-258
DOI:10.5545/sv-jme.2023.787
Original Scientific Paper
Received for review: 2023-09-07
Received revised form: 2024-02-11
Accepted for publication: 2024-04-03

Effect of Laser Parameters on Surface Texture of Polyformaldehyde and Parameter Optimization

Fengren Li[1,2] – Chao Li[1,2,*] – Juan Zhou[3] – Jiantao He[1,2] – Jiebin Wang[1,2] – Cong Luo[1,2] – Si Li[1]

[1] Hunan Institute of Science and Technology, College of Mechanical Engineering, China
[2] Key Laboratory of Intelligent Manufacturing and Service Performance Optimization of Laser and Grinding in Mechanical Industry, China
[3] Yueyang Vocational Technical College, College of Electromechanical Engineering, China

This research aimed to investigate the influence of laser process parameters on the surface texture of Polyformaldehyde (POM) and to improve its processability and process predictability. A comparative experiment and analysis involving multiple processing parameters, including laser power, scanning speed, and pulse width, were conducted on POM. Statistical prediction models of laser processing POM were established among the laser power, scanning speed, pulse width, texture depth, surface roughness at the bottom of texture, and multi-objective optimization and experimental verification of process parameters were carried out based on the grey-Taguchi analysis method. Experimental results show that the laser power and scanning speed significantly affect the texture depth. Higher laser power and lower scanning speed are conducive to forming depth. The surface roughness at the bottom of the texture increases with the increase in scanning speed and shows a tendency to rise and then fall as the laser power increases. The surface roughness and texture depth obtained under the optimal process parameters($A_5B_1C_1$) are 1.373 μm and 466.891 μm, respectively, which were reduced by 10.08 % and increased by 3.42 % compared with the minimum surface roughness and maximum depth in the orthogonal experiments. The validation experiments of the prediction model show that it can meet the reliability requirements, and the errors of the predicted values of depth and surface roughness are 1.86 % and 7.60 %, respectively. The above research provides theoretical and experimental support for the precise control of surface texture prepared by laser processing POM.

Keywords: picosecond laser processing, parameter optimization, polyformaldehyde (POM), grey-Taguchi analysis method, prediction model

Highlights

- *The effect of laser parameters on the surface texture features of POM was studied.*
- *Established prediction models between laser parameters and texture features.*
- *The optimal parameter combination is obtained based on the grey-Taguchi method.*
- *Laser power and scanning speed have a significant effect on texture quality.*

0 INTRODUCTION

With the development of synthesis and processing technology for polymer materials, the use and scale of various polymers are growing rapidly [1] and [2]. As one of the most commonly used polymers today, POM has become a suitable substitute for traditional materials in many application fields (gears, seals, bearings, etc. [3]) due to its high stiffness, hardness, elastic modulus, excellent wear resistance, and low weight [4] to [6]. With the development of technology and industry, relying solely on the performance of the material itself has gradually failed to meet the requirements of surface performance. The method of enhancing surface performance by processing micro-texture on the material surface has been widely studied and applied [7] to [10]. Many techniques for fabricating surface structures have been developed, such as etching technologies [11], atomic layer deposition [12], abrasive jet processing [13], and micro-casting [14]. However, these methods are generally costly, and it is difficult to prepare micro-nanostructures on the material surface, which do not meet the current low-carbon processing concept and high-precision processing requirements.

In recent years, lasers have proven to be a powerful tool for the precise processing of structures at the micron and nanoscale. The unique feature of laser processing is that it can modify materials in multiple length dimensions and produce complex micro- and nanostructures [15] to [17], resulting in better surface properties. Most of the existing research focuses on laser processing of metals [18] and [19] and ceramics [20] and [21], with less emphasis on polymers [22]. The majority of research aims to improve surface performance by altering texture types while studying the geometric quality of the texture itself, and the effect of laser process parameters on the texture quality has become a hot topic in recent years. Zhao et al. [23] systematically investigated the effect of repetition frequency on hole size morphology and described the relationship between repetition

*Corr. Author's Address: College of Mechanical Engineering, Hunan Institute of Science and Technology, Yueyang 414006, China, lch@hnist.edu.cn

frequency and micropore size (such as diameter and depth) during picosecond laser ablation of metallic materials. Deepu et al. [24] investigated the effect of laser fluence, pulse overlap and pulse repetition rate on hole diameter, depth, and other factors. It was found that the best hole geometry could be obtained with a fluence of 0.44 J/cm, 10 kHz repetition rate and 85 % pulse overlap.

At present, the lack of research on process parameters is the key reason for the inability to consistently obtain surface textures with excellent structure and significant functionality. The interaction and coupling between various process parameters also make it difficult to establish a feasible and complete theoretical model. Therefore, to achieve precise control of laser processing and obtain better quality texture, it is crucial to establish a predictive model between process parameters and texture geometric features, as well as to optimize the process parameters. Some scholars have studied the relationship between the geometric characteristics of material surface texture and laser process parameters using various analytical methods. Lian et al. [25] established a predictive model for the relationship between laser process parameters and the width of the clad layer, surface roughness, and dilution rate. They analysed the impact of process parameters on various response variables, and experimental results showed that the predictive model had good accuracy. Cui et al. [26] established regression prediction models between process parameters and coating width, coating height, coating depth, aspect ratio and dilution rate. The average error between the predicted values of each regression prediction model and the experimentally measured values is less than 10 %.

To improve the surface performance of POM materials, it is necessary to achieve precise control of the surface texture of POM. In this paper, the elliptical texture is processed on the surface of POM by picosecond laser, and the influence of process parameters (laser power, scanning speed, pulse width) on the texture characteristics (depth, surface roughness) is investigated, and the relationship between process parameters and texture characteristic morphology is determined. The effect of process parameters on texture characteristics and the interaction between the process parameters were analysed using the grey-Taguchi method, and the optimal combination of process parameters was obtained for the elliptical texture. Also, a prediction model of the geometric characteristics of the surface texture of POM was established, which provides an experimental and theoretical basis for further optimization of ultrafast laser processing of POM materials.

1 EXPERIMENTAL

1.1 Materials and Equipment

The experiment sample is M90-type POM (YUNTIANHUA CO., Ltd., Yunnan, China) with the specification of 25 mm × 25 mm × 10 mm (length×width×thickness). The samples were ultrasonically cleaned in anhydrous ethanol before and after laser processing, then naturally dried and placed on a two-dimensional moving table, which was computer-controlled for precise movement along *x* and *y* directions. The laser processing system used in this experiment is shown in Fig. 1a, where the laser is an infrared ultrashort pulse picosecond laser developed and produced by LinitiaLase, and the main technical parameters of the laser are shown in Table 1. The 3D measuring laser microscope (LEXT

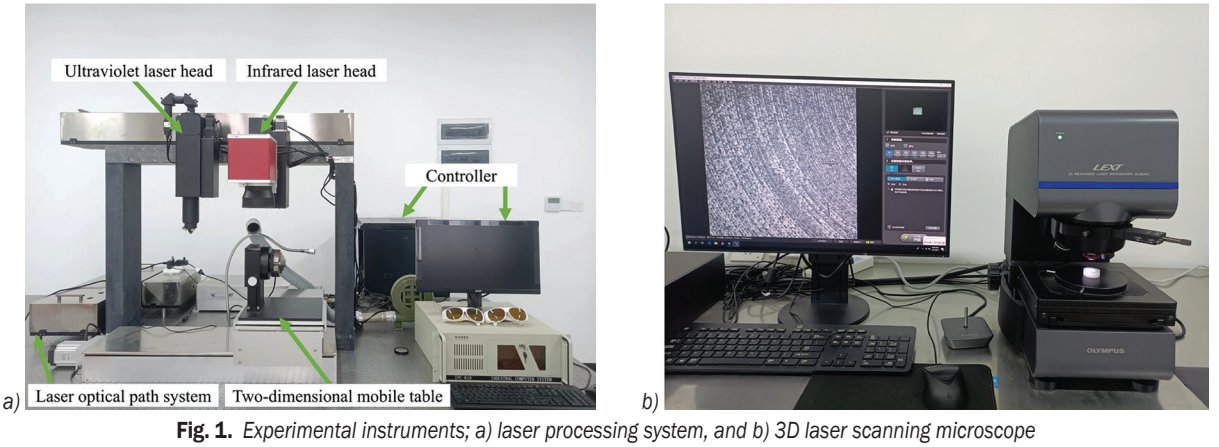

Fig. 1. *Experimental instruments; a) laser processing system, and b) 3D laser scanning microscope*

OLS5000, Olympus) shown in Fig. 1b enables fast and efficient accurate sub-micron 3D measurements and surface roughness measurements. It was used to observe the texture morphology and measure texture depth and surface roughness.

Table 1. *Main technical parameters of ultraviolet nanosecond laser*

Parameter	Value
Central wavelength [nm]	1028±5
Maximum output power [W]	30
Maximum pulse energy [μJ]	200
Laser frequency [kHz]	1 to 200
Pulse width [μs]	0.05 to 50
Beam divergence [urad]	<20
Beam quality [-]	M2<1.2

1.2 Experimental Design

1.2.1 Univariate Experiments

To study the effect of laser parameters on the geometry of the POM ellipse (long axis 1.5 mm × short axis 1 mm) texture, the controlled variable method was used to explore the effect of laser power, scanning speed and pulse width on the depth of texture and surface roughness. Table 2 displays the specific experimental parameters used, while Table 3 outlines the laser parameters that were not discussed in this study. During the laser processing, the POM workpiece is placed on a high-precision motion platform, and the pulse laser with high repetition frequency and high energy density is applied to the surface of the workpiece using different laser processing parameters [26], which is radiated on the surface of the specimen according to the set scanning path and causes it to melt and vaporize [27], thus processing the elliptical texture with a certain depth. The ultrasonic cleaning device was used to clean the processed samples. After natural air drying, the elliptical texture was observed and calculated with a 3D measuring laser microscope on the surface of the POM. To ensure the accuracy of the surface roughness measurement on the bottom surface of the texture, the overall measurement of the centre area of the elliptical texture bottom surface was performed using a 20× magnification, as shown in

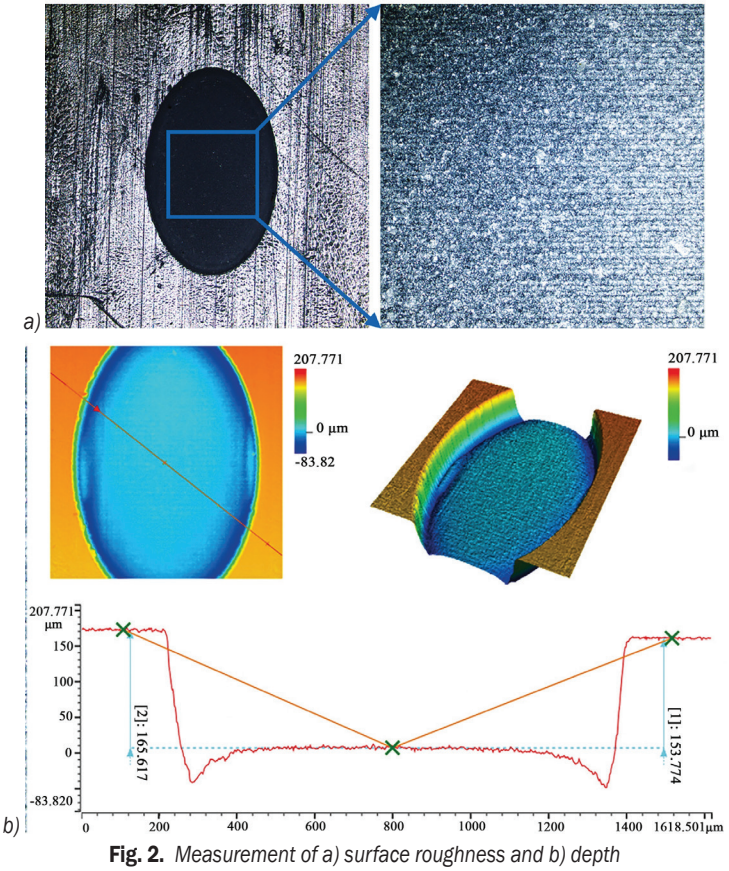

Fig. 2. *Measurement of a) surface roughness and b) depth*

Fig. 2a. The depth is measured as shown in Fig. 2b. Both values are taken as the average value after three repeated measurements.

Table 2. *Laser processing experimental parameters*

Laser power [W]	Scanning speed [mm·s^{-1}]	Pulse width [μs]
19.5, 21, 22.5, 24, 25.5, 27, 28.5, 30	600	12
24	450, 500, 550, 600, 650, 700, 750, 800	12
24	600	4, 12, 20, 28, 36, 44
24	600	12

Table 3. *Values of laser parameters not discussed*

Frequency [kHz]	Current strength [A]	Number of scans [-]	Laser line spacing [mm]	Ring spacing [mm]
60	1	10	0.005	0.5

1.2.2 Orthogonal Experimental Design

The Taguchi method is a local optimization algorithm based on an orthogonal experiment and signal-to-noise ratio (S/N) designed by Genichi Taguchi **[28]**. Orthogonal table design experiments can reasonably reduce the number of experiments and blindness. Statistical analysis of the experimental results with the S/N as a measure of quality characteristics can lead to the best combination of reliable and stable process parameters, achieving a combination of high efficiency and low cost. This article takes the depth of texture and surface roughness as the response targets, and the three process parameters of laser power, scanning speed, and pulse width are the influencing factors. The levels of the three process parameters are shown in Table 4. Based on the Taguchi experiment principle, the L_{25} (5^3) orthogonal experiment table with five levels and three factors is designed as shown in Table 5, where A, B, and C represent laser power, scanning speed, and pulse width, respectively. After the corresponding data were measured experimentally, the influencing factors of each response target were explored independently, and then the multi-mass target optimization problem was transformed into a single-objective optimization problem using grey correlation analysis to obtain the degree of influence **[29]**, trend, and the best process parameter combination of the three process parameters on the response target. The optimal process parameters were also used for laser processing to verify the effectiveness of process parameter optimization, and the accuracy of the model was verified by substituting it into the established prediction model for the solution. The measured data from the orthogonal experiments are shown in Table 6.

Table 4. *Factors and their levels*

Level	Factor		
	A Laser power [W]	B Scanning speed [mm·s^{-1}]	C Pulse width [μs]
1	18	400	4
2	21	500	12
3	24	600	20
4	27	700	28
5	30	800	36

Table 5. *L_{25} (5^3) Taguchi orthogonal experimental design*

No	A	B	C	No	A	B	C
1	18	400	4	14	24	700	4
2	18	500	12	15	24	800	12
3	18	600	20	16	27	400	28
4	18	700	28	17	27	500	36
5	18	800	36	18	27	600	4
6	21	400	12	19	27	700	12
7	21	500	20	20	27	800	20
8	21	600	28	21	30	400	36
9	21	700	36	22	30	500	4
10	21	800	4	23	30	600	12
11	24	400	20	24	30	700	20
12	24	500	28	25	30	800	28
13	24	600	36				

Table 6. *Results of orthogonal experiment*

No	Depth [μm]	Surface roughness [μm]	No	Depth [μm]	Surface roughness [μm]
1	197.142	1.558	14	227.206	3.268
2	171.335	1.527	15	204.575	4.099
3	148.198	1.883	16	394.915	2.429
4	134.415	2.190	17	338.945	2.259
5	118.957	2.559	18	299.383	2.504
6	289.134	1.947	19	267.142	3.812
7	251.768	2.149	20	241.586	4.371
8	216.943	2.618	21	451.443	3.289
9	190.783	3.273	22	394.611	1.942
10	166.790	3.701	23	340.797	3.151
11	354.549	2.237	24	300.774	4.819
12	296.081	2.098	25	267.183	5.598
13	260.960	2.601			

2 RESULTS AND DISCUSSION

2.1 Texture Morphology Analysis

2.1.1 Influence of Laser Power on Texture

To investigate the effect of laser power on the geometry of the texture, the surface of the POM sample was irradiated with lasers at power levels within the range of 19.5 W to 30 W under constant scanning speeds of 600 mm/s and pulse widths of 12 μs. The variation of the relevant parameters is shown in Fig. 3. With the gradual increase in laser power, the depth of elliptical texture shows an increasing trend, increasing from 160.709 μm to 302.197 μm. The increase in laser power means that the energy of individual laser pulses gradually increases, the energy density acting on the surface of POM increases, and when the laser energy density is higher than the ablation threshold of POM, the absorption of laser energy by POM produces ionization. The process of ionization becomes significant with increasing laser power, resulting in an increase in the volume of material removed and a greater depth of texture. Laser radiation to the site, with the increase in depth, began to move away from the original focal surface, and the laser energy to reach the bottom of the texture gradually decreased. Coupled with the gradual increase in the depth of the texture, the formation of molten spatter takes longer to fly out of the texture, as well as the laser processing process generated by the plasma on the laser shielding effect. As a result, the depth of the texture will increase with the laser power and tend to level off.

Meanwhile, it can be seen from Fig. 3 that the surface roughness of the elliptical texture bottom increases with the increase in laser power, but when the power reaches 24 W, the surface roughness reaches the maximum and continues to increase the power afterwards, the surface roughness starts to decrease instead. As shown in Fig. 4, the structure of the bottom surface of the texture structure is relatively regular when the laser power is small (19.5 W to 24 W), and most of the bottom surface is formed by the uniform cooling of the melt that fails to vaporize in time. However, as the laser power gradually increases, the melt vaporized on each laser path increases, and the melt that did not vaporize at this time could not effectively lap to form a good surface, thus making the overall surface roughness gradually increase. Also, when the laser power is higher (25.5 W to 30 W), the macrostructure of the texture bottom surface is poorer, but its overall surface roughness starts to decrease compared to the power of 24 W. This phenomenon is caused as follows: the melt vaporized on the laser sweeping path is more than the non-vaporized melt, and the non-vaporized melt becomes a single individual after cooling, thus forming a structure of multiple crystalline particles on a smooth surface on the bottom surface, at which time the overall surface roughness of the bottom surface will gradually decrease as the smooth surface area increases and the number and volume of crystalline particles decrease.

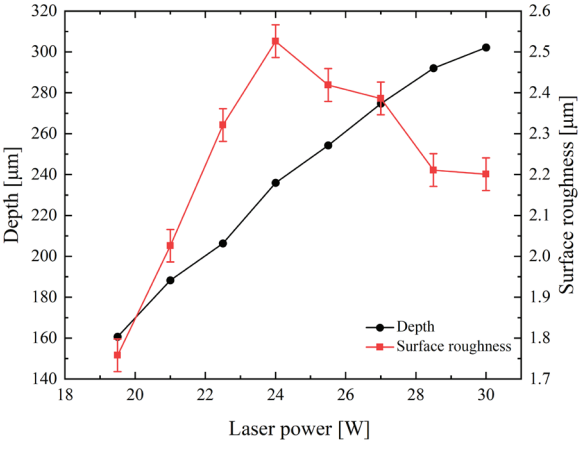

Fig. 3. *The changes in texture depth and surface roughness under different laser power*

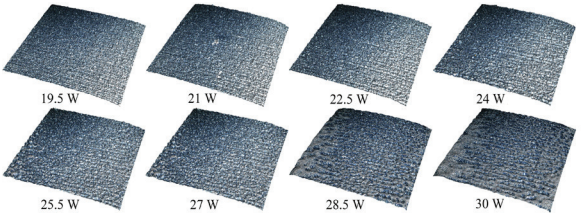

Fig. 4. *Texture bottom morphology under different laser power*

2.1.2 Influence of Scanning Speed on Texture

To further investigate the influence of laser scanning speed on texture, in a fixed other parameter situation, different laser scanning speeds (ranging from 450 mm/s to 800 mm/s with an increment of 50 mm/s) were employed for texture processing. The variations in texture-related parameters are shown in Fig. 5. From Fig. 5, it can be seen that the depth decreases with the increase in scanning speed, with a relatively stable depth variation within the range of 600 mm/s to 650 mm/s. The scanning speed affects the action time of the laser and the material surface. With the increase of the scanning speed, the laser irradiation time per unit area becomes shorter, and the number of times radiated by the pulsed laser becomes

less, the energy absorbed by the material surface decreases, and the material removal rate decreases, resulting in a decrease in the depth of the elliptical texture. Additionally, Fig. 5 indicates that the surface roughness of the bottom surface of the elliptical texture increases with increasing scanning speed, and the increase is gradually increasing. Combined with Fig. 6, it is found that the molten structure formed by laser ablation of POM gradually decreases with increasing scanning speed, and although the decrease of melt-like structure is beneficial to the macroscopic morphology, it has a negative effect on the surface roughness. As a common polymer, the crystallization properties of POM materials are positively correlated with heat treatment time and temperature in a specific temperature range [30]. As the scanning speed increases, the time for the texture to be radiated by the laser becomes shorter, the conduction and diffusion processes of energy on the material are shortened, the heat treatment time is shorter, and the crystallinity of the bottom surface of the texture is poor, which leads to the rise of its overall surface roughness.

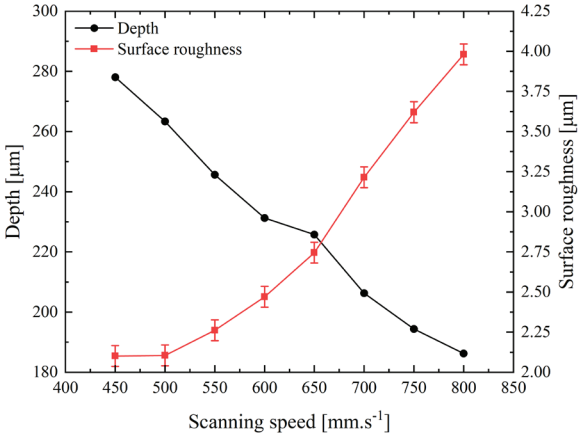

Fig. 5. *The changes in texture depth and surface roughness under different scanning speeds*

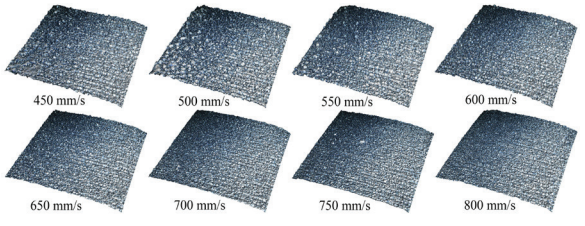

Fig. 6. *Texture bottom morphology under different scanning speed*

2.1.3 Influence of Pulse Width on Texture

Pulse width is an important parameter in laser processing, which represents the duration of laser pulse energy output. Under the condition of unchanged pulse energy, increasing the pulse width will extend the period during which each laser pulse acts on the material surface, consequently elevating the total heat absorbed by the material and expanding the thermally affected zone of the processing site. As can be seen from Fig. 7, the depth of the elliptical texture becomes more significant with increasing pulse width, and the depth of the texture increases from 215.591 μm to 224.512 μm when the pulse width increases from 4 μs to 44 μs, but the overall change is not significant. A comparison with Figs. 3 and 5 shows that the effect of pulse width on depth is much less than that of power and scanning speed. Fig. 7 also shows that the surface roughness of the texture's bottom surface fluctuates between 2.65 μm and 2.95 μm with the variation of pulse width, which is relatively small compared with the influences of power and scanning speed.

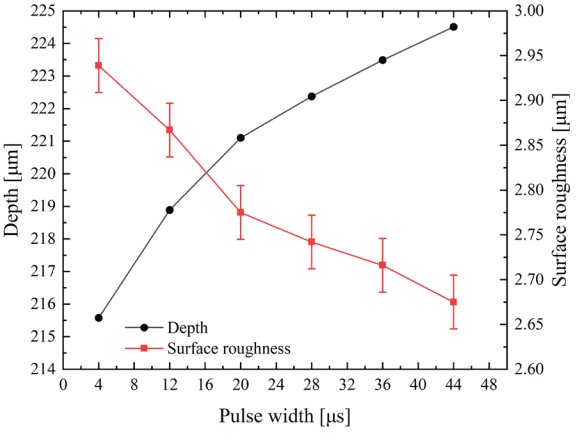

Fig. 7. *The changes of texture depth and surface roughness under different pulse width*

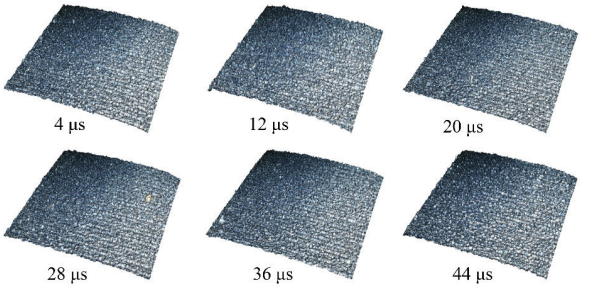

Fig. 8. *Texture bottom morphology under different pulse width*

During the process from a pulse width of 4 μs to 44 μs, the overall surface roughness exhibits a continuous decreasing trend. The rate of decrease is faster when the pulse width increases from 4 μs to 20 μs, while it becomes more moderate when the pulse width increases from 20 μs to 44 μs. From Fig. 8, it can

be observed that the morphology of the texture bottom surface does not undergo significant changes with increasing pulse width. Typically, larger pulse widths imply an extended duration of individual laser pulses and longer conduction times for laser energy inside the material, resulting in increased amounts of melt and corresponding changes in surface morphology. However, for a material like POM, variations in pulse width at the microsecond level have less effect on the melting process.

2.2 Model Building and Parameter Optimization

2.2.1 Model Building

Based on the data results obtained from the orthogonal experiment, the quadratic regression polynomials between laser power p, scanning speed v, pulse width w, depth D, and surface roughness Ra were constructed by Minitab. The obtained expressions are shown in Eqs. (1) and (2). According to the variance analysis results of depth shown in Table 7, the model coefficient P of the depth prediction model is much less than 0.05, indicating the high significance of the model at a 95 % confidence level. The multiple coefficients of determination R^2 value is 0.9957, and the adjusted R^2 value is 0.9945, both of which are close to 1, indicating the reliable predictive power of the model. Fig. 9a shows the residual normal plot of the depth regression model, from which it can be seen that the data points are evenly distributed around the fitted line with no abnormal data points, indicating a good fit for the regression model. In addition, the effect of pulse width on depth is not significant enough to exceed the 95 % confidence level, and variance analysis has automatically eliminated it. Similarly, as shown in Table 8 and Fig. 9b, the model coefficient P is less than 0.001, the P values of linear, square, and interaction terms are all less than 0.05, the multivariate coefficient R^2 is 0.9319, the adjusted R^2 is 0.9091, and the distribution of data points in the residual normal plot is reasonable, indicating that the prediction model has high overall reliability and fit.

2.2.2 Parameter Optimization

The Taguchi method evaluates the results of orthogonal experiments using the S/N ratio, which typically can be classified into three categories based on the research objectives: larger-the-better (LTB), smaller-the-better (STB), and nominal-the-best (NTB) [31]. In this study, the depth and surface roughness of the elliptical texture are chosen as the response variables. The objective was to achieve a large depth while maintaining a low surface roughness at a certain number of processing cycles. Therefore, the LTB criterion was used for the depth target, while the STB criterion was applied for the surface roughness target in calculating the S/N, and the magnitude of the influence of each process parameter on the target was sought using the range analysis. The specific results and data are shown in Tables 9 to 11, and the S/N ratio calculation formula is shown in Eq. (3).

$$D = -341.7 + 50.62p - 0.311v - 0.4673p^2 + 0.000381v^2 - 0.02036pv, \quad (1)$$

$$Ra = 8.74 - 0.0067p - 0.0247v + 0.0884w + 0.000015v^2 + 0.000572ps - 0.000119vw. \quad (2)$$

Table 7. *Variance analysis table of depth*

Source	Degree of freedom	Adj SS	Adj MS	F	P
Model	5	179199	35839.7	873.28	<0.001
Laser power (A)	1	5713	5713.3	139.21	<0.001
Scanning speed (B)	1	355	355.0	8.65	0.008
AA	1	1238	1238.3	30.17	<0.001
BB	1	1018	1017.8	24.80	<0.001
AB	1	3732	3732.3	90.94	<0.001
Pure Error	19	780	41.0		
Total	24	179978			
R^2 = 99.57 %			R^2(adj) = 99.45 %		

Table 8. *Variance analysis table of surface roughness*

Source	Degree of freedom	Adj SS	Adj MS	F	P
Model	6	24.4912	4.08186	41.03	<0.001
Laser power (A)	1	0.8477	0.84766	8.52	0.009
Scanning speed (B)	1	2.1672	2.16720	21.78	<0.001
Pulse width (C)	1	0.9156	0.91561	9.20	0.007
BB	1	1.6432	1.64322	16.52	0.001
AB	1	2.1639	2.16388	21.75	<0.001
BC	1	0.6701	0.67012	6.74	0.018
Pure Error	18	1.7909	0.09950		
Total	24	26.2821			
R^2 = 93.19 %			R^2(adj) = 90.91 %		

The degree of influence of each parameter on the texture depth at different levels can be seen in Tables 9 and 11. Due to the LTB characteristic of depth, when the combination of laser power (A), scanning speed (B), and pulse width (C) is set to $A_5B_1C_3$ (laser power

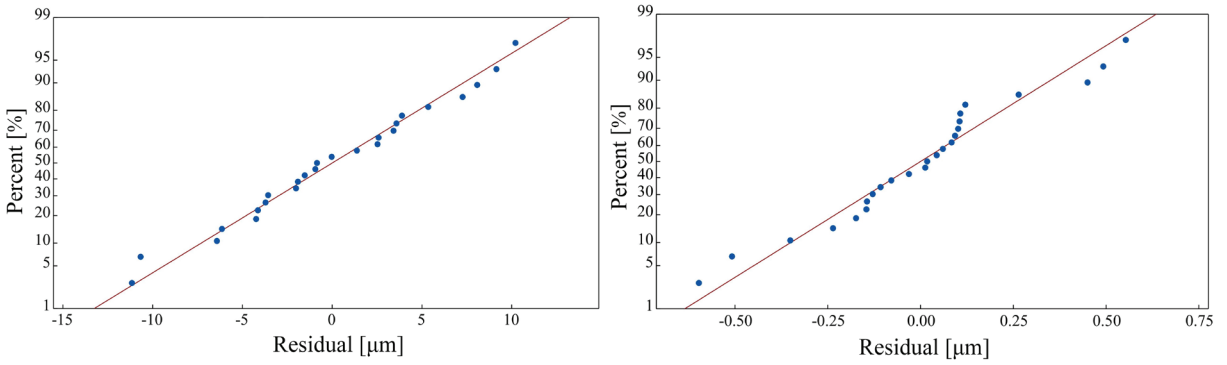

Fig. 9. *Normal probability plot of residuals for a) depth data and b) surface roughness data*

of 30 W, scanning speed of 400 mm/s, pulse width of 20 μs), this combination represents the optimal process parameter combination for controlling texture depth. Additionally, based on the extreme difference, the impact of each parameter on depth can be ranked in descending order as follows: laser power > scanning speed > pulse width. Similarly, the optimal combination of process parameters for controlling the surface roughness of the texture bottom surface is $A_1B_2C_1$ (laser power of 18 W, scanning speed of 500 mm/s, pulse width of 4 μs). The impact of each parameter on surface roughness can be ranked in descending order as follows: scanning speed > laser power > pulse width.

Although the optimal parameters of the two responses are obtained respectively, the optimal parameters of one response quantity could not take into account the other response quantity due to the different influence of each process parameter on both. To obtain the best combination of process parameters with two response quantities, the grey correlation method is used. The grey correlation method is a method to determine the significance of the relationship between factors in the order of grey correlation. The combination of grey relational analysis theory with the Taguchi method provides an effective solution for complex multi-response problems. By transforming multiple laser process parameter optimization problems into optimizing a single grey relational degree problem, the optimal combination of parameters can be obtained to achieve minimal surface roughness and maximum depth. The grey correlation analysis requires a series of calculations on the signal-to-noise data: S/N normalization, calculation of the grey correlation coefficient for each response quantity, and calculation of the grey correlation. The formulas used in the three steps are shown in Eqs. (4) to (6), and the final grey correlation values obtained by the three steps are shown in Table 12.

$$S/N=\begin{cases}-10\log\left(\dfrac{1}{n}\sum_{i=1}^{n}\dfrac{1}{y_i^2}\right) & LTB\\ -10\log\left(\dfrac{1}{n}\sum_{i=1}^{n}y_i^2\right) & STB\end{cases}, \tag{3}$$

where () is the value of the response quantity, is the number of experiments.

$$X_i(k)=\begin{cases}\dfrac{y_i(k)-\min y_i(k)}{\max y_i(k)-\min y_i(k)} & LTB\\ \dfrac{\max y_i(k)-y_i(k)}{\max y_i(k)-\min y_i(k)} & STB\end{cases}, \tag{4}$$

where $X_i(k)$ is the normalized value of the k^{th} response quantity for the i^{th} experiment; $y_i(k)$ is the value of the SNR for the i^{th} experiment of the k^{th} response quantity; $\max y_i(k)$ and $\min y_i(k)$ represent the maximum and minimum values of the k^{th} response volume in the 25 sets of experiments, respectively.

$$GRC_i(k)=\frac{\min_i\left|x_i^0-x_i(k)\right|+\xi\max_i\left|x_i^0-x_i(k)\right|}{\left|x_i^0-x_i(k)\right|+\xi\max_i\left|x_i^0-x_i(k)\right|}, \tag{5}$$

where $GRC_i(k)$ is the value of the grey correlation coefficient of the i^{th} experiment of the k^{th} response; $x_i(k)$ is the normalized value of the k^{th} response quantity for the i^{th} experiment; x_i^0 is the ideal value for the experiment, which is set to 1 in this study; ξ is the distinguishing coefficient which is defined in the range of $0\leq\xi\leq1$, ξ was taken as 0.5 in this study.

$$GRC_i=\frac{1}{n}\sum_{k=1}^{n}GRC_i(k), \tag{6}$$

where GRC_i is the grey correlation value of the i^{th} experiment; $GRC_i(k)$ is the value of the grey

correlation coefficient of the i^{th} experiment of the k^{th} response quantity; n is the number of response quantities and is 2 in this study.

Table 9. *SNR of response targets*

No.	Depth	Surface roughness	No.	Depth	Surface roughness
1	45.896	-3.851	14	47.128	-10.286
2	44.677	-3.677	15	46.217	-12.254
3	43.417	-5.497	16	51.930	-7.709
4	42.569	-6.809	17	50.603	-6.482
5	41.508	-8.161	18	49.525	-7.973
6	49.222	-5.787	19	48.535	-11.623
7	48.020	-6.645	20	47.661	-12.812
8	46.727	-8.359	21	53.092	-10.341
9	45.611	-10.299	22	51.923	-5.765
10	44.443	-11.366	23	50.650	-9.969
11	50.994	-6.993	24	49.565	-13.976
12	49.428	-6.436	25	48.536	-14.961
13	48.331	-8.303			

Table 10. *The SNR mean and range of depth*

Factor level	A	B	C
Mean 1	43.613	50.227	47.783
Mean 2	46.805	48.930	47.860
Mean 3	48.420	47.730	47.931
Mean 4	49.651	46.682	47.838
Mean 5	50.753	45.673	47.829
Range	7.140	4.554	0.148

Table 11. *The SNR mean and range of surface roughness*

Factor level	A	B	C
Mean 1	-5.599	-6.936	-7.848
Mean 2	-8.491	-5.801	-8.662
Mean 3	-8.854	-8.020	-9.185
Mean 4	-9.320	-10.599	-8.855
Mean 5	-11.002	-11.911	-8.717
Range	5.403	6.110	1.337

Table 12. *Grey relational analysis data*

No.	GRC	No.	GRC	No.	GRC
1	0.708	10	0.412	19	0.487
2	0.704	11	0.682	20	0.449
3	0.565	12	0.642	21	0.729
4	0.499	13	0.549	22	0.781
5	0.445	14	0.477	23	0.588
6	0.664	15	0.427	24	0.488
7	0.594	16	0.708	25	0.447
8	0.511	17	0.684		
9	0.448	18	0.593		

According to grey relational analysis theory, the degree of correlation between factors and the system depends on the value of the correlation degree. The larger the correlation deegree value of a process parameter, the greater its response in optimizing the objective function. Fig. 10 shows the main effect plot of the grey correlation of each process parameter, and it can be seen that the optimal process parameter is $A_5B_1C_1$, i.e., the laser power is 30 W, the scanning speed is 400 mm/s, and the pulse width is 4 μs.

2.2.3 Validation Analysis

Since the optimal combination of process parameters ($A_5B_1C_1$) was not included in the orthogonal experiment, a new set of machining experiments was conducted using the optimal parameter combination. Table 13 presents the optimized process parameters and the relevant parameters of the elliptical texture. Combining grey correlation theory with the data from the orthogonal experiment, the minimum surface roughness and maximum depth were selected as references. The surface roughness obtained from the optimized parameters was 1.373 μm, which decreased by 10.08 % compared to the minimum surface roughness obtained from the orthogonal experiment (1.527 μm); the depth obtained from the optimized parameters was 466.891 μm, which increased by 3.42 % compared to the maximum depth obtained from the orthogonal experiment (451.443 μm). The results demonstrate that the effect of the optimized parameters is consistent with the previous expectations, as it enables the simultaneous attainment of low surface roughness and a greater depth. It can also be seen from Fig. 11 that compared to the two texture substrates obtained through separate optimization using the Taguchi method, the substrate prepared after further optimization using the grey correlation method exhibits a greater abundance of molten-like structures.

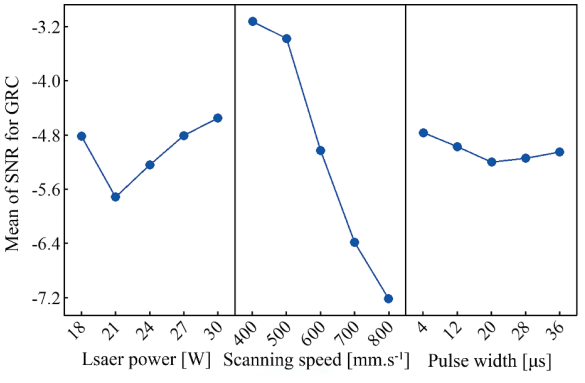

Fig. 10. *Main effects plot for the SNR analysis of GRC*

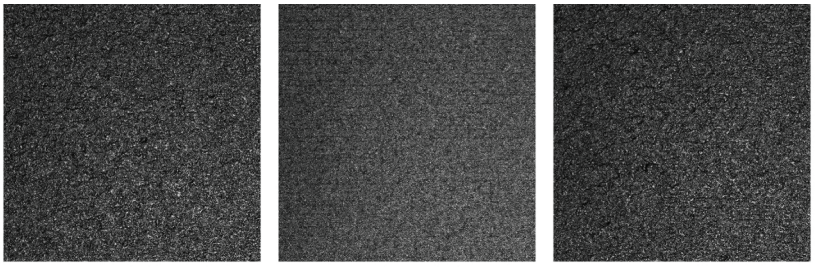

Fig. 11. *Texture bottom morphology under different parameter combinations*

Additionally, these molten structures are distributed in a wider and more uniform manner, which is also the reason for the further reduction in surface roughness. By substituting the optimal combination of process parameters into Eqs. (1) and (2), the predicted values for depth and surface roughness are obtained as 475.570 μm and 1.486 μm, respectively, and the errors between these predicted values and the actual measured values are 1.86 % and 7.60 %. This shows that the predictive model exhibits high accuracy and reliability, meeting the objectives of predicting and optimizing process parameters, and it has a positive effect on the accurate control of the texture morphology and quality as well as the improvement of the efficiency of ablation.

Table 13. *Optimized parameters and response*

Laser power [W]	Scanning speed [mm·s^{-1}]	Pulse width [μs]	Depth [μm]	Surface roughness
30	400	4	466.891	1.373

3 CONCLUSION

This paper investigates the impact of laser process parameters on the surface texture characteristics of POM. The predictive model was established to correlate three laser parameters (laser power, scanning speed, and pulse width) with texture depth and surface roughness at the bottom of the texture. The grey-Taguchi method was employed for multi-objective optimization and experimental verification of the process parameters. The results indicate that with the increase of laser power and the decrease of scanning speed, the depth of the weave gradually increases, but its increase decreases with the further change of these two influencing factors. The surface roughness at the bottom of the texture decreases with increasing pulse width and exhibits a trend of initially increasing and then decreasing with increasing scanning speed, with a maximum value observed at a power of 24 W. The variation of pulse width has no significant effect on either the depth or surface roughness. Multi-objective optimization using the grey-Taguchi method resulted in obtaining the optimal combination of laser parameters as $A_5B_1C_1$ (laser power is 30 W, the scanning speed is 400 mm/s and pulse width is 4 μs). Compared with the corresponding data obtained from the orthogonal experiments, the texture depth increased by 3.42 %, and the surface roughness of the bottom surface decreased by 10.08 % under the optimal parameter combination, achieving a significant optimization of surface roughness while obtaining a larger depth. Experimental validation of the established prediction model using the optimal parameter combination showed that the predicted values of depth and surface roughness had errors of 1.86 % and 7.60 %, respectively, compared to the experimental measurements, and the model was accurate enough to achieve accurate prediction of the surface texture properties of POM.

4 ACKNOWLEDGEMENTS

Financial support for this work was provided by the National Natural Science Foundation of China Youth Project (Grant no. 51905170) and the Natural Science Foundation of Hunan Province (Grant no. 2020JJ4334).

5 REFERENCES

[1] Siddiqui, M.N.S., Pogacnik, A., Kalin, M. (2022). Influence of load, sliding speed and heat-sink volume on the tribological behaviour of polyoxymethylene (POM) sliding against steel. *Tribology International*, vol. 178, part A, art. ID 108029, **DOI:10.1016/j.triboint.2022.108029**.

[2] Friedrich, K. (2018). Polymer composites for tribological applications. *Advanced Industrial and Engineering Polymer Research*, vol. 1, no. 1, p. 3-39, **DOI:10.1016/j.aiepr.2018.05.001**.

[3] Li, J.H., Wang, Y.T., Wang, X.D., Wu, D.Z. (2019). Crystalline characteristics, mechanical properties, thermal degradation kinetics and hydration behavior of biodegradable fibers melt-spun from Polyoxymethylene/Poly(L-lactic acid) blends. *Polymers*, vol. 11, no. 11, art. ID 1753, **DOI:10.3390/polym11111753**.

[4] Matkovič, S., Kalin, M. (2021). Effects of slide-to-roll ratio and temperature on the tribological behaviour in polymer-steel contacts and a comparison with the performance of real-scale gears. *Wear*, vol. 477, art. ID 203789, **DOI:10.1016/j.wear.2021.203789**.

[5] Bazan, P., Kuciel, S., Nykiel, M. (2019). Characterization of composites based on polyoxymethylene and effect of silicone addition on mechanical and tribological behavior. *Polymer Engineering & Science*, vol. 59, no. 5, p. 935-940, **DOI:10.1002/pen.25039**.

[6] Guo, X., Zhang, J., Huang, J. (2015). Poly(lactic acid)/polyoxymethylene blends: Morphology, crystallization, rheology, and thermal mechanical properties. *Polymer*, vol. 69, p. 103-109, **DOI:10.1016/j.polymer.2015.05.050**.

[7] Zhou, Z.Z., Chu, Y.H., Hou, Z.S., Zhou, X.P., Cao, Y. (2022). Modification of frictional properties of hydrogel surface via laser ablated topographical micro-textures. *Nanomaterials*, vol. 12, no. 22, art. ID 4103, **DOI:10.3390/nano12224103**.

[8] Xiao, J.R., Zhang, Y.T., Hu, B., Liu, X.C., Liang, Z.W., Zhao, Z. (2023). Tribological properties of Ti6Al4V alloy composite texture fabricated by ultrasonic strengthening grinding and laser processing. *Materials*, vol. 16, no. 1, art. ID 355, **DOI:10.3390/ma16010355**.

[9] Lu, L.B., Zhang, Z., Guan, Y.C., Zheng, H.Y. (2018). Comparison of the effect of typical patterns on friction and wear properties of chromium alloy prepared by laser surface texturing. *Optics & Laser Technology*, vol. 106, p. 272-279, **DOI:10.1016/j.optlastec.2018.04.020**.

[10] Hoskins, J.K., Zou, M. (2021). Designing a bioinspired surface for improved wear resistance and friction reduction. *Journal of Tribology*, vol. 143, no. 5, art. ID 051107, **DOI:10.1115/1.4050673**.

[11] Xu, S., An, S.O.J., Atsushi, D., Castagne, S. (2016). Development of low-cost deformation-based micro surface texturing system for friction reduction. *International Journal of Precision Engineering and Manufacturing*, vol. 17, p. 1059-1065, **DOI:10.1007/s12541-016-0128-3**.

[12] Li, W.W., Xue, W.B. (2023). Structural characterization of AlN thin films grown on sapphire by atomic layer deposition. *Thin Solid Films*, vol. 773, art. ID 139826, **DOI:10.1016/j.tsf.2023.139826**.

[13] Costa, H., Hutchings, I. (2014). Some innovative surface texturing techniques for tribological purposes. *Proceedings of the Institution of Mechanical Engineers, Part J: Journal of Engineering Tribology*, vol. 229, no. 4, p. 429-448, **DOI:10.1177/1350650114539936**.

[14] Su, X., Shi, L.P., Huang, W., Wang, X.L. (2016). A multi-phase micro-abrasive jet machining technique for the surface texturing of mechanical seals. *The International Journal of Advanced Manufacturing Technology*, vol. 86, p. 2047-2054, **DOI:10.1007/s00170-015-8272-y**.

[15] Stratakis, E., Bonse, J., Heitz, J., Tsibidis, G.D., Skoulas, E., Papadopoulos, A., Mimidis, A., Joel, A.-C., Comanns, P., Krüger, J., Florian, C., Fuentes-Edfuf, Y., Solis, J., Baumgartner, W. (2020). Laser engineering of biomimetic surfaces. *Materials Science and Engineering R: Reports*, vol. 141, art. ID 100562, **DOI:10.1016/j.mser.2020.100562**.

[16] Liu, Y., Li, X., Jin, J., Liu, J., Yan, Y., Han, Z., Ren, L. (2017). Anti-icing property of bio-inspired micro-structure superhydrophobic surfaces and heat transfer model. *Applied Surface Science*, vol. 400, p. 498-505, **DOI:10.1016/j.apsusc.2016.12.219**.

[17] Cho, M.H., Park, S. (2011). Micro CNC surface texturing on polyoxymethylene (POM) and its tribological performance in lubricated sliding. *Tribology International*, vol. 44, no. 7-8, p. 859-867, **DOI:10.1016/j.triboint.2011.03.001**.

[18] Cheng, H., Zhou, F., Fei, Z.H. (2023). Dry friction properties of friction subsets and angle related to surface texture of cemented carbide by femtosecond laser surface texturing. *Coatings*, vol. 13, no. 4, art. ID 741, **DOI:10.3390/coatings13040741**.

[19] Alnusirat, W., Kyrychok, M., Bellucci, S., Gnilitskyi, I. (2021). Impact of ultrashort laser nanostructuring on friction properties of AISI 314 LVC. *Symmetry*, vol. 13, no. 6, art. ID 1049, **DOI:10.3390/sym13061049**.

[20] Liu, Y.Y., Liu, L.L., Deng, J.X., Meng, R., Zou, X.Q., Wu, F.F. (2017). Fabrication of micro-scale textured grooves on green ZrO2 ceramics by pulsed laser ablation. *Ceramics International*, vol. 43, p. 6519-6531, **DOI:10.1016/j.ceramint.2017.02.074**.

[21] Li, D.X., Chen, X.X., Guo, C.H., Tao, J., Tian, C.X., Deng, Y.M., Zhang, W.W. (2017). Micro surface texturing of alumina ceramic with nanosecond laser. *Procedia Engineering*, vol. 174, p. 370-376, **DOI:10.1016/j.proeng.2017.01.155**.

[22] Cheng, B.X., Duan, H.T., Chen, Q., Shang, H.F., Zhang, Y., Li, J., Shao, T.M. (2021). Effect of laser treatment on the tribological performance of polyetheretherketone (PEEK) under seawater lubrication. *Applied Surface Science*, vol. 566, art. ID 150668, **DOI:10.1016/j.apsusc.2021.150668**.

[23] Zhao, W.Q., Shen, X.W., Liu, H.D., Wang, L.Z., Jiang, H.T. (2020). Effect of high repetition rate on dimension and morphology of micro-hole drilled in metals by picosecond ultra-short pulse laser. *Optics and Lasers in Engineering*, vol. 124, art. ID 105811, **DOI:10.1016/j.optlaseng.2019.105811**.

[24] Deepu, P., Jagadesh, T., Muthukannan, D., Jagadeesh, B. (2023). Investigation into femtosecond based laser ablation and morphology of micro-hole in titanium alloy. *Optik*, vol. 274, art. ID. 170519, **DOI:10.1016/j.ijleo.2023.170519**.

[25] Lian, G.F., Yao, M.P., Zhang, Y., Chen, C.R. (2018). Analysis and prediction on geometric characteristics of multi-track overlapping laser cladding. *The International Journal of Advanced Manufacturing Technology*, vol. 97, p. 2397-2407, **DOI:10.1007/s00170-018-2107-6**.

[26] Cui, L.J., Zhang, M., Guo, S.R., Cao, Y.L., Zeng, W.H., Li, X.L., Zheng, B. (2020). Multi-objective numerical simulation of geometrical characteristics of laser cladding of cobalt-based alloy based on response surface methodology. *Measurement and Control*, vol. 54, no. 7-8, p. 1125-1135, **DOI:10.1177/0020294020944955**.

[27] Ren, Y.M., Zhang, Z.Y. (2022). Surface of nanosecond laser polished single-crystal silicon improved by two-step laser irradiation. *Acta Optica Sinica*, vol. 42, no. 7, p. 212-219, **DOI:10.3788/AOS202242.0714004**. (in Chinese)

[28] Suthar, J., Teli, S.N., Murumkar, A. (2021). Drilling process improvement by Taguchi method. *Materials Today: Proceedings*, vol. 47, p. 2814-2819, **DOI:10.1016/j.matpr.2021.03.533**.

[29] Deng, D.W., Li, T.S., Huang, Z.Y., Jiang. H., Yang, S.H., Zhang, Y. (2022). Multi-response optimization of laser cladding for TiC particle reinforced Fe matrix composite based on Taguchi method and grey relational analysis. *Optics & Laser Technology*, vol. 153, art. ID 108259, **DOI:10.1016/j.optlastec.2022.108259**.

[30] Volpe, V., Speranza, V., Schrank, T., Berer, M., Pantani, R. (2022). An investigation of crystallization kinetics of polyoxymethylene in processing conditions. *Polymers for Advanced Technologies*, vol. 34, no. 2, p. 634-645, **DOI:10.1002/pat.5916**.

[31] Chen, W.H., Uribe, M.C., Kwon, E.E, Lin, K.Y.A., Park, Y.K., Ding., L, Saw Huat, L. (2022). A comprehensive review of thermoelectric generation optimization by statistical approach: Taguchi method, analysis of variance (ANOVA), and response surface methodology (RSM). *Renewable and Sustainable Energy Reviews*, vol. 169, art. ID 112917, **DOI:10.1016/j.rser.2022.112917**.

Strojniški vestnik - Journal of Mechanical Engineering 70(2024)5-6, 259-269
DOI:10.5545/sv-jme.2023.890
Original Scientific Paper
Received for review: 2023-12-07
Received revised form: 2024-03-28
Accepted for publication: 2024-04-11

Multi-response Optimization of GTAW Process Parameters in Terms of Energy Efficiency and Quality

An-Le Van[1] – Thai-Chung Nguyen[2] – Huu-Toan Bui[2] – Xuan-Ba Dang[3] – Trung-Thanh Nguyen[2,*]

[1]Nguyen Tat Thanh University, Faculty of Engineering and Technology, Vietnam
[2]Le Quy Don Technical University, Faculty of Mechanical Engineering, Vietnam
[3]Ho Chi Minh City University of Technology and Education, Vietnam

This work optimizes the current (I), voltage (V), flow rate (F), and arc gap (G) of the gas tungsten arc welding (GTAW) of the Ti40A titanium alloy to decrease the heat input (HI) and improve the ultimate tensile strength (TS) and micro-hardness (MH). The radial basis function network (RBFN) was utilized to present performance measures, while weighted principal component analysis (WPCA) and an adaptive non-dominated sorting genetic algorithm II (ANSGA-II) were applied to estimate the weights and generate optimal points. The evaluation via an area-based method of ranking (EAMR) was employed to determine the best solution. The results indicated that the optimal I, V, F, and G are 89 A, 23 V, 20 L/min, and 1.5 mm, respectively. The improvements in the TS and MH were 1.2 % and 19.8 %, respectively, while the HI was saved by 18.4 %. The RBFN models provided acceptable accuracy for prediction purposes. The ANSGA-II provides better optimality than the conventional NSGA-II. The HI, TS, and MH of the practical GTAW Ti40A could be enhanced using optimality. The optimization method could be utilized to deal with optimization problems for not only other GTAW operations but also other machining processes.

Keywords: GTAW, Heat input, Ultimate tensile strength, Micro-hardness, radial basis function network

Highlights

- *Optimizing GTAW operation considering the heat input, ultimate tensile strength, and micro-hardness.*
- *A radial basis function network is utilized to propose the GTAW performance measures.*
- *Process parameters, including the current, voltage, flow rate, and arc gap, were optimized.*
- *An adaptive non-dominated sorting genetic algorithm II was proposed and applied.*

0 INTRODUCTION

Gas tungsten arc welding (GTAW) is a popular welding method that joins metals with a non-consumable electrode. It involves heating the metal to produce a weld pool by creating an arc between the electrode and the specimen. A shielding gas keeps the weld area safe from airborne contaminants. GTAW produces high-quality welds, exact control, excellent weld penetration, minimal spatter, and a variety of metals.

Different GTAW operations have been considered and optimized to enhance the performances measured. For the GTAW Inconel 718 alloy, response surface method (RSM) models of the bead width (*BW*), depth of penetration (*DP*), heat-affected zone (*HAZ*), and area of the fusion zone were developed [1]. The authors stated that weld bead properties were mostly impacted by the welding current (*I*) and torch speed (*S*), respectively. The *BW*, Brinell hardness (*BH*), and micro-hardness (*MH*) were improved for the welded Inconel 625 using the grey relational analysis and TOPSIS [2]. The results presented that the optimal *I, S*, and arc gap (*G*) were 300 A, 90 mm/min, and 5 mm, respectively. In terms of the *I, S,* and *G*, the *DP* and *BW* models of the titanium joints were proposed [3]. The authors claimed that to create TWB joints free of defects, the ideal parameters of 135 A, 4.1 mm/s, and 3 mm may be used. An aspect ratio of 0.421 and the ideal hardness of 262 HB of the welded Inconel 625 could be generated at I = 300 A, S = 75 mm/min, and G = 1 mm using the TOPSIS [4]. For the welded 5052 alloys, predictive models were provided in terms of the *I, V,* and *S* for the penetration shape factor, *MH,* and reinforcement form factor of the weld specimens [5]. The optimal *I*, *V*, and *S* reported were 140 A, 18 V, and 300 mm/min, respectively. The *BW* and *DP* models of the welded AISI316L were proposed in terms of the *I* and *S*, in which the PSO was used to find the best ANN model [6]. The small deviations (less than 4 %) indicated that the developed correlations were efficiently used in the GTAW operation. Wan et al. find that the tensile strength (*TS*) and elongation (*EL*) could be improved using the optimized weld shape [7]; the *TS* and *EL* of the welded 2219-T8 aluminium alloys were enhanced by 70 % and 4 %, respectively. Vijayakumar et al. [8] presented that the peak current of 50 A, inter-pulse current of 30 A, and inter-pulse frequency of 20 kHz could be used to improve the characteristics of the IP-TIG welded Ti6Al4V alloy. The RSM model of the joint strength was developed for the IN-718 weld by Sonar

*Corr. Author's Address: Le Quy Don Technical University, 236 Hoang Quoc Viet, Ha Noi, VietNam, trungthanhnguyen@lqdtu.edu.vn

et al. [9], who found that the developed weld exhibited 32 % higher strength and superior corrosion resistance than TIG ones. The RSM models of the maximum yield strength and *EL* were developed for the IP-TIG welded Alloy 718 joints [10]. The authors stated the yield strength and *EL* of the IP-TIG joint were 94.5 % and 82.9 % of base metal, respectively. The ANOVA is used to determine the optimal values of the GTAW mild steel plates [11]. The maximum impact strength was obtained at the *I* of 158.605, a notch angle of 59°, and a single pass, respectively. A convolutional neural network was used to train the *BW* and *DP* models [12]. The R^2 value of 0.998 indicated that the developed models could be used to control the quality in real time. The Taguchi and RSM were used to enhance the *TS* of the welded SS316L stainless steel pipes [13]; the optimal working cycle and peak current were 66.5 % and 114.7 A, respectively. Deep learning was proposed to predict the *DP* value [14]. The low error level showed that the developed models can be utilized in the GTAW process. Pandya et al. [15] indicated that oxide flux increased the weld penetration and mechanical strength of welded 2205 duplex stainless steel. Moreover, the *DP* of 6.23 mm, *TS* of 775 MPa, and *MH* of 322 HV were obtained using the RSM. Similarly, Baskoro et al. presented that the *DP* and *TS* of the welded 304 stainless steel could be increased by 89.9 % and 17.2 %, respectively, with the SiO_2 flux [16].

However, the limitations of related works can be expressed as follows.

The mechanical and shape characteristics are frequently taken into account, while the heat input has not been discussed. Reducing the heat input will help the GTAW operate more energy-efficiently.

The RSM is widely used to propose performance models, while the application of the ANN has been rare. Moreover, the *HI*, *TS*, and *MH* models have not been developed for the GTAW Ti40A plates.

The impacts of GTAW process parameters on the *HI*, *TS*, and *MH* have not been analysed.

The optimal GTAW parameters have not been selected to improve the HI, TS, and MH simultaneously.

The Taguchi and RSM methods are highly likely to find local outcomes. Therefore, an efficient approach to finding global data is necessary.

1 OPTIMIZING FRAMEWORK

The *HI* is defined as a ratio of energy consumption per length and computed as:

$$HI = \frac{\eta \times I_i \times V_i}{S}, \tag{1}$$

where I_i, V_i, S, and η are the instant current, instant voltage, torch speed, and thermal efficiency, respectively.

The *TS* is computed as:

$$TS = \frac{\sum_{i=1}^{n} TS_i}{n}, \tag{2}$$

where TS_i and n are the tensile strength of the i^{th} sample and the number of samples, respectively.

The *MH* is computed as:

$$MH = \frac{\sum_{i=1}^{n} MH_i}{n}, \tag{3}$$

where MH_i and n are the micro-hardness of the i^{th} location and the number of positions, respectively.

Table 1. *Process parameters of the GTAW operation*

Parameters	Levels
Current, I [A]	70, 90, 110, 130
Voltage, V [V]	22, 23.5, 25, 26
Flow rate, F [L/min]	12, 15, 17, 20
Arc gap, G [mm]	1.5, 2.5, 3.5, 4.5

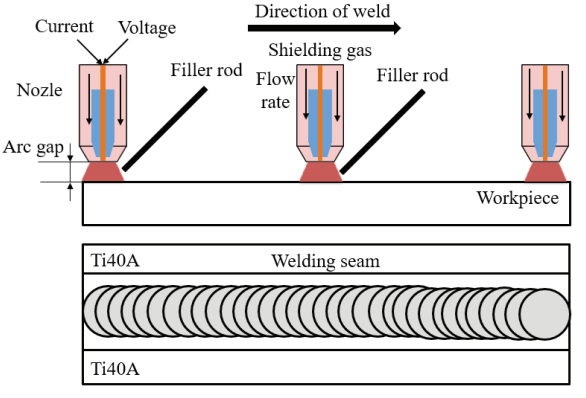

Fig. 1. *The scheme of the GTAW process*

Fig. 1 illustrates the GTAW process. Table 1 displays the process parameters with their respective levels. The machine's manufacturer's recommendations are used to calculate the values of *I* and *V*. The *F* is chosen in accordance with the attributes of the air supplier, whilst the *G* is cited from relevant sources. The optimization issue is expressed as:

Finding $X = [I, V, F, \text{and } G]$.

Maximizing *TS* and *MH*; Minimizing *HI*.

Constraints: 70 A $\leq I \leq$ 130 A; 22 V $\leq V \leq$ 26 V;

12 L/min $\leq F \leq$ 16 L/min; 1.5 mm $\leq G \leq$ 4.5 mm.

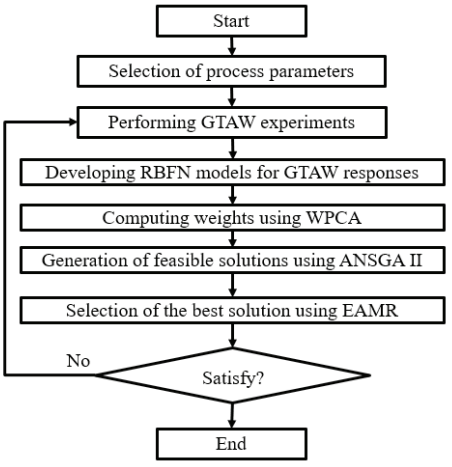

Fig. 2. *Optimization approach for the GTAW*

Fig. 2 shows the optimization framework for the GTAW operation.

Step 1: Use the L_{32} orthogonal array to conduct GTAW experiments [17].

Step 2: The RBFN models of the outputs are developed regarding GTAW parameters [18].

The RBFN with Gaussian function is used to present the correlations between the inputs and outputs. The input parameters are combined into the hidden one, while the output for the given input (s) and vector (c_i) is expressed as:

$$out_i = \exp\left(-\frac{1}{2\sigma^2}\left\|s-c_i\right\|^2\right), \tag{4}$$

where $\|s_i - c_i\|$ is the Euclidean distance between s and c_i.

The Gaussian function is expressed as:

$$\Phi(r) = \exp\left(-\gamma r^2\right), \tag{5}$$

where γ is a parameter that is found using the cross-validation stage.

The RBFN model for a given input s is expressed as:

$$out = w_0 + \sum_{i=1}^{m} w_i \exp\left(-\frac{1}{2\sigma^2}\left\|s-c_i\right\|^2\right), \tag{6}$$

where w_0 and w_m are the bias and weight, respectively.

Step 3: The WPCA is used to compute the weights.

The normalized response (n_r) is computed as:

$$n_r = \frac{R_i(m)}{\sum_{1}^{n} R_i(m)}. \tag{7}$$

The correlative data (S_{jl}) is computed as:

$$S_{jl} = \left[\frac{Cov\left(R_i(j), R_i(l)\right)}{\sigma_{Ri}(j)\times\sigma_{Ri}(\mathrm{l})}\right], \tag{8}$$

where $Cov(R_i(j)$ *and* $Ri(\mathrm{l}))$ denote the covariance of sequences $I_i(j)$ and $I_i(l)$, respectively.

Eigenvalues (λ_k) and eigenvectors (V_{ik}) are computed as:

$$(S-\lambda_k J_m)V_{ik} = 0. \tag{9}$$

The major principal coefficient is computed as follows:

$$PC_m = \sum_{i=1}^{n} I_m(i)\times V_{ik}. \tag{10}$$

Step 4: The ANSGA-II is used to find solutions.

The adaptive crossover probability and adaptive mutation probability are used in the ANSGA-II to identify the best solutions. Fig. 3 illustrates how the ANSGA-II operates.

- Producing initial population $X(0)$ and computing the function value $f(x)$ for each individual.
- The middle generation $X'(t)$ is created by performing the adaptive crossover and mutation operators.
- When an individual's fitness exceeds the average, they can be passed on to the next generation, which lowers the crossover probability (p_c) and mutation probability (p_m). However, if an individual's fitness level is lower than the average, they may be removed, which would result in greater p_c and p_m levels. The crossover and mutation operations' equations are written as follows:

$$p_c = \begin{cases} p_{c1} - \dfrac{p_{c1}-p_{c2}}{f_{\max}-f_{avg}}(f'-f_{avg}) \\ p_{c1} \end{cases}, \tag{11}$$

$$p_m = \begin{cases} p_{m1} - \dfrac{p_{m1}-p_{m2}}{f_{\max}-f_{avg}}(f'-f_{avg}) \\ p_{m1} \end{cases}. \tag{12}$$

- Creating a new non-dominate set $P'(t)$ by joining the non-dominate solutions.
- To create a new population $X(t+1)$, randomly generate new individuals and join them to the non-dominated solutions.

Step 4: The EAMR is used to select the best optimality.

The positive solution is computed as:

$$S_i^+ = v_{i1}^+ + v_{i2}^+ + v_{i3}^+ + ...v_{im}^+. \quad (13)$$

The negative solution is computed as:

$$S_i^- = v_{i1}^- + v_{i2}^- + v_{i3}^- + ...v_{im}^-. \quad (14)$$

The performance indicator (I_i) is computed as:

$$I_i = \frac{S_i^+}{S_i^-}. \quad (15)$$

The best solution is selected with the highest I_i.

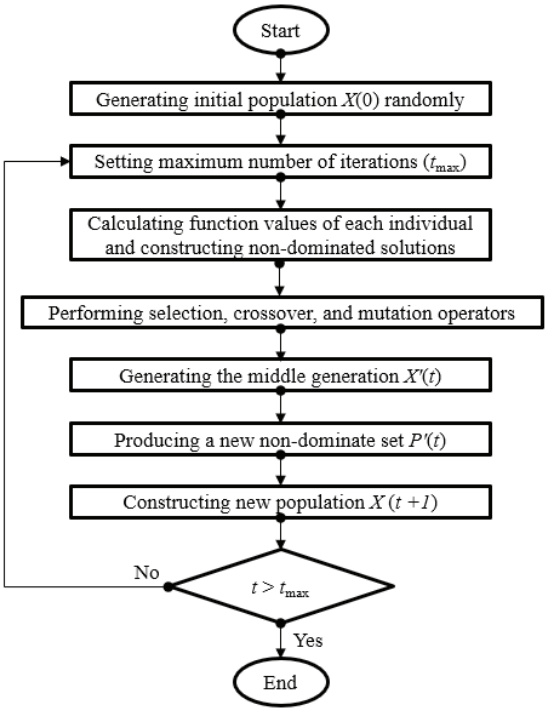

Fig. 3. *The operating principle of the ANSGA-II*

2 EXPERIMENTAL FACILITIES

Using the WEDM method, the specimens are sliced from the Ti40A plates and then cleaned using carbide sheets. The measurements of each specimen are 3 mm in thickness, 64 mm in width, and 80 mm in length. The anti-corrosion cover of the marine ship is mostly made of welded Ti40A plates. Each filler stick has the following measurements: 8 mm for length, 2 mm for breadth, and 3 mm for thickness. The chemical compositions of the Ti40A are shown in Table 2.

All testing is conducted using a ZX7-200 welding machine and a designed fixture (Fig. 4). During the processing stage, two welded layers are produced to enhance the junction. Tensile and micro-hardness tests were conducted using the Exceed E45 and Wilson hardness machines, respectively. The instantaneous voltage and current are measured using the clamp meter known as PAC22.

Fig. 4. *Experiments of the GTAW operation*

Table 2. *Chemical compositions of the Ti40A*

Element	Fe	O	C	N	H	Other	Ti
[%]	0.30	0.25	0.08	0.03	0.015	0.05	Balance

Figs. 5 and 6 display the representative values obtained at experimental No. 3 and 31, respectively.

As shown in Fig. 7, the microstructure of the various welding locations, such as the base material (BM), heat-affected zone (HAZ), and welded zone (WZ), are examined. Fig. 7a displays the BM's microstructure with large particles and irregular dimensions in comparison to the preceding sections. In the welded zone, the grain size is approximately 170 μm. The uniformly fine grain (about 15 μm) without any faults, such as flash, fractures, voids, and porosity, is produced in the welded region (Fig. 7a). In Fig. 7b, the coarser grain and uneven size of the heat-affected zone (HAZ) are detected without any flaws, including voids and pits. Because of the heat from the welding, the grain size in the HAZ is about 105 μm.

3 RESULTS AND DISCUSSIONS

3.1 Impacts of Process Parameters on Responses

The experimental data of the GTAW Ti40A are shown in Table 3.

As the *I* increases from 70 A to 130 A, the *HI* is increased by 52.6 % (Fig. 8a). An increased *I* causes

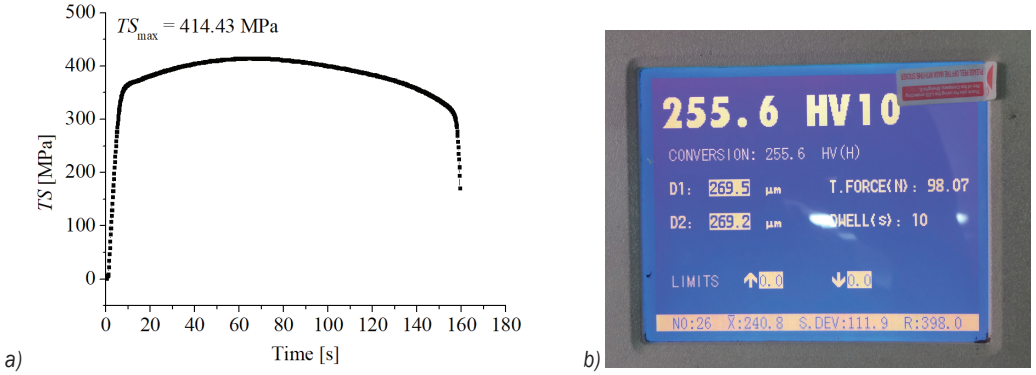

Fig. 5. *Experimental outcomes at the No. 3; a) tensile strength, and b) micro-hardness*

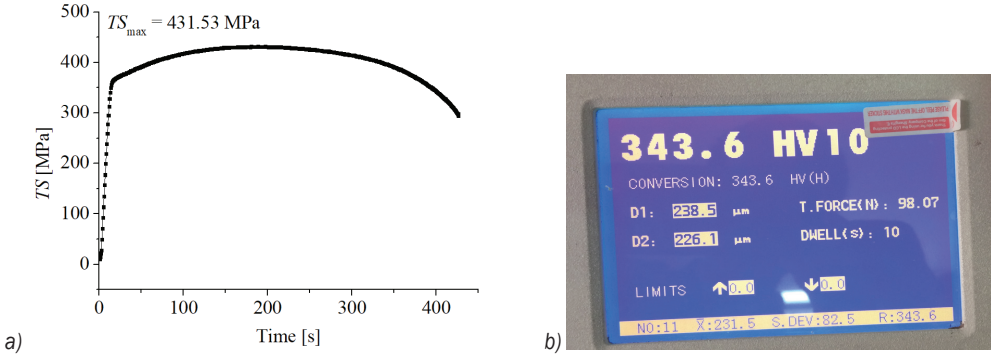

Fig. 6. *Experimental outcomes at the No. 31; a) tensile strength, and b) micro-hardness*

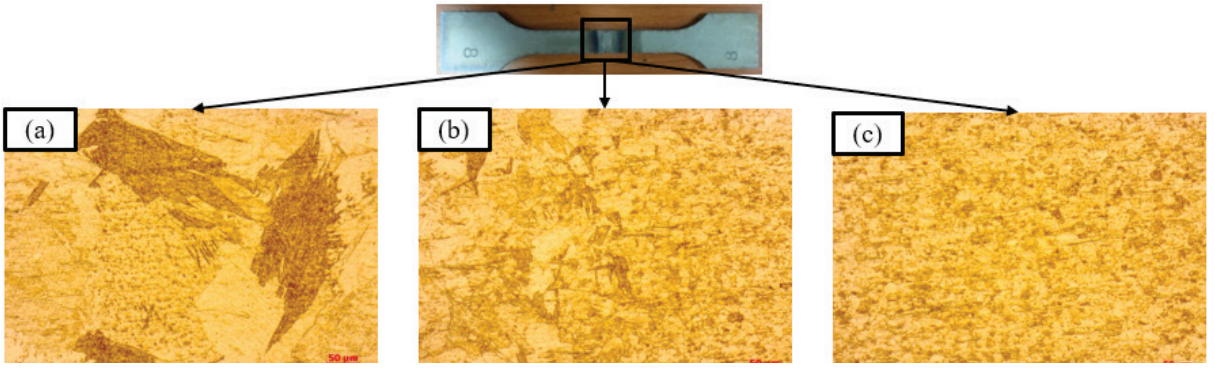

Fig. 7. *Analysis of the micro-structure of different zones*

a higher instant current; hence, more heat input is produced. As *V* increases from 22 V to 26 V, the *HI* is increased by 39.2 % (Fig. 8a). An increased *V* causes a higher arc voltage, leading to higher heat input. The similar impacts of the *I* and *V* on the *HI* were explained in the works of [7], [15], and [16]. As *F* increases from 12 L/min to 20 L/min, the *HI* is decreased by 24.3 % (Fig. 8b). A higher *F* increases the amount of shielding gas, leading to a reduction in the instant current; hence, the *HI* reduces. As the *G* increases from 1.5 mm to 4.5 mm, the *HI* is decreased by 21.3 % (Fig. 8b). A higher *G* increases the electrode stick out, leading to a higher resistance. The instant current decreases, and the *HI* decreases. Similar influences can be found in the literature [19].

The *TS* improves by 18.6 % when the *I* rises from 70 A to 130 A (Fig. 9a). Due to the poor diffusion between the two plates caused by the low energy input supplied at a low *I*, a low *TS* was formed. A greater *I* results in a better fusion and an improvement in the *TS* by increasing the energy delivered to the base metal. As *V* increases from 22 V to 24 V, the *TS* is increased

Table 3. *Experimental results of the GTAW operation*

No.	*I* [A]	*V* [V]	*F* [L/min]	*G* [mm]	*HI* [J/mm]	*TS* [MPa]	*MH* [HV]
Experimental data for developing the models							
1	70	22	12	1.5	762.19	408.68	254.2
2	90	23.5	12	2.5	780.52	427.87	266.5
3	110	25	12	3.5	857.51	431.53	255.6
4	130	26	12	4.5	980.14	432.28	232.7
5	70	23.5	12	1.5	842.05	436.40	251.1
6	90	22	12	2.5	698.62	402.24	273.6
7	110	26	12	3.5	888.90	416.15	238.2
8	130	25	12	4.5	947.38	449.05	252.9
9	90	25	15	1.5	797.86	468.61	259.7
10	70	26	15	2.5	745.81	424.55	253.9
11	130	22	15	3.5	765.12	457.12	273.3
12	110	23.5	15	4.5	680.93	448.88	301.4
13	90	26	15	1.5	826.23	455.23	245.3
14	70	25	15	2.5	716.91	437.75	267.9
15	130	23.5	15	3.5	848.64	479.46	258.2
16	110	22	15	4.5	596.62	426.35	315.9
17	130	22	17	1.5	693.12	479.76	256.8
18	110	23.5	17	2.5	718.72	468.79	279.5
19	90	25	17	3.5	656.18	438.71	288.9
20	70	26	17	4.5	493.63	400.91	294.9
21	130	23.5	17	1.5	772.97	503.87	244.1
22	110	22	17	2.5	637.94	444.34	291.5
23	90	26	17	3.5	685.98	424.17	271.5
24	70	25	17	4.5	463.31	415.23	311.9
25	110	25	20	1.5	729.35	469.54	274.1
26	130	26	20	2.5	870.87	458.71	219.3
27	70	22	20	3.5	388.56	388.73	354.4
28	90	23.5	20	4.5	493.01	422.25	349.7
29	110	26	20	1.5	756.91	455.38	256.4
30	130	25	20	2.5	841.92	474.27	239.8
31	70	23.5	20	3.5	468.43	414.76	344.1
32	90	22	20	4.5	411.09	398.31	364.2
Experimental data for testing models							
33	90	22	20	4.5	411.09	398.31	364.2
34	80	24	13	3	711.62	424.53	272.4
35	100	23	14	2	739.42	455.12	271.8
36	120	24.5	16	4	804.95	467.22	268.6
37	75	24	18	2	649.06	452.62	302.3
38	85	22.5	19	3	524.92	421.51	329.2
39	95	25.5	13	4	741.25	414.83	266.1
40	105	24.5	16	2	769.22	474.26	263.7
41	115	25	18	3.5	779.18	459.98	267.5
42	95	22	19	4.5	450.74	408.80	351.7
43	105	23	20	3	629.07	440.35	316.3
44	95	25.5	15	2	803.78	456.12	252.2
44	120	23.5	18	3.5	748.98	467.86	283.3
45	130	24	16	4.5	851.04	479.81	270.4
46	105	26	17	3	778.37	442.05	251.8
47	90	24	15	3	688.59	444.37	283.4

by 9.4 %, while a further *V* decreases by around 5.3 % in the *TS* (Fig. 9a). A weak joint is created because a low *V* causes a low heat input and a poor specimen combination. The heat input rises with a *V* increase, strengthening the joint. A further *V*, however, transfers too much energy into the base material. The overheating temperature may lead to a higher grain size; hence, the *TS* decreases. Similar impacts of the *I* and *V* can be found in the works of **[7]**, **[13]**, and **[16]**.

As *F* increases from 12 L/min to 16 L/min, the *TS* is increased by 7.5 %, while a further *F* decreases by around 11.1 % in the *TS* (Fig. 9b). A higher *F* may cause a proper welding condition, leading to a lower grain size; hence, the *TS* decreases. However, an excessive *F* decreases the heat input transferred into the base material, leading to an improper fusion; hence, a weak joint is produced. As the *G* increases from 1.5 mm to 4.5 mm, the *TS* is reduced by 10.1 % (Fig. 9b). Higher *G* results in an incorrect fusion due to lower input energy transferred to the base material; hence, the *TS* decreases. The welding gap length and the energy input have an inverse relationship. Consequently, at the lowest *G*, the *TS* can be maximized. Similar results were presented in the literature **[20]**.

The *MH* decreases by 23.3 % when the *I* rises from 70 A to 130 A (Fig. 10a). A rise in the *I* causes the energy input at the welding zone to increase, which raises the grain size and causes the *MH* to drop. The *MH* decreases by 22.5 % when *V* rises from 22 V to 24 V (Fig. 10a). A rise in the *V* results in a higher energy input, which in turn leads the welding area to become coarser; as a result, the *MH* reduces. Similar results were presented in the literature **[5]** and **[20]**.

The *MH* rises by 23.2 % when *F* increases from 12 L/min to 16 L/min (Fig. 10b). A greater *F* is linked to lower energy input, which causes solidification to happen more quickly and produces a higher *MH*. The *MH* increases by 18.5 % as *G* increases from 1.5 mm to 4.5 mm (Fig. 10b). Higher heat input at a low *G* could result in larger grain sizes and a low *MH*. Lower energy input results from a higher *G*. The result is a tiny grain size, which raises the *MH*. Similar outcomes can be found in the work of **[20]**.

3.2 ANOVA Analysis for Welding Responses

ANOVA results for the *HI* model are shown in Table 4. The *I, V, F, G, IF, VG, FG,* I^2, V^2, F^2, and G^2 are significant terms for the *HI* model. The contributions of the *I, V, F*, and *G* are 22.32 %, 15.38 %, 13.31 %, and 11.12 %, respectively. The contributions of the *IF, UG,* and *FG* are 3.43 %, 14.44 %, and 3.83 %,

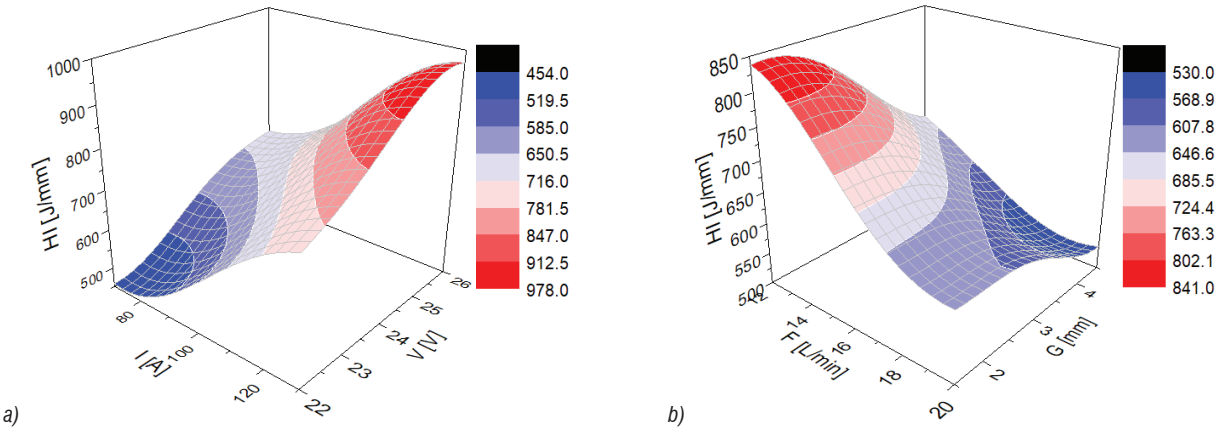

Fig. 8. *The impacts of process parameters on the HI; a) HI versus I and V, and b) HI versus F and G*

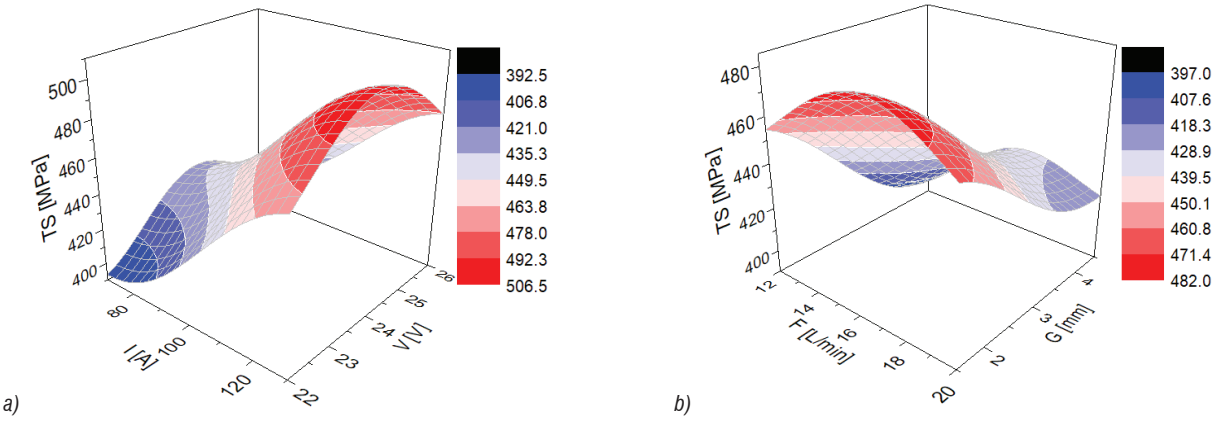

Fig. 9. *The impacts of process parameters on the TS; a) TS versus I and V, and b) TS versus F and G*

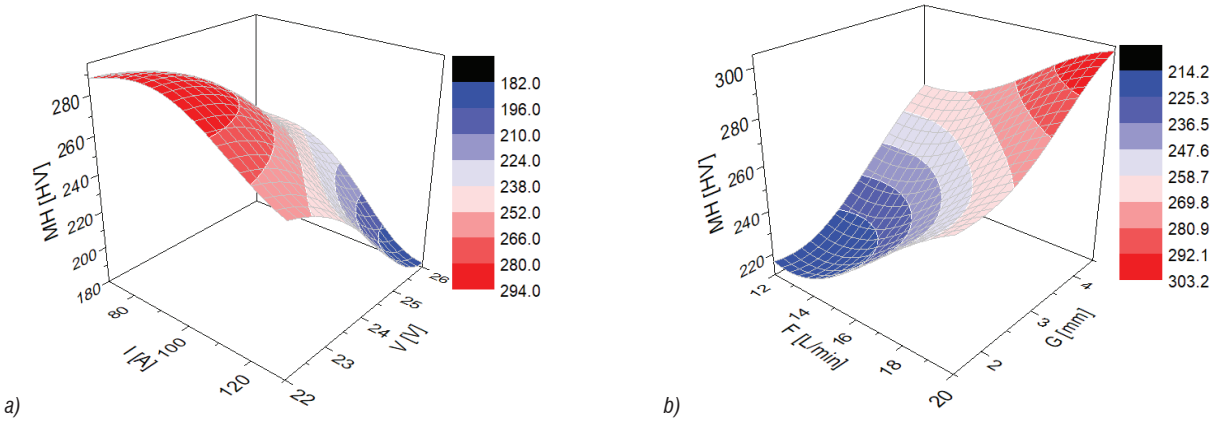

Fig. 10. The impacts of process parameters on the *MH*; *MH* versus *I* and *V*, and b) *MH* versus *F* and *G*

respectively. The contributions of the I^2, V^2, F^2, and G^2 are 4.51 %, 3.18 %, 3.68 %, and 4.12 %, respectively. As a result, the *I* is the most effective factor, followed by the *V, F,* and *G*, respectively.

ANOVA results for the *TS* model are shown in Table 5. The *I, V, F, G, IV, IF, IG, VG, FG,* I^2, V^2, F^2, and G^2 are significant terms for the *HI* model. The contributions of the *I, V, F,* and *G* are 22.18 %, 3.79 %, 5.15 %, and 15.16 %, respectively. The contributions of the *IV, IF, IG, VG*, and *FG* are 2.01 %, 1.31 %, 3.93 %, 1.45 %, and 2.32 %, respectively. The contributions of the I^2, V^2, F^2, and G^2 are 4.43 %,

18.17 %, 14.82 %, and 4.74 %, respectively. As a result, the *I* is the most effective factor, followed by the *G, F*, and *V*, respectively.

Table 4. *ANOVA results for the HI model*

So	*SS*	*MS*	*F* Value	*p*-value
Model	424549.38	30324.96	41.02	< 0.0001
I	380583.72	380583.72	514.77	< 0.0001
V	262248.10	262248.10	354.71	< 0.0001
F	226952.03	226952.03	306.97	< 0.0001
G	189609.81	189609.81	256.46	< 0.0001
IF	58485.76	58485.76	79.11	0.0072
IG	246219.93	246219.93	333.03	< 0.0001
FG	65306.26	65306.26	88.33	0.007
I^2	76901.10	76901.10	104.01	0.0062
V^2	54222.95	54222.95	73.34	0.0071
F^2	62748.57	62748.57	84.87	0.0071
G^2	70251.12	70251.12	95.02	0.0064
Res.	10350.62	739.33		
Cor.	434900.00			
R^2 = 0.9762; Adj. R^2 = 0.9612; Pre. R^2 = 0.9536				

Table 5. *ANOVA results for the TS model*

So	*SS*	*MS*	*F* Value	*p*-value
Model	19509.10	1393.51	49.50505051	< 0.0001
I	19830.89	19830.89	704.47	< 0.0001
V	3388.60	3388.60	120.38	< 0.0001
F	4577.74	4577.74	162.62	< 0.0001
G	13554.39	13554.39	481.51	< 0.0001
IV	1797.12	1797.12	63.84	0.0062
IF	1171.26	1171.26	41.61	0.0094
IG	3513.77	3513.77	124.82	0.0034
VG	1296.43	1296.43	46.05	0.0096
FG	2074.29	2074.29	73.69	0.0058
I^2	3960.81	3960.81	140.70	< 0.0001
V^2	16728.41	16728.41	594.26	< 0.0001
F^2	13250.40	13250.40	470.71	< 0.0001
G^2	4237.98	4237.98	150.55	< 0.0001
Res.	394.08	28.15	3176.16	
Cor.	19903.18			
R^2 = 0.9802; Adj. R^2 = 0.9724; Pre. R^2 = 0.9602				

ANOVA results for the MH model are shown in Table 6. The *I, V, F, G, IV, IF, VF, VG, FG,* I^2, V^2, F^2, and G^2 are significant terms. The contributions of the *I, V, F*, and *G* are 15.66 %, 16.28 %, 15.05 %, and 12.29 %, respectively. The contributions of the *IV, IF, VF, VG,* and *FG* are 3.33 %, 8.85 %, 1.79 %, 2.38 %, and 1.74 %, respectively. The contributions of the I^2, V^2, F^2, and G^2 are 9.46 %, 4.91 %, 3.82 %, and 4.27 %, respectively.

Table 6. *ANOVA results for the MH model*

So	*SS*	*MS*	*F* Value	*p*-value
Model	25581.89	1827.28	38.68	< 0.0001
I	32604.92	32604.92	690.20	< 0.0001
V	33895.79	33895.79	717.52	< 0.0001
F	31334.87	31334.87	663.31	< 0.0001
G	25588.41	25588.41	541.67	< 0.0001
IV	6933.23	6933.23	146.77	0.0012
IF	18426.15	18426.15	390.05	< 0.0001
VF	3726.87	3726.87	78.89	0.0024
VG	4955.28	4955.28	104.90	0.0019
FG	3622.77	3622.77	76.69	0.0026
I^2	19696.20	19696.20	416.94	< 0.0001
V^2	10222.87	10222.87	216.40	< 0.0001
F^2	7953.43	7953.43	168.36	< 0.0001
G^2	8890.36	8890.36	188.20	< 0.0001
Res.	661.33	47.24	4407.39	
Cor.	26243.22			
R^2	0.9748			
R^2 = 0.9748; Adj. R^2 = 0.9742; Pre. R^2 = 0.9586				

Table 7 presents confirmations of the precision of the *HI, TS*, and *MH* models. The small deviations (less than 5 %) indicate the allowable validity of the RBFN correlations.

3.3 Optimal Outcomes Produced by the ANSGA-II

The weights of the *HI, TS*, and *MH* are 0.36, 0.33, and 0.31, respectively. Fig. 11 shows the Pareto graphs produced by ANSGA-II. Consequently, a low *HI* causes a reduction in the *TS* (Fig. 11a), while a larger *HI* results in an enhanced *MH* (Fig. 11b). Accordingly, the optimal point with the highest PI_i is chosen as the best one (Table 8). The best results produced by the *I, V, F*, and *G* are 89 A, 23 V, 20 L/min, and 1.5 mm, respectively (Table 10). Whereas the *TS* and *MH* are improved by 1.2 % and 19.8 %, respectively, the *HI* is down 18.4 %.

3.4 Optimal Outcomes Produced by the NSGA-II

To prove the strength of the proposed approach, the conventional NSGA-II is applied to find optimal data. The optimal values of the *I, V, F*, and *G* are 81 A, 22 V, 19 L/min, and 1.4 mm, respectively (Table 8). The corresponding values of the *HI, TS*, and *MH* are

Table 7. *Comparative data for RBFN models*

No.	*HI* [J/mm]			*TS* [MPa]			*MH* [HV]		
	Actual	Pre.	Error	Actual	Pre.	Error	Actual	Pre.	Error
33	411.09	409.56	0.37	398.31	397.36	0.24	364.2	366.7	-0.69
34	711.62	709.62	0.28	424.53	426.56	-0.48	272.4	274.4	-0.73
35	739.42	741.86	-0.33	455.12	453.21	0.42	271.8	269.3	0.92
36	804.95	806.32	-0.17	467.22	465.98	0.27	268.6	266.7	0.71
37	649.06	650.38	-0.20	452.62	454.82	-0.49	302.3	304.6	-0.76
38	524.92	522.94	0.38	421.51	419.36	0.51	329.2	331.2	-0.61
39	741.25	739.62	0.22	414.83	416.85	-0.49	266.1	268.5	-0.90
40	769.22	771.25	-0.26	474.26	476.29	-0.43	263.7	265.4	-0.64
41	779.18	777.36	0.23	459.98	461.32	-0.29	267.5	265.4	0.79
42	450.74	452.23	-0.33	408.81	410.39	-0.39	351.7	349.6	0.60
43	629.07	628.36	0.11	440.35	438.36	0.45	316.3	318.4	-0.66
44	803.78	805.24	-0.18	456.12	458.81	-0.59	252.2	254.3	-0.83
44	748.98	750.66	-0.22	467.86	465.39	0.53	283.3	281.2	0.74
45	851.04	850.36	0.08	479.81	481.25	-0.30	270.4	272.6	-0.81
46	778.37	779.86	-0.19	442.05	446.08	-0.91	251.8	249.6	0.87
47	688.59	690.46	-0.27	444.37	446.52	-0.48	283.4	285.6	-0.78

Table 8. *Optimization results produced by the ANSGA-II and NSGA-II*

Method	Optimization parameters				Responses			I_i
	I [A]	*V* [V]	*F* [L/min]	*G* [mm]	*HI* [J/mm]	*TS* [MPa]	*MH* [HV]	
Initial values	100	25	15	3.0	764.35	449.47	264.6	
ANSGA-II	89	23	20	1.5	623.46	454.77	317.1	0.936
NSGA-II	81	22	19	1.4	638.31	450.22	316.8	0.869
Improvement by ANSGA-II [%]					-18.4	+1.2	+19.8	

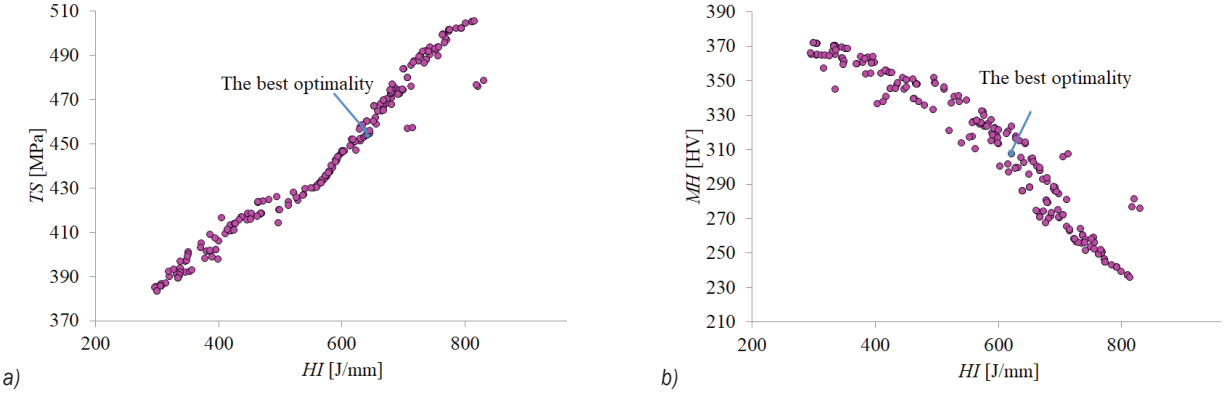

a) b)

Fig. 11. *Pareto fronts generated by ANSGA- II; a) HI versus TS, and b) HI versus MH*

638.31 J/mm, 450.22 MPa, and 316.8 HV. However, the conventional NSGA-II provides a higher *HI* and lower *TS,* as well as *MH*. In comparison to the traditional NSGA-II, it can be stated that the ANSGA-II produces superior optimal results.

3.5 Novelty and Applications of the Findings

The novelty of this work can be expressed as follows.

This work proposed an efficient optimizing algorithm entitled ANSGA-II, which could be effectively applied to solve complicated issues and find global results instead of traditional algorithms.

The trade-off analysis between the *HI*, *TS*, and *MH* was successfully solved using optimal parameters.

The optimality can be used to obtain a sustainable GTAW process.

The highly accurate models of the *HI*, *TS*, and *MH* were developed using the ANN approach, as compared to the conventional RSM ones.

The proposed optimization technique comprising RBFN-ANSGA-II-EAMR can be used to address optimization problems related to various GTAW operations and machining processes.

The applications of the findings can be expressed as follows.

The findings can be utilized to develop an expert system that will allow the GTAW to operate in many industries.

The practical *HI, TS*, and *MH* values of the GTAW Ti40A can be predicted using the RBFN models.

The optimal data can be utilized to improve quality indicators and energy efficiency of the practical GTAW Ti40A.

By leveraging the effects of GTAW inputs on the output, the technological knowledge of the GTAW process can be improved significantly.

The range of output objectives may be considered crucial technical advice for welding researchers.

4 CONCLUSIONS

The objective of the current study was to select the optimal GTAW inputs (*I*, *V*, *F*, and *G*) in order to decrease heat input (*HI*) and increase welding quality (*TS* and *MH*). The ANSGA-II was utilized to produce feasible solutions, and the RBFN method was applied to recommend GTAW solutions. The WPCA and EAMR were applied to calculate the weights and select the best optimal results. The conclusions are presented as follows:

1. The highest *F* and *G* values were recommended, but to reduce the *HI*, the low values of *I* and *V* were used. The medium values of *V* and *F* were addressed, and the highest *I* and lowest *G* were utilized to improve the *TS*. The lowest *I* and *V* were utilized, while the highest *F* and *G* were used to optimize the *MH*.
2. The *HI, TS*, and *MH* increase from 388.56 J/mm to 980.14 J/mm, 388.73 MPa to 530.87 MPa, and 319.3 HV to 364.2 HV, respectively, for the GTAW parameters considered.
3. The *I* and *V* contributed the most to the *HI* and *MH* models. The *I* and *G* were named as the most effective parameter in the *TS* model.
4. The *I, V, F*, and *G* have optimal data of 89 A, 23 V, 20 L/min, and 1.5 mm, in that order. While the *HI* was saved by 18.4 %, the *TS* and *MH* improved by 1.2 % and 19.8 %, respectively.
5. The Pareto graphs produced by the ANGA-II could be used to select optimal parameters and responses for different GTAW purposes.
6. Compared to the conventional NSGA-II, the developed ANSGA-II might be used to tackle complex problems and produce better results.
7. The ANSGA-II could be utilized to obtain global data instead of conventional algorithms.
8. The designed and fabricated fixture can be utilized in other GTAW operations.
9. Improving *HI, TS*, and *MH* are practical benefits to the GTAW Ti40A operation.
10. The impacts of the GTAW factors on air pollution and elongation will be explored in future work.

5 REFERENCES

[1] Sonar, T., Balasubramanian, V., Malarvizhi, S., Venkateswaran, T., Sivakumar, D. (2020). Multi-response mathematical modelling, optimization and prediction of weld bead geometry in gas tungsten constricted arc welding (GTCAW) of Inconel 718 alloy sheets for aero-engine components. *Multiscale and Multidisciplinary Modeling, Experiments and Design*, vol. 3, p. 201-226, **DOI:10.1007/s41939-020-00073-3**.

[2] Sivakumar, J., Vasudevan, M., Korra, N.N. (2020). Systematic welding process parameter optimization in activated tungsten inert gas (A-TIG) welding of Inconel 625. *Transactions of the Indian Institute of Metals*, vol. 73, p. 555-569, **DOI:10.1007/s12666-020-01876-1**.

[3] Karpagaraj, A., Rajesh Kumar, N., Thiyaneshwaran, N., Siva Shanmugam, N., Cheepu, M., Sarala, R. (2020). Experimental and numerical studies on gas tungsten arc welding of Ti-6Al-4V tailor-welded blank. *Journal of the Brazilian Society of Mechanical Sciences and Engineering*, vol. 42, p. 532, **DOI:10.1007/s40430-020-02629-3**.

[4] Sivakumar, J., Korra, N.N. (2021). Optimization of welding process parameters for activated tungsten inert welding of Inconel 625 Using the technique for order preference by similarity to ideal solution methodology. *Arabian Journal for Science and Engineering*, vol. 46, p. 7399-7409, **DOI:10.1007/s13369-021-05409-w**.

[5] Omprakasam, S., Marimuthu, K., Raghu, R., Velmurugan, T. (2022). Statistical modelling and optimization of TIG welding process parameters using Taguchi's method. *Strojniški vestnik - Journal of Mechanical Engineering*, vol. 68, no. 3, p. 200-209, **DOI:10.5545/sv-jme.2021.7414**.

[6] Moghaddam, M.A., Kolahan, F. (2022). Modeling and optimization of A-GTAW process using Box-Behnken design and hybrid BPNN-PSO approach. *Proceedings of the Institution of Mechanical Engineers, Part E: Journal of Process Mechanical Engineering*, vol. 236, no. 3, p. 859-869, **DOI:10.1177/09544089211050457**.

[7] Wan, Z., Meng, D., Zhao, Y., Zhang, D., Wang, Q., Shan, J., Song, J., Wang, G., Wu, A. (2021). Improvement on

the tensile properties of 2219-T8 aluminum alloy TIG welding joint with weld geometry optimization. *Journal of Manufacturing Processes*, vol. 67, p. 275-285, **DOI:10.1016/j.jmapro.2021.04.062**.

[8] Vijayakumar, V., Sonar, T., Venkatesan, S., Negemiya, A., Ivanov, M. (2024). Influence of IP-TIG welding parameters on weld bead geometry, tensile properties, and microstructure of Ti6Al4V alloy joints. *Materials Testing*, **DOI:10.1515/mt-2023-0237**.

[9] Sonar, T., Balasubramanian, V., Malarvizhi, S., Venkateswaran, T., Sivakumar, D. (2021). Maximizing strength and corrosion resistance of InterPulsed TIG welded Superalloy 718 joints by RSM for aerospace applications. *CIRP Journal of Manufacturing Science and Technology*, vol. 35, p. 474-493, **DOI:10.1016/j.cirpj.2021.07.013**.

[10] Sonar, T., Balasubramanian, V., Malarvizhi, S., Venkateswaran, T., Sivakumar, D. (2020). Development of 3-Dimensional (3D) response surfaces to maximize yield strength and elongation of InterPulsed TIG welded thin high temperature alloy sheets for jet engine applications. *CIRP Journal of Manufacturing Science and Technology*, vol. 31, p. 628-642, **DOI:10.1016/j.cirpj.2020.09.003**.

[11] Singh, B.K., Chauhan, N., Mishra, A.K., Yadhuvanshi, A.A., Kumar, A., Ansu, A.K., Goyal, A. (2023). Experimental investigation of welding parameters to enhance the impact strength using gas tungsten arc welding. *International Journal on Interactive Design and Manufacturing*, **DOI:10.1007/s12008-023-01264-1**.

[12] Baek, D., Moon, H.S., Park, S.H. (2024). Optimization of weld penetration prediction based on weld pool image and deep learning approach in gas tungsten arc welding. *International Journal of Advanced Manufacturing Technology*, vol. 130, p. 2617-2633, **DOI:10.1007/s00170-023-12855-3**.

[13] Baskoro, A.S., Widyianto, A., Prasetyo, E., Kiswanto, G. (2024). The Taguchi and response surface method for optimizing orbital pipe welding parameters in pulsed current gas tungsten arc welding (PC-GTAW) for SS316L. *Transactions of the Indian Institute of Metals*, **DOI:10.1007/s12666-023-03254-z**.

[14] Baek, D., Moon, H.S., Park, S.H. (2024). In-process prediction of weld penetration depth using machine learning-based molten pool extraction technique in tungsten arc welding. *Journal of Intelligent Manufacturing*, vol. 35, p. 129-145, **DOI:10.1007/s10845-022-02013-z**.

[15] Pandya, D., Badgujar, A., Ghetiya, N., Oza, A.D. (2022). Characterization and optimization of duplex stainless steel welded by activated tungsten inert gas welding process. *International Journal on Interactive Design and Manufacturing*, **DOI:10.1007/s12008-022-00977-z**.

[16] Baskoro, A.S., Amat, M.A., Widyianto, A., Putra, A.D., Aryadhani, S.A. (2024). Investigation of weld geometry, mechanical properties, and metallurgical observations of activated flux tungsten inert gas (A-TIG) welding on 304 austenitic stainless steel. *Transactions of the Indian Institute of Metals*, vol. 77, p. 897-906, **DOI:10.1007/s12666-023-03180-0**.

[17] Elangandhi, J., Periyagounder, S., Selavaraj, M., Saminatharaja, D. (2023). Mechanical and microstructural properties of B4C/W reinforced copper matrix composite using a friction stir-welding process. *Strojniški vestnik - Journal of Mechanical Engineering*, vol. 69, no. 9-10, p. 388-400, **DOI:10.5545/sv-jme.2023.518**.

[18] Ibrahim, M.A., Çamur, H., Savaş, M., Sabo, A.K. (2022). Multi-response optimization of the tribological behaviour of PTFE-based composites via Taguchi grey relational analysis. *Strojniški vestnik - Journal of Mechanical Engineering*, vol. 68, no. 5, p. 359-367, **DOI:10.5545/sv-jme.2021.7466**.

[19] Singh, V., Chandrasekaran, M., Samanta, S., Devarasiddappa, D., Arunachalam, R. (2021). Sustainability assessment of gas metal arc welding process of AISI 201LN using AHP-TLBO integrated optimization methodology. *Journal of the Brazilian Society of Mechanical Sciences and Engineering*, vol. 43, art. ID 68, **DOI:10.1007/s40430-020-02786-5**.

[20] Bhattacharya, A., Singla, S. (2017). Dissimilar GTAW between AISI 304 and AISI 4340 steel: Multi-response optimization by analytic hierarchy process. *Proceedings of the Institution of Mechanical Engineers, Part E: Journal of Process Mechanical Engineering*, vol. 231, no. 4, p. 824-835, **DOI:10.1177/0954408916641458**.

Strojniški vestnik - Journal of Mechanical Engineering 70(2024)5-6, 270-281
DOI:10.5545/sv-jme.2023.893
Original Scientific Paper
Received for review: 2023-12-08
Received revised form: 2024-03-11
Accepted for publication: 2024-04-15

Experimental Attempts of Using Modulated and Unmodulated Waves in Low-Frequency Acoustic Wave Flame Extinguishing Technology: A Review of Selected Cases

Jacek Wilk-Jakubowski[1,*] – Grzegorz Wilk-Jakubowski[2,3] – Valentyna Loboichenko[4,5]

1 Kielce University of Technology, Poland
2 Old Polish University of Applied Sciences, Poland
3 Institute of Crisis Management and Computer Modelling, Poland
4 University of Sevilla, Higher Technical School of Engineering, Spain
5 Lutsk National Technical University, Ukraine

In practice, some undesired signals perceived as noise (because of the sound sensation) can effectively extinguish flames. This article provides information on the applicability of acoustic waves (a case of using sine waves and sine waves amplitude modulated by a square waveform) in low-frequency acoustic wave flame extinguishing technology based on experimental results obtained from a laboratory stand, which is a scientific novelty. The benefits of using deep neural networks for flame detection based on dedicated solutions developed through international cooperation are also recognized. In addition, the potential advantages of combining both technologies (use in fully automatic systems), limitations, open problems, and plans for further research are identified. The paper concludes that it is possible to extinguish flames as soon as they appear (firebreaks) and prevent large fires from breaking out. This feature may effectively reduce material losses and increase widespread safety.

Keywords: acoustic flame extinguishing, firefighting systems, deep neural networks, electrical and mechanical engineering, fire extinguisher, flame suppression

Highlights

- *An analysis of the use of acoustic waves to extinguish flames shows that this technique is not fully explored.*
- *It is possible to control and extinguish flames using the acoustic method (especially firebreaks), which come from various materials (Class B and C fires).*
- *Both modulated and unmodulated acoustic waves can be applied to extinguish flames.*
- *The sound pressure at which the phenomenon of complete acoustic flame extinguishment was observed oscillates in the approximate range of 115 dB to 130 dB.*
- *Since it is possible to use artificial intelligence for flame detection, combining acoustic technology with artificial intelligence (a smart, environmentally friendly acoustic extinguisher) can bring many tangible benefits to society (including no need for human presence during an extinguishing action).*

0 INTRODUCTION

In practice, acoustic waves have many different applications, such as in industry, which can be exemplified by using low-frequency acoustic waves or infrasound to clean the heating surfaces of power boilers from sediments [1]. Such waves may also be applied in other industrial applications, such as electrostatic precipitators and bag filters, in cyclones, and in reactors of flue gas desulfurization systems [2]. In this regard, mathematical methods can be helpful, e.g., [3]. It should be noted that the cleaning properties of low-frequency acoustic waves were discovered by Matts Olsson, a Swedish engineer, who analysed the motion of dust particles exposed to the infrasound. He showed that the generation of acoustic waves (longitudinal waves) creates local pressures that cause the movement of pollutants at different speeds. The effectiveness of this technique depends on the frequency of the acoustic wave, which is generated in pneumatic generators currently manufactured by many plants around the world [4]. Another example of using acoustic waves can be flame control, which has many applications. Examples include using the acoustic field to reduce the emissions of combustion products such as soot. Moreover, there are numerous uses for controlling flames, such as applying the acoustic field to decrease the release of combustion by-products. However, due to the subject matter of this article, these issues have been omitted. Some items of literature are indicated in the bibliography as a reference to supplement the literature in this area.

Based on previous research, it has been observed that some signals treated in terms of noise can be useful in certain applications, e.g., to extinguish flames. Taking into account the use of acoustic waves to extinguish flames, the acoustic method is based on the use of movement (vibration) of air molecules

*Corr. Author's Address: Kielce University of Technology, Faculty of Electrical Engineering, Automatics and Computer Science, 7 Tysiaclecia Panstwa Polskiego Ave., 25-314, Kielce, Poland, jwilk@tu.kielce.pl

resulting from acoustic waves, which are generated by a sound source. Especially low-frequency waves (bass) are considered as vibrations (oscillations) at sufficiently high sound levels that have extinguishing properties. Because of their length, such waves can reach difficult-to-access places, which is desirable. Since changes in air pressure affect flames with energy dependence on sound intensity, high-power sound sources are recommended [5] and [6]. While challenges such as extinguishing flames from a variety of sources using acoustic waves from high-power sound sources can be addressed by using waves with appropriately selected parameters, it was recognized that more research is needed, especially in the areas of using modulated and unmodulated waves, to discover as much as possible about the capabilities of this as yet unexplored flame extinguishing technique. This is important because waves of different frequencies and shapes, modulated and unmodulated, may be applied to extinguish (e.g., sine wave, sine wave modulated by a square waveform, sine wave modulated by a triangular waveform, etc.) as proven by recent research conducted in Poland. In practice, low-frequency modulated waves can be successfully used to extinguish flames, in addition to unmodulated waves [5] to [9]. The type and parameters of the generated acoustic waves translate into the extinguishing capabilities of the device. This is crucial because with the use of acoustic technology, flames of different materials, such as liquid and gaseous fuel, can be extinguished. From the point of view of extinguishing flames, the range and field of action of this technology are important. The extinguishing effects depend on the power delivered to the sound source and the components of the acoustic extinguisher (additional panels, screens, etc.) [9]. The level of sound pressure depends on the power delivered to the speaker. When modelling using regression functions, it is important to consider the linear increase in sound pressure recorded within a certain range. Thus, the expected values of the explanation variable can be determined in a limited range (modelling known from mathematical sciences may be applied for this purpose) [10] to [12]. The extinguishing effect depends on the frequency of the acoustic wave, which in turn affects the difference in power delivered to the sound source. For the above reasons, the influence of the frequency of the acoustic wave on the minimum electrical power delivered to the extinguisher, giving the extinguishing effect, was analysed.

Since research on this topic, particularly capabilities using sine waves and sine waves amplitude-modulated by rectangular waveforms remains limited, there was a need to fill the gap in this area. Given this knowledge gap, the objectives of the article are reflected and presented in its content. This article is divided into three main parts. The first describes the possibilities of using a smart sensor for flame detection, which can be successfully applied to acoustic technology. In turn, the second part includes and analyses the results of experimental attempts to extinguish flames with unmodulated and modulated waves (with amplitude modulation) using an acoustic extinguisher. In the last part, i.e., in the third part, future research of the smart environmentally friendly acoustic extinguisher, the many benefits of combining the two techniques, and some limitations of this technology (open problems) are pointed out.

1 METHODS

1.1 Theoretical Aspects

For the analysis of aspects of the use of artificial intelligence (AI) for flame detection, the literature review method, the comparative method, as well as some elements of the system analysis and individual cases were applied.

Similar to acoustic waves, artificial intelligence has many applications. It can be used to detect a variety of activities in large areas, such as airports, shopping malls, and other public places, as well as forests, industrial plants, etc. AI-based detection techniques may also be applied to detect a wide range of dangerous events (examples can be gas leaks and water leaks). AI-based systems can be used to detect and respond to potential threats in real time, allowing quick response and mitigation of any potential threats. These systems may monitor and analyse information from various outlets, such as cameras, to detect unusual occurrences, for example, based on pixel colour, and in the event of a positive fire or smoke detection, immediately notify the fire protection services. An advantage of AI-based detection systems is their ability to learn and adapt over time. In practice, protecting people and the targeted management for this purpose is a key issue [13] and [14]. By analysing data from past events, these systems can improve their accuracy and identify patterns that may not be immediately apparent to people. The use of artificial intelligence has allowed people to be removed from the equation of data processing, which can be demonstrated in many applications and also applied in acoustics [15] to [18]. This may lead to more effective prevention and better response times in emergency and crisis situations [13] and [19]. For example, artificial

intelligence can be applied to detect and alert in the event of a fire, particularly in open outdoor spaces. AI-based flame detection systems offer a range of benefits beyond their ability to operate in open spaces. For example, they can provide more accurate and reliable detection than traditional sensors, reducing the risk of false alarms and ensuring that potential fires are identified as quickly as possible. Conventional smoke and temperature sensors are usually installed indoors and are vulnerable to external factors, resulting in a decrease in their effectiveness when used in a large area. This leads to the continued development of detection methods that use artificial intelligence. The smart module using deep neural networks can also be applied to monitor the environment and detect changes in temperature, smoke, or other indicators of potential fire. If any of these indicators are detected, the system may alert the relevant people or authorities, who can then take the necessary steps to prevent a fire from occurring and extinguish it. This module may identify the source of the flames and provide information to the authorities about the location of the fire and its size using, e.g., global navigation satellite systems (GNSS) coordinates. Thus, it becomes possible to capture information in an open landscape **[20]** to **[23]**. For the transmission of information, in addition to terrestrial technologies, satellite communications can be applied **[24]** to **[29]**. Furthermore, AI-based flame detection systems may also be integrated with other indoor systems, such as sprinklers or ventilation systems, to provide a complete fire safety solution.

In practice, a subset of artificial intelligence is machine learning. The use of a subdiscipline, in which the learning process is carried out unsupervised, provides a high-tech alternative to classical temperature or smoke sensors for flame detection. This is deep learning. It can be used to detect flames in a variety of ways, such as using recurrent neural networks (RNNs) to detect temporal patterns in video data and using convolutional neural networks (CNNs) to detect patterns in images. Deep learning may be applied to flame presence detection by analysing the colour and other characteristics of the flame (e.g., to identify the shape and size of the flame), as well as to smoke presence detection by analysing the colour, shape, and size of smoke particles in the environment **[30]** to **[33]**. The selected properties of the flame detection method are included in Table 1 for illustration purposes **[34]**.

Modern flame detection systems based on computer vision and acoustic wave-based extinguishing techniques can work in tandem, automatically initiating extinguishing once a flame is detected, thus minimizing the risk to human life. However, in the event of a false alarm, no significant damage occurs, unlike traditional chemical extinguishing agents. Acoustic waves do not leave any tough stains or damage equipment, making them a non-invasive alternative. Additionally, acoustic technology can effectively extinguish fires in environments full of obstacles, which are characterized by their properties **[35]** to **[37]**. With the use of machine learning, it becomes possible to classify, inter alia, fuel type, flame size, frequency, and extinction or non-extinction status. Sample figures are provided in the article **[36]**.

Table 1. *Properties applied to the flame detection method*

No.	Some examples of the considered properties
1	Color
2	Texture
3	Flicker
4	Shape
5	Dynamics

In practice, an acoustic extinguisher requires only a power source, such as a battery or mains, to effectively extinguish flames. It is particularly effective in extinguishing firebreaks and may be used to extinguish flames caused by substances that are difficult to extinguish using traditional fire protection methods **[9]**, **[38]**, and **[39]**. Information on the state of the art in acoustic flame extinguishing, including the frequency ranges, is presented, inter alia, in **[39]**. This is important because the goal is to find new composites that can be extinguished using acoustic technology. There is some research in nanotechnology, design, and environmentally friendly energy sources around the world **[40]** to **[48]**.

The state of the art in the field of intelligent sensor flame detection capabilities includes information on modern camera-based fire detection techniques (as an aspect of fire management) and the effectiveness of such methods **[7]** to **[9]**, and **[49]** to **[53]**. The smart module that is dedicated for flame detection in the acoustic extinguisher in the Polish-Bulgarian cooperation is included in Fig. 1 **[7]**, **[49]**, **[51]**, and **[53]**.

It uses deep neural networks. It becomes possible to equip an extinguisher with such a module so that an automatically activated extinguisher would reduce the risk of damage from the occurrence and spread of flames. Thus far, the work has considered two models dedicated to embedded systems: mask regions with convolutional neural networks (R-CNN) and single shot detector (SSD) MobileNet. Detection accuracy

exceeds 96 % with the use of the region-based convolutional neural network mask [6] to [9], [51], and [53]. For the second model, i.e., SSD MobileNet, the detection accuracy is equal to 79 % [49] to [53]. In practice, the choice of the applied model is a compromise between the speed of recognition and its accuracy.

Fig. 1. *Flame detection module with the use of deep neural networks*

1.2 Experimental Aspects

In practice, acoustic waves are an effective way to extinguish flames of different sizes and intensities from liquids and gases. They can also be used to control flames originating from different materials. However, there are only a few papers closely related to the study of the possibility of extinguishing flames using acoustic waves, especially when gaseous fuel was used [7] and [54]. Acoustic waves may also be applied to extinguish flames, the source of which is liquid fuel. In this case, extinguishing is observed when the flame is moved away to a distance at which the fuel supply is cut off due to evaporation [9] and [55]. In addition to vaporizing the fuel, extinguishing is also influenced by spreading the flames over the largest possible area, resulting in a temperature change. Therefore, there was a need to fill the gap in this area.

An experimental method was applied to study the extinguishing capabilities in practice. The analysis of selected cases made it possible to evaluate the flame-extinguishing capabilities under specific conditions. The aim of the designers was to build an extinguisher that emits an acoustic beam in the direction of the flame source. The extinguisher has a closed one-sided waveguide of rectangular cross-section with a length of 4.28 m (its narrowing towards the outlet is noticeable). The principle of the waveguide is based on the amplification of the acoustic wave due to the occurrence of the resonance phenomenon. Standing waves appear at the resonant frequency. In practice, the minimum waveguide length at which the phenomenon of acoustic resonance is observed depends on the frequency and is twice as small for a closed, one-sided waveguide compared to an open waveguide [5]. Therefore, taking into account practical considerations (significant waveguide length for low-frequency acoustic waves), it was decided to build a fire extinguisher with a closed one-sided waveguide for acoustic waves with frequencies oscillating around 20 Hz. A test stand, presented in Fig. 2a, was built for this purpose. In addition to unmodulated waves, modulated waves may be applied for flame extinguishing.

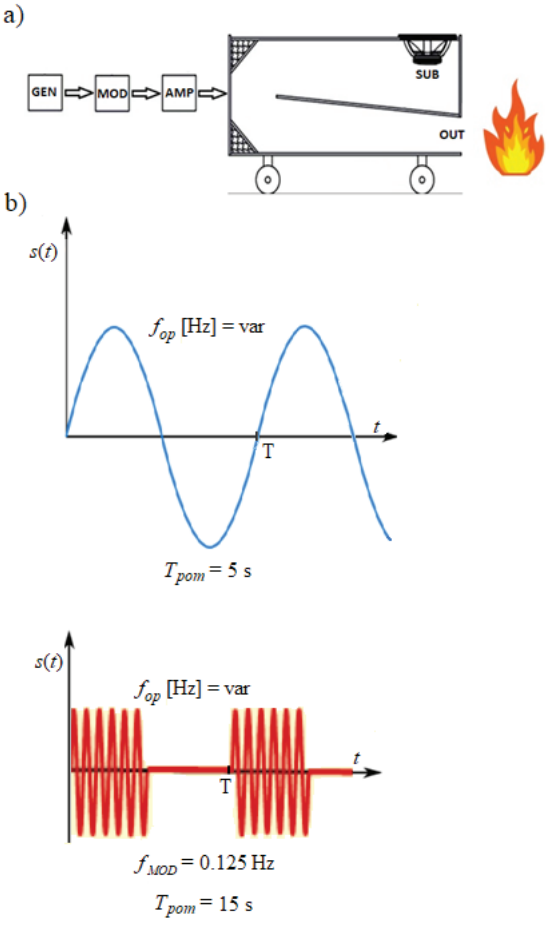

Fig. 2. *a) Components of the acoustic extinguisher: generator (GEN), modulator (MOD), amplifier (AMP), subwoofer, (SUB), outlet (OUT); b) Illustrative figures of the generated signals s(t) in the time domain t for unmodulated and modulated waveforms, respectively*

Analysing the principle of the loudspeaker, when the diaphragm swings out of its equilibrium position, there is a movement of air molecules that resist the moving diaphragm of the loudspeaker. As a result of the density of the particles, the pressure increases. At the same time, the accelerated particles transfer

energy to neighbouring particles, which sets them in motion. Acoustic waves are emitted by both the front and back of the diaphragm of the sound source (the phases of the emitted waves are shifted 180 degrees). After the speaker's diaphragm reaches full tilt, it begins to vibrate in the opposite direction, creating an area of vacuum, which in turn results in the particles being turned back. To ensure that the waves emitted by the front and rear parts of the speaker diaphragm do not cancel each other, an acoustic baffle is applied. In this article, the sine wave and the sinusoidal wave amplitude modulated by a square waveform were used in these experimental attempts (see Fig. 2b). The photos of the experimental stand are presented in Fig. 3.

Fig. 3. *A test stand for the acoustic extinguisher (actual photos)*

In practice, it is easier to extinguish flames in a place with limited oxygen (indoor spaces) than in an outdoor area. However, for the purpose of this research, measurements were taken outdoors under similar conditions, using both modulated and unmodulated waves. This paper presents the results of experiments to extinguish flames coming from a candle (a point source of flames with a flame height of about 2 cm) placed at a distance of 0.5 m behind the extinguisher outlet. During the measurements, the background sound level was about 65 dB. The measurement time (T_{pom}) ranged from 5 seconds to 15 seconds (for unmodulated and modulated waveforms, respectively). A high-power acoustic extinguisher was applied for extinguishing, the sound source of which was a woofer with a nominal power of 1,700 Watts. Because of the properties of low-frequency waves, they reach hard-to-reach places, which is a definite advantage when using acoustic technology to extinguish flames from solids, liquids, and gases. For design reasons (the length of the waveguide), the extinguisher has a rectangular cross-section and a waveguide with a closed end. It is equipped with a Rigol DG4102 generator, a Proel HPX2800 power amplifier, and a B&C 21DS115 speaker. One component of the extinguisher is a modulator, and the other is analogue meters for electrical quantities (voltage, current, and power). All acoustic measurements were made using a dedicated SVAN meter (SVAN 979 model), which is a digital analyser and sound level meter at a distance of 0.5 m from the outlet of the acoustic extinguisher (where the point source of flames was located). To identify the operating frequency of the characteristics of the acoustic extinguisher, the sound pressure characteristics were determined as a function of frequency at a distance of 1 m from the device outlet. For frequencies between 17 Hz and 18 Hz, the minimum impedance level of the acoustic extinguisher of 11.4 Ω was recorded (a frequency of 17.25 Hz was called the operating frequency). A local maximum sound pressure is observed at this frequency. Therefore, for the purposes of the experimental attempts carried out, the working frequencies (f_{op} = var) were chosen to show the extinguishing capabilities of the device for four frequencies close to the working frequency (14 Hz, 16 Hz, 17 Hz, and 20 Hz). The lower frequency was set at 14 Hz (this is the minimum frequency at which it was possible to carry out successful flame extinguishing attempts, taking into account the technical capabilities of the extinguisher, especially the vibration of the speaker diaphragm). The highest frequency, i.e., 20 Hz, was chosen as the upper frequency of work, for which it was possible to acquire data for both unmodulated and modulated waves (a set of combined measurements). It should be noted that the choice of frequency was due to the design limitations of the sound source, including its mechanical load. The results of the experimental measurements are presented and discussed in the next section.

2 RESULTS AND DISCUSSION

2.1 A Case of an Unmodulated Wave

First, tests were conducted for an unmodulated (i.e., sinusoidal) wave and then for a sinusoidal wave amplitude modulated by a square waveform (for f_{MOD} = 0.125 Hz).

Table 2 provides information on the sound pressure level (SPL) required to extinguish flames depending on the operating frequency of the acoustic extinguisher for a sinusoidal wave. The acoustic measurements included in the article are for instantaneous root mean square (RMS) values of SPL according to the IEC 61672 standard (Class 1).

Table 2. *Overview table of the sound pressure values SPL [dB] necessary to extinguish flames as a function of frequency f [Hz] for a sinusoidal wave*

f [Hz]	SPL [dB]	f [Hz]	SPL [dB]
14	116.2	17	122.8
16	121.4	20	125.2

Analysing the data in Table 2, it can be seen that to extinguish flames, for the assumed conditions, the sound pressure level at the flame extinguishing site should be in the approximate range of 115 dB to 125 dB, depending on the given frequency. It should be mentioned that, with the use of all frequencies analysed, extinguishing flames with the acoustic technique proved to be effective. Fig. 4 provides a diagram of the influence of frequencies in the 14 Hz to 20 Hz range on the minimum sound pressure level at which complete flame extinguishment was observed. On the basis of the data obtained, it can be seen that the minimum sound pressure level at which complete flame extinguishment was noticed varies depending on the frequency of the acoustic wave. For a frequency of 14 Hz, it was equal to 116.2 dB. In turn, for the highest of the analysed frequency close to the operating frequency, i.e., 20 Hz, it was equal to 125.2 dB (the difference in sound pressure for the extreme values of the frequency was less than 10 dB, that is, 9 dB).

In Fig. 5, is a diagram showing the influence of frequency in the 14 Hz to 20 Hz range on the minimum electrical power that had to be delivered to the sound source of the extinguisher to completely extinguish flames for a sinusoidal wave.

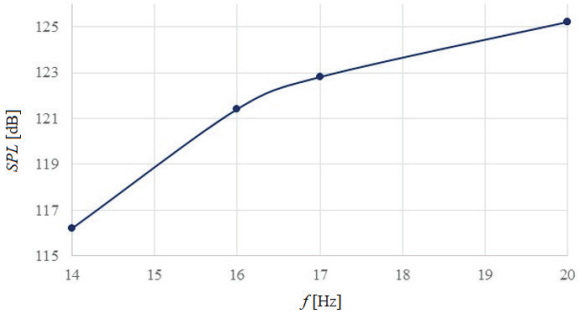

Fig. 4. *The minimum value of SPL [dB] required to extinguish flames depending on the frequency f [Hz] for a sinusoidal wave*

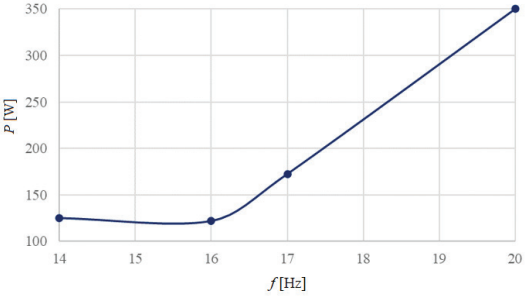

Fig. 5. *Minimum value of electrical power P [W] required to extinguish flames depending on the frequency f [Hz] for a sinusoidal wave*

As can be observed from the data obtained, in the frequency range analysed, there is a noticeable tendency for the power to increase with an increase in the frequency of the acoustic wave. The maximum value of power that had to be delivered to the sound source to extinguish flames was equal to 350 Watts for a sine wave with a frequency of 20 Hz. However, it should be taken into account that a short-term change in atmospheric conditions (in particular, wind speed and direction) can affect the results obtained. Therefore, it is sometimes recommended to repeat the measurements.

2.2 A case of Modulated Wave

The results achieved for a modulated waveform (a case of a sinusoidal wave amplitude modulated by a square waveform) appear to be interesting when compared to an unmodulated wave. Table 3 provides information on the SPL required to extinguish flames depending on the operating frequency of the acoustic extinguisher for a sinusoidal wave amplitude modulated by a square waveform (f_{MOD} = 0.125 Hz).

Analysing the results obtained in Table 3, it can be noted that to extinguish flames, the sound pressure

level at the extinguishing site should be in the approximate range of 120 dB to 130 dB, depending on the adopted frequency (in the analysed cases, it turned out to be slightly higher with measured values for unmodulated waves). However, using all frequencies analysed, the extinguishing of flames with the acoustic technique with amplitude modulation (AM) technique was successful. This shows that the presented method can be applied successfully. It may have potential applications in the extinguishing of difficult-to-extinguish flames from burning materials with different properties. This is important because, as previously stated, low-frequency acoustic waves pass through both solids, liquids, and gases. Fig. 6 provides a diagram of the influence of frequencies in the 14 Hz to 20 Hz range on the minimum sound pressure level at which complete flame extinguishment was observed.

Table 3. *Overview table of the sound pressure values [dB] necessary to extinguish flames as a function of frequency [Hz] for a sinusoidal wave amplitude modulated by a square waveform*

f [Hz]	SPL [dB]	f [Hz]	SPL [dB]
14	122.6	17	124.4
16	124.2	20	126.5

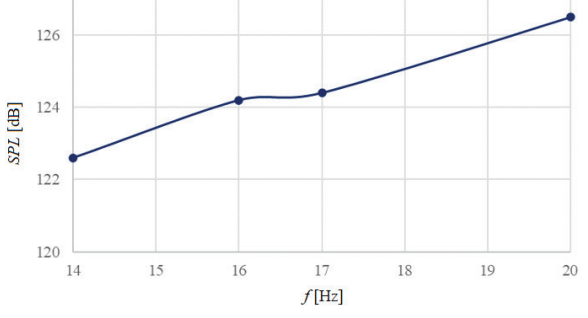

Fig. 6. *The minimum value of SPL [dB] required to extinguish flames depending on the frequency f [Hz] for a sinusoidal wave amplitude modulated by a square waveform*

On the basis of the data measured, it can be seen that the minimum sound pressure level at which complete flame extinguishment was noticed varies depending on the frequency of the acoustic wave. For a frequency of 14 Hz, it was equal to 122.6 dB. In turn, for the highest of the analysed frequency close to the operating frequency, i.e., 20 Hz, it was equal to 126.5 dB. This means that for the frequency range analysed, the difference in sound pressure for extreme frequency values was 3.9 dB. Below, in Fig. 7, is a diagram showing the influence of frequency in the 14 Hz to 20 Hz range on the minimum electrical power that had to be delivered to the extinguisher to completely extinguish flames for waves with the AM modulation technique.

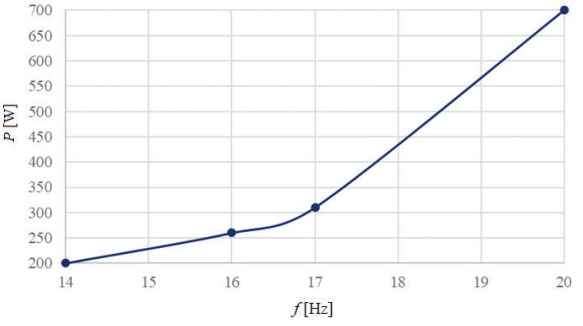

Fig. 7. *The minimum value of electrical power P [W] required to extinguish flames depending on the frequency f [Hz] for a sinusoidal wave amplitude modulated by a square waveform*

As can be seen from the data obtained, similar to Fig. 5, in the frequency range analysed, there is a noticeable tendency for the power to increase with an increase in the frequency of the acoustic wave. The maximum value of power that had to be delivered to the acoustic extinguisher sound source of the acoustic extinguisher to extinguish flames was equal to 700 Watts for a sinusoidal wave amplitude modulated by a square waveform (f_{MOD} = 0.125 Hz) for the highest of the analysed frequency, that is, 20 Hz. This means a twofold increase in the power required to extinguish flames in comparison with an unmodulated (sinusoidal) wave at the SPL of 126.5 dB because, for a sinusoidal wave, the effect of completely extinguishing flames was achieved for the electrical power of 350 Watts (the SPL was equal to 125.2 dB then). This means that moving away from the resonant optimum translates into an increase in the required power to extinguish flames (a rapid increase is noted, which affects the range of safe use of this technology).

Based on an analysis of the data in Figs. 4 to 7, it can be observed that the operating point at or close to the operating frequency of the acoustic extinguisher provides optimal conditions for extinguishing flames with the acoustic technique. Since the diagrams for unmodulated waves (Figs. 4 and 5) as well as for modulated waves (Figs. 6 and 7) come from the same extinguishing attempts (measurements of the acoustic pressure at which complete flame extinguishment was observed and measurements of the electrical power that had to be delivered to the extinguisher to completely extinguish flames), one can see some similarity in the shape of these two characteristics.

3 FUTURE RESEARCH

In the future, in addition to continuing research on the effect of acoustic wave parameters on flame extinguishing, further research is planned in the direction of flame detection. This is due to the fact that the advantages of using acoustic technology may be exploited in combination with artificial intelligence **[56]** to **[59]**, which makes it possible to detect flames and then immediately extinguish them. Due to artificial intelligence, people can be excluded from the data processing chain, while detection and alarming in the case of flame detection can be realized with its help, for example, in an open space **[58]** and **[59]**. Any method that involves computer vision can replace traditional approaches relying on smoke or temperature detectors, which are installed mainly indoors. Additionally, they are susceptible to environmental factors and a significant decrease in their performance is observed when they are used in wide areas. This is reflected in the continuous development of detection techniques using artificial intelligence as an alternative to the classical approach. The benefit is that visible-light or infrared image sequences can be applied effectively to detect flames. The advantage is then a much higher level of intensity of fire pixels compared to other pixels **[56]**, **[57]**, and **[60]** to **[62]**.

In the future, it is planned to analyse the possibilities of flame detection using smart sensors and information on contemporary camera-based fire detection techniques. This step is the first component of fire management before extinguishing the flames, which is the second component of fire management. The performance of these types of methods can be evaluated and compared to other methods. The issue of the use of acoustic waves to extinguish flames may be put together with the use of artificial intelligence for flame detection and the benefit of the solution proposed by combining both techniques. It is possible to use low-cost intelligent sensors to protect humans from exposure to sound waves while extinguishing flames. In practice, the system may be activated automatically without human presence (no need for human involvement when extinguishing flames) **[7]** to **[9]**, **[34]**, and **[49]** to **[53]**. The plan for future work is to improve a prototype of the autonomous acoustic fire extinguisher that will be controlled by software and will use the same electronics to control the motors as the robotic platform (control electronics for motors may be applied in the final version of the smart acoustic extinguisher). Furthermore, the plan is to test several types of neural networks for flame detection and add additional components to enhance the suppression of flames using acoustic waves. The development of AI-powered fire detection systems may represent a significant step forward in fire safety technology. As these systems become more advanced and widely adopted, we can expect to see a reduction in response times for emergency services, tangible and intangible damage, and loss of life.

In practice, the impact of acoustic waves on human health is controversial, as long-term exposure to these waves can cause various adverse effects. The severity of these effects is determined by the frequency of the wave and the sound pressure level. Common side effects include fatigue, headaches, reduced concentration, mood swings, sleepiness, and vibroacoustic disease. It is assumed that a person should not be subjected to infrasound and sound pressure levels that exceed the pain threshold of the human ear (if the sound pressure level exceeds 110 dB, it can cause many complaints **[2]**, **[49]**, and **[63]** to **[65]**). As long as the person is not present during the firefighting process, there is no risk to health. This is particularly important because, as indicated above, low-frequency acoustic waves, while effective in extinguishing fires, can cause some ailments. Although the use of acoustic waves for fire protection has its advantages, careful consideration must be taken to ensure the safety and well-being of people potentially exposed to these waves. On the other hand, the benefit of combining both techniques in an environmentally friendly acoustic extinguisher, including a smart sensor, is that there is no need to involve humans in the extinguishing of flames (no one has to participate in the firefighting action). The system uses acoustic waves that can be activated immediately when a fire is detected. In this way, it is possible to increase the chances that the flames will be detected and extinguished very quickly. It is well known that time is of the essence in fighting fires because the longer a fire lasts, the more it threatens the lives of people and animals and causes more damage, environmental degradation, and financial losses. In addition, this technology may find application when access to classical (i.e., chemical) fire protection measures is limited, or flames are difficult to extinguish using known methods. Furthermore, more research is needed to investigate the potential consequences of low-frequency acoustic waves and high sound pressure on building structures and room equipment (e.g., windows). This is especially relevant for waves of very low frequency and very high sound pressure levels.

4 CONCLUSIONS

As shown in the article, some undesired signals (due to sound sensation) treated in terms of noise can be useful in some applications. An example is the use of acoustic waves to extinguish flames (a scientific novelty). Acoustic extinguishers, in contrast to classic fire extinguishers, are not subject to periodic tank tests. Furthermore, fire extinguishing with their use is characterized by unlimited operation time (the extinguishing agents are sound waves, which do not exhaust). To work, acoustic extinguishers should be powered by a battery or mains. Therefore, this technique is characterized by lower extinguishing costs than traditional extinguishers, which is its undoubted advantage. Another advantage is the lack of environmental degradation and equipment destruction, as is often the case when using conventional fire protection (acoustic waves do not leave stains difficult to remove) **[8]**. Currently, this technology may be applied to extinguish Class B and C fires (the second aspect of fire management) when liquids or gases are burning. On the basis of the results obtained, it can be seen that the sound pressure at which the phenomenon of complete flame extinguishment was observed oscillates between 115 dB and 130 dB. Pressure depends on the electrical power that must be supplied to the extinguisher to extinguish flames (the power delivered to the sound source of the extinguisher ranged from 125 Watts to 700 Watts). As the results show, an acoustic extinguisher generating both unmodulated waves and modulated waves with an experimentally determined operating frequency or a frequency close to the operating frequency can be successfully used to extinguish flames, which can be applied, among other things, to extinguish flames originating from materials that are difficult to extinguish with currently known methods (research is being carried out around the world to find new fire-resistant composites). In addition, the possible change of parameters makes it versatile (it is possible to adapt its parameters to extinguish flames from a specific type of substance). However, it should be emphasized that this is a relatively new way of extinguishing flames (thus far, fully unexplored), so further research is needed to thoroughly understand the extinguishing capabilities of acoustic waves. On the other hand, its use in the presence of humans involves risks, as the influence of acoustic waves on human health is a controversial issue. This is because human beings in acoustic fields (especially long-term exposure) may cause some undesirable diseases. The dimension of the effects for people depends on the frequency of the wave and the sound pressure level. This is important because the pressure required to extinguish flames oscillates and even exceeds the pain threshold of the human ear. As is well known, time is of the essence when fighting fires because the longer a fire lasts, the more it threatens human and animal lives and causes more damage and financial losses. Fortunately, the acoustic system may be equipped with an intelligent module so that flame extinguishing can begin without unnecessary time delay when the flames are detected by a smart sensor and without the need for human presence, as is the case with the use of classic fire extinguishers. Taking into account future research on the smart, environmentally friendly acoustic extinguisher, this article also addresses fire detection (the other aspect of fire management), with a focus on the use of deep learning as a modern alternative to traditional temperature or smoke sensors. In practice, combining these techniques could offer significant benefits for environmental (fire) management and environmental technology (beneficial impact on the environment) **[56]**, **[57]**, **[61]** and **[66]**. Therefore, the advantages of employing acoustic technology can be maximized by integrating it with artificial intelligence, enabling the detection of flames and their prompt extinguishment. This allows us to extinguish flames as soon as they appear (firebreaks) and prevent large fires from spreading. This feature may effectively reduce material losses and increase safety, which is the antithesis of a threat to life. Ultimately, this technique is expected to be applied in industrial plants and production halls. Acoustic extinguishers can be installed in the walls and foundations of rooms, which reveals new possibilities for the application of this technique in the future. Engineering simulation may be used for measurements, including the use of the boundary element method **[67]** and **[68]**, as well as image processing, motion detection and convolutional neural networks **[69]** to **[72]**.

Fortunately, the benefit based on the solution presented by combining both techniques is then that there is no need for human intervention when extinguishing flames. No one has to participate in the firefighting action (the system that uses acoustic waves can be immediately activated when a firebreak is detected). Then, data about the fire detection may be rapidly transmitted to the relevant authorities in the form of a photo and comprehensive information primarily containing the location of the fire detection (including, e.g., the GNSS coordinates). Moreover, the transmitted information can include, among others, details such as the date when the photo was taken, the names of visible and infrared spectrum

images (if necessary), and the corresponding ground truth image (if applicable). A factor in favour of this is that image sequences in the visible or infrared bands can be used successfully for flame detection, as stated in the article.

5 ACKNOWLEDGMENTS

The work has been carried out under the research project InIn+ (no. 3/2017) funded by the Ministry of Science and Higher Education. The authors thank the Kielce University of Technology, the administration of the Universidad de Sevilla, the company of Ryszard Putyra "Ekohigiena Aparatura Ryszard Putyra Sp.J." Środa Śląska (Poland) and "Przedsiębiorstwo Handlowo-Techniczne SUPON Sp. z o.o." Kielce (Poland) for support in this investigation.

6 REFERENCES

[1] Jędrusyna, A., Noga, A. (2012). The use of high power infrasound wave generator for cleaning sediment off heating surfaces in power boilers (Wykorzystanie generatora fal infradźwiękowych dużej mocy do oczyszczania z osadów powierzchni grzewczych kotłów energetycznych). *Industrial Furnaces and Boilers (Piece Przemyslowe & Kotly)*, vol. 11-12, p. 30-37. (in Polish)

[2] Noga, A. (2014). Noga, A. (2014). Review of the state of the art in infrasound technology and the possibility of using acoustic waves to clean power equipment. *Energy Notebooks*, vol. 1, p. 225-234. (in Polish)

[3] Różyło, P. (2023). Failure analysis of beam composite elements subjected to three-point bending using advanced numerical damage models. *Acta Mechanica et Automatica*, vol. 17, no. 1, p. 133-144, **DOI:10.2478/ama-2023-0015**.

[4] Pronobis, M. (2002). Modernization of power boilers. Wydawnictwo Naukowo-Techniczne, Warsaw. (in Polish)

[5] Stawczyk, P., Wilk-Jakubowski, J. (2021). Non-invasive attempts to extinguish flames with the use of high-power acoustic extinguisher. *Open Engineering*, vol. 11, no. 1, p. 349-355, **DOI:10.1515/eng-2021-0037**.

[6] Wilk-Jakubowski, J. (2021). Analysis of flame suppression capabilities using low-frequency acoustic waves and frequency sweeping techniques. *Symmetry*, vol. 13, no. 7, 1299, **DOI:10.3390/sym13071299**.

[7] Wilk-Jakubowski, J., Stawczyk, P., Ivanov, S., Stankov, S. (2022). The using of deep neural networks and natural mechanisms of acoustic waves propagation for extinguishing flames. *International Journal of Computational Vision and Robotics*, vol. 12, no. 2, p. 101-119, **DOI:10.1504/IJCVR.2021.10037050**.

[8] Wilk-Jakubowski, J. (2023). Experimental investigation of amplitude-modulated waves for flame extinguishing: A case of acoustic environmentally friendly technology. *Environmental and Climate Technologies*, vol. 27, no. 1, p. 627-638, **DOI:10.2478/rtuect-2023-0046**.

[9] Wilk-Jakubowski, J.L, Loboichenko, V., Wilk-Jakubowski, G., Yılmaz-Atay, H., Harabin, R., Ciosmak, J., Ivanov, S., Stankov, S. (2023). Acoustic firefighting method on the basis of European research: a review. *Akustika*, vol. 46, no. 46, p. 31-45, **DOI:10.36336/akustika20234631**.

[10] Marek, M. (2013). Wykorzystanie ekonometrycznego modelu klasycznej funkcji regreThe use of the econometric model of the classical linear regression function to conduct quantitative analyses in economic sciences. *The role of computer science in economic and social sciences. Innovations and interdisciplinary implications*. Wydawnictwo WSH, Kielce. (in Polish)

[11] Marek, M. (2021). Aspects of road safety: A case of education by research - analysis of parameters affecting accident. *CEUR Workshop Proceedings*, 3061, p. 64-75.

[12] Marek, M. (2022). Bayesian regression model estimation: A road safety aspect. *Lecture Notes in Networks and Systems*, vol. 393, no. 5, p. 163-175, **DOI:10.1007/978-3-030-94191-8_13**.

[13] Wilk-Jakubowski, G., Harabin, R., Ivanov, S. (2022). Robotics in crisis management: A review. *Technology in Society*, vol. 68, 101935, **DOI:10.1016/j.techsoc.2022.101935**.

[14] Wilk-Jakubowski, G., Harabin, R., Skoczek, T., Wilk-Jakubowski, J. (2022). Preparation of the police in the field of counter-terrorism in opinions of the independent counter-terrorist sub-division of the regional police headquarters in Cracow. *Slovak Journal of Political Sciences*, vol. 22, no. 2, p. 174-208, **DOI:10.34135/sjps.220202**.

[15] Oktovani, T., Prayoga Kasmo, A.B. (2023). Analysis of Factors Influencing Intention to Purchase "Portable Fire Extinguisher" for Residential House in DKI Jakarta. *Dinasti International Journal of Digital Business Management*, vol. 4, no. 5, p. 994-1008, **DOI:10.31933/dijdbm.v4i5.2018**.

[16] Sharma, D., Sharma, B., Mantri, A., Goyal, N., Singla, N. (2022). Dhwani fire: Aerial system for extinguishing fire. *ECS Transactions*, vol. 107, no. 1, p. 10295-10301, **DOI:10.1149/10701.10295ecst**.

[17] Azeta, J., Ayoade, I., Nwakanma, C., Akande, T. (2023). Implementing a prototype autonomous fire detecting and firefighting robot. *Preprints*, **DOI:10.20944/preprints202305.2010.v1**.

[18] Płaza, M., Trusz, S., Kęczkowska, J., Boksa, E., Sadowski, S., Koruba, Z. (2022). Machine learning algorithms for detection and classifications of emotions in contact center applications. *Sensors*, vol. 22, no. 14, 5311, **DOI:10.3390/s22145311**.

[19] Aymerich-Franch, L., Ferrer, I. (2022). Liaison, safeguard, and well-being: Analyzing the role of social robots during the COVID-19 pandemic. *Technology in Society*, vol. 70, 101993, **DOI:10.1016/j.techsoc.2022.101993**.

[20] Levterov, A., Statyvka, E. (2022). Determination of parameters of an acoustic device for rescuers' equipment. *Problems of Emergency Situations*, vol. 1, p. 280-295, **DOI:10.52363/2524-0226-2022-36-21**. (in Ukrainian)

[21] Azarenko, O., Honcharenko, Y., Divizinyuk, M., Mirnenko, V., Strilets, V., Wilk-Jakubowski, J.L. (2022). Influence of anthropogenic factors on the solution of applied problems

of recording language information in the open area. *Social Development and Security*, vol. 12, no. 3, p. 135-143, **DOI:10.33445/sds.2022.12.3.12**.

[22] Gelfert, S. (2022). Novel mobile robot concept for human detection in fire smoke indoor environments using deep learning. *8th International Conference on Robotics and Artificial Intelligence*, **DOI:10.1145/3573910.3573913**.

[23] Azarenko, O., Honcharenko, Y., Divizinyuk, M., Mirnenko, V., Strilets, V., Wilk-Jakubowski, J.L. (2022). The influence of air environment properties on the solution of applied problems of capturing speech information in the open terrain. *Social Development and Security*, vol. 12, no. 2, p. 64-77, **DOI:10.33445/sds.2022.12.2.6**.

[24] Wilk-Jakubowski, J. (2021). A review on information systems engineering using VSAT networks and their development directions. *Yugoslav Journal of Operations Research*, vol. 31, no. 3, p. 409-428, **DOI:10.2298/YJOR200215015W**.

[25] Ma, Y., Jiang, H., Li, J., Yu, H., Li, C., Zhang, D. (2021). Design of marine satellite communication system based on VSAT technique. *International Conference on Computer, Internet of Things and Control Engineering*, p. 126-129, **DOI:10.1109/CITCE54390.2021.00031**.

[26] Wilk-Jakubowski, J. (2018). Total signal degradation of polish 26-50 GHz satellite systems due to rain. *Polish Journal of Environmental Studies*, vol. 27, no. 1, p. 397-402, **DOI:10.15244/pjoes/75179**.

[27] Šerić, L., Stipanicev, D., Krstinić, D. (2018). ML/AI in intelligent forest fire observer network. *International Conference on Management of Manufacturing Systems*, **DOI:10.4108/eai.6-11-2018.2279681**.

[28] Wilk-Jakubowski, J. (2018). Predicting satellite system signal degradation due to rain in the frequency range of 1 to 25 GHz. *Polish Journal of Environmental Studies*, vol. 27, no. 1, p. 391-396, **DOI:10.15244/pjoes/73906**.

[29] Wilk-Jakubowski, J. (2018). Measuring rain rates exceeding the polish average by 0.01%. *Polish Journal of Environmental Studies*, vol. 27, no. 1, p. 383-390, **DOI:10.15244/pjoes/73907**.

[30] Yamagishi, H., Yamaguchi, J. (2000). A contour fluctuation data processing method for fire flame detection using a color camera. *26th Annual Conference of the IEEE Industrial Electronics Society*, vol. 2, p. 824-829, **DOI:10.1109/IECON.2000.972229**.

[31] Levterov, A., Statyvka, Y. (2023). Influence of smoke density on the parameters of the acoustic device of rescuer equipment. *Problems of Emergency Situations*, vol. 1, p. 95-106, **DOI:10.52363/2524-0226-2023-37-7**. (in Ukrainian)

[32] Liu, Z.G., Yang, Y., Ji, X.H. (2016). Flame detection algorithm based on a saliency detection technique and the uniform local binary pattern in the YCbCr color space. *Signal, Image and Video Processing*, vol. 10, p. 277-284, **DOI:10.1007/s11760-014-0738-0**.

[33] Chen, X., Zhang, X., Zhang, Q. (2014). Fire alarm using multi-rules detection and texture features classification in video surveillance. *7th International Conference on Intelligent Computation Technology and Automation*, **DOI:10.1109/ICICTA.2014.71**.

[34] Loboichenko, V., Wilk-Jakubowski, J., Wilk-Jakubowski, G., Harabin, R., Shevchenko, R., Strelets, V., Levterov, A., Soshinskiy, A., Tregub, N., Antoshkin, O. (2022). The use of acoustic effects for the prevention and elimination of fires as an element of modern environmental technologies. *Environmental and Climate Technologies*, vol. 26, no. 1, p. 319-330, **DOI:10.2478/rtuect-2022-0024**.

[35] Tiwari, R.G., Agarwal, A.K., Jindal, R.K., Singh, A. (2022). Experimental evaluation of boosting algorithms for fuel flame extinguishment with acoustic wave. *International Conference on Innovation and Intelligence for Informatics, Computing, and Technologies*, p. 413-418, **DOI:10.1109/3ICT56508.2022.9990779**.

[36] Taspinar, Y.S., Koklu, M., Altin, M. (2021). Classification of flame extinction based on acoustic oscillations using artificial intelligence methods. *Case Studies in Thermal Engineering*, vol. 28, 101561, **DOI:10.1016/j.csite.2021.101561**.

[37] Yi, E.Y., Lee, E., Bae, M.J. (2017). A study on the directionality of sound fire extinguisher in electric fire. *Convergence Research Letter of Multimedia Services Convergent with Art, Humanities, and Sociology*, vol. 3, no. 4, p. 1449-1452.

[38] Vovchuk, T.S., Wilk-Jakubowski, J.L., Telelim, V.M., Loboichenko, V.M., Shevchenko, R.I., Shevchenko, O.S., Tregub, N.S. (2021). Investigation of the use of the acoustic effect in extinguishing fires of oil and petroleum products. *SOCAR Proceedings*, no. 2, p. 24-31, **DOI:10.5510/OGP2021SI200602**.

[39] Yılmaz-Atay, H., Wilk-Jakubowski, J.L. (2022). A review of environmentally friendly approaches in fire extinguishing: from chemical sciences to innovations in electrical engineering. *Polymers*, vol. 14, no. 6, 1224, **DOI:10.3390/polym14061224**.

[40] Rabajczyk, A., Zielecka, M., Gniazdowska, J. (2022). Application of nanotechnology in extinguishing agents. *Materials*, vol. 15, no. 24, 8876, **DOI:10.3390/ma15248876**.

[41] Strelets, V.V., Loboichenko, V.M., Leonova, N.A., Shevchenko, R.I., Strelets, V.M., Pruskyi, A.V., Avramenko, O.V. (2021). Comparative assessment of environmental parameters of foaming agents based on synthetic hydrocarbon used for extinguishing the fires of oil and petroleum products. *SOCAR Proceedings*, no. 2, p. 1-10, **DOI:10.5510/OGP2021SI200537**.

[42] Li, Q., Li, Z., Chen, R., Zhang, Z., Ge, H., Zhou, X., Pan, R. (2021). Numerical study on effects of pipeline geometric parameters on release characteristics of gas extinguishing agent. *Symmetry*, vol. 13, no. 10, 1766, **DOI:10.3390/sym13122440**.

[43] Szcześniak, A., Szcześniak, Z. (2021). Algorithmic method for the design of sequential circuits with the use of logic elements. *Applied Sciences*, vol. 11, no. 23, 11100, **DOI:10.3390/app112311100**.

[44] Zobenko, O., Loboichenko, V., Lutsenko, Y., Pidhornyy, M., Zemlianskyi, O., Hrushovinchuk, O., Blyashenko, O, Servatyuk, V. (2023). Study of the features of the protection of energy system elements caused by excessive local heating. *Water and Energy International*, vol. 65, no. 10, p. 34-40.

[45] Uddin, Z., Qamar, A., Alharbi, A.G., Orakzai, F.A., Ahmad, A. (2022). Detection of multiple drones in a time-varying scenario using acoustic signals. *Sustainability*, vol. 14, no. 7, 4041, **DOI:10.3390/su14074041**.

[46] Viriyawattana, N., Sinworn, S. (2023). Performance improvement of the dry chemical-based fire extinguishers using nanocalcium silicate synthesised from biowaste. *Journal of Fire Sciences*, vol. 41, no. 3, p. 73-88, **DOI:10.1177/07349041231168**.

[47] Chomać-Pierzecka, E., Gąsiński, H., Rogozińska-Mitrut, J., Soboń, D., Zupok, S. (2023). Review of selected aspects of wind energy market development in Poland and Lithuania in the face of current challenges. *Energies*, vol. 16, no. 1, 473, **DOI:10.3390/en16010473**.

[48] Chomać-Pierzecka, E., Sobczak, A., Urbańczyk, E. (2022). RES Market development and public awareness of the economic and environmental dimension of the energy transformation in Poland and Lithuania. *Energies*, vol. 15, no. 15, 5461, **DOI:10.3390/en15155461**.

[49] Ivanov, S., Stankov, S., Wilk-Jakubowski, J., Stawczyk, P. (2021). The using of deep neural networks and acoustic waves modulated by triangular waveform for extinguishing fires. *International Workshop on New Approaches for Multidimensional Signal Processing*, vol. 216, p. 207-218, **DOI:10.1007/978-981-33-4676-5_16**.

[50] Ivanov, S., Stankov, S. (2022). The artificial intelligence platform with the use of DNN to detect flames: A case of acoustic extinguisher. *Lecture Notes in Networks and Systems*, vol. 371, p. 24-34, **DOI:10.1007/978-3-030-93247-3_3**.

[51] Wilk-Jakubowski, J., Stawczyk, P., Ivanov, S., Stankov, S. (2022). High-power acoustic fire extinguisher with artificial intelligence platform. *International Journal of Computational Vision and Robotics*, vol. 12, no. 3, p. 236-249, **DOI:10.1504/IJCVR.2021.10039861**.

[52] Ivanov, S., Stankov, S. (2021). Acoustic extinguishing of flames detected by deep neural networks in embedded systems. The International Archives of the Photogrammetry, Remote Sensing and Spatial Information Sciences, vol. XLVI-4/W5-p. 307-312, **DOI:10.5194/isprs-archives-XLVI-4-W5-2021-307-2021**.

[53] Wilk-Jakubowski, J., Stawczyk, P., Ivanov, S., Stankov, S. (2022). Control of acoustic extinguisher with deep neural networks for fire detection. *Elektronika ir Elektrotechnika*, vol. 28, no. 1, p. 52-59, **DOI:10.5755/j02.eie.24744**.

[54] Niegodajew, P., Łukasiak, K., Radomiak, H., Musiał, D., Zajemska, M., Poskart, A., Gruszka, K. (2018). Application of acoustic oscillations in quenching of gas burner flame. *Combustion and Flame*, vol. 194, p. 245-249, **DOI:10.1016/j.combustflame.2018.05.007**.

[55] McKinney, D.J., Dunn-Rankin, D. (2007). Acoustically driven extinction in a droplet stream flame. *Combustion Science and Technology*, vol. 161, p. 27-48, **DOI:10.1080/00102200008935810**.

[56] Foley, D., O'Reilly, R. (2018). An evaluation of convolutional neural network models for object detection in images on low-end devices. *CEUR Workshop Proceedings*, vol. 2259, p. 64-75.

[57] Chen, T., Wu, P., Chiou, Y. (2004). An early fire-detection method based on image processing. *International Conference on Image Processing*, vol. 3, p. 1707-1710, **DOI:10.1109/ICIP.2004.1421401**.

[58] Guo, L. (2023). An integrated design method of robot intelligent joints based on artificial intelligence. *Proceedings of SPIE - the International Society for Optical Engineering*, vol. 12604, 1260448, **DOI:10.1117/12.2674672**.

[59] Natividad, L.R.Q. (2021). Initial response intelligent fire extinguisher robot: A prototype. *Journal of Engineering Science and Technology*, vol. 17, p. 138-146.

[60] Kong, S.G., Jin, D., Li, S., Kim, H. (2016). Fast fire flame detection in surveillance video using logistic regression and temporal smoothing. *Fire Safety Journal*, vol. 79, p. 37-43, **DOI:10.1016/j.firesaf.2015.11.015**.

[61] Janků, P., Komínková Oplatková, Z., Dulík, T. (2018). Fire detection in video stream by using simple artificial neural network. *Mendel*, vol. 24, p. 55-60, **DOI:10.13164/mendel.2018.2.055**.

[62] Pérez, Y., Pastor, E., Planas, E., Plucinski, M., Gould, J. (2011). Computing forest fires aerial suppression effectiveness by IR monitoring. *Fire Safety Journal*, vol. 46, no. 1-2, p. 2-8, **DOI:10.1016/j.firesaf.2010.06.004**.

[63] Tempest, W. (1976). *Infrasound and Low Frequency Vibration*. Academic Press Inc., London.

[64] Kim, Y.S., Lee, J.Y., Yoon, Y.G., Oh, T.K. (2022). Effectiveness analysis for smart construction safety technology (SCST) by test bed operation on small-and medium-sized construction sites. *International Journal of Environmental Research and Public Health*, vol. 19, no. 9, 5203, **DOI:10.3390/ijerph19095203**.

[65] Loreto, S.D., Lori, V., Serpilli, F., Lops, C., Ricciutelli, A., Montelpare, S. (2023). "Great food, but the noise?": Relationship between perceived sound quality survey and non acoustical factors in one hotel restaurant in Italy. *Building Acoustics*, vol. 30, no. 4, p. 425-443, **DOI:10.1177/1351010X231191439**.

[66] Yılmaz-Atay, G., Loboichenko, V., Wilk-Jakubowski, J.L. (2024). Investigation of calcite and huntite hydromagnesite mineral in co-presence regarding flame retardant and mechanical properties of wood composites. *Cement Lime Concrete*. (accepted for publication)

[67] Furlan, M., Boltežar, M. (2004). The boundary-element method in acoustics - an example of evaluating the sound field of a DC electric motor. *Strojniški vestnik - Journal of Mechanical Engineering*, vol. 50, no. 2, p. 115-128.

[68] Barbarulo, A., Riou, H., Kovalevsky, L., Ladeveze, P. (2014). PGD-VTCR: A reduced order model technique to solve medium frequency broad band problems on complex acoustical systems. *Strojniški vestnik - Journal of Mechanical Engineering*, vol. 16, no. 5, p. 307-313, **DOI:10.5545/sv-jme.2014.1834**.

[69] Taspinar, Y.S., Koklu, M., Altin, M. (2021). Fire detection in images using framework based on image processing, motion detection and convolutional neural network. *International Journal of Intelligent Systems and Applications in Engineering*, vol. 9, no. 4, p. 171-177, **DOI:10.18201/ijisae.2021473636**.

[70] Taspinar, Y.S., Koklu, M., Altin, M. (2022). Acoustic-driven airflow flame extinguishing system design and analysis of capabilities of low frequency in different fuels. *Fire Technology*, vol. 58, p. 1579-1597, **DOI:10.1007/s10694-021-01208-9**.

[71] Koklu, M., Taspinar Y.S. (2021). Determining the extinguishing status of fuel flames with sound wave by machine learning methods. *IEEE Access*, vol. 9, p. 207-216, **DOI:10.1109/ACCESS.2021.3088612**.

Strojniški vestnik - Journal of Mechanical Engineering 70(2024)5-6, 282-292
DOI:10.5545/sv-jme.2023.682
Original Scientific Paper
Received for review: 2023-06-08
Received revised form: 2024-02-06
Accepted for publication: 2024-04-12

Evaluation of the Condition of the Bottom of the Tanks for Petroleum Products-Forecast of the Remaining Operating Life

Aleš Povše[1] – Saša Skale[2] – Jelena Vojvodić Tuma[3]
[1]Jožef Stefan International Postgraduate School, Slovenia
[2]SKALA, Saša Skale s.p., Slovenia
[3]Institute for Energy Engineering, Dr. Jelena Vojvodić Tuma s.p., Slovenia

Corrosion rate measurements in the tank enable us to develop a new model for predicting the remaining operating period of the tank. The empirical model for the study of bottom plate thicknesses and corrosion pits is more conservative than the standard linear model, as it considers the autocatalytic nature of the corrosion process. We used the double exponential distribution of maximum values (Gumbel's) to evaluate the maximum depth of pits, and the double exponential distribution of minimum values to evaluate the minimum values of the plate thickness. A comparison of the values of the parameters obtained using linear extrapolation and exponential models indicates the unreliability of linear extrapolation, since disregarding dynamic processes underestimates the actual rate of corrosion.
Keywords: pitting, storage tank bottom, time-dependent reliability, corrosion model

Highlights
- *The class of tank bottom metal plates can significantly affect on the prediction of the remaining operating period of the tank.*
- *Improving the reliability of measurements of the condition of the tank bottom by statistical analysis of extreme values.*
- *New model for predicting the remaining operating period of the tank.*
- *Improving the reliability of the remaining tank operating period prediction model using actually calculated tank bottom corrosion rates.*
- *The proposed model is more reliable than the established models and is consistent with the actual consequences of tank bottom corrosion.*

0 INTRODUCTION

When storing fuels in tanks, complete bottom tightness must be ensured. A potential fuel spill can result in ecological and economic damage. From long-standing monitoring of the condition of the internal surfaces of the tanks it follows that the presence of water makes the internal surfaces of the tanks the most congested. The presence of aqueous solutions at the bottom of the tank, in addition to general corrosion, allows the development of more problematic forms of local corrosion such as pitting and microbiological corrosion. Pitting may also appear independently from microbiological corrosion. Rapid progression of local forms of corrosion can lead to premature failure of the tank bottom, especially if adequate anti-corrosion protection system is not provided on surfaces contacting petroleum products. The combination of local corrosion and the absence of anti-corrosion protection system resulted in leaking of tank bottom constructed of nominal 8 mm carbon steel plates after 6 years of tank operation.

During the regular periodic inspections of the tanks, it is necessary to reliably assess the progress of corrosion in the future operating period. The generally established methodology for predicting the remaining operational life of the tank bottom is based on non-destructive measurements of the thickness of the bottom plate with magnetic flux, ultrasound and measurements of the depth of corrosion damage with mechanical measures **[1]**. The corrosion rate is estimated from the measurements based on extrapolation to the previously known or initial condition of the tank bottom. The most unfavorable measured values, such as the minimum measured bottom plate thickness or the maximum measured depth of corrosion damage, are taken into account in the assessment. Construction of tank bottom must be also taken in account. In our case of double bottom tanks, with vacuumed interspace between bottoms, corrosion is limited to surfaces contacting petroleum products. In single bottom tanks can additional corrosion also occur from outside contacting soil or concrete.

Corrosion rates estimated in this way are usually of the order of 0.1 mm/year to 0.2 mm/year **[2]** and **[3]**. This is significantly less than experience and data show us about the possible rates of pitting (0.5 mm/year to 1.5 mm/year) or microbiological corrosion (0.5 mm/year to 2 mm/year) **[2]** and **[3]**. Therefore, the estimates of measurements carried out in accordance with standard methodology **[1]**, significantly

*Corr. Author's Address: Jožef Stefan International Postgraduate School, Slovenia, ales.povse@petrol.si

underestimate the actual rate of corrosion progression in the presence of local form of corrosion.

One of the reasons for the unreliability of the standard corrosion prediction model is the lack of measurements of tank bottom plate thickness, as only a limited number of measurements are usually available. For this purpose, a statistical methodology of extreme values was developed for laboratory measurements during simulations of actual corrosion on objects. This, based on the hypothesis that the statistical distribution of measurements is the same on all parts of the surface, enables the evaluation of extreme values for the minimum bottom plate thickness or the maximum depth of corrosion damage. This approach improves the reliability of the corrosion progression prediction compared to the standard linear model.

The reliability of the prediction of the remaining service life of the tank bottom depends on the reliability of the assessment of the existing condition, the assessment of the corrosion rate and the adequacy of the model for the evaluation of the course of the corrosion rate. A linear model of corrosion progression with a constant corrosion rate is established in the technical regulations [1]. This is based on the lowest measured bottom plate thickness and an estimate of the corrosion rate based on a linear extrapolation to the previously known condition of the tank bottom. More reliable approach is use of extreme value estimates, again with linear extrapolation to a known initial state [4]. In case of accumulated data (databases), as is case for marine ships, prediction of thickness loss and corrosion rates can be estimated with statistical models [5] to [11]. In case of above ground storage tanks, in best case (but usually not), we have plate thickness measurements from previous tank inspection.

Laboratory monitoring of corrosion processes has shown that the progression of corrosion can be described, depending on the nature of the corrosion, with two empirical models for passivation and active dissolution of steel. Laboratory empirical models are based on a large number of plate thickness measurements over at least three-time intervals, which are then correlated in an empirical model. In reality, however, this type of data is not available to us [12].

Long inspections intervals, currently lasting at least every 10 years, tank design and design imperfections, stored fuels and their quality, frequency of drainage, refill intervals, micro location of tank, cathodic protection of external tank bottoms contacting concrete foundations are some main factors which influence corrosion rates on internal surfaces of bottoms. During tank inspections we discovered significant differences on neighboring tanks of the same construction, age, design and stored fuel, probably due to variations of fuel quality. These are some main reasons, why laboratory simulations of internal tank exposure, progress of corrosion rates through time may significantly differ from reality and cannot be used for a reliable prediction for the remaining service life.

In our previous work, we performed established electrochemical measurements (anodic polarization) in the studied tank before replacing the upper tank bottom. Measured spots plates were cut out and tank measurements verified in controlled laboratory conditions [13].

Replacing the bottom plates of the tank allowed us to measure the actual corrosion rates, while we were able to use the laboratory empirical model for active steel dissolution [13]. The empirical parameters of the model were evaluated based on extreme values of ultrasonic measurements of bottom plate thickness, pit depth and measured corrosion rates. The obtained corrosion progression model allowed us to predict the remaining service life of the tank bottom significantly more reliably compared to the standard linear model [1]. The results of our model were consistent with the observed actual condition of the reservoir bottom plates.

1 EXPERIMENT

Measurements of bottom plate thickness and pit depth were made at the bottom of an above-ground, double bottom tank for the storage of petroleum products with a volume of 55,000 m^3. The tank was built in 2006 [14] and [15]. After six years of operation, a bottom leak was detected. The measurements in the tank were carried out before the bottom plates were replaced. Corrosion was limited to surfaces contacting petroleum products.

1.1 Measurements of the Remaining Bottom Plate Thickness

Measurements of the remaining bottom plate thickness (Tables 1 and 3) were carried out with an Elcometer 204 Steel Ultrasonic Thickness Gauge, in accordance with the standard SIST EN 14127 [16]. The meter has a measuring range from 0.63 mm to 199.99 mm and a resolution of 0.01 mm and a reliability of ±2 %.

From 12 to 18 measurements were performed on each of the eleven measuring spots, in size approximately 1.5 m × 1.5 m. The nominal thickness

Table 1. *Bottom plate thickness measured by ultrasound [mm]*

No	Measurement point										
	1	2	3	4	5	6	7	8	9	10	11
1	9.27	8.24	8.43	8.56	8.97	8.42	8.55	8.21	8.50	7.70	8.12
2	9.61	8.21	8.69	8.16	9.04	9.03	8.52	8.13	8.93	7.92	6.08
3	9.32	8.26	8.41	8.54	8.78	8.77	8.57	8.37	8.60	8.29	6.54
4	9.25	8.25	8.72	8.65	8.83	8.45	7.30	8.47	8.35	8.90	5.58
5	9.49	8.22	8.56	8.21	8.61	8.40	8.26	8.64	8.72	8.16	6.30
6	8.66	8.26	8.72	8.27	9.03	8.56	8.40	8.15	8.88	8.08	7.98
7	8.77	8.22	8.56	8.53	8.86	8.59	8.28	8.23	8.57	7.20	8.89
8	9.22	8.23	8.56	8.50	8.73	8.68	8.20	8.33	8.58	7.67	5.93
9	8.74	8.23	8.39	8.57	8.73	8.63	8.70	8.66	8.69	7.66	8.01
10	9.28	8.28	8.78	8.33	8.58	8.60	8.62	8.58	8.72	8.77	6.65
11	8.70	8.23	8.40	8.17	8.97	8.61	8.51	8.18	8.67	7.19	5.96
12	8.75	8.29	8.69	8.48	8.93	8.63	8.66	8.32	8.67	7.93	6.15
13	9.02	8.27	8.58	8.34	8.68	8.30		8.11	8.70	7.64	5.77
14	8.66	8.24	8.76	8.53	8.80	8.37		8.26	7.49	7.81	7.57
15	8.61	8.28	8.50	8.89	8.60			8.51	8.60	7.48	7.52
16	8.63	8.26	8.49					8.32		7.20	
17	9.31										
18	8.62										

of the tank bottom plate was 8 mm. According to the standard [17], for class C, a tolerance of 0 mm to +1.4 mm is allowed. Due to the inclination of the bottom towards the center of the tank, corrosion loads are greatest in the middle of the tank, where we have the water phase zone [2], [3], [18], and [19]. A decrease in bottom plate thickness towards the center of the tank is expected.

1.2 Corrosion Pits Depth Measurements

Corrosion pits depths (Tables 2 and 4) were measured with a KS Tools digital depth gauge 300.0550 with a measurement range of 0 mm to 40 mm and a measurement uncertainty of ± 0.01 mm, the diameter of the needle was 2 mm.

We performed 14 to 18 measurements at eleven measurement spots, in size approximately 1.5 m × 1.5 m. The deepest pit of 3.45 mm was measured at the measuring point number 11. Comparable to ultrasonic measurements, the depth of pits increases towards the center of the tank bottom.

1.3 Calculations and Evaluations of Measurements

From the extreme values of spot measurement series, we compiled an empirical cumulative distribution using the average ranking method [12]. This is optimized non-linearly with a selected statistical distribution [12] and [20]. The series of corrosion rates (Table 5) was evaluated with a normal distribution [12], [13], and [20]. Extreme values of the pit depth (Table 4) and the remaining thickness of the bottom plates (Table 3) were evaluated with double exponential distributions of minimum and maximum values. The optimized empirical cumulative distributions allow us to estimate the maximum corrosion rate, the lowest residual thickness, and the deepest ulcers at the bottom of the tank (Table 6), with a chosen confidence of 99 % or return interval 100 with assumption that determined cumulative distributions are valid over all internal surfaces of upper tank bottom [12].

Corrosion is an electrochemical process for which the exponential model (kinetics of chemical reactions) applies [5], [7] to [12]:

$$x - a_0 = k(t - t_i)^n, \tag{1}$$

where x is pit depth, t_i time at which local corrosion occurs, a_0 initial value of pit depth, k and n empirical kinetic constants.

Derivation of Eq. (1) over time gives us the corrosion rate (v_{corr}):

$$v_{corr} = \left(\frac{dx}{dt} \right)_t = nk(t - t_i)^{n-1}. \tag{2}$$

Empirical kinetic constants (k, n) are calculated from the combination of Eqs. (1) and (2).

Table 2. *Pit depths [mm]*

No	Measurement point										
	1	2	3	4	5	6	7	8	9	10	11
1	0.84	0.08	1.47	0.60	0.06	0.13	1.19	1.71	0.03	2.98	2.61
2	0.56	0.20	1.86	0.84	0.12	0.07	0.41	0.19	0.00	2.62	3.16
3	0.88	0.06	3.26	1.89	0.07	0.22	0.55	1.50	0.05	0.94	2.69
4	0.55	0.11	1.20	1.12	0.05	0.09	0.96	1.39	0.09	1.36	2.09
5	0.61	0.07	1.52	1.51	0.09	0.16	0.35	0.87	0.03	2.44	2.63
6	0.91	0.17	1.43	1.70	0.05	0.07	0.47	0.67	0.04	1.91	2.58
7	0.85	0.10	1.47	0.97	0.05	0.33	0.51	1.06	0.05	2.42	2.86
8	1.48	0.14	1.75	0.52	0.04	0.07	0.91	1.49	0.13	2.54	2.73
9	0.71	0.14	1.87	2.25	0.31	0.00	1.30	1.31	0.13	2.29	2.95
10	0.71	0.03	1.18	2.50	0.33	0.09	1.06	0.85	0.08	0.85	3.31
11	0.83	0.17	1.54	1.20	0.32	0.03	0.82	0.45	0.09	1.17	3.41
12	0.63	0.00	1.89	2.34	0.06	0.39	1.21	0.99	0.13	2.63	2.93
13	0.58	0.16	2.70	1.52	0.20	0.15	0.98	2.12	0.01	1.98	3.45
14	0.70	0.14	1.32	2.19	0.21	0.19	0.49	2.52	0.20	2.02	2.95
15	0.76	0.18	0.70	2.41	0.24	0.07		2.27	0.09	2.36	2.63
16	0.79	0.07	1.51	2.40	0.26			1.58	0.08	2.32	
17	0.45	0.11	1.30	2.34	0.41			2.43	0.12		
18		0.08	1.30								

$$n = \left(\frac{dx}{dt}\right)_t \frac{\left(t - t_i\right)}{\left(x - a_0\right)}, \tag{3}$$

$$k = \frac{\left(x - a_0\right)}{\left(t - t_i\right)^n} = \frac{1}{n}\left(\frac{dx}{dt}\right)_t \left(t - t_i\right)^{1-n}. \tag{4}$$

For new plates are initial pit depths (a_0) zero. In absence of intermediate measurements, we assumed that initial time (t_i) for occurrences of local corrosion is also zero, which is valid in worst case scenario – immediate formation of pits.

The quality of the correlation is evaluated with the coefficient of determination **[20]**:

$$R^2 = 1 - \frac{\sum_{I=1}^{n}\left[F_{eks}\left(x\right) - F_{mod}\left(x_i\right)\right]^2}{\sum_{I=1}^{n}\left[F_{eks}\left(x_i\right) - \overline{F_{eks}}\right]^2}, \tag{5}$$

where R^2 is coefficient of determination, $F_{eks}(x_i)$ empirical cumulative distribution of measurements, $F_{mod}(x_i)$ selected theoretical cumulative distribution and $\overline{F_{eks}}$ average value of empirical cumulative distribution of measurements.

2 RESULTS

Optimization of empirical cumulative distributions significantly improved coefficient of determination for both double exponential distributions and slightly for normal distribution. Extreme values were calculated from optimized empirical cumulative distributions for 99 % confidence (Table 6), where and are location and scale parameters (Eq. (6) and (7)), mean and standard deviation for normal distribution, coefficient of determination (Eq. (5)) and estimated extreme value. Statistically estimated extreme values in comparison to measured extreme values are more conservative and presented a more reliable state of tank bottom in worst case scenario – bottom leakage.

2.1 Evaluation of the Remaining Operating Time of the Tank Bottom

Corrosion damage can be roughly divided into two groups: uniform and local corrosion. Uniform corrosion results in a general reduction in bottom plate thickness. Localized corrosion causes corrosion damage in the form of pits and cracks.

The condition of the tank bottom, from the corrosion point of view, is evaluated by the remaining thickness of the bottom plate and the depth of the pits. Evaluating the time dependence of bottom plate thickness or pit depth requires at least two sets of measurements at different time periods. In practice, the problem of corrosion is only encountered during the prescribed periodical inspection of the condition of the tank. We do not have intermediate measurements, so a linear extrapolation of the rate determination to the new state of the tank is used to predict the remaining operating time of the tank. Most

Table 3. *Recapitulation of minimum bottom plate thicknesses [mm]*

Measurement spot	1	2	3	4	5	6	7	8	9	10	11
Number of measurements	18	16	16	15	15	14	12	16	15	16	15
Average thickness [mm]	9.00	8.25	8.58	8.45	8.81	8.57	8.38	8.34	8.58	7.85	6.87
Mean thickness [mm]	8.90	8.25	8.56	8.50	8.80	8.60	8.52	8.32	8.67	7.76	6.54
Standard deviation [mm]	0.34	0.02	0.13	0.2	0.16	0.19	0.38	0.18	0.33	0.51	1.05
Minimum measured thickness [mm]	8.61	8.21	8.39	8.16	8.58	8.30	7.30	8.11	7.49	7.19	5.58

Table 4. *Recapitulation of maximum depth of corrosion pits [mm]*

Measurement spot	1	2	3	4	5	6	7	8	9	10	11
Number of measurements	17	18	18	17	17	15	14	17	17	16	15
Average pit depth [mm]	0.76	0.11	1.63	1.66	0.17	0.14	0.80	1.38	0.08	2.05	2.87
Mean pit depth [mm]	0.71	0.11	1.49	1.70	0.12	0.09	0.87	1.39	0.08	2.31	2.86
Standard deviation [mm]	0.23	0.06	0.58	0.69	0.12	0.11	0.33	0.68	0.05	0.64	0.36
Maximum measured pit depth [mm]	1.48	0.20	3.26	2.50	0.41	0.39	1.30	2.52	0.20	2.98	3.45

Table 5. *Corrosion rates in the tank [mm/year] [4]*

Measurement spot	1	2	3	4	5	6	7	8	9	10	11
Corrosion rate	0.33	0.35	0.82	0.37	1.34	0.91	0.93	1.15	1.15	1.59	1.17

Table 6. *Optimisation and estimation of extreme values for pit depth, plate thickness and corrosion rate with 99 % confidence*

Distribution	Pit depth		Plate thickness		Corrosion rates	
	Double exponential of max.		Double exponential of min.		Normal	
	Theoretical	Optimised	Theoretical	Optimised	Theoretical	Optimised
$\lambda(\mu^{(*)})$ [mm]	1.1125	1.0165	7.9060	8.2588	0.9191	0.9399
$a/(\sigma^{(*)})$ [mm]	1.0026	1.5104	0.6931	0.6323	0.4218	0.5183
R^2 [-]	0.758	0.937	0.869	0.928	0.938	0.945
x [mm]	5.7	8.50	4.7	5.1	1.9	2.1

Table 7. *Empirical model parameters calculation for active dissolution – Eq. (1), and Figs. (3), (4) and (5)*

Time [years]	Pit Depth		Plate thickness			
	Measured	Estimated	Measured / (1)nominal Class C		Estimated / (1)nominal Class C	
0			8.0 mm(1)	9.4 mm(1)	8.0 mm(1)	9.4 mm(1)
7	3.5 mm	8.5 mm	5.6 mm		5.1 mm	
	Empirical calculated parameters for Eq. (1):					
n	4.3420	1.7624	6.1901	3.9215	5.1655	3.4837
k	0.0007386	0.2754	0.00001421	0.001854	0.0001250	0.004891

of material is lost due to uniform corrosion. Local corrosion represents only small portion of overall loss but presents major threat for tank bottom tightness due to significantly higher corrosion rates. Local corrosion rates, with time, can vary from decreasing (passivation) to increasing (active dissolution). In absence of localized corrosion, linear extrapolation to initial known state of tank bottom may provide good corrosion rate estimate. But in case of presence of local corrosion, even one pit is enough for loss of tank bottom tightness. For evaluation of remaining service life, model for active dissolution is more appropriate. **[1]**, **[4]**, **[12]**, and **[21]** to **[23]**.

2.2 Estimate Bottom Plate Thickness

The plate thickness on the bottom was evaluated using a double exponential distribution of the minimum values **[12]**.

A double exponential distribution of minimum values was used to estimate the thickness of the bottom plate:

$$F_{-1}(x) = 1 - \exp\left[-\exp\left(\frac{x-\lambda}{\alpha}\right)\right], \quad (6)$$

where $F_{-1}(x)$ is the cumulative distribution function of the minimum values, the location parameter, and is the distribution width parameter.

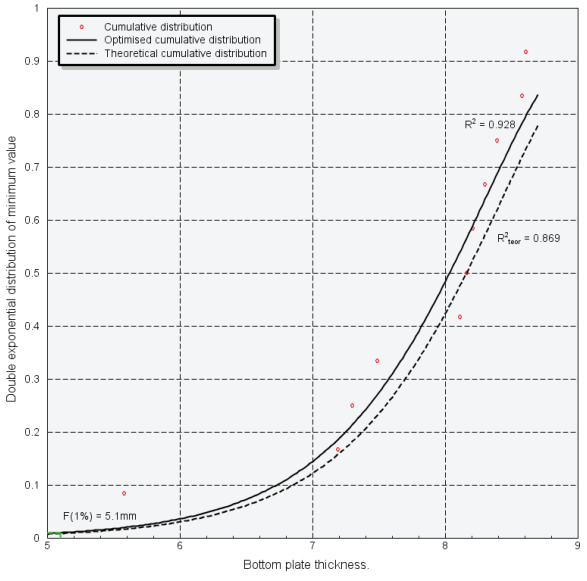

Fig. 1. *Estimate of minimum bottom plate thickness*

The measured minimum values for each measurement spots were subjected to empirical cumulative distribution using the average ranking method. This was optimized as double exponential distribution of minimum values, using the Newton-Raphson algorithm (Fig. 1). The minimum bottom plate thickness 5.1 mm (with 99 % confidence) was estimated from an optimized double exponential cumulative distribution of minimum values.

2.3 Evaluation of the Maximum Depth of Pits

The pit depths on the bottom were evaluated using a double exponential distribution of the maximum values [12].

We used (Gumbel's) distribution to evaluate the maximum depth of pits:

$$F_{1}(x) = \exp\left[-\exp\left(-\frac{x-\lambda}{\alpha}\right)\right], \quad (7)$$

where $F_{-1}(x)$ is the cumulative distribution function of maximum values, λ is the location parameter, α is the distribution width parameter.

The maximum measured depths for each measurement site were subjected to empirical cumulative distribution using the average ranking method. This was optimized as double exponential distribution of maximum values with the Newton-Raphson algorithm (Fig. 2). The maximum pit depth 8.5 mm (with 99 % confidence) was estimated from the optimized double exponential cumulative distribution of maximum values.

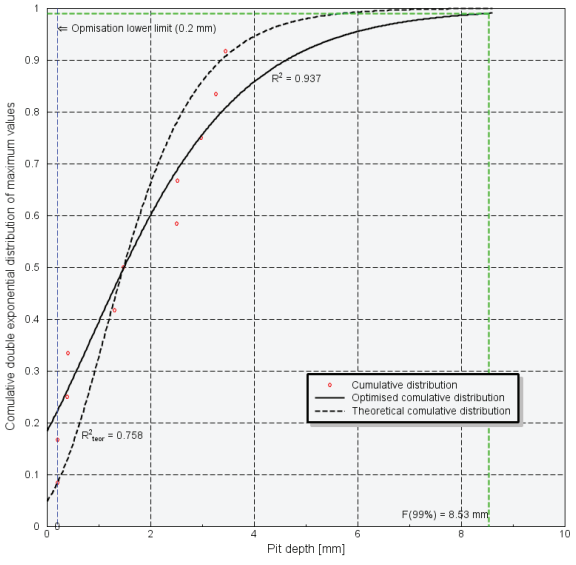

Fig. 2. *Evaluation of the maximum depth of pits*

3 DISCUSSION

The definition of time models for the evaluation of the remaining operating life of the bottom of the tanks requires the implementation of many series of measurements of corrosion parameters (plate thickness, depth of pits) after different time periods of operation, which are usually not available or have not been carried out. Therefore, linear extrapolation is used to predict the remaining service life of tank bottoms. In the past, the relatively poor reliability of linear extrapolation of corrosion parameters led to the development of statistical methods for the evaluation of extreme values, which allowed us to make more reliable estimates of the remaining service life. The statistics of extreme values allow us to more conservatively predict critical corrosion parameters, such as the minimum bottom plate thickness and the maximum depth of pits [12]. Especially in case of local corrosion presence.

Evaluating corrosion rate allowed us to use a real-time model to predict the remaining service life of the

tank. Compared to linearly extrapolated time models, exponential time models allow for a more reliable prediction of the remaining operating life of the tank.

In our case, the estimation of corrosion rate, based on the linear extrapolation of bottom plate thicknesses, to the initial design state, was in the range from 0.6 mm/year to 0.7 mm/year. The rate of corrosion in the linear extrapolation of pit depths was in the range of 0.5 mm/year to 1.2 mm/year.

Estimated rate of corrosion (2.1 mm/year) from empirical normal distribution and even max. measured corrosion rate (1.6 mm/year) are significantly higher than estimation with linear extrapolation. Even with additional 1.4 mm from upper allowed initial thickness of plates, we failed to estimate actual corrosion rates in tank, with linear extrapolation of extreme values. Therefore, we are of the opinion that from the point of view of predicting the remaining operating life of the tank, empirical model for active dissolution [12] is a better solution.

3.1 Prediction of the Remaining Operating Life of a Tank Bottom

The established and prescribed way of predicting the remaining operating life of the tank bottom is based on linear extrapolation of the established tank condition [4], and [24]. The rate of corrosion is evaluated linearly, based on comparison with previous measurements of bottom plate thickness and depth of pits or to the initial design state. When evaluating the state of the tank bottom, estimated extreme statistical values [4], [12], [21], [22], and [25] are conservatively used instead of direct measurements.

To predict the remaining operating life, in addition to the condition assessment, an assessment of the corrosion rate based on transient measurements or even the condition of the initial design of the tank bottom is essential. The long intervals between prescribed periodical inspections (10 years or more) and the high costs associated with carrying out inspections practically make it impossible for us to carry out more frequent condition measurements.

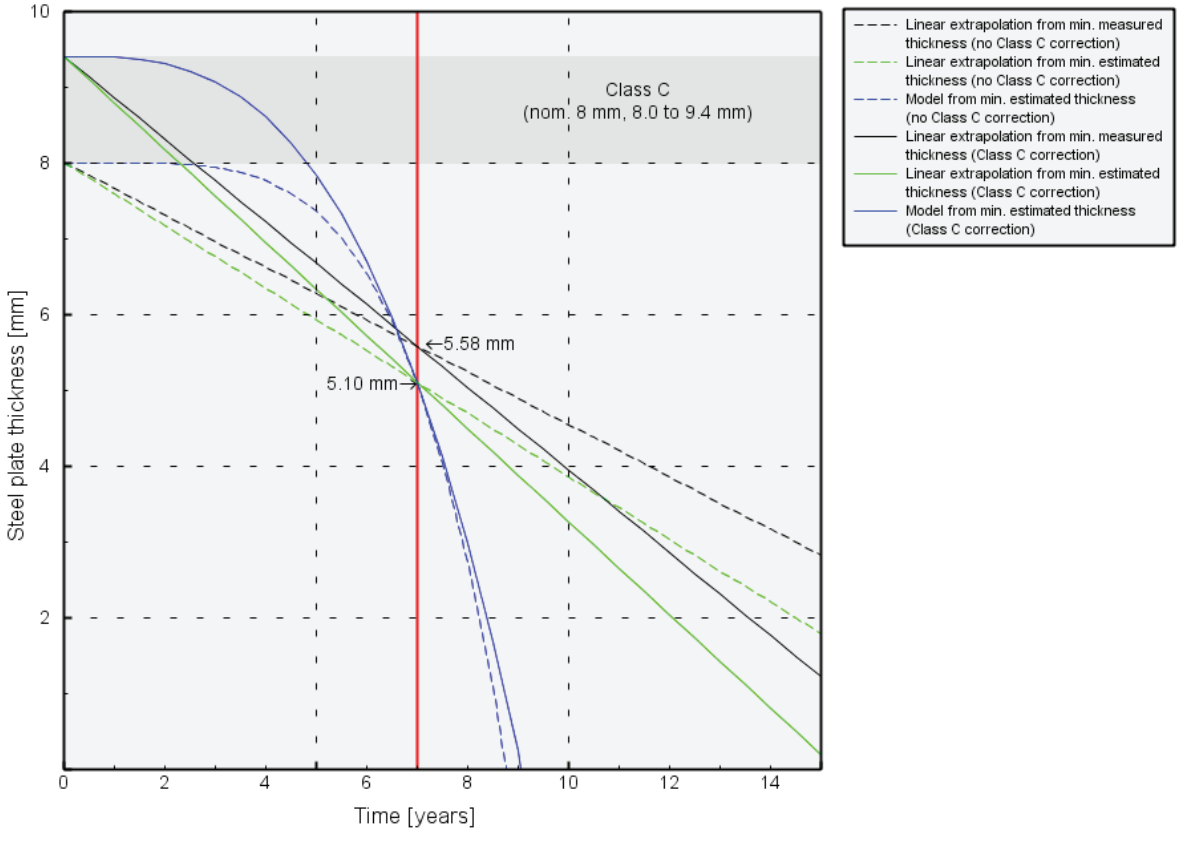

Fig. 3. *Prediction of service life from ultrasonic bottom plate thickness measurements: Comparison of empirical model (Eq. (1)) with established linear extrapolation model, based on minimal measured and minimal estimated plate thickness to initial state; Effect of Class C plate thickness tolerances on service life is also presented*

The problem of predicting the remaining operating life is therefore only encountered when corrosion is discovered at the bottom of the tank.

The material for bottom plate is standardized into classes that, among other things, define thickness tolerances. The most demanding class "C" according to EN 10029 [17] is usually used for the bottom of the tanks, which does not allow negative deviations from the nominal plate thickness. However, it allows limited positive deviations. In the case of our tank bottom, plate with a nominal thickness of 8 mm was used, which allows a maximum thickness of 9.4 mm.

In the case where the initial state of the bottom plate is defined only nominally, when evaluating the corrosion rate, we are confronted with the designed state, where the thickness of the bottom plate is defined in the interval between the nominal and the maximum permissible thickness of the bottom plate. In our case, the projected bottom plate thickness is between 8 mm and 9.4 mm. There is a significant difference between the corrosion rates estimated based on the nominal and the maximum allowable thickness (Fig. 3). For example, depending on plate thickness interval, corrosion rates (9.4 mm to 5.1 mm) per 7 years or (8.0 mm to 5.1 mm) per 7 years. Even much greater than the difference in estimated corrosion rates between the minimum measured and the minimum statistically estimated bottom plate thickness.

The reliability of the corrosion rate estimation when intermediate measurements are not available can also be strongly influenced by the time of corrosion initiation. The later the time of initiation, the higher the corrosion rate. When evaluating the rate of corrosion based on measurements of the depth of corrosion damage, the influence of thickness tolerances for the bottom plate class does not apply, since there are no corrosion pits at the start of operation. The influence of the bottom plate class is shown in the prediction of the remaining service life, since the exceeded nominal thickness of the bottom plate cannot reliably predict failure.

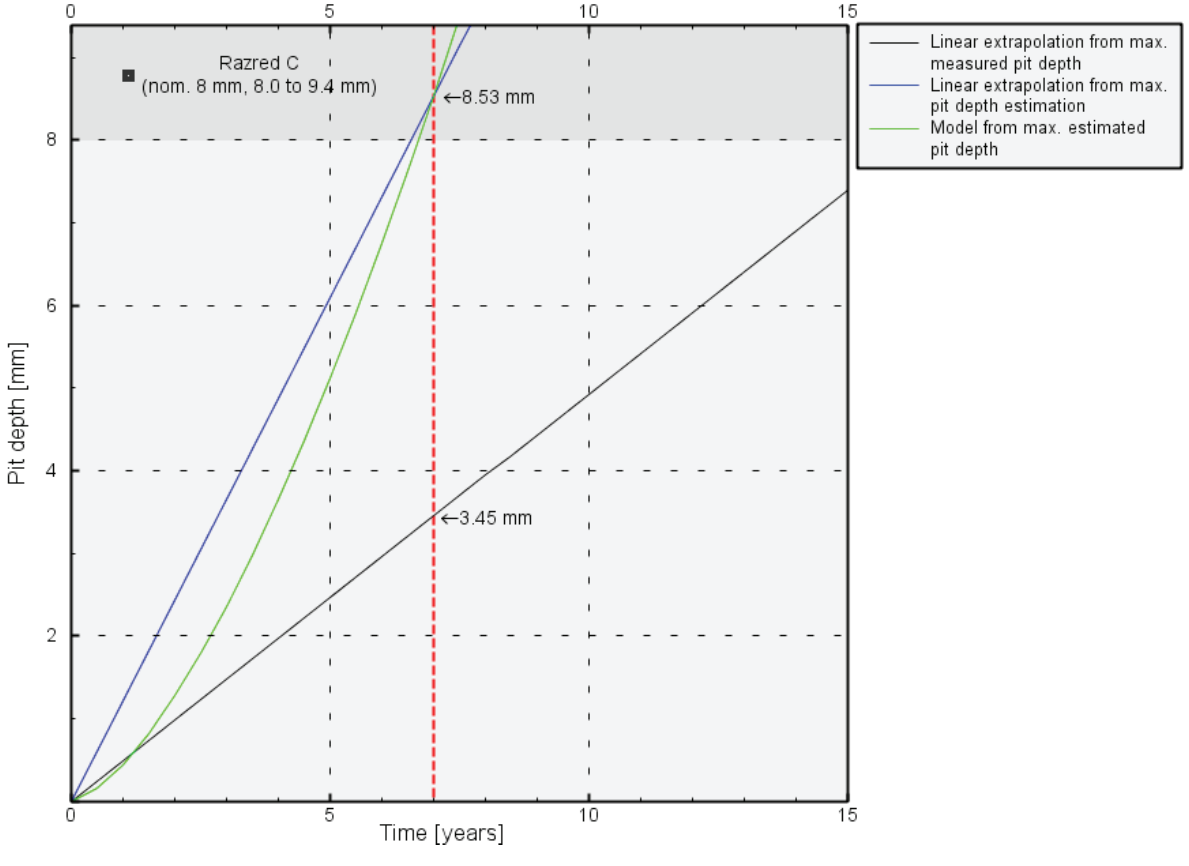

Fig. 4. *Prediction of operating life based on corrosion pit depth measurements: Comparison of empirical model (Eq. (1)) with established linear extrapolation model, based on maximal measured and maximal estimated pit depth to initial state*

The linear corrosion prediction is also strongly influenced by the initiation time of local corrosion. From the point of view of the linear prediction of the corrosion rate, based on the designed state, due to the lack of knowledge of the initiation time, we underestimated the corrosion rate.

Linear predictions of the remaining operating life of the tank bottom, in the absence of intermediate measurements of the tank condition, are not reliable.

When evaluating the measurements with the double statistic of extreme values, we found an interesting difference between ultrasound and pit depth measurements. The difference between the measured and estimated extreme values is significantly higher and thus more conservative when measuring the depth of pits than when measuring the bottom plate thickness (Figs. 3 and 4).

Evaluating the rate of corrosion in conjunction with an assessment of the condition of the tank allows us to use the empirical model (Eq. (1), Table 7) to predict the remaining service life of the tank bottom. Unreliability of the initial plate thickness and unknown initiation time only affect the shape of the empirical model curves for plate thickness, (Figs. 3 and 4).

With the empirical model of bottom plate thicknesses (Fig. 3), the unreliability of initial plate thickness is reflected in significantly smaller differences compared to linear models. The empirical model that considers the minimum initial bottom plate thickness is more conservative compared to the model that considers the maximum allowable thickness, due to higher value of parameter . Curve shape parameters are significantly above value 1. Corrosion rates (Eq. (2)) increase through time. Parameter is corrosion rate constant rather than corrosion rate as in linear approximations of empirical model in Eq. (1).

The exponential model for pit depth is more conservative compared to the linear model, but the difference is significantly smaller compared to

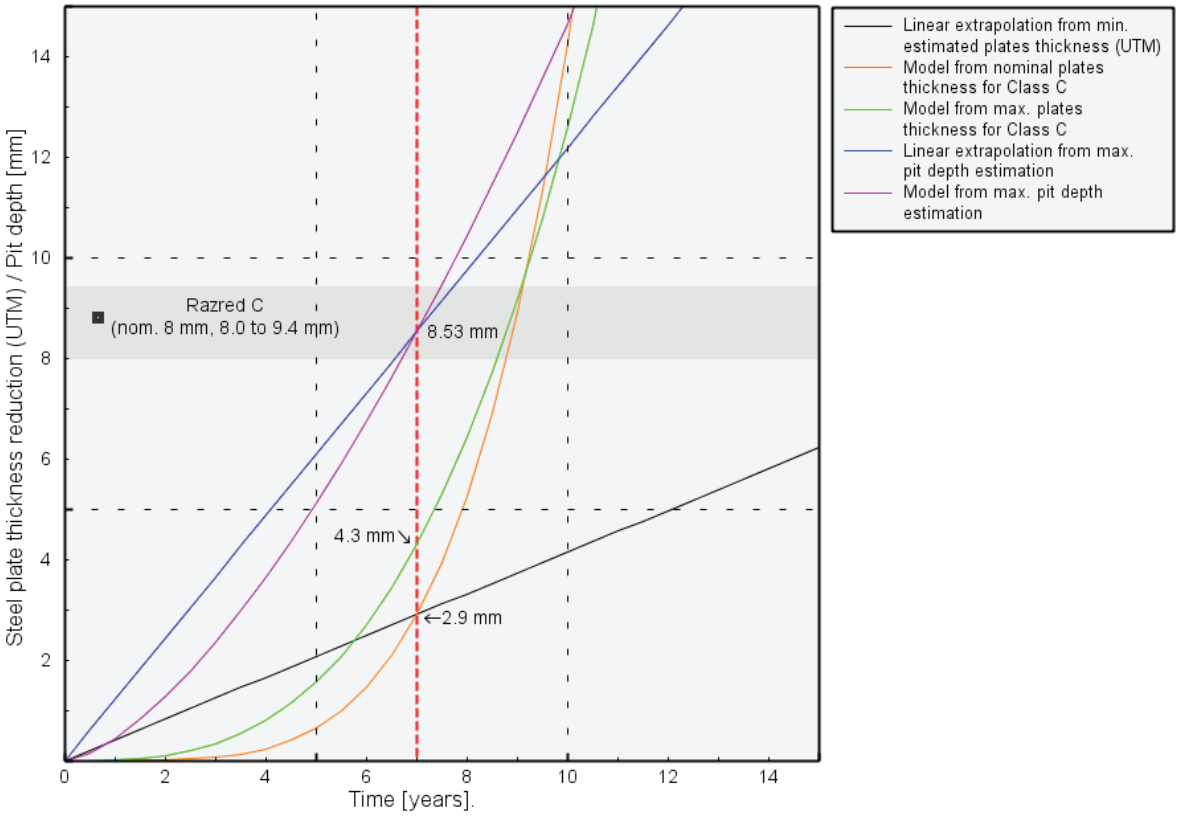

Fig. 5. *Comparison of models for predicting the remaining service life of the tank bottom: Informative comparison of empirical models (Eq. (1)) for pit depth and plate thickness measurements; For direct comparison of reliability, steel plate thickness reduction is calculated as difference between initial plate state and empirical model for plate thickness (red and green curve); Additional lines for linear extrapolation, based on statistically estimated values for maximal pit depth and minimal plate thickness are added*

models for bottom plate thickness based on ultrasound measurements.

Reliable comparison of bottom plate thickness model with pit depth models is not possible (Fig. 5). Ultrasonic measurements on the uneven surface of the bottom plate give us the thickness between the apparent plane in the pit profile and the bottom surface of the bottom plate. Initial interval of plate thickness prevents any reliable estimation of uniform corrosion. Pit depth measurements do not consider thickness loss due to uniform corrosion and are limited by the diameter of the depth gauge needle.

Depth of pits or the thinning of the bottom plate at which the bottom of the tank fails is equal to the nominal thickness of the bottom plate. The exception is the empirical models, which considers the initial thickness of plates 9.4 mm (Fig. 5). In our case, after seven years of operation of the tank, we were faced with a leak in the bottom of the tank, which is also confirmed by the statistical analysis of the depth of the pits.

4 CONCLUSION

In the experiment, we compared different models for predicting the remaining operational life of the tank bottom. Conventional linear time models for predicting the remaining operating life of the tank bottom **[4]**, and **[24]** are not reliable in the case of local forms of corrosion.

Empirical model in Eq. (1) enables us to make better predictions of the remaining operational life of the tank bottom, which require the implementation of several series of measurements of the tank's condition during its operational period. In practice, data on the state of the tank bottom within the legally prescribed inspection intervals are not available to us. Therefore, the use of an exponential model to predict the remaining operating life based on the actual state of the tank bottom is not possible.

The exponential model of pit depths increase is more conservative than the linear model. The bottom plate thickness measurements, even after extreme values analysis, fail to predict tank bottom failure as the minimum estimated bottom plate thickness was 5.1 mm. The reason for this is probably related to the geometry of the probe of the ultrasonic meter and the rugged topography of the bottom plate surfaces.

When determining the condition of the bottom of the tank with ultrasound, the performance of reliable measurements requires additional grinding of the bottom plate surfaces to the depth of the pit, otherwise the measurement is not reliable due to the relatively large surface area of the measuring probe. Therefore, models for predicting the remaining service life of the tank bottom based on ultrasonic measurements (without grinding) of bottom plate thicknesses fail in case of local corrosion. The assessment of the remaining service life based on measurements of the depth of pits is more reliable and faster in the case of local corrosion, as it does not require additional preparation of the bottom plate surface for measurements.

In the water phase, the presence of salts or micro-organisms results in significantly higher corrosion rates than would be expected from the values published in the literature **[2]**, **[3]**, **[26]**, **[27]**. This confirms the established requirement for adequate service and anti-corrosion protection of tank bottoms **[28]**, **[29]**, and **[30]**.

Some empirical cumulative distributions obtained in other tanks showed bi-modal distribution patterns, when we observed different types of local corrosion on separate parts of bottom. Further studies will be focused on possible influence of type of corrosion on empirical distributions to improve estimation of extreme pit depths.

5 REFERENCES

[1] API Standard 653:2014. *Tank inspection, repair, alteration and reconstruction*, American Petroleum Institute, Washington, D.C..

[2] Shreir, L.L., Jarman, R.A., Burstein, G.T. (2000). *Corrosion*, 3rd edition, Butterworth-Heinemann, Boston.

[3] *Uhlig's Corrosion Handbook* (2000). 2nd edition, Revie, R.W. (ed.), CANMET Materials Technology Laboratory Ottawa, Ottawa.

[4] RR16:2002. *Guidelines for Use of Statistics for Analysis of Sample Inspection of Corrosion*, TWI Limited, Cambridge.

[5] Ivošević, Š., Meštrović, R., Kovač, N. (2019). Probabilistic estimates of corrosion rate of fuel tank structures of aging bulk carriers. *International Journal of Naval Architecture and Ocean Engineering*, vol. 11, no. 1, p. 165-177, **DOI:10.1016/j.ijnaoe.2018.03.003**.

[6] Ivošević, Š., Meštrović, R., Kovač, N. (2019). A comparison of some multi-parameter distributions related to estimation of corrosion rate of aging bulk carriers. *Trends in the Analysis and Design of Marine Structures*, Soares, C.G., Parunov, J. (eds.). Taylor & Francis Group, London, p. 403-410, **DOI:10.1201/9780429298875-47**.

[7] Ivošević, Š., Meštrović, R., Kovač, N. (2020). A probabilistic method for estimating the percentage of corrosion depth on the inner bottom plates of aging bulk carriers. *Journal of Marine Science and Engineering*, vol. 8, no. 6, 442, **DOI:10.3390/jmse8060442**.

[8] Ivošević, Š., Kovač, N., Momčilović, N., Vukelić, G. (2022). Evaluation of the corrosion depth of double bottom longitudinal girder on aging bulk carriers. *Journal of Marine*

Science and Engineering, vol. 10, no. 10, 1425, **DOI:10.3390/jmse10101425**.

[9] Soares, C.G., Garbatov, Y. (1999). Reliability of maintained, corrosion protected plates subjected to non-linear corrosion and compressive loads. *Marine Structures*, vol. 12, no. 6, p. 425-445, **DOI:10.1016/S0951-8339(99)00028-3**.

[10] Yamamoto, N., Kumano, A., Matoba, M. (1994). Effect of corrosion and its protection on hull strength (2nd report). *Journal of the Society of Naval Architects of Japan*, vol. 1994, no. 176, p. 281-289, **DOI:10.2534/jjasnaoe1968.1994.176_281**.

[11] Qin, S., Cui, W. (2003). Effect of corrosion models on the time-dependent reliability of steel plated elements. *Marine Structures*, vol. 16, no. 1, p. 15-34, **DOI:10.1016/S0951-8339(02)00028-X**.

[12] Kowaka, M. (1994). *Introduction to Life Prediction of Industrial Plant Materials, Application of the Extreme Value Statistical Method for Corrosion Analysis*, Allerton Press, New-York.

[13] Povše, A., Skale, S., Vojvodič Tuma, J. (2022). Evaluation of the Corrosion Rate at the Bottom of the above - Ground Tank for Storage of Petroleum Products. *European Journal of Engineering and Technology Research*, vol. 7, no. 2, p. 44-49, **DOI:10.24018/ejeng.2022.7.2.2709**.

[14] API Standard 650:2012. *Welded Steel tanks for Oil Storage*. American Petroleum Institute, Washington, D.C..

[15] Eurocode 3:2004. *Design of Steel Structures*. CEN, European committee for standardization, Brussels.

[16] SIST EN 14127:2011. *Non-destructive Testing - Ultrasonic Thickness Measurement*. CEN, European committee for standardization, Brussels.

[17] SIST EN 10029:2011. *Hot-rolled Bottom Plate Steel, 3 mm Thick or Above - Tolerances on Dimensions and Shape*. CEN, European committee for standardization, Brussels.

[18] Groysman, A. (2014). *Corrosion in Systems for Storage and Transportation of Petroleum Products and Biofuels, Identification, Monitoring and Solutions*. Springer, Dordrecht Heidelberg New York London, **DOI:10.1007/978-94-007-7884-9**.

[19] Graver, D.L. (1985). *Corrosion Data Survey - Metals Section*, 6th edition. NACE, Houston.

[20] Devore, J.L. (2012). *Probability and Statistics for Engineering and the Sciences*, 8th edition. Brooks/Cole, Boston.

[21] Gumbel, E.J. (1958). *Statistics of Extremes*, Columbia University Press, New York, **DOI:10.7312/gumb92958**.

[22] Gumbel, E.J. (1954). *Statistical Theory of Extreme Values and Some Practical Applications*. National Bureau of Standards Applied Mathematics Series, Washington, D.C..

[23] Marcus, P. (ed.) (2002). *Corrosion Mechanism in Theory and Practice*, 2nd edition. Taylor & Francis Group, London.

[24] West, J.M. (1973). *Basic Electrochemistry*, Van Nostrand Reinhold, New York.

[25] Tan, H.Y. (2017). *Statistical Methods for the Analysis of Corrosion Data for Integrity Assessments*, Brunel University, London.

[26] Mobin, M., Malik, A.U., Al-Fozan, S., Al-Muaili, F. (2007). Corrosion failure of bottom plates of aboveground storage tank. *Journal of Failure Analysis and Prevention*, vol. 7, no. 1, p. 18-22, **DOI:10.1007/s11668-006-9010-4**.

[27] Groysman, A. (2005). *Corrosion of aboveground fuel storage tanks*. NACE, Materials Performance, vol. 44, no. 9, p. 44-48.

[28] API Recommended practice 652:2014. *Linings of Aboveground Petroleum Storage Tank Bottoms*, 4th edition. American Petroleum Institute, Washington, D.C..

[29] SIST EN 14015:2005. *Specification for the design and manufacture of site built, vertical, cylindrical, flat-bottomed, above ground, welded, steel tanks for the storage of liquids at ambient temperature and above*. European Committee for Standardization, Brussels.

[30] Celin, R., Vojvodič-Tuma, J., Kosec, G. (2004). *Inspecting an above-ground storage tank*. Materials and Technologies, vol. 57, no. 6, p. 367-367.

Strojniški vestnik - Journal of Mechanical Engineering 70(2024)5-6, 293-310
DOI:10.5545/sv-jme.2024.991
Original Scientific Paper
Received for review: 2024-03-19
Received revised form: 2024-04-22
Accepted for publication: 2024-04-22

Research on Attitude Analysis of Hydraulic Support Based on Column Length

Mingfei Mu[1] – Bowen Xie[1] – Yang Yang[1,2,3,*]

[1] Shandong University of Science and Technology, College of Mechanical and Electrical Engineering, China
[2] Shandong Provincial Key Laboratory of Mining Mechanical Engineering, China
[3] Collaborative Innovation Center of Mine Intelligent Equipment and Technology, China

The existing hydraulic support attitude monitoring and control methods integrate multiple sensing technologies, but it is difficult to apply and promote due to unclear monitoring mechanisms, complicated types, and a large number of sensors. Aiming at the problem of attitude monitoring and control of hydraulic support, firstly, the kinematics mathematical model of hydraulic support is established by the key marker point method and the two-dimensional bar system model, and the forward and inverse solution algorithm of hydraulic support attitude based on the double-drive length of front and rear columns is proposed. Secondly, the rigid body dynamics simulation model of hydraulic support is constructed to verify the theoretical analytical model and prove the correctness of the algorithm. The rigid body simulation model can be used as the attitude monitoring system of hydraulic support. Thirdly, considering the influence of material elastic deformation, a rigid-flexible coupling dynamic simulation model of hydraulic support is established to explore the influence of elastic deformation of components on the attitude of hydraulic support and its causes. On this basis, the rigid-flexible coupling dynamic simulation model of the hydraulic support with clearance is established by replacing the revolute pair in the simulation model with the solid axis pin connection unit. The influence of the axis pin connection clearance on the attitude of the hydraulic support and its causes are explored, and the actual attitude and change characteristics of the hydraulic support under simulated real conditions are obtained. Finally, considering the force compression of the hydraulic cylinder of the column, the rigid-flexible and machine-liquid coupling dynamic simulation model of the hydraulic support with clearance is constructed. The loading test proves that the force compression of the hydraulic cylinder has a great influence on the attitude of the hydraulic support, indicating that when adjusting the attitude of the hydraulic support, the theoretical flow calculation cannot be used, and the column length should be directly measured. In this paper, the analytic method of the hydraulic support attitude is studied and verified using numerical calculation and simulation analysis, and the rigid-flexible coupling dynamic simulation model is built to study the various factors affecting the hydraulic support attitude. The research results of this paper can provide a theoretical basis and technical support for the attitude monitoring and control of hydraulic support.

Keywords: analysis of hydraulic support attitude, simulation analysis, rigid-flexible coupling, axis pin connection clearance, hydraulic cylinder stiffness

Highlights

- *The forward and inverse solution algorithm of hydraulic support attitude based on front and rear columns double drive length is proposed, and a method of hydraulic support attitude monitoring and control based on column length is proposed.*
- *The influence of material elastic deformation and axis pin connection clearance on the attitude of hydraulic support and its causes are explored, and the actual attitude and variation characteristics of hydraulic support under simulated real conditions are obtained.*
- *Considering the force compression of the column hydraulic cylinder, the rigid-flexible and machine-liquid coupling dynamic simulation model of the hydraulic support with clearance is constructed, and the influence of the force compression of the hydraulic cylinder on the attitude of the hydraulic support is explored through the loading test.*

0 INTRODUCTION

With the National Development and Reform Commission and eight other ministries and commissions jointly issuing "guidance on accelerating the intelligent development of coal mines", China's intelligent coal mine construction has entered a new stage [1] to [3]. The intelligent mining technology of the working face, which is mainly characterized by intelligent, cooperative control of a fully mechanized mining equipment group, is the key to the construction of intelligent coal mines [4]. Hydraulic support is an important supporting equipment of fully mechanized mining face in the process of coal production. It is one of the key electromechanical equipment to realize the "few people" and "unmanned" of a fully mechanized mining face, which directly affects the production safety and mining efficiency of the whole fully mechanized mining face. Hydraulic supports play a crucial role in achieving automatic and intelligent mining on fully mechanized faces by providing adaptive support to the surrounding rock [5] and [6]. The ability of these supports to intelligently detect and precisely evaluate their position and attitude is fundamental to their effectiveness in adapting to the

*Corr. Author's Address: College of Mechanical and Electrical Engineering, Shandong University of Science and Technology, Qingdao, China, yang.yang@sdust.edu.cn

surrounding rock. However, challenges in this area remain unresolved.

To promote the intelligent development of coal mining and ensure the normal support attitude of hydraulic support, many experts and scholars at home and abroad have carried out research on the monitoring and control technology of hydraulic support attitude. Ren et al. [7] used multi-sensor measurement technology to collect 15 independent parameters of the full-position attitude of a fully mechanized mining equipment group and designed a multi-parameter measurement system for a full-position attitude of a fully mechanized mining equipment group. Li and Ren [8] pointed out that the measurement effect of the existing measurement technology is greatly affected by the geological conditions of the working face, and the measurement accuracy, comprehensiveness, and automation of the measurement parameters need to be further improved. Most mines still need to adopt traditional manual measurement methods. Pang et al. [9] proposed an analytical method for the attitude and height of hydraulic support based on the column jack stroke and the balance jack stroke drive and used three calculation methods for attitude analysis. Wang et al. [10] used UNITY3D software to establish the multi-axis pin constraint model of hydraulic support and realized the attitude solution and monitoring of hydraulic support under different axis pin clearance. Chen et al. [11] applied the fusion technology of wide-angle ultrasonic sensors and inclination sensors to the attitude monitoring of hydraulic support. Zhang et al. [12] proposed a hydraulic support attitude detection method based on the principle that three points can determine a plane. Liang et al. [13] used a grating tilt sensor to realize online hydraulic support attitude monitoring and proposed an error compensation method for tilt monitoring. Zeng et al. [14] used automated dynamic analysis of mechanical systems) (ADAMS) software to construct a numerical simulation model of hydraulic support and study the position and dynamic response of hydraulic support under double impact load. Ge et al. [15] used the virtual software Unity 3D to construct the coal mining working environment and realized the adjustment of the supporting attitude of the hydraulic support to the surrounding rock of the coal seam in the virtual environment. Wang et al. [16] used three red-green-blue-depth (RGB-D) cameras to obtain the point cloud of the hydraulic support from different angles to obtain the complete point cloud information of the hydraulic support and realize the attitude and straightness measurement of the hydraulic support group. Yang et al. [17] designed a novel method for measuring the attitude and straightness of hydraulic support based on the "motion process recovery method" and established an automatic online measurement system. According to the complementary characteristics of a magnetometer, accelerometer, and gyroscope, Lu et al. [18] designed a supporting attitude sensing system composed of an inertial measurement unit and micro-electro-mechanical system (MEMS). Wang et al. [19] and [20] proposed a real-time virtual monitoring method for intelligent, fully mechanized mining faces by using virtual reality monitoring technology and carried out intelligent monitoring of fully mechanized mining face driven by (VR) augmented reality (AR) and virtual reality (VR) fusion. Szurgacz et al. [21] introduced a new method for monitoring and detecting the cross-section geometry of hydraulic support based on a new measurement system for the torsion angle of mechanical elements of hydraulic support cross-section. The posture of hydraulic support is calculated based on the tilt angle of the roof beam, base beam, shield beam, and four-bar mechanism obtained with the tilt sensor. Szurgacz et al. [22] proposed hydraulic support design and test methods based on predicted loads affecting roof supports, selected support types, support component testing, and allowable support operating conditions, and based on analysis of safety and control systems, develop an integrated method for testing and evaluating the possibility of using hydraulic supports under specific mining and geological conditions.

The above research provides theoretical and engineering practice support for the attitude detection of hydraulic support. However, most of the existing detection methods use sensors to directly detect the attitude of executive parts such as the roof beam and shield beam or use a variety of sensor signal fusion methods to obtain the attitude information of hydraulic support. This leads to the use of a variety of sensors, a large number of sensors, and a high cost, which is not conducive to wide application. Moreover, these studies did not consider the impact of stent deformation and other factors on stent attitude monitoring.

To monitor and control the attitude of hydraulic support better and further explain the cause of attitude error of hydraulic support, an analytical model of hydraulic support attitude theory based on the length of front and rear columns is proposed. The attitude information of the whole hydraulic support can be obtained by the length of the front and rear columns. The support height and the inclination angle of each component can be calculated by the length of the front and rear columns. The length of the front and

rear columns can also be calculated using the support height and the inclination angle of the top beam to guide the attitude monitoring and control of the hydraulic support. The theoretical analytical model is verified by the simulation to ensure its accuracy and reliability, and three factors that may affect the monitoring and control accuracy are analysed to determine the influence of different factors on the analytical accuracy. The research results provide a more efficient method for attitude monitoring and control of hydraulic support, theoretical support for attitude analysis error analysis of hydraulic support, and in-depth technical support for attitude research of hydraulic support.

The main scientific contributions of this paper are as follows:

1. An algorithm for calculating the attitude of hydraulic support based on the double driving length of the front and rear columns is proposed, and a method for monitoring and controlling the attitude of hydraulic support based on the length of columns is further proposed.
2. The influence of elastic deformation of material and pin joint clearance on the attitude of hydraulic support and its causes are discussed, and the actual attitude and change characteristics of hydraulic support under simulated real conditions are obtained.
3. The hydraulic cylinder's force compression is considered and the rigid-flexible mechanical-hydraulic coupling dynamic simulation model of hydraulic support with clearance is established.

The detailed work of this paper is as follows. Section 1 establishes the kinematics mathematical model of hydraulic support, puts forward the forward and inverse solution algorithm of hydraulic support attitude based on double drive length of front and rear columns, and puts forward a method of hydraulic support attitude monitoring and control based on column length. Section 2 establishes the rigid body dynamics simulation model of hydraulic support and verifies the theoretical analysis model. Section 3 establishes the rigid-flexible coupling dynamic simulation model of hydraulic support to explore the influence of elastic deformation of components on the attitude of hydraulic support and its causes. Section 4 establishes the equivalent prototype of hydraulic support and further verifies the theoretical analysis model of hydraulic support attitude and the rigid body dynamics simulation model of hydraulic support through experiments. Section 5 establishes the rigid-flexible coupling dynamics simulation model of hydraulic support with clearance to explore the influence of pin clearance on the attitude of hydraulic support and its causes. Section 6 establishes the rigid-flexible and mechanical-hydraulic coupling dynamic simulation model of hydraulic support with clearance considering compression of the hydraulic cylinder and studies the influence of compression of the hydraulic cylinder on the attitude of hydraulic support through a loading test. Section 7 provides conclusions.

1 ANALYTICAL MODEL CONSTRUCTION OF HYDRAULIC SUPPORT ATTITUDE THEORY

1.1 Hydraulic Support Kinematics Mathematical Model Construction

The main moving parts of the four-column top coal caving hydraulic support include the base, the top beam, the shield beam, the front column, the rear column, the front connecting rod, and the rear connecting rod. The components are connected by axis pins, as shown in Fig. 1. The front column and the rear column are the driving components. The hydraulic cylinders of the two can be regarded as two sliding joints because they belong to two different kinematic branches; the hydraulic support can be regarded as a parallel robot with a top beam as an actuator [23].

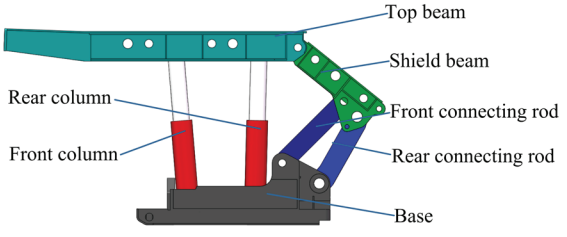

Fig. 1. *Four-column top coal caving hydraulic support main motion mechanism diagram*

The formula for calculating the degree of freedom of parallel mechanism is [24] and [25]

$$F = s \times (n - m - 1) + \sum_{i=1}^{m} f_i - v - q, \tag{1}$$

where s *is* the order of the mechanism, $s = 6 - \lambda$, λ the number of public constraints of the institution, n the number of components of the mechanism, m the number of motion pairs of the mechanism, f_i the number of relative degrees of freedom of the i^{th} motion pair, v the number of virtual constraint, and q local degree of freedom of the mechanism.

There are three common constraints in hydraulic support, so $\lambda = 3$, The order of the mechanism $s = 6 - \lambda = 6 - 3 = 3$. There are nine main moving parts

and 11 motion pairs in the hydraulic support, so $n=9$, $m=11$. There are no virtual constraints and local degrees of freedom, so $v=0$, $q=0$. The degree of freedom of the main motion mechanism of the four-column top coal caving hydraulic support can be calculated by Eq. (1) as follows:

$$F = 3\times(9-11-1)+11 = 2. \tag{1}$$

Since the hydraulic cylinders of the front and rear columns provide two drives, the number of drives is equal to the number of degrees of freedom, and the mechanism has a certain movement [26] and [27]. When the length of the front and rear columns is known, the support height and the inclination angle of each component can be calculated by the forward kinematics solution. When the support height and the inclination angle of the top beam are known, the length of the front and rear columns can also be calculated by inverse kinematics.

The virtual prototype of the hydraulic support is measured, and the axis pin connection clearance is not considered. According to the structural size, the equivalent two-dimensional bar diagram of the hydraulic support shown in Fig. 2 is drawn [28].

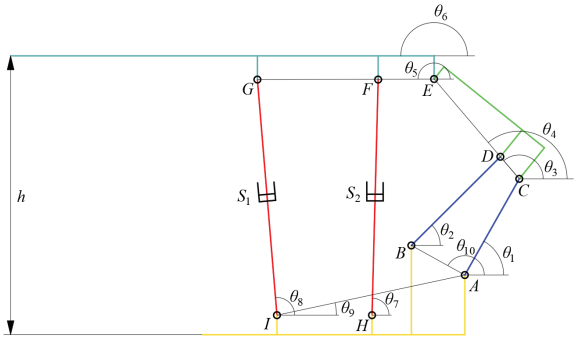

Fig. 2. *Hydraulic support equivalent two-dimensional bar diagram*

There are three kinematic chains from the base to the top beam, and the vector loop equations are

$$\begin{cases} \overline{AC}+\overline{CD}=\overline{AB}+\overline{BD} \\ \overline{HI}+\overline{IG}=\overline{HF}+\overline{FG} \\ \overline{IA}+\overline{AC}+\overline{CE}+\overline{EG}=\overline{IG} \end{cases}. \tag{2}$$

The nonlinear equations with S_1, S_2, and θ as variables can be obtained from this vector loop equation.

$$\begin{cases} L_{AC}\times\sin\theta_1+L_{CD}\times\sin\theta_3=L_{AB}\times\sin\theta_{10}+L_{BD}\times\sin\theta_2 \\ L_{HI}\times\sin\pi+S_1\times\sin\theta_3=S_2\times\sin\theta_7+L_{FG}\times\sin\theta_6 \\ L_{IA}\times\sin\theta_9+L_{AC}\times\sin\theta_1+L_{CE}\times\sin\theta_4+L_{EG} \\ \times\sin\theta_5=L_{IG}\times\sin\theta_8 \\ L_{AC}\times\cos\theta_1+L_{CD}\times\cos\theta_3=L_{AB}\times\cos\theta_{10}+ \\ L_{BD}\times\cos\theta_2 \\ L_{HI}\times\cos\pi+S_1\times\cos\theta_3=S_2\times\cos\theta_7+L_{FG}\times\cos\theta_6 \\ L_{IA}\times\cos\theta_9+L_{AC}\times\cos\theta_1+L_{CE}\times\cos\theta_4+ \\ L_{EG}\times\sin\theta_5=L_{IG}\times\sin\theta_8 \\ \theta_{10}=\pi-\arctan\dfrac{265}{478} \\ \theta_3=\theta_4+0.07 \\ \theta_5=\theta_6+0.18 \end{cases} \tag{3}$$

The distance from the front end of the top beam to the ground is the support height h, and the relationship between the support height h and other variables can be expressed as

$$\begin{cases} h=175+S_1\times\sin\theta_8+213\times\sin(\theta_6-\dfrac{\pi}{2})+2207\times\sin\theta_6 \\ h=175+S_2\times\sin\theta_7+213\times\sin(\theta_6-\dfrac{\pi}{2})+3287\times\sin\theta_6 \end{cases}. \tag{4}$$

The relationship between S_1, S_2 and h and other variables can be obtained by deformation.

$$\begin{cases} S_1=\dfrac{h-175-213\times\sin(\theta_6-\dfrac{\pi}{2})-2207\times\sin\theta_6}{\sin\theta_8} \\ S_2=\dfrac{h-175-213\times\sin(\theta_6-\dfrac{\pi}{2})-3287\times\sin\theta_6}{\sin\theta_7} \end{cases}. \tag{5}$$

For the forward solution, under the premise that S_1 and S_2 are known, the forward solution equations of kinematics can be obtained by combining Eqs. (3) and (4).

$$\begin{cases} L_{AC}\times\sin\theta_1+L_{CD}\times\sin\theta_3=L_{AB}\times\sin\theta_{10}+L_{BD}\times\sin\theta_2 \\ L_{HI}\times\sin\pi+S_1\times\sin\theta_3=S_2\times\sin\theta_7+L_{FG}\times\sin\theta_6 \\ L_{IA}\times\sin\theta_9+L_{AC}\times\sin\theta_1+L_{CE}\times\sin\theta_4+L_{EG}\times\sin\theta_5=L_{IG}\times\sin\theta_8 \\ L_{AC}\times\cos\theta_1+L_{CD}\times\cos\theta_3=L_{AB}\times\cos\theta_{10}+L_{BD}\times\cos\theta_2 \\ L_{HI}\times\cos\pi+S_1\times\cos\theta_3=S_2\times\cos\theta_7+L_{FG}\times\cos\theta_6 \\ L_{IA}\times\cos\theta_9+L_{AC}\times\cos\theta_1+L_{CE}\times\cos\theta_4+L_{EG}\times\sin\theta_5=L_{IG}\times\sin\theta_8 \\ \theta_{10}=\pi-\arctan\dfrac{265}{478} \\ \theta_3=\theta_4+0.07 \\ \theta_5=\theta_6+0.18 \\ h=175+S_1\times\sin\theta_8+213\times\sin(\theta_6-\dfrac{\pi}{2})+2207\times\sin\theta_6 \\ h=175+S_2\times\sin\theta_7+213\times\sin(\theta_6-\dfrac{\pi}{2})+3287\times\sin\theta_6 \end{cases} \tag{6}$$

For the inverse solution, under the premise that the support height h and the top beam inclination angle θ_6 are known, the inverse solution equations can be obtained by combining Eqs. (3) and (5).

$$\begin{cases} L_{AC}\times\sin\theta_1 + L_{CD}\times\sin\theta_3 = L_{AB}\times\sin\theta_{10} + L_{BD}\times\sin\theta_2 \\ L_{HI}\times\sin\pi + S_1\times\sin\theta_3 = S_2\times\sin\theta_7 + L_{FG}\times\sin\theta_6 \\ L_{IA}\times\sin\theta_9 + L_{AC}\times\sin\theta_1 + L_{CE}\times\sin\theta_4 + \\ L_{EG}\times\sin\theta_5 = L_{IG}\times\sin\theta_8 \\ L_{AC}\times\cos\theta_1 + L_{CD}\times\cos\theta_3 = L_{AB}\times\cos\theta_{10} + L_{BD}\times\cos\theta_2 \\ L_{HI}\times\cos\pi + S_1\times\cos\theta_3 = S_2\times\cos\theta_7 + L_{FG}\times\cos\theta_6 \\ L_{IA}\times\cos\theta_9 + L_{AC}\times\cos\theta_1 + L_{CE}\times\cos\theta_4 + \\ L_{EG}\times\sin\theta_5 = L_{IG}\times\sin\theta_8 \\ \theta_{10} = \pi - \arctan\dfrac{265}{478} \\ \theta_3 = \theta_4 + 0.07 \\ \theta_5 = \theta_6 + 0.18 \\ h = 175 + S_1\times\sin\theta_8 + 213\times\sin(\theta_6 - \dfrac{\pi}{2}) + 2207\times\sin\theta_6 \end{cases} . \quad (7)$$

$$\begin{cases} h = 175 + S_2\times\sin\theta_7 + 213\times\sin(\theta_6 - \dfrac{\pi}{2}) + 3287\times\sin\theta_6 \\ S_1\times\sin\theta_8 = h - 175 - 213\times\sin(\theta_6 - \dfrac{\pi}{2}) - 2207\times\sin\theta_6 \\ S_2\times\sin\theta_7 = h - 175 - 213\times\sin(\theta_6 - \dfrac{\pi}{2}) - 3287\times\sin\theta_6 \end{cases},$$

1.2 Forward and Inverse Attitude Solution of Hydraulic Support Based on Iterative Approach Principle

In science and engineering, the solution of nonlinear equations is a very important topic. The traditional Newton iterative method and the string cut method have serious initial value dependence and local convergence. Therefore, in the process of forward and inverse solutions, the traditional analysis method is not used, but the *fsolve* function in MATLAB is used to numerically solve the two nonlinear equations. The *fsolve* function defaults to the trust-region-dogleg algorithm, and its core is to use the trust region to compensate for the limitations of the Newton method [29].

The nonlinear equations of forward solution are written into MATLAB, and the *fsolve* function is used for calculation. The forward solution algorithm is as follows [30] and [31].

```
S1 = 2119.2297; S2 = 2112.7186;
f = @(x)([990*cos(x(1)) + 260.4611*cos(x(3)) -
546.5428*cos(pi - arctan(265/478)) - 1125*cos(x(2));
    990*sin(x(1)) + 260.4611*sin(x(3)) - 546.5428*
sin(pi - arctan(265/478)) - 1125*sin(x(2));
    850*-1 + S1*cos(x(8)) - S2*cos(x(7)) -
1080*cos(x(6));
    850*0 + S1*sin(x(8)) - S2*sin(x(7)) -
1080*sin(x(6));
    1718.1385*cos(arctan(360/1680)) + 990*cos(x(1)) +
1175.3931*cos(x(4)) + 1580*cos(x(5)) - S1*cos(x(8));
    1718.1385*sin(arctan(360/1680)) + 990*sin(x(1)) +
1175.3931*sin(x(4)) + 1580*sin(x(5)) - S1*sin(x(8));
    0.00314 - x(5) + x(6);
    0.00122 - x(3) + x(4);]);
x = fsolve(f,[1 1 1 1 3 3 1 1])
h = S1*sin(x(8)) + 175 + 213*sin(x(6) - pi/2) +
2207*sin(x(6))
qingjiao = x(6)
```

After inputting the length S_1 and S_2 of the front and rear columns, the support height *h*, the top beam inclination angle *qingjiao,* and the inclination angle of each component are obtained.

Similarly, the nonlinear equations of the inverse solution are written into MATLAB, and the *fsolve* function is called to calculate. The inverse solution algorithm is as follows.

```
h = 2500; p = pi;
f = @(x)([990*cos(x(1)) + 260.4611*cos(x(3)) -
546.5428*cos(pi - arctan(265/478)) - 1125*cos(x(2));
    990*sin(x(1)) + 260.4611*sin(x(3)) - 546.5428*
sin(pi - arctan(265/478)) - 1125*sin(x(2));
    850*-1 + (h - 175 - 213*sin(p - pi/2) - 2207*sin(p))/
sin(x(8))*cos(x(8)) - x(6)*cos(x(7)) - 1080*cos(p);
    850*0 + (h - 175 - 213*sin(p - pi/2) - 2207*sin(p))/
sin(x(8))*sin(x(8)) - x(6)*sin(x(7)) - 1080*sin(p);
    1718.1385*cos(arctan(360/1680)) + 990*cos(x(1)) +
1175.3931*cos(x(4)) + 1580*cos(x(5)) - (h - 175 - 213*
sin(p - pi/2) - 2207*sin(p))/sin(x(8))*cos(x(8));
    1718.1385*sin(arctan(360/1680)) + 990*sin(x(1)) +
1175.3931*sin(x(4)) + 1580*sin(x(5)) - (h - 175 - 213*
sin(p - pi/2) - 2207*sin(p))/sin(x(8))*sin(x(8));
    0.00314 - x(5) + p;
    0.00122 - x(3) + x(4);]);
x = fsolve(f,[1 1 1 1 3 2000 1 1])
S1 = (h - 175 - 213*sin(p - pi/2) - 2207*sin(p))/
sin(x(8))
S2 = x(6)
```

After inputting the support height h and the top beam inclination angle p, the lengths S_1 and S_2 of the front and rear columns are obtained.

1.3 Attitude Monitoring and Control Method of Hydraulic Support Based on Theoretical Analysis

In practical application, the displacement sensor can be used to monitor the length of the column to realize the attitude monitoring and control of the hydraulic support. For example, if you want to control the hydraulic support with a top beam angle to a certain support height, you only need to input the required support height and top beam angle into the forward solution program to obtain the required length of the front and rear columns, and then control the hydraulic system according to the reading of the displacement sensor. Drive the front and rear columns to the calculated length to complete the hydraulic support attitude control. Similarly, if you want to monitor the attitude of the hydraulic support, you only need to read the length of the front and rear columns through the displacement sensor and enter the forward solution program to obtain the height and angle information of the current top beam and the inclination angle of each component. The process continues to achieve continuous monitoring of the hydraulic support, and its monitoring and control process is shown in Fig. 3.

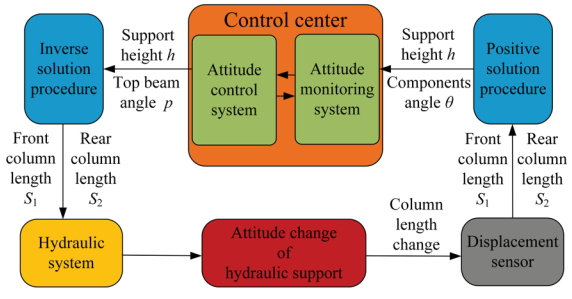

Fig. 3. *Hydraulic support attitude monitoring and control process*

2 VERIFICATION OF THEORETICAL ANALYTICAL MODEL OF HYDRAULIC SUPPORT BASED ON DYNAMIC SIMULATION

2.1 The Rigid Body Simulation Model of Hydraulic Support is Established

The three-dimensional model of the hydraulic support is imported into ADAMS through the ".xt" file interface. Rotating pairs are added at each hinge point of the hydraulic support, the direction is consistent with the direction of the hinge point rotation axis. Moving pairs are added between the piston rod and hydraulic cylinder of the column and the tail beam jack, and the direction is consistent with the axial direction of the piston rod. Ball pairs are added between the column sockets of the column and the top beam and the base, and fixing pairs are added between the base and the ground, as shown in Fig. 4. Because this paper mainly studies the relationship between the front and rear columns and the attitude of the hydraulic support, a 0-size drive is added to the moving pair between the insert plate and the tail beam and between the insert plate and the tail beam to make it temporarily fixed, while the corresponding driving function is added to the moving pair on the four columns for simulation test.

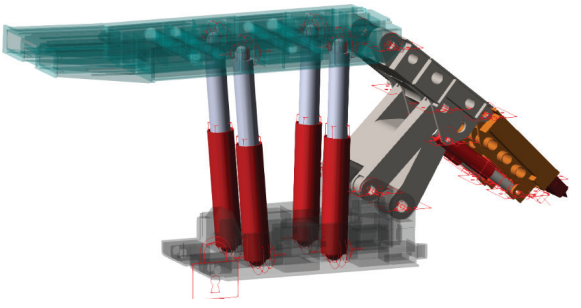

Fig. 4. *Rigid body simulation model of hydraulic support*

From 1700 mm to 2500 mm, a support height is taken every 10 mm, and the top beam inclination angle $p = pi$ is taken. The theoretical and analytical data of front and rear column lengths S_1 and S_2 under different support heights are input into MATLAB, respectively.

In ADAMS, a point drive is added to the top beam to make the top beam move downward horizontally. A reference quantity is taken every 10 mm from 0 mm to 800 mm to test, corresponding to the support height of 1700 mm to 2500 mm. The distance between the ball pairs at both ends of the front and rear columns is measured to obtain the simulation data of the length of the front and rear columns.

2.2 Verification of Theoretical Analytical Model of Hydraulic Support Based on Rigid Simulation

Some test data records the length of the front and rear columns at different support heights. Based on the simulation data, the inverse solution error of the theoretical analytical model is calculated, as shown in Fig. 5.

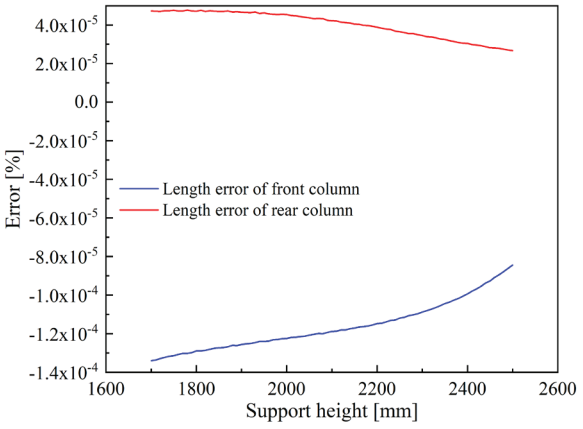

Fig. 5. *Error analysis of theory analytical inverse solution*

From the analysis of the results, the errors of the two are increasing with the decrease in support height. The maximum error of the length calculation of the front column appears when the support height is 1700 mm, which is -1.3397×10^{-4} %. The maximum error of the length calculation of the rear column appears when the support height is 1700 mm, which is 4.73114×10^{5} %. The error is very small, which can meet the requirements of regulating the attitude of hydraulic support through inverse kinematics. It is proved that the theoretical analysis method of inverse kinematics is correct, and the rigid body simulation model is correct.

Table 1. *Theoretical analysis and rigid body simulation support height data under different front and rear column lengths*

Length of front column [mm]	Length of rear column [mm]	Theoretical analysis data	Rigid body simulation data
		Support height [mm]	Support height [mm]
2100	2100	2467.1747	2467.1680
2000	2000	2365.7415	2365.7341
1900	1900	2265.1403	2265.1325
1800	1800	2164.7995	2164.7916
1700	1700	2064.3262	2064.3184
1600	1600	1963.4376	1963.4301
1500	1500	1861.9223	1861.9150
1400	1400	1759.6215	1759.6145

In MATLAB, the lengths S_1 and S_2 of multiple front and rear pillars are input into the forward solution algorithm to obtain the corresponding support height. In ADAMS, the drive is added to the moving pairs on the front and rear columns, respectively, so that the front and rear reach the corresponding length input in the forward solution algorithm, and the simulation data of the support height are measured, some data of support height under different column lengths are shown in Table 1.

Based on the rigid body simulation data, the forward solution error of the theoretical analytical data is calculated, as shown in Fig. 6.

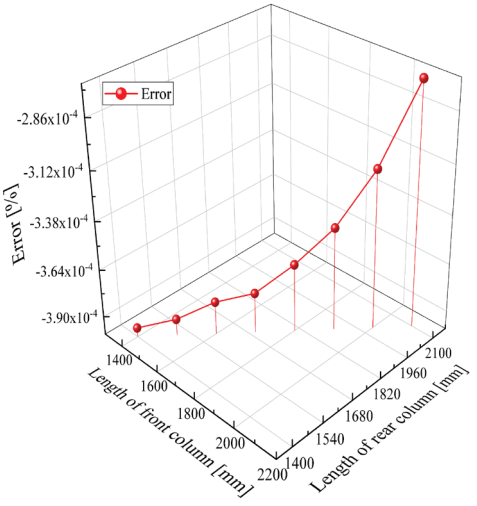

Fig. 6. *Error analysis of theory analytical forward solution*

From the analysis of the results, as the length of the front and rear columns decreases, the error of the support height increases; the maximum error is -3.9498×10^{-4} % when the length of the front and rear columns is 1400 mm. The error is very small, which can meet the requirements of regulating the attitude of hydraulic support through forward kinematics. It is proved that the theoretical analysis method of forward kinematics is correct, and the rigid body simulation model is correct.

The rigid body simulation model can be used as a hydraulic support attitude monitoring system. The real-time change of the hydraulic support attitude can be displayed by inputting the length data of the front and rear columns into the simulation system.

3 ATTITUDE ANALYSIS OF HYDRAULIC SUPPORT CONSIDERING DEFORMATION

3.1 Dynamic Simulation Model Construction of Rigid-Flexible Coupling Hydraulic Support

In the actual production process, although the length of the front and rear columns can be accurately monitored and used as a known quantity to calculate the hydraulic support's attitude information, the hydraulic support will inevitably deform due to its own weight and the pressure from the roof, which

will negatively impact the hydraulic support's attitude control and monitoring.

To make the simulation closer to the real working condition and explore the influence of component deformation on attitude control and monitoring of hydraulic support, a rigid-flexible coupling dynamic simulation model of hydraulic support is established, as shown in Fig. 7. In hyper-mesh software, mesh division is carried out on the top beam, shield beam, front connecting rod, rear connecting rod, tail beam and plugboard of hydraulic support through its pre-processing function [32] to [35]. Specific parameters of flexible body parts are as follows: mesh type: tetrahedral mesh, mesh size: 30 mm, material type: isotropic, elastic modulus E: 21000 MPa, shear modulus G: 81000 MPa, Poisson ratio: 0.3, density: 7860 kg/m^3, constraint mode number: 6. After mesh division is completed, a flexible volume file with suffix '.mnf' is generated. Based on the rigid simulation model of hydraulic support established in Section 2.1, rigid parts are accurately replaced by corresponding flexible body parts by the "three-point method" [36] to [38], and flexible body parts are linked by rigid nodes and rotating pairs. In the rigid-flexible coupling dynamics simulation model of hydraulic support, the base and column are rigid parts, and the column is connected with the top beam and the column socket of the base by ball pairs. The piston rods and hydraulic cylinders of the front and rear columns are connected by a moving pair, and drive is added to the moving pair to drive the columns to present different lengths.

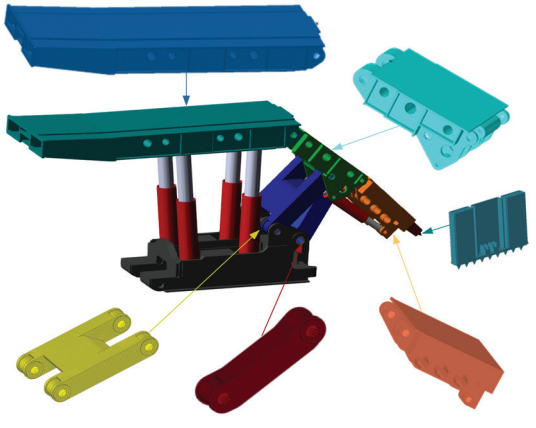

Fig. 7. *Rigid-flexible coupling dynamic simulation model of hydraulic support*

3.2 Attitude Error Analysis of Hydraulic Support Considering Material Deformation

The length of the front and rear pillars and the support height in the rigid body simulation data are taken, and the driving function of the front and rear pillars in the rigid-flexible coupling model of the hydraulic support is adjusted to make the front and rear pillars reach the multiple sets of test lengths in rigid body simulation in turn. The support height h is measured and recorded.

The attitude error of the rigid-flexible coupling simulation data is calculated based on the rigid body simulation data, as shown in Fig. 8.

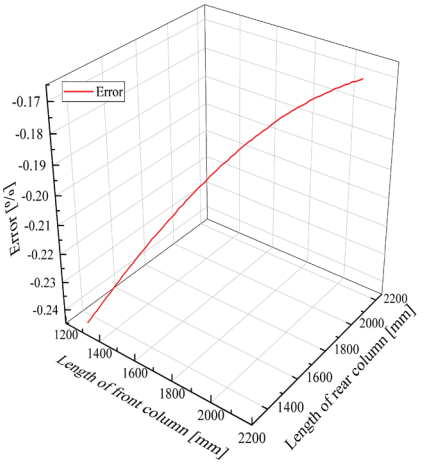

Fig. 8. *Rigid-flexible coupling dynamics simulation error of hydraulic support*

From the analysis of the results, the maximum error occurs when the length of the front column is 1323.0649 mm, the length of the rear column is 1323.0649 mm, and the error is -0.2412 mm. The minimum error is -0.1679 mm when the length of the front column is 2119.2297 mm, and the length of the rear column is 2112.7186 mm. The average error is -0.1948 mm. This error is only considering the weight of the hydraulic support, and the deformation of each component is small. If the hydraulic support is in the bearing state to bear the roof pressure, this error will be amplified. The error curve in Fig. 8. shows that as the length of the front and rear columns decreases, the error of the support height increases. To explore the causes of this trend, the force of the hinge points of each component at different heights is measured, and the force change curve is obtained, as shown in Fig. 9. From the curve, it can be seen that with the shortening of the front and rear columns, the height of the support decreases, and the force at the hinge point of the rear connecting rod-base, the rear connecting rod-shield beam and shield beam-top beam increases obviously. Due to the increase in force, deformation will inevitably increase, which will lead to an increase in error. This error is only considering the self-weight of the hydraulic support, and the deformation of each

component is small. If the hydraulic support is in the bearing state to bear the roof pressure, this error will be amplified. Therefore, in the process of monitoring or regulating the attitude of the hydraulic support, it is necessary to consider the error caused by the deformation of the hydraulic support.

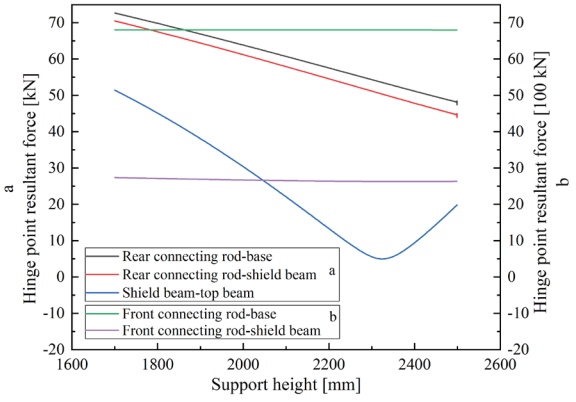

Fig. 9. *Hydraulic support rigid-flexible coupling dynamics simulation hinge point force analysis*

4 EXPERIMENTAL VERIFICATION OF ATTITUDE ANALYSIS BASED ON EQUAL SCALE PROTOTYPE OF HYDRAULIC SUPPORT

4.1 Establishment of Experimental System for Attitude Analysis of Hydraulic Support

According to the hinge position and component length of the two-dimensional rod system model of hydraulic support in Fig. 1, the equivalent prototype of each component of hydraulic support with equal scale of 20:1 is obtained, as shown in Fig. 10. Four column lengths of 2100 mm, 1900 mm, 1700 mm, and 1500 mm (the size in the equivalent prototype is 105, 95, 85, 75, respectively) are selected to obtain equivalent column links of four lengths as shown in Fig. 11.

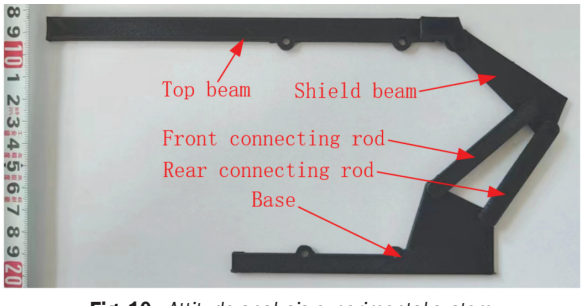

Fig. 10. *Attitude analysis experimental system of hydraulic support*

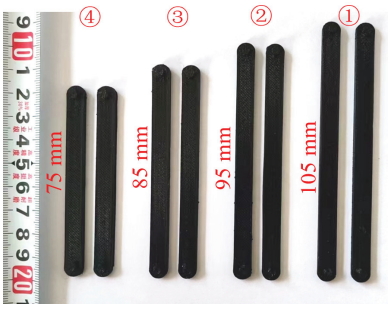

Fig. 11. *Hydraulic support column equivalent links*

4.2 Inverse Solution Experiment of Hydraulic Support Attitude

Respectively adjust the support height of hydraulic support to 2500 mm, 2300 mm, 2100 mm, and 1900 mm (The size in the equivalent prototype is 125, 115, 105, and 95, respectively), and the top beam is parallel to the base plate. A vernier caliper is used to measure the column lengths S_1 and S_2 under four different heights, as shown in Fig. 12.

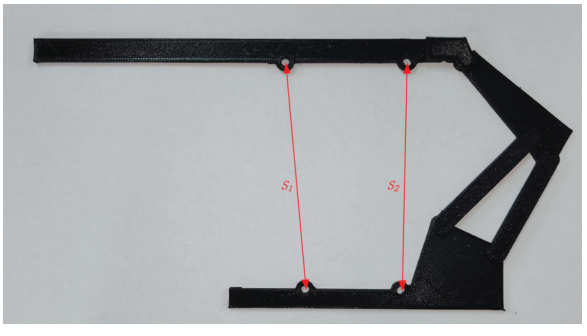

Fig. 12. *Inverse solution experiment of hydraulic support attitude*

4.3 Forward Solution Experiment of Hydraulic Support Attitude

The equivalent connecting rod for four kinds of column length is installed in the attitude analysis experimental system of hydraulic support, and the vertical distance (support height) from the front end of the top beam to the bottom of the base is measured by a vernier caliper. Thus, the support height parameters of hydraulic support under four kinds of column lengths are obtained, as shown in Fig. 13.

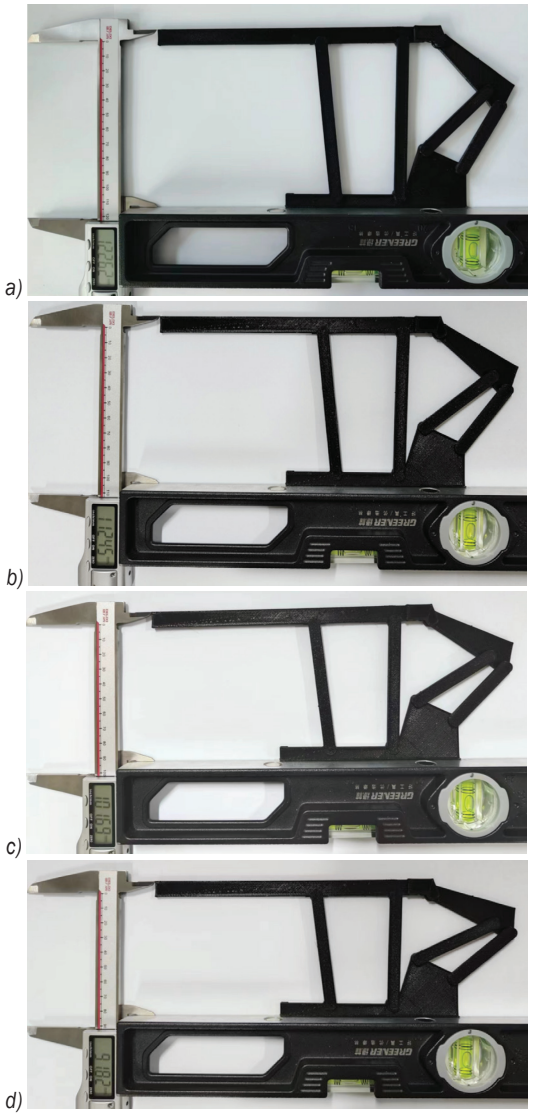

Fig. 13. *Forward solution experiment of hydraulic support attitude at column length: a) 105 mm, b) 95 mm, c) 85 mm, and d) 75 mm*

4.4 Analysis of Experimental Results of Attitude Analysis of Hydraulic Support

The length of the front and rear columns obtained from the inverse solution experiment of hydraulic support attitude is compared with the theoretical analysis value, and the error between them is analysed. The experimental analysis data are shown in Table 2.

According to the experimental results of the hydraulic support inverse solution, the theoretical analytical value is compared with the experimental value, and the error is less than 1 %.

The length of the front and rear columns obtained from the forward solution experiment of hydraulic support attitude is compared with the theoretical analysis value, and the error between them is analysed. The experimental analysis data are shown in Table 3.

Table 2. *Comparison of inverse solution results*

Support height [mm]	Theoretical analysis [mm]		Experimental calculation [mm]		Error [%]	
	S1	S2	S1	S2	S1	S2
125	105.96	105.64	105.50	105.33	0.43	0.29
115	96.00	95.64	95.10	95.32	0.94	0.33
105	86.02	85.65	85.85	85.01	0.20	0.75
95	76.07	75.66	75.98	75.21	0.12	0.59

Table 3. *Comparison of forward solution results*

Column length [mm]	Theoretical analysis [mm]	Experimental calculation [mm]	Error [%]
105	123.36	122.62	0.60
95	113.26	112.45	0.72
85	103.22	101.69	1.48
75	93.10	91.82	1.37

According to the experimental results of the hydraulic support forward solution, the theoretical analytical value is compared with the experimental value, and the error is less than 1.5 %.

5 ANALYSIS OF THE INFLUENCE OF CLEARANCE ON THE ATTITUDE OF HYDRAULIC SUPPORT

5.1 Construction of Rigid-Flexible Coupling Dynamics Simulation Model of Hydraulic Support with Clearance

Ideally, due to the four-link structure of the support, stable movement is achieved on the premise of maintaining stability. However, due to the constraints of production design, assembly error, friction, and wear, it is inevitable that there will be a clearance between the axis pin and the pinhole of each hinge point, which will affect the overall attitude of the support. In order to ensure the accuracy of attitude monitoring and control of hydraulic support **[39]** to **[41]**, it is necessary to study it.

Based on the rigid-flexible coupling model of the hydraulic support in Fig. 7, in the third section, the revolute joints of the hinge points of each component are deleted, and then the axis pin is added at the shaft hole. The axis pin material, length, and size are shown in Table 4. Collision contact constraints are added between the axis pin and the two connected components, respectively. The rigid-flexible coupling dynamic simulation model of the hydraulic support with clearance is shown in Fig. 14.

Table 4. *Axis pin parameter*

Position	Axis pinhole diameter [mm]	Axis pin diameter [mm]	Axis pin length [mm]	Axis pin material
Top beam Shield beam	101	100	500	40Cr
Shield beam Front connecting rod	101	100	380	40Cr
Shield beam Rear connecting rod	140	139	550	40Cr
Base Front connecting rod	101	100	380	40Cr
Base Rear connecting rod	140	139	550	40Cr

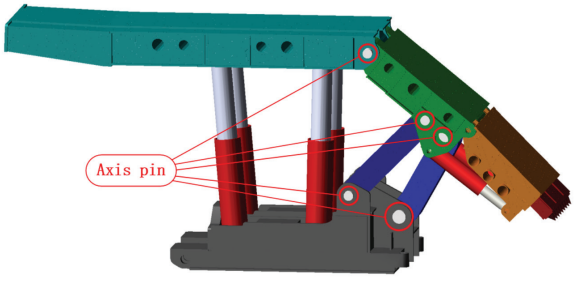

Fig. 14. *Rigid-flexible coupling dynamics simulation model of hydraulic support with clearance*

The lengths of the front and rear pillars are changed to the corresponding lengths of the support height of 2490 mm, which are 2109.2965 mm and 2102.7118 mm, respectively.

5.2 Analysis of Hydraulic Support Attitude Error Considering Axis Pin Connection Clearance

The change of support height with the length of the front and rear columns are shown in Fig. 15. From Fig. 15 it can be seen that the error between it and the rigid body simulation support height is about 2 mm. When the length of the front column is 2109.2965 mm, and the length of the rear column is 2102.7118 mm, the rigid-flexible coupling dynamics simulation support height of the hydraulic support with clearance is 2492.2649 mm, while the rigid body simulation support height is 2490 mm, and the error is 2.2649 mm. When the length of the front and rear columns just begins to decrease, the blue curve is below the red curve and then rises rapidly to the top of the red curve. The two curves intersect briefly. This is because the hydraulic support model is flexible except for the base. At the beginning of the simulation, the components are drooped by gravity, resulting in a decrease in the support height. Subsequently, because the influence of the axis pin connection clearance on the attitude of the hydraulic support is much greater than the influence of the elastic deformation due to gravity, the support height increases rapidly. The tail end of the top beam is reduced due to the height of the axis pin clearance, and the length of the column is temporarily unchanged, resulting in the "head-up" phenomenon of the hydraulic support. This simulation model proves that the axis pin connection clearance has a great influence on the attitude monitoring and control of the hydraulic support, which is a factor that must be considered.

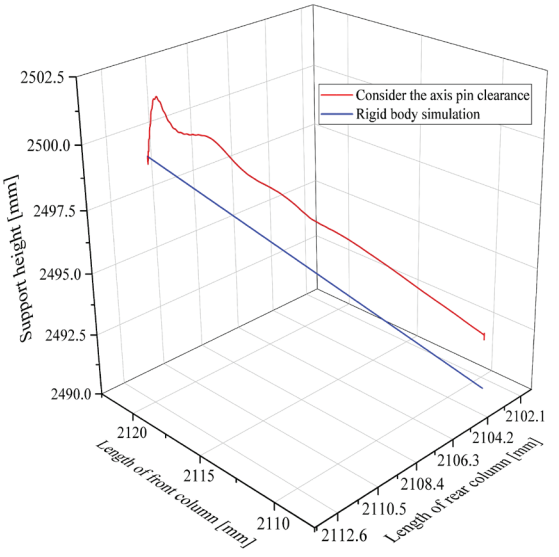

Fig. 15. *Comparison of support height between rigid-flexible coupling dynamics simulation and rigid body simulation of hydraulic support with clearance*

6 STUDY ON DYNAMIC PERFORMANCE OF RIGID-FLEXIBLE AND MACHINE-LIQUID COUPLING OF HYDRAULIC SUPPORT WITH CLEARANCE

6.1 Construction of Rigid-Flexible and Machine-Liquid Coupling Dynamics Simulation Model of Hydraulic Support with Clearance

When the attitude adjustment of the hydraulic support is carried out by calculating the theoretical flow, the force compression of the column hydraulic cylinder will lead to the deviation between the actual attitude and the expected attitude of the hydraulic support. Therefore, it is necessary to study the force compression and variable stiffness of the hydraulic cylinder before and after the hydraulic support.

In the hydraulic cylinder system of the front and rear columns, the volume of the hydraulic oil in the

hydraulic cylinder is not immutable when subjected to external pressure, and it is gradually compressed with the increase of external pressure, similar to the compressed spring, so the hydraulic oil in the rod cavity and the rodless cavity of the hydraulic cylinder can be equivalent to a certain stiffness spring. The stiffness of the hydraulic cylinder can be composed of two parts, one is the emulsion stiffness, and the other is the piston rod stiffness. Because the bulk modulus of the hydraulic oil is Kv = 1.4 GPa to 2 GPa, and the bulk modulus of the steel is between 196 GPa to 206 GPa, which is 100 to 150 times that of the hydraulic oil, the piston rod can be treated as a rigid body [42] to [44]. The structural characteristics of the hydraulic cylinder are shown in Fig. 16.

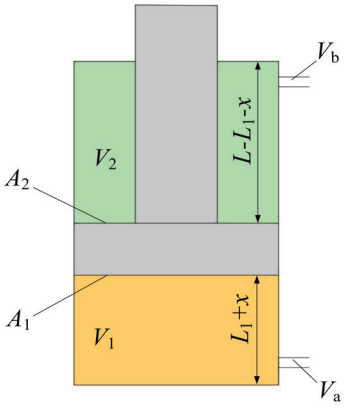

Fig. 16. *Column hydraulic cylinder structure diagram*

In Fig. 16 each symbol means: A_1 is the cross-sectional area of the rodless chamber piston of the hydraulic cylinder,

A_2 the cross-sectional area of the hydraulic cylinder rod cavity, L effective stroke of hydraulic cylinder, L_1 the current oil height of hydraulic cylinder rodless cavity, x vibrational displacement of the system, V_1 the volume of oil in rodless cavity of hydraulic cylinder, V_2 the volume of oil in the rod cavity of hydraulic cylinder, V_a the volume of oil in hydraulic cylinder rodless cavity hydraulic pipeline, and V_b the volume of oil in hydraulic cylinder rod cavity hydraulic pipeline.

The total equivalent stiffness of the hydraulic cylinder is

$$k = k_1 + k_2, \tag{8}$$

where k_1 is the equivalent stiffness of oil in the rodless cavity and k_2 is the equivalent stiffness of oil in the rod cavity.

$$k = \frac{pA}{x}. \tag{9}$$

The bulk modulus β_e of hydraulic oil is an important reference index for the classification and selection of hydraulic oil, which indicates the degree of compressibility of hydraulic oil in the hydraulic cylinder cavity. The larger the β_e, the more difficult the hydraulic oil in the hydraulic cylinder is to be compressed; the smaller the β_e, the easier the hydraulic oil in the hydraulic cylinder to be compressed. According to the compressible characteristics of hydraulic oil, the bulk modulus of hydraulic oil can be obtained as

$$\beta_e = \frac{pV}{dV} = \frac{pV}{Ax}. \tag{10}$$

Substituting Eq. (10) into Eq. (9) can get:

$$k = \frac{\beta_e A^2}{V}. \tag{11}$$

According to the structural characteristics of hydraulic cylinder

$$V_1 = (L_1 + x)A_1 + V_a, \tag{12}$$

$$V_2 = (L - L_1 - x) \times A_2 + V_b. \tag{13}$$

Substituting Eqs. (12) and (13) into Eq. (11) can get

$$k_1 = \frac{\beta_e A_1^2}{(L_1 + x)A_1 + V_a}, \tag{14}$$

$$k_2 = \frac{\beta_e A_2^2}{(L - L_1 1x)A_2 + V_b}. \tag{15}$$

Substituting Eqs. (14) and (15) into Eq. (8) can get

$$k = k_1 + k_2 = \frac{\beta_e A_1^2}{(L_1 + x)A_1 + V_a} + \frac{\beta_e A_2^2}{(L - L_1 - x)A_2 + V_b}. \tag{16}$$

Since the values of x, V_a, and V_b are so small that they can be neglected in the calculation, Eq. (16) can be simplified to

$$k = \frac{\beta_e A_1}{L_1} + \frac{\beta_e A_2}{L - L_1}. \tag{17}$$

The structural parameters of the column hydraulic cylinder are shown in Table 5.

Table 5. *Column hydraulic cylinder structure parameters*

Hydraulic cylinder type	Hydraulic cylinder inner diameter	Piston rod diameter	Hydraulic cylinder effective stroke
Single stretching	230	210	1071

Eq. (17) is input into MATLAB, and the effective stroke L_1 is 1071 mm. According to the piston rod diameter of 210 mm and the hydraulic cylinder diameter of 230 mm, A_1 = 41547.5621 mm², A_2 = 6911.5037 mm² is calculated. Taking 5 º% emulsion as an example, β_e = 1.82×10³ MPa. Through MATLAB calculation, the oil height of the rodless cavity and the total equivalent stiffness curve of the column hydraulic cylinder are obtained, as shown in Fig. 17. It can be seen from the diagram that with the increase of the height of the rodless cavity oil, the total equivalent stiffness of the column hydraulic cylinder shows a trend of decreasing first and then increasing, and the slope is small and stable in the middle of 300 mm to 900 mm interval, while the slope is large and the change is fast in the 100 mm to 300 mm and 900 mm to 1000 mm intervals at both ends.

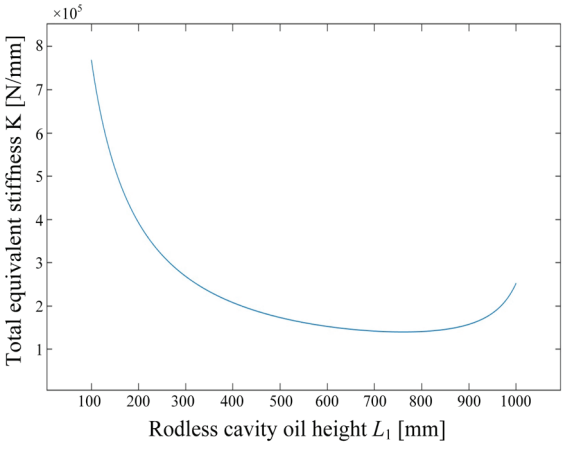

Fig. 17. *The change of total equivalent stiffness of column hydraulic cylinder*

The formula of oil height and column length can be obtained from the structure of the column hydraulic cylinder.

$$L_1 = L_0 - 1193, \tag{18}$$

where L_0 is the total length of the column.

After measurement, the length of the front column is 2119.2297 mm, and the length of the rear column is 2112.7186 mm. The front column L_1 is 923.2297 mm, and the rear column L_2 is 919.7186 mm. Substituting L_1 and L_2 into Eq. (17), the equivalent stiffness of the front and rear columns is 168528.1897 N/mm and 165366.3258 N/mm.

Based on the rigid-flexible coupling dynamic simulation model of the hydraulic support with clearance in Fig. 14, the four columns of the front and rear groups are replaced by the spring damping system.

The stiffness of the spring damping system that replaces the front and rear columns is set to the calculated value of the current height, and the rigid-flexible and machine-liquid coupling dynamics simulation model of the hydraulic support with clearance is completed, as shown in Fig. 18.

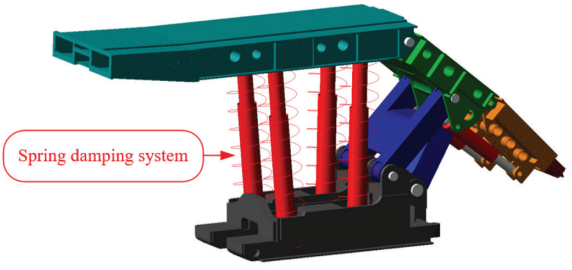

Fig. 18. *Rigid-flexible and machine-liquid coupling dynamics simulation model of hydraulic support with clearance*

The hydraulic support is statically loaded to test the attitude change of the support system under static load. Therefore, the static loading model of the hydraulic support is established as shown in Fig. 19.

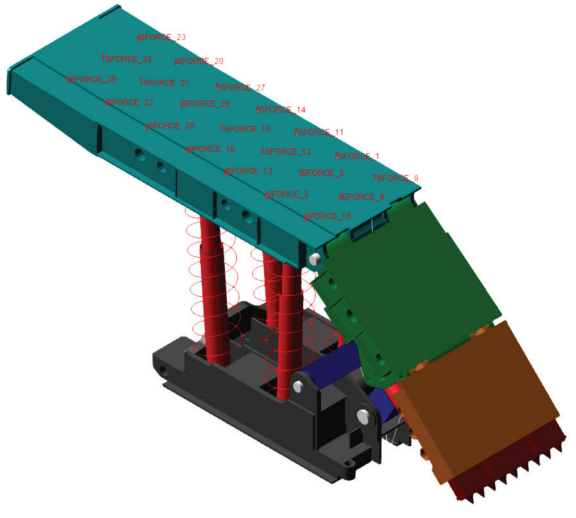

Fig. 19. *Static loading model of hydraulic support*

The rated working resistance of the hydraulic support studied in this paper is 5200 kN, so the vertical static load should be set to 5200 kN. Because the top beam is a flexible body, loading the working resistance directly at one point will cause abnormal deformation. Therefore, it is loaded with 21 loading positions at equal intervals. The force at each loading position is the same as 247619.0476 N, and the sum is the rated working resistance. The loading method is shown in Fig. 19. In order to avoid the formation of sudden load, the spring damping system makes

it difficult to restore the equilibrium state. The step function *STEP* (time, 0, 0, 0.5, 247619.0476) is used to increase the resultant force from 0 to the rated working resistance within 0.5 s, and the simulation time is set to 1 s.

6.2 Attitude Error Analysis of Hydraulic Support Considering Elastic Deformation of Hydraulic Cylinder

The change of the support height of the hydraulic support in the loading test is shown in Fig. 20. The support height begins to decrease from 2500 mm under the action of self-weight and working resistance, and finally stabilizes at 2409.1314 mm, and the reduction of the support height is 90.8686 mm. If it is loaded at other support heights, due to the change in hydraulic cylinder stiffness, the support height will change differently. The results show that in the process of attitude monitoring and regulation of hydraulic support if the length of the column is indirectly calculated by monitoring the flow, the actual attitude of the hydraulic support will have a great error with the expected attitude, which will have a negative impact on the attitude adjustment of the hydraulic support. Therefore, the theoretical flow calculation cannot be used when adjusting the attitude of the hydraulic support, and the length of the column should be directly measured.

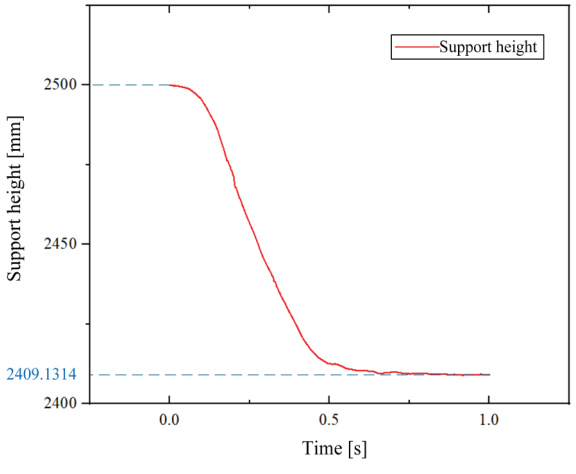

Fig. 20. *The change of support height in the loading test*

7 CONCLUSIONS

In this paper, a theoretical, analytical model of hydraulic support attitude based on the length of the front and rear columns is proposed, and a rigid body simulation model of hydraulic support is established to verify the theoretical, analytical model. Three factors that may affect the attitude monitoring and control accuracy of hydraulic support, such as material elastic deformation, Axis pin connection clearance, and hydraulic cylinder force compression, are analysed. The influence of various factors on the attitude of hydraulic support is studied, and the following conclusions were obtained:

1. The theoretical analytical model of hydraulic support attitude is proposed, which can solve the attitude of hydraulic support through the length of the front and rear columns. Based on this algorithm, a method of attitude monitoring and control of hydraulic support based on column length is proposed.
2. The rigid body simulation model of hydraulic support is established to verify the theoretical analytical model. The maximum error of forward and inverse solutions is not more than 4.73114×10^{-5} %, which proves that the theoretical analytical results are accurate and reliable and also proves the correctness of the rigid body simulation model. The rigid body simulation model can be used as a hydraulic support attitude monitoring system without considering the elastic deformation of the material and the clearance of the pin connection unit.
3. The rigid-flexible coupling dynamic simulation model of hydraulic support is constructed. When the support height is 1700 mm, the elastic deformation of hydraulic support components leads to the error of support height of hydraulic support of -0.2412 mm. As the length of the front and rear columns gradually decreases, the hinge point force under the self-weight condition of the hydraulic support gradually increases, which leads to an increase in the support height error. The elastic deformation factor has a smaller impact on the support attitude when the support height of the hydraulic support is higher.
4. The rigid-flexible coupling dynamic simulation model of hydraulic support with clearance is constructed; the support height is 2490 mm, compared with the rigid body simulation results, the support height error is 2.2649 mm, and the axis pin connection clearance is a factor that must be considered in the attitude solution of the hydraulic support.
5. The rigid-flexible and mechanical-hydraulic coupling dynamics simulation model of the hydraulic support with clearance is established. In the loading test with a support height of 2500 mm, the hydraulic support's height is reduced by

90.8686 mm. When the hydraulic support attitude is adjusted, the theoretical flow calculation cannot be used, and the column length should be directly measured.

6. Through the comparative analysis of the support height error of hydraulic support under three different influencing factors of material elastic deformation, axis pin connection clearance, and hydraulic cylinder force compression, it can be concluded that among the three influencing factors, the hydraulic cylinder force compression has the greatest influence on the attitude of hydraulic support, and the material elastic deformation has the least influence. Compared with the other two factors, the influence of material elastic deformation is only 1/9 or less.

The research provides theoretical support for the monitoring and control of hydraulic support attitude, which is of great significance to promoting intelligent mining in coal mines.

The limitation of this paper lies in only studying the position and attitude of hydraulic support and cannot obtain the position and attitude information of the whole hydraulic support in space, such as yaw angle, roll angle and pitch angle, and only studies a single hydraulic support. There are two directions for future research. Direction 1: Study the attitude of a base or hydraulic support in space and obtain the attitude information of the whole support in space through a single component. Direction 2: Calculate the overall position and attitude of the hydraulic support group and monitor the overall position and attitude of the support group through the geometric relationship of the adjacent frame.

The changing working attitude of hydraulic support significantly affects the support's bearing characteristics and may even damage its structural components. To ensure efficient, safe, continuous, and stable production in a comprehensive mechanized coal mining face, intelligent monitoring and proper control of the wave pressure support attitude are crucial to prevent shearer top beam cutting, balance jack breakage, and excessive top beam inclination. Many scholars have studied the attitude of hydraulic support deeply, such as the design of mine hydraulic support height measurement system based on an inclination sensor published by Huang et al. **[45]**, the design of hydraulic support posture dynamic monitoring and control system published by Lu et al. **[46]**, the sensing and data processing technology of hydraulic support state published by Pang et al. **[47]**, and the support posture and driving jack in the initial supporting stage published by Hu et al. **[48]**. These studies try to use different inclination sensors and different filtering algorithms to analyse the support attitude perception results of hydraulic support, develop hydraulic support attitude and support height monitoring system, improve the perception accuracy of inclination sensors and the analysis efficiency of hydraulic support attitude. These researches are based on a large number of sensors for information fusion, which is costly and difficult to apply and popularize. The attitude analysis method of hydraulic support proposed in this paper only needs two groups of sensors to measure the length of the front and rear columns, and the attitude information of hydraulic support can be obtained, which is less in the number of sensors and low in cost and easy to popularize.

8 DISCUSSION

Much research has been conducted on the position and attitude monitoring of hydraulic support, but there are differences in the types, numbers, and installations of sensors, as well as research priorities and directions.

For example, Chen et al. **[11]** studied the fusion technology of wide-angle ultrasonic sensor and inclination sensor in Research on attitude monitoring method of advanced hydraulic support based on multi-sensor fusion, which was applied to attitude monitoring of advanced hydraulic support in harsh underground environments. They established a measurement model based on advanced hydraulic support kinematics and then proposed yaw angle and roll angle calculation algorithms based on ultrasonic ranging data to achieve multi-sensor-based advanced hydraulic support attitude monitoring. Chen's research **[11]** calculates the position of hydraulic support through a variety of sensors, and the number of sensors is large, the variety is large, and the cost is high, which is not conducive to practical application. This paper only needs two groups of sensors to measure the length of the front and rear columns. The number of sensors is small, the cost is low, and it is easy to be popularized. Lu et al. **[18]** proposed a method for attitude monitoring of hydraulic support in A portable support attitude sensing system for accurate attitude estimation of hydraulic support based on an unscented Kalman filter. According to the complementary characteristics of a magnetometer, accelerometer, and gyroscope, a supporting attitude sensing system composed of an inertial measurement unit and MEMS was designed. The attitude of hydraulic support is improved by the multi-sensor information fusion method, but the emphasis is on the yaw angle, roll angle, and pitch angle of hydraulic support in space. Both this paper

and Lu's research are aimed at the attitude of hydraulic support, but the object of this paper is the posture of hydraulic support itself, which has not been studied by Lu et al. [18].

9 ACKNOWLEDGEMENT

This work was supported by National Natural Science Foundation of Shandong Province (Grant No. ZR2022QE022), Innovation Ability Improvement Project of Science and Technology smes in Shandong Province (Grant No. 2022TSGC2413), Jining City key research and development project (Grant No. 2022HHCG010).

10 REFERENCE

[1] Wang, G., Liu, F., Pang, Y., Ren, H., Ma, Y. (2019). Intelligent coal mine-core technical support for high-quality development of coal industry. *Journal of China Coal Society*, vol. 44, no. 2, p. 349-357, **DOI:10.13225/j.cnki.jccs.2018.2041**. (in Chinese)

[2] Wang, G., Ren, H., Pang, Y., Cao, X., Zhao, G., Chen, H., Du, Y., Mao, S., Xu, Y., Ren, S., Cheng, J., Liu, S., Fan, J., Wu, Q., Meng, X., Yang, J., Yu, B., Xuan, H., Sun, X., Zhang, D., Wang, H. (2020). Advances in research and engineering of coal mine intelligent (primary stage) technology system. *Coal Science and Technology*, vol. 48, no. 7, p. 1-27, **DOI:10.13199/j.cnki.cst.2020.07.001**. (in Chinese)

[3] Liu, F., Cao, W., Zhang, J., Cao, G., Guo, L. (2021). Progress of scientific and technological innovation in China ‘s coal industry and the development direction of the 14th Five-Year Plan. *Journal of China Coal Society*, vol. 46, no. 1, p. 1-15, **DOI:10.13225/j.cnki.jccs.2021.0042**. (in Chinese)

[4] Bao, J., Zhang, Q., Ge, S., Hu, E., Yuan, X., Yang, Y., Yin, Y., Lu, Y. (2023). Key basic research and application practice of unmanned auxiliary transportation system in coal mine. *Journal of China Coal Society*, vol. 48, no. 2, p. 1085-1098, **DOI:10.13225/j.cnki.jccs.2022.1600**. (in Chinese)

[5] Zhang, K., Sun, Z., Liu, Y., Li, Y., Du, M., Ma, Y., Wei, X., Xu, Y., Wang, X., Yu, T., Ding, C. (2023). Research and experimental verification of advanced hydraulic support attitude perception method based on information fusion technology. *Journal of China Coal Society*, p. 1-14, **DOI:10.13225/j.cnki.jccs.2022.0621**. (in Chinese)

[6] Lian, Z., Yuan, X., Gao, F., Liao, Y., Guo, Y., Zhao, R. (2020). Network intelligent sensing control method of hydraulic support. *Journal of China Coal Society*, vol. 45, no. 6, p. 2078-2089, **DOI:10.13225/j.cnki.jccs.ZN20.0361**. (in Chinese)

[7] Ren, H., Zhao, G., Zhou, J., Wen, Z., Ding, Y., Li, S. (2020). Full pose measurement and virtual simulation control technology of intelligent mining equipment. *Journal of China Coal Society*, vol. 45, no. 3, p. 956-971, **DOI:10.13225/j.cnki.jccs.SJ20.0335**. (in Chinese)

[8] Li, S., Ren, H. (2020). Research status and prospect of pose measurement technology of ‘ three machines ‘ equipment in fully mechanized mining face. *Coal Science and Technology*, vol. 48, no. 9, p.218-226, **DOI:10.13199/j.cnki.cst.2020.09.028**. (in Chinese)

[9] Pang, Y., Liu, X., Wang, H., Jiang, Z., Guan, S., Zhang, Z., Wang, W. (2023). Analytical method of support attitude and height of hydraulic support based on jack stroke drive. *Journal of Mining & Safety Engineering*, p. 1-14. (in Chinese)

[10] Wang, X., Cui, T., Xie, J., Shen, H., Liu, Y., Wang, B. (2021). Virtual simulation method of hydraulic support motion considering pin clearance. *Coal science and technology*, vol. 49, no. 2, p. 186-193, **DOI:10.13199/j.cnki.cst.2021.02.022**. (in Chinese)

[11] Chen, H., Chen, H., Xu, Y., Zhang, D., Ma, Y., Mao, J. (2022). Research on attitude monitoring method of advanced hydraulic support based on multi-sensor fusion. *Measurement*, vol. 187, 110341, **DOI:10.1016/j.measurement.2021.110341**.

[12] Zhang, Y., Zhang, H., Gao, K., Xu, W., Zeng, Q. (2019). New method and experiment for detecting relative position and attitude of the hydraulic support. *IEEE Access*, vol. 7, p. 181842-181854, **DOI:10.1109/ACCESS.2019.2958981**.

[13] Liang, M., Fang, X., Li, S., Wu, G., Ma, M., Zhang, Y. (2019). A fiber Bragg grating tilt sensor for attitude monitoring of hydraulic supports in coal mine working face. *Measurement*, vol. 138, p. 305-313, **DOI:10.1016/j.measurement.2019.02.060**.

[14] Zeng, X., Meng, G., Zhou, J. (2018). Analysis on the pose and dynamic response of hydraulic support under dual impact loads. *International Journal of Simulation Modelling*, vol. 17, no. 1, p. 69-80, **DOI:10.2507/ijsimm17(1)412**.

[15] Ge, X., Xie, J., Wang, X., Liu, Y., Shi, H. (2020). A virtual adjustment method and experimental study of the support attitude of hydraulic support groups in propulsion state. *Measurement*, vol. 158, 107743, **DOI:10.1016/j.measurement.2020.107743**.

[16] Wang, B., Xie, J., Wang, X., Liu, S., Liu, Y. (2021). A new method for measuring the attitude and straightness of hydraulic support groups based on point clouds. *Arabian Journal for Science and Engineering*, vol. 46, p. 11739-11757, **DOI:10.1007/s13369-021-05689-2**.

[17] Yang, X., Wang, R., Wang, H., Yang, Y. (2020). A novel method for measuring pose of hydraulic supports relative to inspection robot using LiDAR. *Measurement*, vol. 154, p. 107452, **DOI:10.1016/j.measurement.2019.107452**.

[18] Lu, X., Wang, Z., Tan, C., Yan, H., Si, L., Wei, D. (2020). A portable support attitude sensing system for accurate attitude estimation of hydraulic support based on unscented Kalman filter. *Sensors*, vol. 20, no. 19, 5459, **DOI:10.3390/s20195459**.

[19] Wang, X., Liu, S., Wang, X., Xie, J., Wang, B., Wang, Z. (2022). Research and experiment on key technologies of intelligent monitoring of fully mechanized mining face driven by AR / VR fusion. *Journal of China Coal Society*, vol. 47, no. 2, p. 969-985, **DOI:10.13225/j.cnki.jccs.2021.1113**. (in Chinese)

[20] Wang, X., Xie, J., Hao, S., Li, J., Yang, Z., Ren, F., Bao, Q. (2020). Real-time virtual monitoring method and key technology of intelligent fully mechanized mining face. *Journal of China Coal Society*, vol. 45, no. 6, p. 1984-1996, **DOI:10.13225/j.cnki.jccs.zn20.0342**. (in Chinese)

[21] Szurgacz, D., Brodny, J. (2019). Tests of geometry of the powered roof support section. *Energies*, vol. 12, no. 20, 3945, **DOI:10.3390/en12203945**.

[22] Szurgacz, D., Brodny, J. (2020). Adapting the powered roof support to diverse mining and geological conditions. *Energies*, vol. 13, no. 2, 405, **DOI:10.3390/en13020405**.

[23] Chen, G., Zhang, Z., Kong, L., Wang, H. (2020). Analysis and validation of a flexible planar two degrees-of-freedom parallel manipulator with structural passive compliance. *Journal of Mechanisms and Robotics*, vol. 12, no. 1, 011011, **DOI:10.1115/1.4045036**.

[24] Hamida, I. B., Laribi, M. A., Mlika, A., Romdhane, L., Zeghloul, S., Carbone, G. (2021). Multi-objective optimal design of a cable driven parallel robot for rehabilitation tasks. *Mechanism and Machine Theory*, vol. 156, 104141, **DOI:10.1016/j.mechmachtheory.2020.104141**.

[25] Yiyang, L., Xi, J., Hongfei, B., Zhining, W., Liangliang, S. (2021). A general robot inverse kinematics solution method based on improved PSO algorithm. *IEEE Access*, vol. 9, p. 32341-32350, **DOI:10.1109/ACCESS.2021.3059714**.

[26] Bai, Y., Luo, M., Pang, F. (2021). An algorithm for solving robot inverse kinematics based on FOA optimized BP neural network. *Applied Sciences*, vol. 11, no. 15, 7129, **DOI:10.3390/app11157129**.

[27] Luo, G., Zou, L., Wang, Z., Lv, C., Ou, J., Huang, Y. (2021). A novel kinematic parameters calibration method for industrial robot based on Levenberg-Marquardt and Differential Evolution hybrid algorithm. *Robotics and Computer-Integrated Manufacturing*, vol. 71, 102165, **DOI:10.1016/j.rcim.2021.102165**.

[28] Feng, Z., Xie, J., Yan, Z., Mei, Z., Zheng, Z., Li, T. (2023). An information processing method of software and hardware coupling for VR monitoring of hydraulic support groups. *Multimedia Tools and Applications*, vol. 82, p. 19067-19089, **DOI:10.1007/s11042-022-14128-9**.

[29] Gong, W., Liao, Z., Mi, X., Wang, L., Guo, Y. (2021). Nonlinear equations solving with intelligent optimization algorithms: A survey. *Complex System Modeling and Simulation*, vol. 1, no. 1, p. 15-32, **DOI:10.23919/CSMS.2021.0002**.

[30] Nadeem, M., He, J.-H. (2021). He-Laplace variational iteration method for solving the nonlinear equations arising in chemical kinetics and population dynamics. *Journal of Mathematical Chemistry*, vol. 59, p. 1234-1245, **DOI:10.1007/s10910-021-01236-4**.

[31] Rasheed, M., Shihab, S., Rashid, T., Enneffati, M. (2021). Some step iterative method for finding roots of a nonlinear equation. *Journal of Al-Qadisiyah for Computer Science and Mathematics*, vol. 13, no. 1, p. 95-102, **DOI:10.29304/jqcm.2021.13.1.753**.

[32] David Müzel, S., Bonhin, E. P., Guimarães, N. M., Guidi, E. S. (2020). Application of the finite element method in the analysis of composite materials: A review. *Polymers*, vol. 12, no. 4, p. 818, **DOI:10.3390/polym12040818**.

[33] Guo, Q., Yao, W., Li, W., Gupta, N. (2021). Constitutive models for the structural analysis of composite materials for the finite element analysis: A review of recent practices. *Composite Structures*, vol. 260, 113267, **DOI:10.1016/j.compstruct.2020.113267**.

[34] Bagha, A. K., Bahl, S. (2021). Finite element analysis of VGCF/pp reinforced square representative volume element to predict its mechanical properties for different loadings. *Materials Today: Proceedings*, vol. 39, p. 54-59, **DOI:10.1016/j.matpr.2020.06.108**.

[35] Zeng, Q., Li, Y., Yang, Y. (2021). Dynamic analysis of hydraulic support with single clearance. *Strojniški vestnik - Journal of Mechanical Engineering*, vol. 67, no. 1-2, p. 53-66, **DOI:10.5545/sv-jme.2020.6998**.

[36] Kardani, N., Zhou, A., Nazem, M., Shen, S.-L. (2021). Improved prediction of slope stability using a hybrid stacking ensemble method based on finite element analysis and field data. *Journal of Rock Mechanics and Geotechnical Engineering*, vol. 13, no. 1, p. 188-201, **DOI:10.1016/j.jrmge.2020.05.011**.

[37] Duan, T., Wei, J., Zhang, A., Xu, Z., Lim, T.C. (2021). Transmission error investigation of gearbox using rigid-flexible coupling dynamic model: Theoretical analysis and experiments. *Mechanism and Machine Theory*, vol. 157, 104213, **DOI:10.1016/j.mechmachtheory.2020.104213**.

[38] Xie, Y., Zeng, Q., Jiang, K., Meng, Z., Li, Q., Zhang, J. (2022). Investigation of dynamic behaviour of four-leg hydraulic support under double-impact load. *Strojniški vestnik - Journal of Mechanical Engineering*, vol. 68, no. 6, p. 385-394, **DOI:10.5545/sv-jme.2022.54**.

[39] Ren, H., Zhang, D., Gong, S., Zhou, K., Xi, C., He, M., Li, T. (2021). Dynamic impact experiment and response characteristics analysis for 1: 2 reduced-scale model of hydraulic support. *International Journal of Mining Science and Technology*, vol. 31, no. 3, p. 347-356, **DOI:10.1016/j.ijmst.2021.03.004**.

[40] Meng, Z.S., Zhang, J.M., Xie, Y.Y., Lu, Z.G., Zeng, Q.L. (2021). Analysis of the force response of a double-canopy hydraulic support under impact loads. *International Journal of Simulation Modelling*, vol. 20, p. 766-777, **DOI:10.2507/IJSIMM20-4-CO18**.

[41] Guo, C., Mao, J., Xie, M. (2022). Analysis of energy absorption characteristics of corrugated top beams of anti-impact hydraulic supports. *Alexandria Engineering Journal*, vol. 61, no. 5, p. 3757-3772, **DOI:10.1016/j.aej.2021.08.077**.

[42] Liu, Z., Li, P., Jiang, J., Liu, B. (2021). Research on vibration characteristics of mill rolls based on nonlinear stiffness of the hydraulic cylinder. *Journal of Manufacturing Processes*, vol. 64, p. 1322-1328, **DOI:10.1016/j.jmapro.2021.02.063**.

[43] Jaiswal, S., Sopanen, J., Mikkola, A. (2021). Efficiency comparison of various friction models of a hydraulic cylinder in the framework of multibody system dynamics. *Nonlinear Dynamics*, vol. 104, p. 3497-3515, **DOI:10.1007/s11071-021-06526-9**.

[44] Stawinski, L., Skowronska, J., Kosucki, A. (2021). Energy efficiency and limitations of the methods of controlling the hydraulic cylinder piston rod under various load conditions. *Energies*, vol. 14, no. 23, p. 7973, **DOI:10.3390/en14237973**.

[45] Huang, H., Wang, F., Tian C., Zhao, W., Cao, G. (2018). Design of mine hydraulic support height measurement system based on inclination sensor. *Coal Science and Technology*, vol. 46, no. 03, p. 124-129+193, **DOI:10.13199/j.cnki.cst.2018.03.021**. (in Chinese)

[46] Lu, T., Ma, P., Feng, Z., Yu, J. (2014). Design of Dynamic Monitoring and Control System for Hydraulic Support Attitude. *Coal Science and Technology*, vol. 42, no. S1, p. 169 -170,172, **DOI:10.13199/j.cnki.cst.2014.s1.071**. (in Chinese)

[47] Pang, Y. (2021). Perception and data processing technology of hydraulic support support. *Industry and Mine Automation*, vol. 47, no. 11, p. 66-73, **DOI:10.13272/j.issn.1671-251x.2021040061**. (in Chinese)

[48] Hu, X., Liu, X. (2021). The mapping and adjustment strategy of support pose and driving jack in initial bracing stage. *Journal of Mining and Safety Engineering*, vol. 38, no. 04, p. 666 -677, **DOI:10.13545/j.cnki.jmse.2020.0158**. (in Chinese)

Vsebina

Strojniški vestnik - Journal of Mechanical Engineering
letnik 70, (2024), številka 5-6
Ljubljana, maj-junij 2024
ISSN 0039-2480

Izhaja dvomesečno

Razširjeni povzetki (extended abstracts)

Strojniški vestnik - Journal of Mechanical Engineering 70(2024)5-6, SI 23

Prejeto v recenzijo: 2024-02-29
Prejeto popravljeno: 2024-03-08
Odobreno za objavo: 2024-03-26

O eksperimentalnem določanju Poissonovega količnika za kamninam podobne materiale z uporabo korelacije digitalne slike (DIC)

Pino Koc*
Univerza v Ljubljani, Fakulteta za matematiko in fiziko, Slovenija

Članek primerja rezultate dveh najpogosteje uporabljenih eksperimentalnih tehnik za določanje deformacije enoosno tlačno obremenjenega valjastega kamnitega ali iz kamninam podobnih materialov izdelanega preizkušanca, in sicer z uporabo merilnih lističev in z uporabo korelacije digitalne slike (DIC). Metodi sta uporabljeni za določanje statičnega Poissonovega količnika pri razmeroma majhnih tlakih v kamnini, ko ima poroznost v materialu še velik vpliv na rezultate.

Medtem ko tehnika merilnih lističev meri deformacije preizkušanca le lokalno na mestu pritrditve merilnega lističa, je DIC optična tehnika, ki meri deformacije na celotnem, s kamerami posnetem območju preizkušanca. Pri nehomogenih materialih, kar kamnine pogosto so, lahko lokalno merjenje deformacij poda zavajujoče rezultate. Ker je določanje Poissonovega količnika razmeroma zahtevna naloga, pri kateri že majhne merilne negotovosti vodijo do bistveno različnih rezultatov, je vsakršno izboljšanje merilne tehnike dobrodošlo.

Namen raziskave je ugotoviti, v kolikšni meri je določanje Poissonovega količnika izboljšano z izkoriščanjem meritev celotnega vidnega (s kamerami posnetega) polja v primerjavi s konvencionalno tehniko točkovno postavljenih merilnih lističev.

Eksperimentalno delo je razdeljeno na dva dela. Prvi del uvaja koncept virtualnega eksperimentiranja, pri katerem deformacije na površini valjastega preizkušanca, pridobljene z računalniško simulacijo enoosnega tlačnega testa, v nadaljevanju z namenskim programom predelamo tako, da posnemajo tako meritve merilnih lističev, kot tudi meritve DIC merilne verige. V drugem delu je izveden realni enoosni tlačni test na valjastem preizkušancu, izdelanem iz peščenjaka. Med izvajanjem testa je bilo z dvema kamerama s tehniko DIC izmerjeno polje deformacij preizkušanca na nekoliko manj, kot polovici valjaste površine preizkušanca. Te meritve so v osnovi služile za nadaljnje določanje Poissonovega količnika. Poleg tega pa, ker realne meritve z merilnimi lističi niso bile izvedene, so na mestih, kjer bi merilni lističi sicer bili nalepljeni, bile odčitane ustrezne deformacije (aksialne ali obodne, odvisno od orientacije merilnega lističa) iz DIC merilne verige. Z namenom boljše statistične analize rezultatov je bilo stohastično izbranih več deset mest za odčitavanje deformacij merilnih lisičev.

Rezultati kažejo, da je mogoče Poissonov količnik izmeriti z DIC z manjšo merilno negotovostjo, kot s konvencionalno tehniko merilnih lističev. Standardni odklon izračunanega Poissonovega količnika je v primeru virtualnega eksperimenta 3,4 krat večji pri merilnih lističih, kot pri DIC merilni tehniki, pri realnem eksperimentu pa 2,7 krat večji. V nasprotju z običajnimi merilniki napetosti so se nove optične tehnike, kot je stereo DIC, izkazale sposobne zajeti makroskopski, t. j. ne zgolj lokalni, Poissonov količnik z večjo natančnostjo in tako zožati merilno negotovost.

Poudarki:

- Za ovrednotenje standardnega odklona Poissonovega količnika pri dveh merilnih tehnikah, z merilnimi lističi in s korelacijo digitalne slike (DIC), se uporablja koncept virtualnega eksperimentiranja.
- Za merjenje Poissonovega količnika in primerjavo obeh merilnih tehnik je bil na valjastem vzorcu peščenjaka izveden enoosni tlačni test.
- V nasprotju z običajnimi merilni lističi se z novimi optičnimi tehnikami, kot je stereo DIC, izkaže, da lahko izmerijo Poissonov količnik na tipičnem preizkušancu za tlačni test z večjo natančnostjo.

Ključne besede: Poissonov količnik, korelacija digitalne slike (digital image correlation), merilni listič, kamninam podobni materiali, enoosni tlačni test

*Naslov avtorja za dopisovanje: Univerza v Ljubljani. Fakulteta za matematiko in fiziko, Slovenija, pino.koc@fmf.uni-lj.si

Strojniški vestnik - Journal of Mechanical Engineering 70(2024)5-6, SI 24

Prejeto v recenzijo: 2023-02-22
Prejeto popravljeno: 2023-05-31
Odobreno za objavo: 2023-06-22

Dvostransko krčenje odebelitev na koncih paličastih surovcev

Anh Tu Do[1,*] – Aleksey Vladimirovich Chernyaev[2]
[1] Univerza Phenikaa, Fakulteta za strojnštvo in mehatroniko, Vietnam
[2] Državna univerza v Tuli, Rusija

Znani postopki za plastično preoblikovanje osno simetričnih delov z odebelitvami na obeh koncih in pripadajoča orodja imajo več znatnih pomanjkljivosti. Zaradi le-teh se lahko poslabša kakovost in poviša cena izdelkov, omejene pa so tudi tehnološke proizvodne zmogljivosti. Za izdelavo odebelitev se praviloma uporabljajo alternativni postopki. V članku je predstavljen predlog metode za sočasno kovanje odebelitev na obeh koncih paličastih surovcev v deljenem orodju ter stroja za kovanje.

Definicija problema:

- Predlog metode za sočasno kovanje odebelitev na obeh koncih paličastih surovcev v deljenem orodju ter pripadajoče kovaške opreme.
- Opredelitev vpliva geometrijskih dimenzij obdelovanca in trenja na moč pri kovanju.
- Ocena napetostno-deformacijskega stanja v obdelovancu in poškodb materiala v zadnjem koraku kovanja izdelkov iz zlitine AA5056.
- Izdelava diagrama za določitev potrebnega števila operacij za kovanje osno simetričnih delov z odebelitvami na obeh koncih iz zlitine AA5056.

Za določitev potrebne moči za kovanje je bila opravljena simulacija procesa po metodi končnih elementov v programskem paketu QForm. Opredeljena je odvisnost med silo kovanja ter geometrijskimi dimenzijami obdelovanca in trenjem na kontaktnih površinah. Ocenjena je podvrženost materiala obdelovanca AA5056 poškodbam in izdelan je diagram za določitev potrebnega števila kovaških operacij.

Na podlagi rezultatov raziskave je podan predlog za kovanje osno simetričnih delov z odebelitvami na obeh koncih iz palic enotnega preseka, s čimer so bile razširjene tehnološke možnosti za hladno kovanje malih in preciznih delov kompleksnih oblik, ki zagotavlja izboljšanje produktivnosti in zmanjšanje izgub materiala.

Rezultati modeliranja kovanja polnih osno simetričnih delov z odebelitvami na obeh koncih iz cilindričnih surovcev so pokazali, da na sile pri kovanju vplivajo geometrijski parametri orodja in surovca: radij zaokrožitve orodne gravure, radij zaokrožitve utopa, začetni in končni premer surovca ter količnik trenja na stiku orodja in surovca. S tem je podana kvantitativna ocena vpliva omenjenih parametrov v obravnavanem razponu.

Narejena je tudi ocena podvrženosti materiala surovca poškodbam v nevarnih točkah. S tem je opredeljeno območje stopenj deformacije in sprememb geometrije izdelka za izkovanje polnih osno simetričnih delov z odebelitvami na obeh koncih v eni oz. dveh preoblikovalnih operacijah.

Ključne besede: hladno kovanje, krčenje, odebelitev na koncih, sila, podvrženost materiala poškodbam

*Naslov avtorja za dopisovanje: Fakulteta za strojništvo in mehatroniko, Univerza Phenikaa, Yen Nghia, Ha Dong, Hanoi 12116, Vietnam, tu.doanh@phenikaa-uni.edu.vn

Strojniški vestnik - Journal of Mechanical Engineering 70(2024)5-6, SI 25

Prejeto v recenzijo: 2023-08-27
Prejeto popravljeno: 2023-12-08
Odobreno za objavo: 2024-03-12

Vpliv specifične hitrosti črpalnih turbin na hidravlične prehodne pojave

Zdravko Giljen[1,*] – Miloš Nedeljković[1] – Yongguang Cheng[2]
[1] Univerza v Beogradu, Fakulteta za strojništvo, Srbija
[2] Univerza v Vuhanu, Državni laboratorij za vodne vire in hidroenergetiko, Kitajska

Glavni namen članka je analiza prehodnih pojavov pri različnih specifičnih hitrostih (*nq*) za tri modelne črpalne turbine, namenjene črpalni hidroelektrarni Bajina Bašta, ter analiza trajektorij delovnih točk med prehodnimi pojavi za vse tri črpalne turbine (*nq* = 27, 38 in 50). Predmet raziskave so krivulje karakteristik v štirih kvadrantih (4Q), podane v obliki Suterjevih krivulj (dobavna višina in moment *Wh* in *Wm* v odvisnosti od kota θ) za različna odprtja vodilnika treh modelnih črpalnih turbin pri različnih specifičnih hitrostih. Karakteristike 4Q so bile uporabljene kot vhodni podatki za razvoj numerične kode za preračun sočasne razbremenitve obeh črpalnih turbin. Opredeljeni so robni pogoji za vsako vozlišče (črpalno turbino). Avtorji so razvili numerično kodo za preračun prehodnih pojavov na podlagi metode karakteristik (MOC) (ta je bila pozneje nadgrajena z analizo vedenja sistema krmiljenja) ter jo uporabili na testnem primeru ČHE Bajina Bašta za izračun prehodnih pojavov in trajektorije delovne točke med zaustavitvijo. Matematični model je oblikovan na podlagi rezultatov preizkusov modelne črpalne turbine (karakteristike 4Q so podane v obliki Suterjevih krivulj *Wh* in *Wm*) ter enačb dinamike enote. Upoštevane so vse komponente hidravličnega sistema ČHE Bajina Bašta z ustreznimi enačbami. Predstavljena je primerjava izračunov za ČHE Bajina Bašta (dobavna višina spiralnega ohišja, pretok, vrtilna hitrost in dobavna višina sesalne cevi), ki razkriva znatne razlike med vrednostmi za različne specifične hitrosti. Podani so rezultati izračunov za prehodne pojave dveh črpalnih turbin v ČHE Bajina Bašta ob sočasni razbremenitvi črpalne turbine 1 pri moči 281 MW (turbinski način) in črpalne turbine 2 pri moči 284 MW (turbinski način, vrednosti moči so bile izmerjene med dejansko razbremenitvijo). Pri vrednosti *nq* = 27 (izvirna specifična hitrost črpalnih turbin v ČHE) je rezultate izračunov mogoče primerjati s terenskimi meritvami, medtem ko je za vrednosti *nq* = 38 in *nq* = 50 mogoče predstaviti samo rezultate izračunov.

Uporabljen je bil pristop z analizo negativnega vpliva specifične hitrosti *nq* med prehodnim pojavom na črpalni turbini. V teoretičnem delu študije je podan pregled literature na temo raziskav prehodnih pojavov na črpalnih turbinah in črpalkah. Predstavljeni so analiza rezultatov izračunov prehodnih pojavov na dveh črpalnih turbinah (pri različnih vrednostih *nq* = 27, 38 in 50), spremembe tlaka v spiralnem ohišju, tlak v sesalni cevi, vrtilna hitrost, pretok in odprtje vodilnika. Analiziran je vpliv specifične hitrosti *nq* na prehodne pojave.

Predstavljeni so izračuni sprememb tlaka, vrtilne hitrosti in pretoka v obratovalnih režimih postroja, pomembna pa je predvsem uporaba teh rezultatov za določitev parametričnih trajektorij pretoka in hitrosti ($Q_{11} - n_{11}$) za delovne točke. Opisano je nestabilno vedenje črpalne turbine v turbinskem režimu. Trajektorije periodično potekajo tudi skozi območje vzvratnega črpanja, kar je še posebej izraženo ob karakterističnih S-krivuljah in lahko povzroči večje nestabilnosti obratovanja med prehodnimi pojavi.

Rezultati izračunov so bili potrjeni s terenskimi preizkusi. Primerjavo izmerjenih vrednosti in izračunov ovirajo negotovosti, povezane s terenskimi meritvami. Težavo pri vodnih sistemih predstavlja neznana količina zraka, ki je ujet na določenih mestih v sistemu. Med prehodnimi pojavi lahko pride do izločanja raztopljenih plinov v območjih nizkega tlaka. Izločitev manjših količin plina ima velik vpliv na valovno hitrost, ta pojav pa znatno vpliva na čas in velikost tlaka. Dejanske karakteristike črpalnih turbin, črpalk in turbin za vse delovne cone turbostrojev v primeru odpovedi niso znane. Računalniške simulacije niso vključevale vseh omenjenih parametrov, zato je mogoče pričakovati določene napake oz. neujemanje izračunov z meritvami.

Predstavljena je primerjava izračunov za ČHE Bajina Bašta (dobavna višina spiralnega ohišja, pretok, vrtilna hitrost in dobavna višina sesalne cevi), ki razkriva znatne razlike med rezultati za različne specifične hitrosti. Iz tega sledi sklep, da različne specifične hitrosti signifikantno vplivajo na prehodne pojave v črpalnih turbinah. Pomemben prispevek članka je podrobna analiza trajektorije delovne točke med prehodnimi pojavi za vse tri modele črpalnih turbin. Delovna točka se premika iz turbinske cone (III) v cono vzvratnega črpanja (IV), črpalna turbina pa deluje vzdolž karakteristične S-krivulje. To povzroča težave pri razbremenitvi zaradi neobičajnega povišanja vodnega tlaka in okrepitve vibracij, ki ogrožajo stabilnost stroja. Pričujoča analiza prvič kvantitativno razkriva negativni vpliv specifične hitrosti *nq* na tovrstno vedenje strojev. Predstavljeni rezultati bodo uporabni za projektante črpalnih hidroelektrarn pri izbiri gonilnikov s primerno specifično hitrostjo *nq*.

Ključne besede: hidravlični prehodni pojavi, črpalna turbina, vpliv specifične hitrosti, razbremenitev, trajektorija delovne točke, metoda karakteristik

*Naslov avtorja za dopisovanje: Univerza v Beogradu, Fakulteta za strojništvo, Kraljice Marije 16, 11120 Beograd, Srbija, zgiljen@gmail.com

Strojniški vestnik - Journal of Mechanical Engineering 70(2024)5-6, SI 26

Prejeto v recenzijo: 2023-09-07
Prejeto popravljeno: 2024-02-11
Odobreno za objavo: 2024-04-03

Vpliv in optimizacija parametrov laserskega teksturiranja površine poliformaldehida (POM)

Fengren Li[1,2] – Chao Li[1,2,*] – Juan Zhou[3] – Jiantao He[1,2] – Jiebin Wang[1,2] – Cong Luo[1,2] – Si Li[1]

[1] Kolidž za strojništvo, Znanstveno-tehniški inštitut v Hunanu, Kitajska
[2] Državni laboratorij za pametno proizvodnjo in optimizacijo storitev na področju laserske obdelave in brušenja v strojništvu, Kitajska
[3] Kolidž za elektromehaniko, Poklicni tehniški kolidž Yueyang, Kitajska

Lasersko teksturiranje lahko znatno izboljša površinske lastnosti materiala POM (obstojnost proti obrabi, hidrofobnost itd.). Izbor primernih parametrov za lasersko mikroteksturiranje površin je zato pomembna raziskovalna tema.

Pomanjkanje raziskav o vplivu procesnih parametrov je danes glavni vzrok za nezmožnost doslednega doseganja strukturno vrhunskih in funkcionalnih mikrotekstur na površini POM. Za natančno vodenje laserske obdelave delov iz materiala POM in doseganje kakovostnejših površin je potrebna optimizacija pri izbiri parametrov laserske obdelave ter opredelitev modelov za napovedovanje geometrijskih lastnosti tekstur na podlagi omenjenih parametrov.

Pričujoča študija obravnava vpliv treh parametrov pikosekundnega laserja (moč, hitrost premikanja in širina impulzov) na globino tekstur in hrapavost površine na dnu tekstur. Postavljen je tudi model za napovedovanje globine in hrapavosti na dnu tekstur. Z večciljno optimizacijo parametrov laserja po analitični metodi Grey-Taguchi je bila opredeljena optimalna kombinacija parametrov za visokokakovostno mikroteksturiranje.

Rezultati eksperimentov so pokazali, da je globina mikrotekstur povezana predvsem s skupnim vnosom energije laserja. Večja moč in nižja hitrost premikanja laserja pomagata pri doseganju večje globine. Hrapavost na dnu mikrotekstur je odvisna od morfologije strjevanja raztaljenega materiala. Sprva se povečuje in nato zmanjšuje z višanjem moči laserja ter je v pozitivni korelaciji s hitrostjo premikanja. Sprememba širine impulzov le minimalno vpliva na kakovost mikrotekstur. Vrednosti hrapavosti in globine tekstur pri optimalnih parametrih procesa ($A_5B_1C_1$) sta znašali 1,373 μm in 466 μm. V primerjavi z minimalno hrapavostjo površine in največjo globino, ki sta bili doseženi v ortogonalnih eksperimentih, se je površinska hrapavost zmanjšala za 10,08 %, globina pa se je povečala za 3,33 %. Napaki modela za napovedovanje globine in površinske hrapavosti znašata 1,93 oz. 7,60 %, model pa torej izpolnjuje zahteve glede zanesljivosti.

Članek obravnava samo vplivne faktorje kot so moč laserja, hitrost premikanja in širina impulzov, nadaljnje raziskave pa bodo lahko zajele še parametre kot sta število prehodov in pot laserja za dodatno izboljšanje točnosti napovedi.

Študija zagotavlja teoretično in eksperimentalno podporo uporabi pikosekundnih laserjev pri izdelavi visokokakovostnih mikrotekstur na površini POM.

Ključne besede: obdelava s pikosekundnim laserjem, optimizacija parametrov, poliformaldehid (POM), analitična metoda Grey-Taguchi, model za napovedovanje, mikrotekstur

*Naslov avtorja za dopisovanje: Kolidž za strojništvo, Znanstveno-tehniški inštitut v Hunanu, Yueyang 414006, Kitajska, lch@hnist.edu.cn

Strojniški vestnik - Journal of Mechanical Engineering 70(2024)5-6, SI 27

Prejeto v recenzijo: 2023-12-07
Prejeto popravljeno: 2024-03-28
Odobreno za objavo: 2024-04-11

Večkriterijska optimizacija parametrov procesa TIG varjenja za energijsko učinkovitost in kakovost

An-Le Van[1] – Thai-Chung Nguyen[2] – Huu-Toan Bui[2] – Xuan-Ba Dang[3] – Trung-Thanh Nguyen[2,*]

[1] Univerza Nguyen Tat Thanh, Hošiminh, Vietnam
[2] Tehniška univerza Le Quy Don, Hanoj, Vietnam
[3] Tehniška in pedagoška univerza v Hošiminhu, Hošiminh, Vietnam

Pričujoče delo obravnava optimizacijo toka (*I*), napetosti (*V*), pretoka (*F*) in dolžine obloka (*G*) pri TIG varjenju materiala Ti40A za zmanjšanje vnosa toplote (*HI*) ter izboljšanje porušitvene natezne trdnosti (*TS*) in mikrotrdote (*MH*).

Varjenje TIG je uveljavljen postopek za spajanje materialov z netaljivo elektrodo. Vpliv mehanskih lastnosti in oblik na varjenje TIG je pogosto upoštevan, medtem ko vnos toplote še ni bil raziskan. Z zmanjšanjem vnosa toplote je mogoče izboljšati energijsko učinkovitost varjenja TIG. Tudi vpliv parametrov procesa TIG na vrednosti *HI*, *TS* in *MH* še ni bil preučen.

Za uvedbo kriterijev zmogljivosti je bilo uporabljeno omrežje radialnih baznih funkcij (RBFN), za oceno vrednosti uteži in določitev optimalnih točk pa sta bila uporabljena utežena analiza glavnih komponent (WPCA) in adaptivni genetski algoritem z nedominantnim razvrščanjem II (ANSGA-II). Za določitev najboljše rešitve je bila uporabljena metoda razvrščanja na osnovi površin (EAMR).

Sledijo rezultati:

- Optimalne vrednosti *I*, *V*, *F* in *G* znašajo 89 A, 23 V, 20 l/min in 1,5 mm. Vrednosti *TS* in *MH* sta se izboljšali za 1,2 in 19,8 %, medtem ko je prihranek pri *HI* znašal 18,4 %.
- Modeli RBFN zagotavljajo sprejemljivo točnost za potrebe napovedovanja. Metoda ANSGA-II omogoča boljšo optimizacijo kot konvencionalna metoda NSGA-II.
- Vrednosti *HI*, *TS* in *MH* po TIG varjenju materiala Ti40A je mogoče optimizirati tudi v praksi.

Vpliv faktorjev varjenja TIG na onesnaženje zraka in raztezke bo obravnavan v nadaljnjih raziskavah.

Prispevki pričujočega dela in eksperimentalne analize:

- Optimizacija postopka varjenja TIG z ozirom na vnos toplote, porušitveno natezno trdnost in mikrotrdoto.
- Uporaba omrežja radialnih baznih funkcij za določitev kriterijev zmogljivosti postopka TIG.
- Predlog in uporaba adaptivnega genetskega algoritma II z nedominantnim razvrščanjem.

Ključne besede: varjenje TIG, vnos toplote, porušitvena natezna trdnost, mikrotrdota, omrežje radialnih baznih funkcij, optimizacija

*Naslov avtorja za dopisovanje: Le Quy Don tehniška univera, 236 Hoang Quoc Viet, Ha Noi, Vietnam, trungthanhnguyen@lqdtu.edu.vn

Strojniški vestnik - Journal of Mechanical Engineering 70(2023)5-6, SI 28

Prejeto v recenzijo: 2023-12-08
Prejeto popravljeno: 2024-03-11
Odobreno za objavo: 2024-04-15

Eksperimentalna uporaba moduliranih in nemoduliranih nizkofrekvenčnih akustičnih valov za gašenje plamena: pregled izbranih primerov

Jacek Wilk-Jakubowski[1,*] – Grzegorz Wilk-Jakubowski[2,3] – Valentyna Loboichenko[4,5]
[1] Tehniška univerza v Kielcah, Poljska
[2] Stara poljska univerza za aplikativne vede, Poljska
[3] Inštitut za krizno upravljanje in računalniško modeliranje, Poljska
[4] Univerza v Sevilli, Višja tehniška šola, Španija
[5] Nacionalna tehniška univerza v Lucku, Ukrajina

Pričujoči članek obravnava različne vidike protipožarne zaščite. Obvladovanje požarov je v praksi zelo širok pojem, ki med drugim zajema: (1) zaznavanje plamena, vključno z obdelavo slike in umetno inteligenco, ter (2) gašenje plamena.

Cilj članka je obravnava drugega vidika obvladovanja požarov, konkretno gašenja s pomočjo akustičnih valov (2), ter se osredotoča na eksperimentalne poskuse uporabe moduliranih in nemoduliranih nizkofrekvenčnih akustičnih valov za gašenja plamenov. Zvočna valovanja, ki jih sicer zaznavamo kot nezaželen hrup, se lahko v praksi namreč učinkovito uporabljajo za gašenje.

Najprej je predstavljeno stanje razvoja tehnologije, temu sledijo metode in naprava za gašenje, zgradba sistema za merjenje položaja in končno rezultati eksperimentov. Članek predstavlja nove, eksperimentalno pridobljene znanstvene ugotovitve v zvezi z uporabo nizkofrekvenčnih akustičnih valov (sinusnih valov in valov, amplitudno moduliranih s kvadratno valovno obliko) za gašenje plamena. Opisano je delovanje akustične metode za gašenje in predstavljeni so rezultati preizkusov njene učinkovitosti na laboratorijskem preizkuševališču z visokozmogljivo akustično gasilno napravo. Eksperimenti so dokazali uporabnost moduliranih in nemoduliranih nizkofrekvenčnih zvočnih valovnih oblik za gašenje. Preizkusi so v obeh primerih uspeli. V praksi velja, da se z nižanjem frekvence akustičnih valov povečuje stopnja turbulentnosti plamena. Izkazalo se je, da je z ustreznim generiranjem in usmerjanjem zvočnih valov mogoče pogasiti plamen. Pridobljeni podatki so predstavljeni v obliki preglednic in diagramov. Zvočni valovi lahko prehajajo skozi različne materiale (trdne, kapljevije in plinaste), zato je akustična metoda uporabna tako za gašenje snovi kakor tudi za podporo/obvladovanje zgorevalnega procesa na težko dosegljivih mestih.

Predstavljene so tudi prednosti uporabe globokih nevronskih mrež za zaznavanje plamena na podlagi namenskih rešitev, oblikovanih v mednarodnem sodelovanju. Opredeljene so potencialne prednosti kombiniranja obeh tehnologij (v popolnoma avtomatiziranih sistemih), omejitve, odprta vprašanja in načrti za prihodnost. Eksperimentalne raziskave osvetljujejo nov pristop h gašenju požarov (zlasti s protipožarnimi preprekami). Ta okoljsko varna tehnika lahko na dolgi rok postane dodatno sredstvo ali podpora pri protipožarni zaščiti, njene aplikacije pa je mogoče pričakovati v industrijskih postrojenjih in v proizvodnih obratih. Akustične gasilne sisteme je mogoče vgraditi v stene in temelje, s čimer se odpirajo nove možnosti za njihovo uporabo. Članek se zaključi s sklepom, da je plamene mogoče pogasiti takoj, ko se pojavijo, in tako preprečiti izbruh hujšega požara. Tako se učinkovito zmanjša materialna škoda in izboljša splošna varnost.

Ključne besede: akustično gašenje plamena, gasilni sistemi, globoke nevronske mreže, elektrotehnika in strojništvo, protipožarne prepreke, gasilni sistem, dušenje plamena

*Naslov avtorja za dopisovanje: Kielce tehniška univerza, Fakulteta za elektrotehniko, Avtomatiko in računalništvo, 7 Tysiaclecia Panstwa Polskiego Ave., 25-314, Kielce, Poljska, jwilk@tu.kielce.pl

Strojniški vestnik - Journal of Mechanical Engineering 70(2024)5-6, SI 29

Prejeto v recenzijo: 2023-06-08
Prejeto popravljeno: 2024-02-06
Odobreno za objavo: 2023-064-12

Vrednotenje stanja dna rezervoarjev za naftne derivate- napoved preostale dobe trajanja

Aleš Povše[1] – Saša Skale[2] – Jelena Vojvodić Tuma[3]
[1]Mednarodna podiplomska šola Jožefa Stefana, Slovenija
[2]SKALA, Saša Skale s.p., Slovenija
[3]Inštitut za energetski inženiring, , Dr. Jelena Vojvodić Tuma s.p., Slovenija

Dolgi časovni intervali (običajno vsaj 10 let) med pregledi stanja notranjosti nadzemnih rezervoarjev za skladiščenje naftnih derivatov predstavljajo, v primeru ugotovljenih korozijskih poškodb, pomemben problem za napoved preostale obratovalne dobe rezervoarja.

Stanje dna rezervoarja smo ovrednotili z neporušitvenimi meritvami debeline pločevine z ultrazvokom in meritvami globine korozijskih poškodb z iglo. Zaradi velike površine dna rezervoarja in omejenega časa za meritve je delež površin z izvedenimi meritvami majhen. Nezanesljivost omejenega števila meritev glede na površino dna smo izboljšali z uporabo ekstremne statistike. Ekstremne vrednosti, kot je minimalna debelina pločevin in maksimalna globina korozijskih razjed, se ocenijo iz uporabljenih porazdelitev. Uporabili smo dvojno eksponentno porazdelitev maksimumov (Gumbel-ova porazdelitev) za oceno maksimalne globine korozijskih razjed. Za oceno minimalne debeline pločevin, dna rezervoarja, pa smo uporabili dvojno eksponentno porazdelitev minimalnih vrednosti.

Pri obeh porazdelitvah smo ekstremne vrednosti, minimalno debelino pločevine in maksimalno globino korozijskih razjed, ocenili z gotovostjo 90 %. Meritve hitrosti korozije na dnu nadzemnih rezervoarjev za skladiščenje naftnih derivatov, so nam omogočile razvoj novega modela za napoved preostale uporabne dobe rezervoarja. To nam je omogočilo izračun parametrov eksponentnega empiričnega modela za aktivno raztapljanje jekla. Pri standardnih modelih se hitrost korozije oceni z linearno ekstrapolacijo meritev na začetno (projektno) stanje dna rezervoarja. Pri tem je pomembno tudi upoštevati razliko med dejanskimi in nominalnimi debelinami pločevine dna. Začetno stanje dna je namreč znano samo na podlagi podatkov iz projektne dokumentacije. Ta opredeli zgolj razred in nominalno debelino pločevin, kar pa praktično prepreči zanesljivo linearno ekstrapolacijo debelin pločevine na začetno stanje. Ravno tako pa povzroči nezanesljivost pri opredelitvi limit za odpoved rezervoarja. V našem delu smo izhodno debelino pločevine upoštevali minimalno možno debelino razreda uporabljene pločevine dna in opozorili na razlike pri oceni hitrosti korozije zaradi nezanesljivosti začetnih debelin pločevin, omejenega števila meritev in uporabljenega modela za napoved preostale obratovalne dobe rezervoarja. Nezanesljivost zaradi poznavanja začetne debeline pločevine nam pri linearnih modelih prepreči zanesljivo oceno hitrosti korozije. S stališča linearnih modelov so boljše ocene hitrosti korozije na osnovi meritev globine razjed, kjer je nezanesljivost zgolj pri limiti za odpoved rezervoarja.

Primerjava ocen hitrosti korozije, pridobljenih z linearno ekstrapolacijo in eksponentnimi modeli je pokazala nezanesljivost linearnega modela. Ta zaradi neupoštevanja dinamične narave korozijskih procesov na dnu korozijskih razjed, znatno podceni hitrosti korozije. Pokazali smo, da so uveljavljeni standardni modeli za napoved preostale obratovalne dobe rezervoarjev nezanesljivi. Še posebno v primerih, ko imamo na dnu rezervoarja lokalne korozijske poškodbe. Linearni modeli namreč ne upoštevajo sprememb hitrosti korozije zaradi mehanizma aktivnega raztapljanja jekla na dnu razjed. Predlagani eksponentni empirični model bolje upošteva spremembe hitrosti korozije s časom zaradi aktivnega (pospešenega) raztapljanja materiala na dnu korozijskih razjed, kar je posledica lokalnih mehanizmov korozije. Izmerjene hitrosti korozije so bile bistveno višje od z linearno ekstrapolacijo ocenjenih vrednosti.

Zato predlagan model, v primerjavi s standardnim linearnim modelom, omogoča bistveno bolj zanesljivo in konservativno napoved preostale obratovalne dobe rezervoarja.

Ključne besede: luknjičasta korozija, dno rezervoarja za skladiščenje, časovno odvisna zanesljivost, korozijski model

*Naslov avtorja za dopisovanje: Mednarodna podiplomska šola Jožefa Stefana, Ljubljana, Slovenija, ales.povse@petrol.si

Strojniški vestnik - Journal of Mechanical Engineering 70(2024)5-6, pp1-pp30

Prejeto v recenzijo: 2024-03-19
Prejeto popravljeno: 2024-04-22
Odobreno za objavo: 2024-04-22

Analiza orientacije hidravličnega podporja na podlagi dolžine stojk

Mingfei Mu[1] – Bowen Xie[1] – Yang Yang[1,2,3,*]

[1] Kolidž za strojništvo in elektrotehniko, Znanstveno tehniška univerza v Šandongu, Kitajska
[2] Državni laboratorij province Šandong za rudarsko strojništvo, Kitajska
[3] Sodelovalno inovacijsko središče za pametno opremo in tehnologijo v rudarstvu, Kitajska

Obstoječe metode za nadzor in nastavljanje orientacije hidravličnega podporja vključujejo različne zaznavalne tehnologije, njihova realizacija pa je težavna zaradi nejasnih mehanizmov nadzora ter kompleksnih in mnogoštevilnih senzorjev. Za razrešitev problema nadzora in nastavljanja orientacije hidravličnega podporja je najprej vzpostavljen matematični model kinematike hidravličnega podporja po metodi ključnih označevalnih točk in model dvodimenzionalnih palic. Podan je predlog algoritma za reševanje (v smeri naprej in nazaj) orientacije hidravličnega podporja na podlagi dolžine dvojnega pogona sprednjih in zadnjih stojk. Nato je oblikovan model dinamike togih teles za simulacijo hidravličnega podporja, namenjen preverjanju teoretičnega analitičnega modela in potrditvi algoritma. Model za simulacijo togih teles je mogoče uporabiti za nadzor hidravličnega podporja. Ob upoštevanju vpliva elastičnih deformacij materiala je postavljen togo-fleksibilni sklopljeni model za simulacijo dinamike hidravličnega podporja, namenjen preučitvi vpliva elastičnih deformacij komponent na orientacijo hidravličnega podporja ter njihovih vzrokov. Na osnovi tega je bil oblikovan togo-fleksibilni sklopljeni model za simulacijo dinamike hidravličnega podporja z zračnostjo tako, da je bil rotacijski sklep v simulacijskem modelu zamenjan s polnim sornikom in luknjo. Preučen je vpliv zračnosti zveze sornika in luknje na orientacijo hidravličnega podporja in njeni vzroki. Določena je dejanska orientacija in karakteristike sprememb hidravličnega podporja v simuliranih realnih pogojih. Ob upoštevanju stiskalne sile hidravličnih cilindrov stojk je bil oblikovan model za simulacijo dinamike hidravličnega podporja z zračnostjo in togo-fleksibilno ter mehansko-hidravlično sklopitvijo. Obremenilni preizkus je dokazal, da ima stiskalna sila hidravličnega cilindra velik vpliv na orientacijo hidravličnega podporja. Pri njenem nastavljanju zato ni mogoče uporabiti teoretičnih izračunov pretoka ter je treba neposredno meriti dolžino stojk.

Glavni znanstveni prispevki:

1. Algoritm za izračun orientacije hidravličnega podporja z dolžino dvojnega pogona sprednjih in zadnjih stojk, metoda za nadzor in nastavljanje orientacije na podlagi dolžine stojk.
2. Analiza vpliva elastičnih deformacij materiala in zračnosti zveze sornik-luknja na orientacijo, določitev dejanske orientacije v simuliranih pogojih.
3. Upoštevanje stiskalne sile hidravličnih cilindrov, določitev togo-fleksibilno in mehansko-hidravlično sklopljenega modela za simulacijo dinamike podporja z zračnostjo.

Omejitve članka: Obravnavana sta samo položaj in orientacija hidravličnega podporja. Popolnih podatkov o položaju in orientaciji celotnega podporja v prostoru (koti zasuka okrog treh prostorskih osi) ni mogoče pridobiti, upoštevana pa je samo ena podpora.

Smeri prihodnjih raziskav:

1. Analiza orientacije osnove ali hidravličnega podporja v prostoru, določitev orientacije celotnega podporja prek ene same komponente.
2. Popoln izračun položaja in orientacije podporne skupine, nadzor skupine na podlagi geometrijskih odvisnosti sosednjega ogrodja.

Ključne besede: analiza orientacije hidravličnega podporja, simulacijska analiza, togo-fleksibilna sklopitev, zračnost zveze sornik-luknja, togost hidravličnega cilindra, kinematična analiza

*Naslov avtorja za dopisovanje: Kolidž za strojništvo in elektrotehniko, Znanstveno tehniška univerza v Šandongu, Šandong, Kitajska, yang.yang@sdust.edu.cn

Guide for Authors

All manuscripts must be in English. Pages should be numbered sequentially. The manuscript should be composed in accordance with the Article Template given above. The suggested length of contributions is 10 to 20 pages. Longer contributions will only be accepted if authors provide justification in a cover letter. For full instructions see the Information for Authors section on the journal's website: http://en.sv-jme.eu .

SUBMISSION:

Submission to SV-JME is made with the implicit understanding that neither the manuscript nor the essence of its content has been published previously either in whole or in part and that it is not being considered for publication elsewhere. All the listed authors should have agreed on the content and the corresponding (submitting) author is responsible for having ensured that this agreement has been reached. The acceptance of an article is based entirely on its scientific merit, as judged by peer review. Scientific articles comprising simulations only will not be accepted for publication; simulations must be accompanied by experimental results carried out to confirm or deny the accuracy of the simulation. Every manuscript submitted to the SV-JME undergoes a peer-review process.

The authors are kindly invited to submit the paper through our web site: http://ojs.sv-jme.eu. The Author is able to track the submission through the editorial process - as well as participate in the copyediting and proofreading of submissions accepted for publication - by logging in, and using the username and password provided.

SUBMISSION CONTENT:

The typical submission material consists of:

- A **manuscript** (A PDF file, with title, all authors with affiliations, abstract, keywords, highlights, inserted figures and tables and references),
- Supplementary files:
  - a **manuscript** in a WORD file format
  - a **cover letter** (please see instructions for composing the cover letter)
  - a ZIP file containing **figures** in high resolution in one of the graphical formats (please see instructions for preparing the figure files)
  - possible **appendicies** (optional), cover materials, video materials, etc.

Incomplete or improperly prepared submissions will be rejected with explanatory comments provided. In this case we will kindly ask the authors to carefully read the Information for Authors and to resubmit their manuscripts taking into consideration our comments.

COVER LETTER INSTRUCTIONS:

Please add a **cover letter** stating the following information about the submitted paper:

1. Paper **title**, list of **authors** and their **affiliations**. **One** corresponding author should be provided.
2. **Type of paper**: original scientific paper (1.01), review scientific paper (1.02) or short scientific paper (1.03).
3. A **declaration** that neither the manuscript nor the essence of its content has been published in whole or in part previously and that it is not being considered for publication elsewhere.
4. State the **value of the paper** or its practical, theoretical and scientific implications. What is new in the paper with respect to the state-of-the-art in the published papers? Do not repeat the content of your abstract for this purpose.
5. We kindly ask you to suggest at least two **reviewers** for your paper and give us their names, their full affiliation and contact information, and their scientific research interest. The suggested reviewers should have at least two relevant references (with an impact factor) to the scientific field concerned; they should not be from the same country as the authors and should have no close connection with the authors.
6. Please confirm that authors are willing/able to pay the Open Access **publication fee** as indicated in the Guide for Authors under Publication Fee, available at https://www.sv-jme.eu/guide-for-authors-online/.

FORMAT OF THE MANUSCRIPT:

The manuscript should be composed in accordance with the Article Template. The manuscript should be written in the following format:

- A **Title** that adequately describes the content of the manuscript.
- A list of **Authors** and their **affiliations**.
- An **Abstract** that should not exceed 250 words. The Abstract should state the principal objectives and the scope of the investigation, as well as the methodology employed. It should summarize the results and state the principal conclusions.
- 4 to 6 significant **key words** should follow the abstract to aid indexing.
- 4 to 6 **highlights;** a short collection of bullet points that convey the core findings and provide readers with a quick textual overview of the article. These four to six bullet points should describe the essence of the research (e.g. results or conclusions) and highlight what is distinctive about it.
- An **Introduction** that should provide a review of recent literature and sufficient background information to allow the results of the article to be understood and evaluated.
- A **Methods** section detailing the theoretical or experimental methods used.
- An **Experimental section** that should provide details of the experimental set-up and the methods used to obtain the results.
- A **Results** section that should clearly and concisely present the data, using figures and tables where appropriate.
- A **Discussion** section that should describe the relationships and generalizations shown by the results and discuss the significance of the results, making comparisons with previously published work. (It may be appropriate to combine the Results and Discussion sections into a single section to improve clarity.)
- A **Conclusions** section that should present one or more conclusions drawn from the results and subsequent discussion and should not duplicate the Abstract.
- **Acknowledgement** (optional) of collaboration or preparation assistance may be included. Please note the source of funding for the research.
- **Nomenclature** (optional). Papers with many symbols should have a nomenclature that defines all symbols with units, inserted above the references. If one is used, it must contain all the symbols used in the manuscript and the definitions should not be repeated in the text. In all cases, identify the symbols used if they are not widely recognized in the profession. Define acronyms in the text, not in the nomenclature.
- **References** must be cited consecutively in the text using square brackets [1] and collected together in a reference list at the end of the manuscript.
- **Appendix(-icies)** if any.

SPECIAL NOTES

Units: The SI system of units for nomenclature, symbols and abbreviations should be followed closely. Symbols for physical quantities in the text should be written in italics (e.g. *v*, *T*, *n*, etc.). Symbols for units that consist of letters should be in plain text (e.g. ms^{-1}, K, min, mm, etc.). Please also see: http://physics.nist.gov/cuu/pdf/sp811.pdf .

Abbreviations should be spelt out in full on first appearance followed by the abbreviation in parentheses, e.g. variable time geometry (VTG). The meaning of symbols and units belonging to symbols should be explained in each case or cited in a **nomenclature** section at the end of the manuscript before the References.

Figures (figures, graphs, illustrations digital images, photographs) must be cited in consecutive numerical order in the text and referred to in both the text and the captions as Fig. 1, Fig. 2, etc. Figures should be prepared without borders and on white grounding and should be sent separately in their original formats. If a figure is composed of several parts, please mark each part with a), b), c), etc. and provide an explanation for each part in Figure caption. The caption should be self-explanatory. Letters and numbers should be readable (Arial or Times New Roman, min 6 pt with equal sizes and fonts in all figures). Graphics (submitted as supplementary files) may be exported in resolution good enough for printing (min. 300 dpi) in any common format, e.g. TIFF, BMP or JPG, PDF and should be named Fig1.jpg, Fig2.tif, etc. However, graphs and line drawings should be prepared as vector images, e.g. CDR, AI. Multi-curve graphs should have individual curves marked with a symbol or otherwise provide distinguishing differences using, for example, different thicknesses or dashing.

Tables should carry separate titles and must be numbered in consecutive numerical order in the text and referred to in both the text and the captions as Table 1, Table 2, etc. In addition to the physical quantities, such as *t* (in italics), the units [s] (normal text) should be added in square brackets. Tables should not duplicate data found elsewhere in the manuscript. Tables should be prepared using a table editor and not inserted as a graphic.

REFERENCES:

A reference list must be included using the following information as a guide. Only cited text references are to be included. Each reference is to be referred to in the text by a number enclosed in a square bracket (i.e. [3] or [2] to [4] for more references; do not combine more than 3 references, explain each). No reference to the author is necessary.

References must be numbered and ordered according to where they are first mentioned in the paper, not alphabetically. All references must be complete and accurate. Please add DOI code when available. Examples follow.

Journal Papers:

Surname 1, Initials, Surname 2, Initials (year). Title. *Journal*, volume, number, pages, DOI code.

[1] Hackenschmidt, R., Alber-Laukant, B., Rieg, F. (2010). Simulating nonlinear materials under centrifugal forces by using intelligent cross-linked simulations. *Strojniški vestnik - Journal of Mechanical Engineering*, vol. 57, no. 7-8, p. 531-538, DOI:10.5545/sv-jme.2011.013.

Journal titles should not be abbreviated. Note that journal title is set in italics.

Books:

Surname 1, Initials, Surname 2, Initials (year). Title. Publisher, place of publication.

[2] Groover, M.P. (2007). *Fundamentals of Modern Manufacturing*. John Wiley & Sons, Hoboken.

Note that the title of the book is italicized.

Chapters in Books:

Surname 1, Initials, Surname 2, Initials (year). Chapter title. Editor(s) of book, book title. Publisher, place of publication, pages.

[3] Carbone, G., Ceccarelli, M. (2005). Legged robotic systems. Kordić, V., Lazinica, A., Merdan, M. (Eds.), Cutting Edge Robotics. Pro literatur Verlag, Mammendorf, p. 553-576.

Proceedings Papers:

Surname 1, Initials, Surname 2, Initials (year). Paper title. Proceedings title, pages.

[4] Štefanić, N., Martinčević-Mikić, S., Tošanović, N. (2009). Applied lean system in process industry. *MOTSP Conference Proceedings*, p. 422-427.

Standards:

Standard-Code (year). Title. Organisation. Place.

[5] ISO/DIS 16000-6.2:2002. *Indoor Air – Part 6: Determination of Volatile Organic Compounds in Indoor and Chamber Air by Active Sampling on TENAX TA Sorbent, Thermal Desorption and Gas Chromatography using MSD/FID.* International Organization for Standardization. Geneva.

WWW pages:

Surname, Initials or Company name. Title, from http://address, date of access.

[6] Rockwell Automation. Arena, from *http://www.arenasimulation.com*, accessed on 2009-09-07.

EXTENDED ABSTRACT:

When the paper is accepted for publishing, the authors will be requested to send an **extended abstract** (approx. one A4 page or 3500 to 4000 characters or approx. 600 words). The instruction for composing the extended abstract are published on-line: http://www.sv-jme.eu/information-for-authors/ .

COPYRIGHT:

Authors submitting a manuscript do so on the understanding that the work has not been published before, is not being considered for publication elsewhere and has been read and approved by all authors. The submission of the manuscript by the authors means that the authors automatically agree to publish the paper uder CC-BY 4.0 Int. or CC-BY-NC 4.0 Int. when the manuscript is accepted for publication. All accepted manuscripts must be accompanied by a Copyright Agreement, which should be sent to the editor. The work should be original work by the authors and not be published elsewhere in any language without the written consent of the publisher. The proof will be sent to the author showing the final layout of the article. Proof correction must be minimal and executed quickly. Thus it is essential that manuscripts are accurate when submitted. Authors can track the status of their accepted articles on https://en.sv-jme.eu/.

PUBLICATION FEE:

Authors will be asked to pay a publication fee for each article prior to the article appearing in the journal. However, this fee only needs to be paid after the article has been accepted for publishing. The fee is 380 EUR (for articles with maximum of 6 pages), 470 EUR (for articles with maximum of 10 pages), plus 50 EUR for each additional page. The additional cost for a color page is 90.00 EUR (only for a journal hard copy; optional upon author's request). These fees do not include tax.

Strojniški vestnik -Journal of Mechanical Engineering
Aškerčeva 6, 1000 Ljubljana, Slovenia, e-mail: info@sv-jme.eu

9 770039 248001
ISSN 0039-2480

http://www.sv-jme.eu

Contents

Papers